

Plasma-assisted synthesis of transition metal-based nanostructures for zinc-air batteries

Dissertation

zur Erlangung des Doktorgrades

der Mathematisch-Naturwissenschaftlichen Fakultät

der Christian-Albrechts-Universität zu Kiel

vorgelegt von

He Li (李贺)

Kiel, 2024

This work was supervised by Prof. Dr. Jan Benedikt, and carried out at the Institute for Experimental and Applied Physics in Kiel University.

First examiner: Prof. Dr. Jan Benedikt

*Institute for Experimental and Applied Physics
Christian-Albrechts-Universität zu Kiel*

Second examiner: Prof. Dr. Lorenz Kienle

*Chair for Synthesis and Real Structure
Department of Materials Science
Faculty of Engineering
Christian-Albrechts-Universität zu Kiel*

Date of the oral examination: 29.07.2024

Kiel, 2024

ABSTRACT

Rechargeable zinc-air batteries, which present the advantages of low cost, high theoretical energy density and intrinsic safety, have been considered as a promising energy storage device to replace the current lithium-based batteries. The practical performance of rechargeable zinc-air batteries is strongly related to the reaction rate of the oxygen-involved reaction at their air cathodes, including the oxygen evolution reaction (OER) during the charge process and the oxygen reduction reaction (ORR) during the discharge process. Although noble-metal-based materials exhibit the highest electrocatalytic activities for these reactions, their high prices and poor stability still hinder them for future applications. Therefore, finding an efficient bifunctional electrocatalyst is necessary for the commercial applications of rechargeable zinc-air batteries.

Transition metal-based catalysts have been accepted as promising candidates to replace these noble-metal-based catalysts owing to their low cost, natural abundance and high stability. In this thesis, a self-supported catalyst of spinel NiCo_2O_4 nanowires coated on the commercial carbon paper was synthesized by a hydrothermal method followed by an annealing process. To further enhance the electrocatalytic performance of the catalyst, the low-pressure plasma treatments based on different gases were conducted to tune its electronic structure and optimize its surface properties. The main works are as follows:

1. Nitrogen doping engineering is a competitive strategy that effectively improves the electrocatalytic activity of spinel oxides. In this study, N_2 plasma was employed to synthesize nitrogen-doped NiCo_2O_4 nanostructures with excellent conductivity and abundant active sites, which exhibited enhanced OER and ORR performance compared to the pristine NiCo_2O_4 . In addition, the zinc-air battery with the modified catalyst also showed a small charge-discharge voltage gap and greatly improved long-term cycling stability.

2. The generation of oxygen vacancies at the surfaces of spinel oxides is an effective strategy for enhancing their electrocatalytic performance. In this study, the plasma treatment based on a gas mixture of H₂/Ar was applied to generate oxygen vacancies at the NiCo₂O₄ nanowire surfaces. The gas mixture was more effective than the pure Ar plasma treatment. The catalyst modified by H₂/Ar plasma for 7.5 min exhibited more active sites, higher conductivity, and better intrinsic activities than the pristine NiCo₂O₄ and the Ar plasma-modified catalysts, resulting in its optimal electrocatalytic performance for both OER and ORR.

3. Anchoring Pt atoms on conductive supports is a facile and effective approach for the synthesis of highly active and low-cost Pt-based catalysts. In this work, the self-supported material of spinel NiCo₂O₄ nanowires coated on commercial carbon paper as an excellent OER catalyst was used as an ideal substrate. Subsequently, Pt atoms were anchored on NiCo₂O₄ nanowires with the assistance of plasma reduction of H₂PtCl₆. The prepared catalyst exhibited excellent OER and ORR electrocatalytic performance under alkaline conditions.

4. Plasma surface modification is becoming increasingly popular as an effective and economical technique for preparing high-performance catalysts. However, most of the published works on plasma-assisted materials focus on investigating the change of material properties and only provide an optimal operating condition of the plasma device for the treatment process. To gain a deeper understanding of the modification process, it is essential to monitor the plasma properties, including ion composition, density, and energy distribution. In this study, N₂ plasma was employed to modify the single-layer graphene and carbon papers. During the plasma treatment, an energy-selective mass spectrometer was connected to the substrate holder near samples and used to monitor the plasma properties.

ZUSAMMENFASSUNG

Wiederaufladbare Zink-Luft-Batterien, die sich durch niedrige Kosten, hohe theoretische Energiedichte und inhärente Sicherheit auszeichnen, gelten als vielversprechende Energiespeicher, die die derzeitigen Lithiumbatterien ersetzen könnten. Die praktische Leistung von wiederaufladbaren Zink-Luft-Batterien hängt stark von der Reaktionsgeschwindigkeit der Sauerstoffreaktion an ihren Luftkathoden ab, einschließlich der Sauerstoffentwicklungsreaktion (OER) während des Ladevorgangs und der Sauerstoffreduktionsreaktion (ORR) während des Entladevorgangs. Obwohl Materialien auf Edelmetallbasis die höchste elektrokatalytische Aktivität für diese Reaktionen aufweisen, sind sie aufgrund ihres hohen Preises und ihrer geringen Stabilität für künftige Anwendungen noch nicht geeignet. Daher ist die Suche nach einem effizienten bifunktionalen Elektrokatalysator für die kommerzielle Anwendung von wiederaufladbaren Zink-Luft-Batterien notwendig.

Katalysatoren auf der Basis von Übergangsmetallen gelten aufgrund ihrer geringen Kosten, ihres natürlichen Vorkommens und ihrer hohen Stabilität als vielversprechende Kandidaten, um diese Katalysatoren auf Edelmetallbasis zu ersetzen. In dieser Arbeit wurde ein selbsttragender Katalysator aus einem NiCo_2O_4 -Spinell mit Nanodrähten, der auf handelsübliches Kohlenstoffpapier beschichtet ist, durch eine hydrothermale Methode und einer anschließenden Wärmebehandlung synthetisiert. Um die elektrokatalytische Leistung des Katalysators weiter zu verbessern, wurden Niederdruck-Plasmabehandlungen mit verschiedenen Gasen durchgeführt, um seine elektronische Struktur zu modifizieren und seine Oberflächeneigenschaften zu optimieren. Die wichtigsten Arbeiten sind die folgenden:

1. Die Stickstoffdotierung ist eine wettbewerbsfähige Strategie, die die elektrokatalytische Aktivität von Spinellen effektiv verbessert. In dieser Studie wurde N_2 -Plasma verwendet, um stickstoffdotierte NiCo_2O_4 -

Nanostrukturen mit hervorragender Leitfähigkeit und reichlich aktiven Stellen zu synthetisieren, die eine verbesserte OER- und ORR-Leistung im Vergleich zu unbehandeltem NiCo_2O_4 zeigten. Darüber hinaus zeigte die Zink-Luft-Batterie mit dem modifizierten Katalysator auch eine kleine Ladung-Entladung-Spannungslücke und stark verbesserte langfristige Zyklenstabilität.

2. Die Erzeugung von Sauerstofffehlstellen an den Oberflächen von Spinellen ist eine effektive Strategie zur Verbesserung ihrer elektrokatalytischen Leistung. In dieser Studie wurde die Plasmabehandlung auf der Basis eines H_2/Ar -Gasgemischs angewandt, um Sauerstofffehlstellen an den Oberflächen der NiCo_2O_4 -Nanodrähte zu erzeugen. Das Gasgemisch war effektiver als die reine Ar-Plasmabehandlung. Der Katalysator, der durch H_2/Ar -Plasma für 7,5 Minuten modifiziert wurde, wies mehr aktive Stellen, eine höhere Leitfähigkeit und bessere intrinsische Aktivitäten als das ursprüngliche NiCo_2O_4 und die durch Ar-Plasma modifizierten Katalysatoren auf, was zu einer optimalen elektrokatalytischen Leistung sowohl für OER als auch ORR führte.
3. Die Verankerung von Pt-Atomen auf leitfähigen Trägern ist ein einfacher und effektiver Ansatz für die Synthese von hochaktiven und kostengünstigen Pt-basierten Katalysatoren. In dieser Arbeit wurde das selbsttragende Material des NiCo_2O_4 -Spinell mit Nanodrähten, das auf handelsüblichem Kohlenstoffpapier als ausgezeichneter OER-Katalysator beschichtet ist, als ideales Substrat verwendet. Anschließend wurden Pt-Atome mit Hilfe der Plasmareduktion von H_2PtCl_6 auf NiCo_2O_4 -Nanodrähten verankert. Der hergestellte Katalysator zeigte unter alkalischen Bedingungen eine ausgezeichnete elektrokatalytische Leistung bei OER und ORR.
4. Die Oberflächenmodifizierung durch Plasma wird als wirksame und

wirtschaftliche Technik zur Herstellung von Hochleistungskatalysatoren immer beliebter. Die meisten veröffentlichten Arbeiten über plasmagestützte Materialien konzentrieren sich jedoch auf die Untersuchung der Veränderung von Materialeigenschaften und geben nur die optimalen Betriebsbedingungen für die Plasmakammer an. Um ein tieferes Verständnis des Modifikationsprozesses zu erlangen, müssen die Plasmaeigenschaften, einschließlich der Ionenzusammensetzung, der Dichte und der Energieverteilung, unbedingt gemessen werden. In dieser Studie wurde N₂-Plasma zur Modifizierung der Oberfläche von Kohlenstoffpapier eingesetzt. Während der Plasmabehandlung wurde ein energiselektives Massenspektrometer statt dem Substrathalter angeschlossen und zur Überwachung der Plasmaeigenschaften verwendet.

CONTENTS

ABSTRACT	v
ZUSAMMENFASSUNG	vii
1. INTRODUCTION	1
1.1 Scope of this work.....	3
1.2 References.....	4
2. FUNDAMENTAL	7
2.1 Rechargeable zinc air battery	8
2.1.1 Configuration of zinc-air batteries.....	8
2.1.2 Oxygen-involved reactions.....	10
2.1.3 Bifunctional electrocatalysts	11
2.2 Plasma technology	17
2.2.1 Basic conception of plasma	18
2.2.2 Low-temperature plasma	21
2.2.3 Plasma sheath.....	22
2.2.4 Plasma type.....	23
2.3 Plasma technologies in material research.....	26
2.3.1 Plasma surface interaction.....	26
2.3.2 Plasma surface modification for transition-metal-based catalysts.....	29
2.4 References.....	30
3. EXPERIMENTAL METHODS AND SETUPS	47
3.1 Material preparation	48
3.1.1 Hydrothermal method.....	48
3.1.2 Equipment for the hydrothermal method.....	49
3.1.3 Hydrothermal synthesis of electrocatalysts.....	50
3.2 Plasma setups.....	51
3.3 Plasma characterization.....	54
3.3.1 Energy resolved ion mass spectrometry (ERIMS)	54

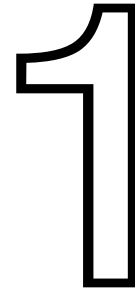
3.3.2 Plasma characterization by ERIMS	54
3.4 Material characterization	56
3.4.1 Electrochemical measurement	56
3.4.2 Scanning Electron Microscope	58
3.4.3 Transmission Electron Microscope	58
3.4.4 Energy Dispersive X-ray spectroscopy	59
3.4.5 X-ray powder diffractometer	59
3.4.6 Raman spectroscopy	60
3.4.7 Specific surface area and pore size distribution	60
3.5 References	61
4. Nitrogen-doped NiCo₂O₄ nanowires on carbon paper as a self-supported air cathode for rechargeable Zn-air batteries	65
5. Plasma-engineering of oxygen vacancies on NiCo₂O₄ nanowires with enhanced bifunctional electrocatalytic performance for rechargeable zinc-air battery.....	81
6. Plasma-engineering of Pt-decorated NiCo₂O₄ nanowires with rich oxygen vacancies for enhanced oxygen electrocatalysis and zinc-air battery performance.....	95
7. Mass spectrometry facilitates the precise control of N₂ plasma surface modification.....	113
8. CONCLUSION	137
9. Appendix	141
9.1 Nitrogen-doped NiCo ₂ O ₄ nanowires on carbon paper as a self-supported air cathode for rechargeable Zn-air batteries	142
9.2 Plasma engineering of oxygen vacancies on NiCo ₂ O ₄ nanowires with enhanced bifunctional electrocatalytic performance for rechargeable zinc-air batteries.....	156
9.3 Plasma-engineering of Pt-decorated NiCo ₂ O ₄ nanowires with rich oxygen vacancies for enhanced oxygen electrocatalysis and zinc-air battery performance	171

长风破浪会有时，直挂云帆济沧海。

----李白

A time will come to ride the wind and cleave the waves,
I'll set my cloud-white sail and cross the sea which raves.

-----Bai Li (Translated by Yuanhong Xu)



INTRODUCTION

With the fast development of the economy, global energy demand is also growing at a rapid pace ^[1-2]. At the same time, the consumption of traditional fossil fuels has resulted in serious environmental pollution and subsequent energy depletion problems ^[3-4]. To meet these issues, there is an urgent need to develop and utilize renewable energy sources, including solar, wind, and hydro energies ^[5]. However, the generation of the renewable energy is highly dependent on weather and geographical location. Therefore, it is necessary to develop efficient energy conversion and storage systems to store these fluctuating energies, such as rechargeable batteries. Moreover, high-performance batteries are also important for the development of portable electronics and electric vehicles ^[6]. Currently, lithium-ion batteries still dominate the battery market due to their reliable performance and mature production and supply chain. However, after a long period of development, they are still constrained by the scarcity of lithium metal, low energy density and fire issues, which limit their potential for future applications ^[7-8]. Therefore, designing and developing new battery technologies is a matter of great urgency.

Among various battery technologies, rechargeable zinc-air batteries (RZABs) have recently received increasing attention due to their intrinsic safety, low cost, and large specific energy density [9-10]. As aqueous electrolyte cells, RZABs are safer than lithium-ion batteries with organic electrolytes because they do not present explosion or flammability hazards under high loads [11]. Moreover, the reserves of zinc resources on Earth are also higher than those of lithium, and zinc metals are more available than lithium metals [12]. Furthermore, RZABs present a high theoretical energy density of 1086 W h kg⁻¹, which is 2.5 times higher than that of lithium-ion batteries [13]. These advantages make RZABs promising energy storage technologies to replace lithium-ion batteries for electronic equipment. However, the practical performance of RZABs remains unsatisfactory due to the sluggish kinetics of the oxygen evolution reaction (OER) during the charge process and oxygen reduction reaction (ORR) during the discharge process at their air cathodes [14]. Therefore, the key challenge in developing this type of battery is to find an efficient bifunctional electrocatalyst for these oxygen-related reactions.

To date, noble-metal-based materials are still recognized as the most active electrocatalysts. Commercial Pt/C catalysts exhibit the fastest ORR activity, and Ir/C or RuO₂ catalysts show excellent OER performance [15-16]. However, their scarcity, high price and poor stability hinder them in large-scale applications. Transition-metal-based materials, especially spinel oxides, have recently emerged as promising alternatives to these noble-metal catalysts owing to their low cost, natural abundance and high stability [17-18]. However, they also exhibit poor conductivity and low intrinsic catalytic activity, resulting in unsatisfactory battery performance. Previous studies have shown that the electronic structure of spinel oxides can be modified by surface modification, thereby optimizing their physical, chemical, and electrochemical properties [19-20]. A variety of chemical and physical techniques have been developed to modify the surfaces of spinel oxides, including thermal treatment [21], chemical reduction [22] and plasma treatment [23]. Among these methods, plasma treatment is an effective approach for surface modification, offering a short duration, minimal damage and reduced energy and precursor consumption.

1.1 Scope of this work

The objective of this study is to improve the electrocatalytic performance of spinel oxides for both OER and ORR with the assistance of plasma technologies. The present work is divided into the following chapters:

- Chapter 1: The background and motivation to the research
- Chapter 2: The general concept of rechargeable zinc-air batteries, the development of electrocatalysts, and the fundamental principles of plasma and related technologies
- Chapter 3: Introduction of electrocatalyst synthesis methods, an overview of plasma reactors and material characterization methods
- Chapter 4: The peer-reviewed article "*Nitrogen-doped NiCo₂O₄ nanowires on carbon paper as a self-supported air cathode for rechargeable Zn-air batteries*"
He Li, Sadegh Askari, Jihao Wang, Niklas Wolff, Malte Behrens, Lorenz Kienle, Jan Benedikt, International Journal of Hydrogen Energy, 2023, 48, 26107-26118.
[DOI: 10.1016/j.ijhydene.2023.03.146]
- Chapter 5: The peer-reviewed article "*Plasma-engineering of oxygen vacancies on NiCo₂O₄ nanowires with enhanced bifunctional electrocatalytic performance for rechargeable zinc-air battery*"
He Li, Jihao Wang, Tim Tjardts, Igor Barg, Haoyi Qiu, Martin Müller, Jan Krahmer, Sadegh Askari, Salih Veziroglu, Cenk Aktas, Lorenz Kienle, Jan Benedikt, Small, 2024, 20, 2310660.
[DOI: 10.1002/smll.202310660]
- Chapter 6: Manuscript "*Plasma-engineering of Pt decorated NiCo₂O₄ nanowires with rich oxygen vacancies for enhanced oxygen electrocatalysis and zinc-air battery performance*"
He Li, Jihao Wang, Tim Tjardts, Haoyi Qiu, Martin Müller, Salih Veziroglu, Cenk Aktas, Lorenz Kienle, Jan Benedikt
-----Under Submission-----
- Chapter 7: Manuscript "*Mass spectrometry facilitates the precise control of N₂ plasma surface modification*"
He Li, Martin Müller, Christian Schulze, Haoyi Qiu, Jan Benedikt
- Chapter 8: Conclusion
- Chapter 9: Appendix

1.2 References

- [1] J. Scheffran, M. Felkers, R. Froese, Economic growth and the global energy demand, *Green Energy to Sustainability: Strategies for Global Industries*, 2020, 1-44.
- [2] T. Ahmad, D. D. Zhang, A critical review of comparative global historical energy consumption and future demand: The story told so far, *Energy Reports*, 2020, 6, 1973-1991.
- [3] S. Yi, K. R. Abbasi, K. Hussain, A. Albaker, R. Alvarado, Environmental concerns in the United States: Can renewable energy, fossil fuel energy, and natural resources depletion help? *Gondwana Research*, 2023, 117, 41-55.
- [4] J. N. Wang, W. Azam, Natural resource scarcity, fossil fuel energy consumption, and total greenhouse gas emissions in top emitting countries, *Geoscience Frontiers*, 2024, 15, 101757.
- [5] T. Z. Ang, M. Salem, M. Kamarol, H. S. Das, M. A. Nazari, N. Prabakaran, A comprehensive study of renewable energy sources: Classifications, challenges and suggestions, *Energy Strategy Reviews*, 2022, 43, 100939.
- [6] S. Sharma, A. K. Panwar, M. M. Tripathi, Storage technologies for electric vehicles, *Journal of Traffic and Transportation Engineering (English Edition)*, 2020, 7, 340-361.
- [7] L. Usai, J. J. Lamb, E. Hertwich, O. S. Burherim, A. H. Strømman, Analysis of the Li-ion battery industry in light of the global transition to electric passenger light duty vehicles until 2050, *Environmental Research: Infrastructure and Sustainability*, 2022, 2, 011002.
- [8] Z. A. Kader, A. Marshall, J. Kennedy, A review on sustainable recycling technologies for lithium-ion batteries, *Emergent Materials*, 2021, 4, 725-735.
- [9] X. M. Lv, Z. L. Wang, Z. Z. Lai, Y. P. Liu, T. Y. Ma, J. X. Geng, Z. Y. Yuan, Rechargeable zinc–air batteries: Advances, challenges, and prospects, *Small*, 2023, 20, 2306396.
- [10] X. W. Zhong, Y. Y. Shao, B. Chen, C. Li, J. Z. Sheng, X. Xiao, B. M. Xu, J. Li, H. M. Cheng, G. M. Zhou, Rechargeable zinc–air batteries with an ultralarge discharge capacity per cycle and an ultralong cycle life, *Advanced Materials*, 2023, 35, 2301952.
- [11] J. Pan, Y. Y. Xu, H. Yang, Z. H. Dong, H. F. Liu, B. Y. Xia, Advanced architectures and relatives of air electrodes in Zn–air batteries, *Advanced Science*, 2018, 5, 1700691.

- [12] V. Moreau, P. C. Reis, F. Vuille, Enough metals? Resource constraints to supply a fully renewable energy system, *Resources*, 2019, 8, 29.
- [13] D. Dechenback, J. K. Schneider, A long-overlooked pitfall in rechargeable zinc–air batteries: Proper electrode balancing, *Advanced Materials Interfaces*, 2023, 10, 2202494.
- [14] Y. G. Zhao, D. P. Saseendran, C. Huang, C. A. Triana, W. R. Marks, H. Chen, H. Zhao, G. R. Patzke, Oxygen evolution/reduction reaction catalysts: from in situ monitoring and reaction mechanisms to rational design, *Chemical Reviews*, 2023, 123, 6257-6358.
- [15] R. Qin, G. Z. Chen, X. T. Feng, J. N. Weng, Y. H. Han, Ru/Ir-Based electrocatalysts for oxygen evolution reaction in acidic conditions: From mechanisms, optimizations to challenges, *Advanced Science*, 2309364.
- [16] X. F. Ren, Y. R. Wang, A. M. Liu, Z. H. Zhang, Q. Y. Lv, B. H. Liu, Current progress and performance improvement of Pt/C catalysts for fuel cells, *Journal of Materials Chemistry A*, 2020, 8, 24284-24306.
- [17] K. Zahra, T. Noor, N. Iqbal, N. S. Akbar, A review on the modification strategies of transition metal based bifunctional electrocatalysts for air-cathode in zinc-air batteries, *Journal of Energy Storage*, 2024, 88, 111565.
- [18] Z. Y. Shao, X. T. Wu, X. F. Wu, S. H. Feng, K. K. Huang, Synthesis and advantages of spinel-type composites, *Materials Chemistry Frontiers*, 2023, 7, 5288-5308.
- [19] Y. W. Dai, J. Yu, M. Ni, Z. P. Shao, Rational design of spinel oxides as bifunctional oxygen electrocatalysts for rechargeable Zn-air batteries, *Chemical Physics Reviews*, 2020, 1, 011303.
- [20] X. M. Liu, X. Y. Cui, K. Dastafkan, H. F. Wang, C. Tang, C. Zhao, A. B. Chen, C. X. He, M. H. Han, Q. Zhang, Recent advances in spinel-type electrocatalysts for bifunctional oxygen reduction and oxygen evolution reactions, *Journal of Energy Chemistry*, 2021, 53, 290-302.
- [21] P. Zhang, S. L. Xie, P. H. Deng, S. M. Huang, Y. P. Li, Z. M. Liu, Y. J. Wang, X. H. Lu, Oxygen-deficient NiCo₂O₄ nanowires as the robust cathode for high-performance nickel–zinc batteries, *Journal of Materials Research*, 2022, 37, 2185-2194.
- [22] S. J. Peng, F. Gong, L. L. Li, D. S. Yu, D. X. Ji, T. R. Zhang, Z. Hu, Z. Q. Zhang, S. L. Chou, Y. H. Du, S. Ramakrishna, Necklace-like multishelled hollow spinel oxides with oxygen vacancies for efficient water electrolysis, *Journal of the American Chemical*

Society, 2018, 140, 13644-13653.

[23] L. Xu, Q. Q. Jiang, Z. H. Xiao, X. Y. Li, J. Huo, S. Y. Wang, L. M. Dai, Plasma-engraved Co_3O_4 nanosheets with oxygen vacancies and high surface area for the oxygen evolution reaction, *Angewandte Chemie International Edition*, 2016, 55, 5277-5281.

欲穷千里目，更上一层楼。

-----王之涣

You can enjoy a grander sight,
by climbing to a greater height.

-----Zhihuan Wang (Translated by Yuanhong Xu)

2

FUNDAMENTAL

This chapter provides the fundamental background knowledge of the processes and devices utilized in this thesis. First, the general concept of rechargeable zinc-air batteries (RZABs) and the development of electrocatalysts are introduced. Then, the basic principles of plasma and related technologies used in the material field are presented.

2.1 Rechargeable zinc air battery

Currently, lithium-ion batteries, with their reliability and mature production and supply chain, still dominate the battery market for electronic equipment and even electric cars. However, their high price, relatively low energy density and safety concerns have prompted research into alternative energy storage systems ^[1-3]. Among various novel energy-related systems, the metal-air battery, known as the “ultimate storage battery”, has recently attracted considerable attention and is expected to become the next-generation power source for the electronics industry ^[4-9]. A standard metal-air battery consists of an air electrode as the positive cathode, a metal electrode as the anode, and an alkaline solution as an electrolyte. They use oxygen as the reactant at their positive electrode, resulting in a high energy density of up to four times that of lithium-ion batteries ^[10]. Moreover, they also present many advantages including environmental friendliness, low cost and intrinsic safety. According to the metals used in the negative electrode, metal-air batteries are classified as zinc-air batteries (ZABs), aluminum-air batteries, iron-air batteries, lithium-air batteries, potassium-air batteries and sodium-air batteries. Among them, zinc- and iron-air batteries are the most widely studied, and ZABs present a higher energy density and cell voltage than iron-air batteries ^[11].

2.1.1 Configuration of zinc-air batteries

Zinc metal, one of the most abundant elements on Earth, has been employed as a metal electrode for nearly 200 years. In 1832, Alessandro Volta constructed the first zinc-based battery, employing zinc and copper as electrodes and acid solution or seawater as the electrolyte ^[12]. Subsequently, ZABs were first assembled in 1878 with zinc, silver, and KOH solution as the anode, air cathode, and electrolyte, respectively ^[13]. However, the practical performance of ZABs was unsatisfactory for commercial applications at that time. Afterwards, with the rapid development of gas diffusion electrodes, primary non-rechargeable ZABs were used commercially in railroad lamps during the 1930s. Now, they are being employed in many areas, such as hearing, medical and signal devices. To further expand the scope of their application, numerous efforts have been made to develop high-performance rechargeable ZABs ^[14-16].

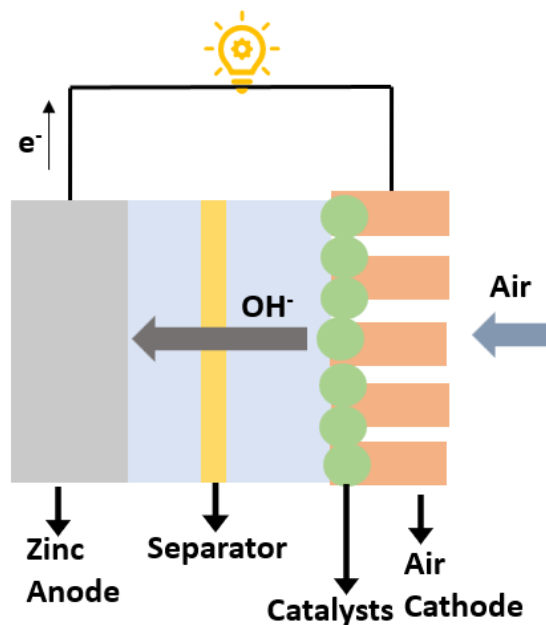
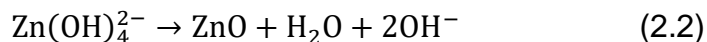
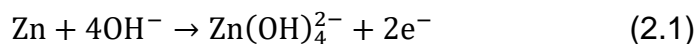


Figure 2.1 the configuration of zinc-air batteries

As illustrated in Figure 2.1, a standard zinc-air battery consists of a zinc anode, a membrane separator, a permeable air cathode and an alkaline electrolyte. Current is generated by the transfer of electrons produced by redox reactions at the electrode surfaces. During the discharge process, zinc anode metal is oxidized to Zn^{2+} ions and loses two electrons, which then react with OH^- to form $\text{Zn}(\text{OH})_4^{2-}$. Once the $\text{Zn}(\text{OH})_4^{2-}$ ions reach saturation, the decomposition reaction results in the formation of zinc oxides. At the same time, oxygen from the surrounding atmosphere diffuses to the cathode surface and reacts with H_2O and the migrated electrons to form OH^- ions. Finally, the OH^- ions generated at the cathode surface migrate to the anode through the electrolyte, completing the battery system ^[17]. During the charge process, all reactions are reversed. The overall reactions can be summarized as follows:

The discharge process:

At the zinc metal electrode:



At the air electrode:

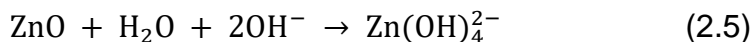


Overall:

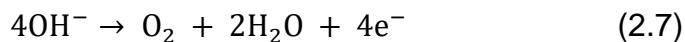


The charge process:

At the zinc metal electrode:



At the air electrode:



Overall:



The theoretical operation voltage of primary ZABs is calculated to be 1.65 V vs. SHE. However, their practical discharge voltages are always below 1.2 V, and their charge voltages are much higher than 1.65 V at an acceptable discharge/charge current density. This degradation is attributed to the large overpotential of the oxygen-involved reactions at the air cathode ^[18]. Therefore, the key challenge in developing high-performance RZABs is the design of an efficient bifunctional electrocatalyst for these oxygen-involved reactions.

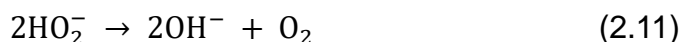
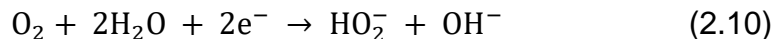
2.1.2 Oxygen-involved reactions

The oxygen reduction reaction (ORR) and oxygen evolution reaction (OER) are two main reactions occurring at the air cathode of RZABs. These reactions are closely related to the overall performance of RZABs ^[19-23]. The ORR process occurs during the discharge process. Firstly, oxygen from the air diffuses onto the electrocatalyst surface, where it reacts with the electrons and H₂O to form OH⁻ ions. Subsequently, these OH⁻ ions migrate to the anode through the electrolyte and are involved in the anode reactions, constituting the complete battery system. The ORR process can be divided into two categories: the two-electron pathway and the four-electron pathway, which are based on the oxygen absorption configurations ^[24]. Compared to the two-electron pathway which results in the generation of corrosive intermediates damaging the electrodes, the four-electron pathway is more suitable for RZABs. The following is a summary of the related reactions of ORR:

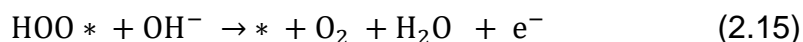
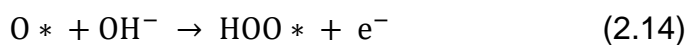
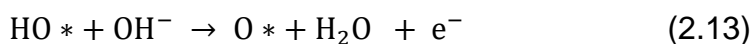
Four-electron pathway:



Two-electron pathway:



The mechanism of the OER process during the charge process is simpler than that of the ORR process. The overall reaction composes by the follow steps (* is the active site at catalyst surface):



Therefore, developing an efficient bifunctional electrocatalyst for both OER and ORR, particularly with a four-electron pathway during the ORR process, is essential to enhance the performance of rechargeable ZABs.

2.1.3 Bifunctional electrocatalysts

As mentioned above, oxygen-involved reactions at the cathode involve complex reaction steps associated with multiple oxygen intermediates. Therefore, electrocatalysts play a key role in the performance of RZABs [19, 25-29]. Over the past few decades, various electrocatalysts have been designed and applied in RZABs, including noble-metal-based electrocatalysts, carbon-based electrocatalysts and transition-metal-based electrocatalysts. Among them, noble-metal-based electrocatalysts remain the benchmark, where commercial Pt/C catalysts present the best ORR performance, and IrO₂ or RuO₂ materials exhibit the fastest OER activities [30]. However, their high cost, scarcity, and mono-functionality, severely hinder their commercial applications in RZABs. Moreover, the Pt/C catalyst is easily deactivated in contact with methanol, while the IrO₂ and RuO₂ catalysts are oxidized to unstable intermediates of IrO₃ and RuO₄ at a high working potential, resulting in the instability of electrocatalysts during battery operation [31-33]. Carbon-based materials have also been employed as OER and ORR electrocatalysts owing to their high specific surface area, excellent conductivity and good stability [34-35].

Nevertheless, their predominant two-electron pathway during the ORR process and terrible OER performances have constrained their advancement in RZABs. Recently, transition-metal-based materials have emerged as promising candidates to replace these noble-metal-based electrocatalysts.

Transition-metal-based materials have been identified as the next generation of bifunctional electrocatalysts for the OER and ORR process due to their low cost, high stability and rich redox chemistry, including transition-metal oxides, transition-metal nitrides, transition-metal sulfides and transition-metal selenides [36-44]. Among them, spinel-structure catalysts have received considerable attention owing to their distinctive electronic structures [45].

A typical spinel-structure material can be briefly described as AB_2X_4 , where A = Li, Zn, Co, Ni, Mg, Fe and others; B = Al, Cr, Mn, Fe, Co, Ni, Mo and others; X = O, N, S, Se and others. The anions (X) are arranged in the cubic close-packing, while the metal cations (A and B) occupy one-eighth of the tetrahedrally and one-half of the octahedrally coordinated sites [46]. As illustrated in Figure 2.2, spinel oxides can be classified into three categories based on the distribution of the cations between octahedral and tetrahedral sites, the normal spinel, the inverse spinel and the mixed spinel [47]. Take the spinel $MgFe_2O_4$ as an example, a more accurate structural formula for this compound is $(Mg_{1-x}Fe_x)_{Tet}(Mg_xFe_{2-x})_{Oct}O_4$. In the normal-spinel structure ($x = 0$), Mg^{2+} ions and Fe^{3+} ions occupy the tetrahedral and octahedral sites, respectively. In the inverse spinel structure ($x = 1$), half of Fe^{3+} ions are in tetrahedral sites, while other metal ions occupy octahedral sites. When $0 < x < 1$, the spinel oxide is named as the mixed-spinel structure.

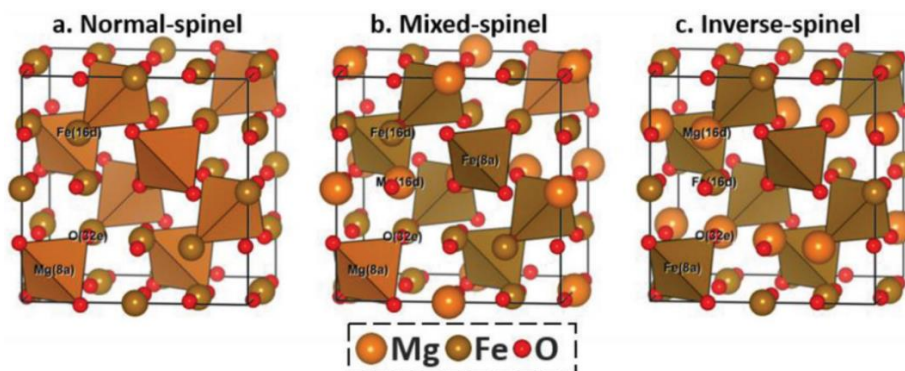


Figure 2.2 Structures of a) normal-spinel, b) mixed-spinel, c) inverse-spinel $MgFe_2O_4$. [47]
Copyright 2019, WILEY-VCH Verlag GmbH & Co. KGaA, Weinheim

Although previous literature has reported the excellent performance of spinel oxides for OER and ORR processes, the practical performance of these catalysts is still far from satisfactory due to their poor conductivity and low intrinsic activity [48-49]. Numerous strategies have been designed to optimize their electronic structures and improve their electrocatalytic activities, including defect engineering, heteroatom doping, morphology control, interface engineering, and growth on conductive substrates [50-54].

(1) Defect engineering

Defect engineering is a highly promising approach to enhance the electrocatalytic performance of spinel oxides. The presence of structural defects in spinel oxides optimizes their electronic structures and adjusts their surface chemical states, increasing their conductivity and the number of available active sites, thereby resulting in enhanced electrocatalytic performance. Two types of structural defects have been identified in spinel oxides: cationic defects (metal defects) and anionic defects (oxygen defects) [55-57].

Cationic defects in spinel oxides can influence their electronic structure, conductivity, and stability. Firstly, the generation of metal defects results in the transformation of spinel oxides from a semiconductor to a semi-metal, thereby facilitating electronic delocalization and enhancing their conductivity [58-59]. Moreover, these metal defects in the spinel oxide also regulate their electronic properties, increasing oxygen adsorption capability and optimizing the reaction energy barrier [60-61]. Furthermore, metal defects show greater stability than anionic defects [55]. In this regard, Li *et al.* fabricated the metal-defected spinel $Mn_xCo_{3-x}O_4$ catalyst through a solvothermal method followed by thermal calcination [60]. The metallic ratios were controlled owing to the differing formation rates of manganese and cobalt glycerolate, with the generation of metal vacancies occurring simultaneously. As a result, the presence of these metal vacancies increases the surface conductivity and enhances the O_2 adsorption capacity, resulting in excellent ORR performance. Moreover, Zheng *et al.* prepared abundant Co defects on spinel $NiCo_2O_4$ with excellent OER performance [61].

Although the generation of metal defects on the spinel oxides can improve their electrocatalytic performance, their formation energy is much higher than that of anionic defects [62]. Oxygen vacancies as a common anionic defect in spinel oxides have also

been well studied. Previous literature demonstrates that generating oxygen vacancies in spinel oxides can tailor their surface structures and optimize the adsorption and dissociation of oxygen intermediates during electrocatalysis reactions [57]. Numerous techniques have been employed to introduce oxygen vacancies in spinel oxides, including thermal annealing, chemical reduction, cation doping, and plasma treatment [63-66]. Lim *et al.* prepared the NiCo₂O₄ catalyst with abundant oxygen vacancies as an excellent ORR catalyst [67]. The introduction of oxygen vacancies not only improves the electrical conductivity of the catalyst but also increases the number of active sites by tuning the ion ratio of Co²⁺/Co³⁺ and Ni²⁺/Ni³⁺. Another effective approach to generate oxygen vacancies in spinel oxides is the replacement of cations, which can reduce the formation energy of oxygen vacancies. Wang *et al.* demonstrated that V doping can also introduce oxygen vacancies in NiCo₂O₄ which exhibits enhanced OER performance. However, oxygen vacancies can easily disappear in highly oxidizing environments, especially during the OER process [68]. To address this challenge, Wang *et al.* designed a lower valence-state doping strategy to stabilize the oxide vacancies of CoOOH.

(2) Heteroatom doping

Heteroatom doping in spinel oxides can be achieved in two ways: cation doping and anion doping [57, 69-70]. Tuning cation/anion doping in spinel oxides will modulate their electronic structure and enhance their intrinsic catalytic kinetics, thereby achieving high performance for both OER and ORR [71].

Cation doping is the process of replacing part of the original cations with other cations to synthesize polymetallic spinel compounds. The differing electronegativities and polarities of the metal ions allow the doped metal cations to redistribute electrons in spinel oxides, thereby modulating their electronic structure. Tan *et al.* reported the synthesis of Ni- or Fe-doped Co₃O₄ nanoplates [72]. The doped metal cations increased the surface energy per unit area and optimized the adsorption energy of oxygen species. Moreover, Liu *et al.* also prepared a Ni-doped Co₃O₄ as an excellent ORR electrocatalyst for zinc-air batteries [73]. The Ni cations were directly introduced into the octahedral sites of Co₃O₄, which promoted the charge accumulation of Co³⁺ and charge transfer during the electrocatalysis process, thus optimizing the adsorption energy of oxygen

intermediates and improving the ORR performance.

In addition to cation doping, introducing anions, such as N, P and S, into spinel oxides could modify the electronic structure of adjacent cations, thus optimizing the surface properties of catalysts and improving their intrinsic activity for oxygen electrocatalysis [74-75]. Yin *et al.* prepared NiO/CoN nanowires by annealing NiCo₂O₄ nanowires in a flowing NH₃ atmosphere [76]. The modified catalyst exhibited excellent OER and ORR performance due to the synergistic effect of the high oxidation capability for cobalt, the presence of more oxygen vacancies, and the strongly interconnected nanointerface between CoN and NiO domains. Similarly, doping S could also increase the conductivity and intrinsic electrocatalytic activities of CoMn₂O₄ nanomaterials [77]. Moreover, Xiao *et al.* prepared a phosphorus-doped Co₃O₄ catalyst (P-Co₃O₄) with abundant oxygen vacancies [78]. The doped P anions not only stabilize the oxygen vacancies at the catalyst surfaces but also increase their surface conductivity and optimize the adsorption energy of oxygen intermediates, thus improving their electrocatalytic performance.

(3) Morphology control

In addition to defect engineering and heteroatom doping to achieve optimal electronic structures, reasonable morphology design is also an effective strategy to increase the specific surface area and available active sites of spinel oxides, resulting in enhanced electrocatalytic performance [79-81]. He *et al.* prepared ultrathin Co₃O₄ nanofilm as a 2D nano-catalyst for OER and ORR processes [82]. The catalyst exhibits enhanced bifunctional activity compared to Co₃O₄ nanoparticles owing to the increase of active sites, larger surface area and enrichment of Co³⁺ ions. Moreover, Devaguptapu *et al.* prepared three types of NiCo₂O₄ catalysts with different morphologies by using different templates: a template-free approach, a SiO₂ hard template, and a P-123 soft template [83]. Compared to the spherical morphology of the SiO₂-templated NiCo₂O₄ catalyst, the P-123 templated catalyst presents a loose nanoneedle cluster with a high specific surface area and abundant meso- and macro-pores, resulting in its excellent OER and ORR performance.

The exposed crystal planes of spinel oxides can be controlled by adjusting their morphologies, which are also highly related to their electrocatalytic performance [84]. Liu

et al. prepared Co_3O_4 nanocubes, nanosheets and nanoplates by solvothermal and hydrothermal methods [85]. The characterizations indicate that the nanocubes are surrounded by the six [100] planes, the nanosheets dominantly expose [110] planes, and the nanoplates mainly present [111] planes. Moreover, the [110] plane with Co^{3+} and Co^{2+} exhibits high activity for OER, while the [100] and [111] planes show excellent ORR performance.

(4) Interface engineering

Interface engineering is employed to construct rational heterojunctions to improve the electrocatalytic performance of spinel oxides [86-88]. Well-designed heterojunctions can induce electronic modulation, accelerate electron transfer, and optimize reaction energy barriers during oxygen electrocatalysis, thereby resulting in excellent electrocatalytic performances. Zhang *et al.* synthesized $\text{NiO/NiCo}_2\text{O}_4$ porous nanofibers via the electrospinning method followed by the annealing process [89]. The formation of heterostructure in the catalyst increases the concentrations of Ni^{3+} and Co^{3+} and promotes the d-band center of Ni 3d and Co 3d to the Fermi level, improving the intrinsic activity of the catalyst and accelerating electron transfer during the oxygen electrocatalysis. Xu *et al.* prepared the $\text{Fe}_2\text{N/CoFe}_2\text{O}_4$ nano-heterostructure by a nucleation strategy [90]. The interfacial interactions between Fe_2N and CoFe_2O_4 not only increase the number of active sites and facilitate mass transfer, but they also stabilize the electrocatalytic activity by maintaining the surface integrity and exposed active sites. Moreover, the heterogeneous interfaces between transition alloys and oxides have also been studied to accelerate the OER and ORR process [91].

(5) Growth on conductive substrates

Although spinel-oxide-based catalysts in the form of ultrasmall nanoparticles exhibit a high specific surface area with abundant active sites, they suffer from low conductivity and agglomeration during the working process, leading to inferior electrocatalytic performance [92-93]. To address this issue, growing nanostructured and nanosized catalyst on conductive substrates has been studied [94]. Among the various conductive substrates, carbon-based materials, such as carbon black, graphene, and nanotubes, are ideal carriers for enhancing the conductivity and stability of this kind of catalysts.

Ma *et al.* prepared NiCo₂O₄ nanoparticles on N-doped graphene nanosheets [95]. The graphene support effectively reduces the aggregation of NiCo₂O₄ nanoparticles and enhances the charge transfer capacity. Zhang *et al.* fabricated manganese-cobalt spinel nanoparticles on carbon nanotubes which exhibited superior OER and ORR activity compared to the commercial Pt/C catalysts [96]. Moreover, the formation of interfaces between spinel oxides and carbon substrates could also optimize the intrinsic activity of spinel oxides for oxygen electrocatalysis. Chen *et al.* employed density functional theory (DFT) calculations to identify the active sites of NiCo₂O₄ deposited on N-doped carbon nanotubes during the ORR process [97]. The intrinsic activity of Co^{III} and Ni^{III} active sites for ORR is enhanced under the support effect, which is attributed to the weakened binding of *OH. Moreover, the rate-determining step of the ORR process at the catalyst surface is also altered when NiCo₂O₄ is anchored on N-doped nanotubes via the Co^{II} ions.

Currently, the reported electrocatalysts are primarily synthesized in powder form [98-99]. However, to prepare the air electrode, these catalyst powders must be mixed with polymeric binders, which inevitably lowers the surface conductivity of the electrode and covers the active area of the catalyst, leading to the degradation of battery performance. In contrast, self-supported bifunctional electrocatalysts can be directly assembled in the air cathode without any additional binders [100]. Xu *et al.* directly deposit (Ni, Co)₃O₄ nanosheets on Ni foam via an electrodeposition coupled electrochemical oxidation process [101]. This self-supported catalyst exhibited a lower gap potential than the mixed noble-metal-based catalyst. In addition, the hydrothermal method has been employed to synthesize spinel oxides on carbon paper as efficient bifunctional catalysts [102-103].

2.2 Plasma technology

Plasma is often regarded as the fourth state of matter, following the solid, liquid, and gaseous states [104]. As illustrated in Figure 2.3, under a fixed pressure, a solid substance in thermal equilibrium will undergo a phase transition to a liquid state when the temperature increases sufficiently. As the temperature rises, the liquid will evaporate into gas molecules or atoms and move randomly in all directions. As the temperature increases further, these gas species will decompose into charged particles, and the

matter will now be in the plasma state. Therefore, plasma is also defined as a partially or fully ionized gas comprising a significant number of electrons and ions. Indeed, plasma constitutes more than 99% of the observable universe, including the sun, all other stars, and most of the interstellar matter. In addition to these natural plasmas, artificial plasmas have been generated and applied in numerous material technologies. These plasma-based technologies, which facilitate the efficient fabrication of functional materials through the etching and deposition processes, have been indispensable to the fields of material science and engineering.

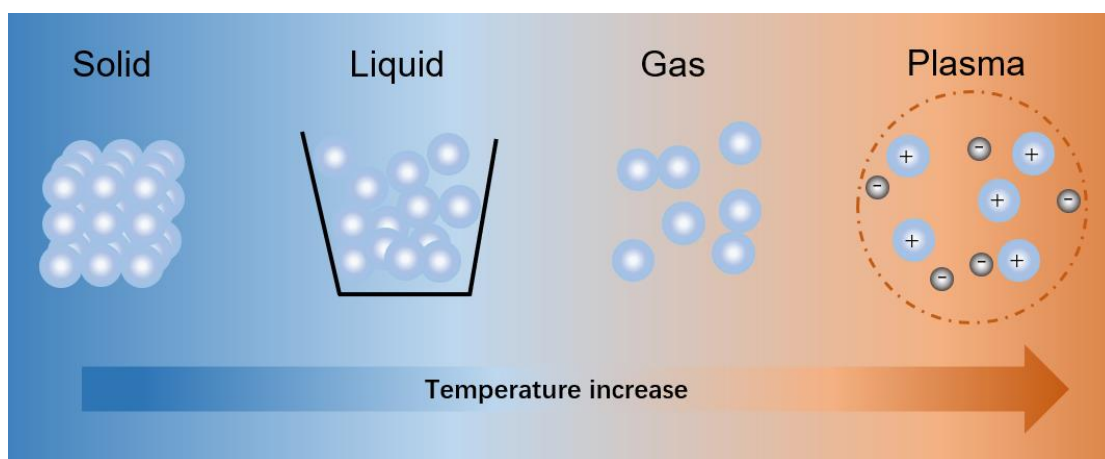


Figure 2.3 Illustrate of the four states of matter.

This chapter just briefly introduces the fundamental aspects of low-temperature, low-pressure, and non-equilibrium plasmas, which were employed in the synthesis of efficient electrocatalysts. Further details regarding the plasma and related technologies can be found in these books [105-107].

2.2.1 Basic conception of plasma

Many randomly moving neutral and charged particles come together to form a quasi-neutral matter called plasma, which exhibits collective effects [108]. However, to identify a plasma, the following three conditions must be met.

- (1) The characteristic length (L) of the plasma should be sufficiently larger than the Debye length (λ_D), which means $L \gg \lambda_D$.

Although plasma exhibits the macroscopic characteristic of electrical quasi-neutrality,

this characteristic does not exist in some special areas of plasma. Besides the boundaries area, here, the minimum electrically neutral distance was proposed and named the Debye shielding length or the Debye length (λ_D) given as:

$$\lambda_D = \sqrt{\frac{\epsilon_0 \cdot k \cdot T_e}{n_e \cdot e^2}} \quad (2.1)$$

where ϵ_0 is the permittivity of vacuum, k is the Boltzmann constant, T_e , n_e and e are the electron temperature, density and charge, respectively. Particles in a sphere area with radius λ_D cannot be affected by the charged particle field outside this sphere. As a quasi-neutral gas, the plasma L should be sufficiently larger than λ_D .

- (2) The number of charged particles (N_D) in a Debye sphere should be much larger than 1, which means $N_D \gg 1$.

This condition can be expressed as the Debye length (λ_D) should be larger than the average distance between particles (d). This is because the Debye shielding effect is proposed based on the assumption that a large number of particles are present in a Debye sphere and only in this case is the shielding effective.

- (3) The plasma frequency should be larger than the collision frequency of charged particles and neutral particles.

The plasma frequency is the oscillation frequency of the charged particles in the plasma and it is the frequency with which they are able to react to local disturbance of the charge quasi-neutrality induced for example by electromagnetic radiation or modulated external electric field. The positive ions and electrons can be separated by this external disturbance and the produced electric field will result in the harmonic electron oscillation in the stationary background of heavy positive ions (the oscillatory ion movement is negligible for the typical low-temperature plasmas and external field frequencies above 10 MHz). The corresponding electron oscillation frequency is designated as the plasma frequency:

$$\omega_{p,e} = \sqrt{\frac{n_e \cdot e^2}{\epsilon_0 \cdot m_e}} \quad (2.2)$$

The plasma frequency should be larger than the collision frequency of charged and

neutral particles to maintain the collective behavior of the plasma. This condition indicates that electrons are unable to dissipate their oscillation energy through collision with neutral particles, thereby maintaining the plasma oscillation. This condition is often not fulfilled by atmospheric plasmas, where we speak about collision dominated plasmas.

In addition to the aforementioned characteristics, two other crucial parameters in plasma are also important: particle number density (n) and plasma temperature (T).

The n of the plasma must satisfy the quasi-neutral condition, which can be expressed in the case of electropositive plasmas without negative ions as follows:

$$n_e = \sum Z_i n_i \quad (2.3)$$

here n_e is the electron density in the plasma, n_i and Z_i are the density and charge number of the α ion, respectively. In general, the ionization degree of plasma can be expressed as follows

$$x_{iz} = \frac{n_i}{n_g + n_i} \quad (2.4)$$

where n_g is the density of neutral species. When $x_{iz} \approx 1$, the plasma is fully ionized and when $x_{iz} \ll 1$, the plasma is weakly ionized.

Plasma temperature, including electron temperature (T_e), ion temperature (T_i) and gas temperature (T_{gas}) are the common parameters used in the plasma system. The differences of these three temperatures allow for the classification of plasma into two categories: high-temperature plasma and low-temperature plasma. A high-temperature plasma is a fully ionized gas in thermodynamic equilibrium, with all particles exhibiting similar temperature $T_e = T_i = T_{gas} = 10^6 \sim 10^8 K$, which is much higher than the ambient temperature. Most of the plasmas in the universe are high-temperature plasmas. In contrast, low-temperature plasma is a partially ionized gas with T_i and T_{gas} typically being much lower than T_e due to the greater mass of ions and neutral particles compared to electrons. These are usually low-pressure plasmas where mainly electrons are heated by the external fields and where the collision frequency is too low for effective energy exchange between electrons and heavy species.

2.2.2 Low-temperature plasma

Low-temperature plasmas providing the desired chemically reactive environments in the plasma area or at the interface between plasma and substrate have been employed in a multitude of applications, including lighting, functional materials, and water purification, and have significantly impacted the quality of life [109-111]. In particular, their capacity to fabricate microelectronic devices has facilitated the information technology revolution [112].

There are two types of low-temperature plasma: thermal plasma and non-thermal plasma (nonequilibrium plasma). Thermal plasma, also called local-thermal equilibrium plasma, is usually generated by arc discharge under high-pressure conditions close to atmospheric pressure. The electrons, ions, and neutral particles in plasma undergo enough collisions need for fully exchanging kinetic energy and reaching a thermal equilibrium state. These particles in the plasma have similar high temperatures ($T_e \approx T_i \approx T_{gas} = 10^3 \sim 10^5 K$). In the non-thermal plasma, due to their small mass, the electrons get the energy from the electric field rapidly, however, they cannot subsequently transfer the energy to heavy particles promptly, thus the non-thermal plasma is under a non-thermal-equilibrium state and exhibits a much higher T_e than T_i and T_{gas} . Among various non-thermal plasmas, glow discharge, radio frequency capacitively or inductively coupled plasmas (CCP and ICP respectively), and microwave discharge are usually generated under low pressure (lower than several hundred Pa), while corona discharge and dielectric barrier discharge can be generated under high pressure (close to atmospheric pressure) through short pulse discharge modes.

Non-thermal plasma is commonly used for the surface modification and synthesis of functional materials [113-114]. In addition to the presence of numerous highly reactive species within the plasma region, the average temperature of non-thermal plasma is maintained at a low level, which enables the modification of temperature-sensitive substrates. In this thesis, non-thermal plasma at low pressure was generated and used to modify the surfaces of the $NiCo_2O_4$ or carbon paper and to optimize their electrocatalytic performances.

2.2.3 Plasma sheath

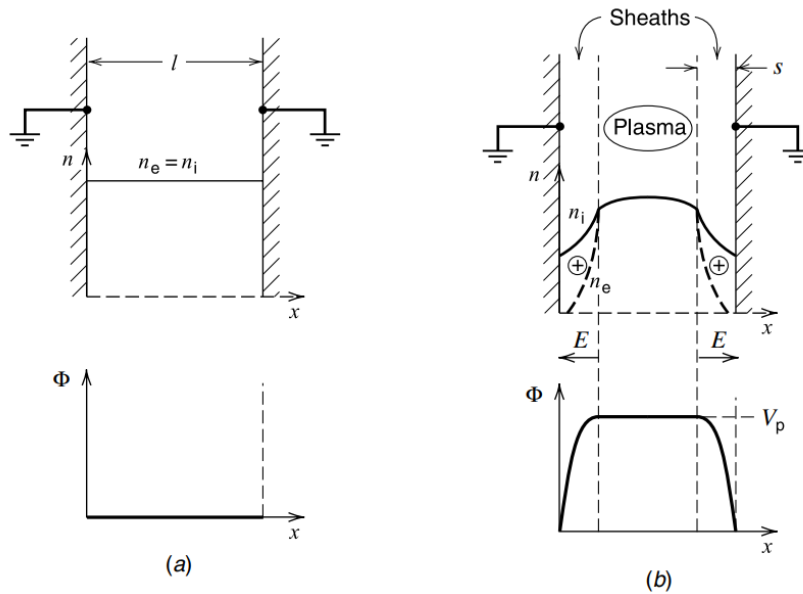


Figure 2.4 The formation of plasma sheath, (a) initial ion and electron densities and potential; (b) densities, electric field and potential after formation of the sheath. ^[106] Copyright 2005, John Wiley & Sons, Inc.

In a plasma device, the plasma is in a limited space surrounded by the chamber walls. Near the walls, a potential exists to confine the charged particles, which balances the positive and negative currents reaching the walls. In a plasma without an external electromagnetic field, the electrons move much faster than the ions toward the walls, and thus the plasma is positively charged to the walls. The region with a positive space between the plasma and the chamber wall charge is named the plasma sheath.

To study the generation of the plasma sheath (Child-Langmuir models), it is essential to recognize that electrons in the plasma have a much lower mass and higher temperature than ions, resulting in their much higher mobility. Figure 2.4 (a) shows the redistribution of the charges in a plasma of width l , surrounded by two grounded plate electrodes that can absorb charged particles. At the initial stage (a), a uniform distribution of charges with $n_i = n_e$ is assumed between the electrode plates and the electric potential Φ and the electric field E_x are both zero in the plasma area. But it is not a stable situation, because the high-mobility electrons rapidly move to the boundaries and are absorbed by the metal plates. After a very short time, in the region

near the electrode plate, the number of electrons is much lower than the number of ions ($n_i \gg n_e$) and thin positive ion sheathes ($s \ll l$) are formed (Figure 2.4 (b)). Subsequently, a potential profile ($\Phi(x)$) is generated, whereby the plasma is positively charged in relation to the electrode plates. This positive potential will impede the movement of electrons and accelerate the movement of ions towards the electrode plates [106].

The plasma sheath has a significant effect on the ion-flux energy distribution function, thus impacting the surface treatment process [115-116]. At very low pressure (~ 1 Pa), ions pass through the sheath layer without collisions, and their energy distribution function is only related to the sheath voltage as the ion enters the sheath. The ion energy is further modulated at rf plasmas by the variation of sheath potential drop. At higher pressures, ion-neutral particle collisions within the sheath strongly affect the ion energy distribution function.

2.2.4 Plasma type

Based on the different power supplies, non-thermal plasma can be classified into direct current (DC) plasma and alternating current (AC) plasma. Compared to the DC plasma, AC plasma doesn't require closed conductive circuit and can be used for the treatment of dielectric substrates. One of the most common AC plasmas is radio frequency (RF) plasma which has been widely utilized in material science applications [117]. The ion energy in RF plasma can easily reach several eV or even higher after acceleration across the sheath, which can be used to facilitate chemical/physical reactions at material surfaces without causing significant damage to the bulk material. There are two types of RF plasma: capacitively coupled plasma (CCP) and inductively coupled plasma (ICP).

Figure 2.5(a) schematically presents a typical CCP device with internal electrodes facing each other. During the discharge process, an RF power is applied to generate a high-frequency electric field between the two electrodes. The electrons with a light mass between these two electrodes can rapidly respond to changes in the high-frequency electromagnetic field and continuously absorb energy from the electric field.

These electrons collide with gas molecules to generate new electron ion pairs and maintain the plasma. This type of plasma device exhibits a highly efficient and stable discharge, which is easy to apply in large-area processes. Figure 2.5(b) shows another type of CCP discharge with external ring-shaped electrodes positioned on a glass tube at appropriate distance. The RF electric field applied to the electrodes penetrates the glass wall and maintains the plasma. Compared to the internal electrode type of CCP devices, those with external electrodes are easier to construct and they can generate purer plasma with less sputtering impurities, rendering them suitable for treatment of high-purity materials. In summary, CCP devices have a relatively simple structure but low energy transmission efficiency, so they are usually employed to generate a low-density plasma for plasma cleaning, surface modification, and thin film deposition [118-120].

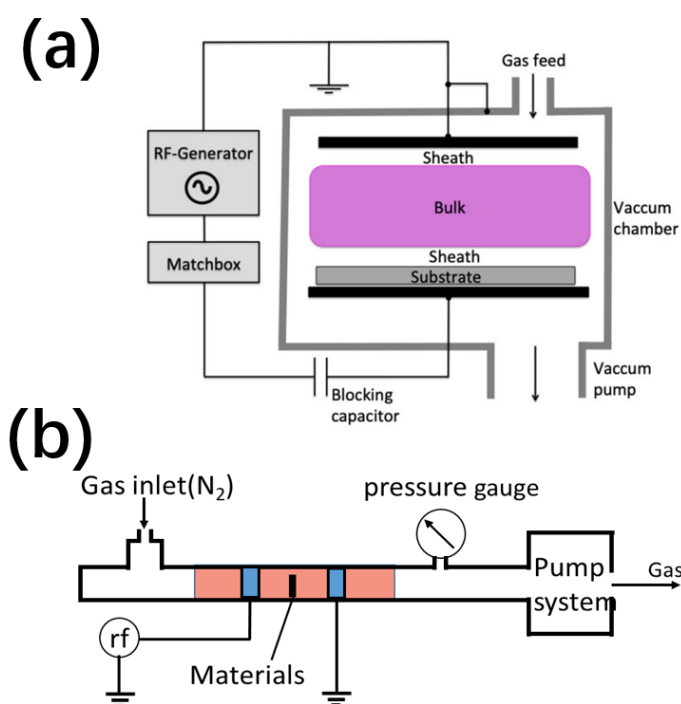


Figure 2.5 Schematic diagrams of CCP devices: (a) internal electrodes forming a capacitor in the vacuum chamber [117] Copyright 2020, AIP Publishing, and (b) external ring-shaped electrodes out of a dielectric tube.

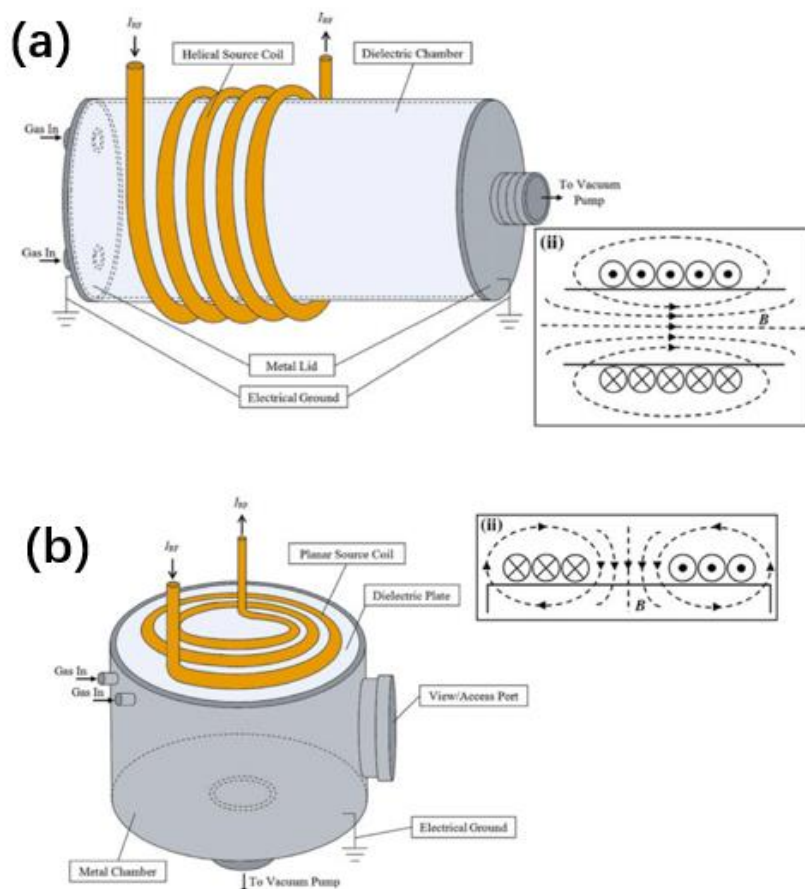


Figure 2.6 Schematic diagram of ICP devices (a) helical coil ICP and (b) planar coil ICP.^[121] Copyright 2017, Springer, Singapore.

As shown in Figure 2.6, according to the shape and location of the coil, ICP devices are divided into helical coil ICP and planar coil ICP [121]. During the discharge process, an RF current passes through the coil, generating a high-frequency magnetic field in the discharge area. The electrons will be accelerated in the induced electric field and collide with gas molecules to generate plasma. This discharge mode is called H-mode. The existence of a toroidal electric field in ICP devices increases the movement route of electrons and reduces the loss of charged particles at the chamber wall, leading to a relatively high plasma density. In contrast, when the RF current is lower, a high voltage drop is observed between the windings of the coil, thereby driving the discharge process. This mode is called E-mode and the plasma density under this mode is lower than that of H-mode. In summary, the ICP discharge presents good

stability and efficient energy transfer and these ICP devices are usually used to generate a high-density plasma for material deposition, etching, and ion-assisted deposition [122].

2.3 Plasma technologies in material research

The highly reactive environment provided by the various species, including electrons, ions, radicals, excited particles, and neutral particles in plasma, enables plasma treatment to be a clean, environmentally friendly, and simple process [121-125]. Moreover, this process also offers the following advantages: (1) This modification process only optimizes the surface properties of the materials without affecting their bulk performances. (2) This modification process is highly efficient in optimizing the surface properties with a short duration, low temperature, and minimized energy and precursor consumption. (3) This modification process is easily controlled through adjustment of the working parameters. (4) This modification process is easily scaled up to industrial production. Therefore, plasma technologies have been widely used in the etching, deposition or other modifications of solid surfaces [126].

2.3.1 Plasma surface interaction

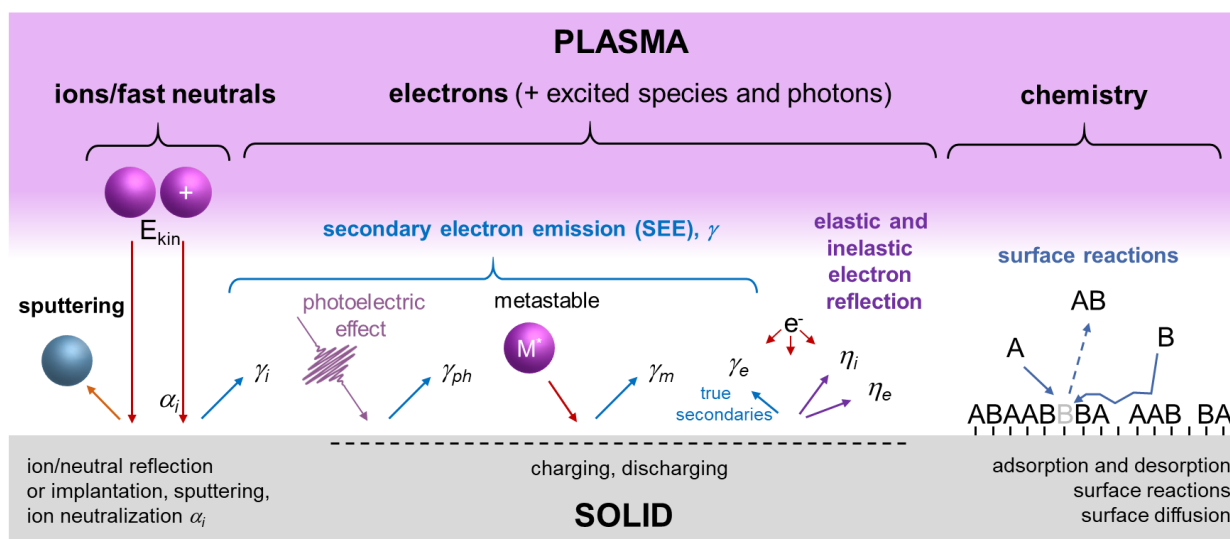


Figure 2.7 Schematic illustration of the plasma-surface interactions at the material surface.

Plasma-surface interactions are complex processes at the interface between the plasma and material surfaces. These interactions are a key factor in the functionalization of materials, as they can modify their surface properties and optimize their performance. However, the plasma-surface interface is a complex and dynamic system and the interactions at this interface involve a wide range of physical and chemical processes (Figure 2.7) ^[127]. A few plasma-surface interactions, judged to be important for this work, will be introduced briefly.

(1) Plasma etching

Etching is a general term for the removal of materials by solution, reactive ions or other mechanical means. It is mainly divided into wet etching and dry etching. Dry etching generally refers to plasma surface etching, in which the surface of the material is selectively etched by the reaction gas ionized into plasma and other free radicals that react with the material. The etched material is converted to the gas phase and evacuated by the vacuum pump. There are three common low-pressure plasma processes that can be used to remove material from solid surfaces, namely sputtering, chemical etching and reactive ion etching ^[128].

a) Sputtering

Sputtering is a physical process in which atoms are removed from material surfaces by rapid vaporization and ejected outward due to the impact of energetic ions. During the sputtering etching process, the substrate is placed on a negative potential holder in a vacuum reaction chamber. The introduced gas is ionized into positively charged ions. These ions are accelerated in the electric field to bombard the substrate surface. When the energy transferred by the bombarding ions to the atoms being hit is greater than the binding energy of the atoms. These atoms will be separated from their original positions and splashed out, forming sputtering etching.

b) Chemical etching

In chemical etching, the plasma provides only gas-phase etching atoms or molecules that react chemically with the surface to form gas-phase products. The process is highly chemically selective.

c) Reactive ion etching

In reactive ion etching, the plasma provides both etching atoms/molecules and energetic ions. It is a combination of sputtering and chemical etching. The ions carry sufficient energy to break the chemical bonds of the atoms at the substrate surface, thus lowering the activation energy and increasing the reaction rate of chemical etching. In chemical etching, reaction by-products formed on the substrate surface may act as inhibitors for the chemical etching. The energetic ions can remove these reaction by-products from the surface by physical sputtering, exposing the original material for removal by the chemically reactive species. For this reason, the etching effect of reactive ion etching is much better than that of pure chemical etching or sputter etching alone.

(2) Plasma surface modification

Surface modification has been regarded as an effective method to optimize the surface properties of materials and improve their electrochemical performance. Compared to other methods, plasma surface modification can directly modify the catalyst surface with few impurities and short duration owing to the presence of highly active species. There are three common plasma surface modification processes for materials: plasma cleaning, plasma surface functionalization and plasma surface etching [129-131].

a) Plasma cleaning

The active species in plasma can effectively remove impurities and organic compounds on the material surfaces, making the surface thoroughly clean and greatly improving the surface performance of the material.

b) Plasma surface functionalization

The active species in plasma can collide with the substrate surfaces and break the chemical bonds of the substrate, thus replacing the material atoms with different atoms or introducing functional groups on the substrate surfaces to optimize their properties. Plasma surface functionalization includes surface passivation, defect generation, heteroatom doping and surface ion implantation.

c) plasma surface etching

The active species in plasma bombard the material surface and undergo complex physical and chemical reactions, producing a strong etching effect and removing some unstable layers to improve the stability of the material surface.

(3) Plasma-enhanced deposition

Plasma-enhanced deposition has been widely used to deposit thin films by enhancing the activity of material precursors through plasma activation to increase the surface reaction rate, and significantly reduce the deposition temperature. Due to the presence of highly reactive substances, including reactive ions, electrons, radicals, and other excited species, thermochemical reactions and complex plasma chemical reactions occur simultaneously on the substrate surface, and the film grows rapidly under the combined action of these two reactions. Sputtering deposition and plasma-enhanced chemical vapor deposition are two common technologies of plasma-enhanced deposition ^[132].

2.3.2 Plasma surface modification for transition-metal-based catalysts

Inspired by many advantages of plasma technologies, they have been extensively used to fabricate efficient oxygen electrocatalysts. In this section, we briefly introduce the applications of plasma technologies in the surface modification of transition-metal-based electrocatalysts.

Defect engineering, especially the generation of oxygen vacancies, is a promising approach to enhance the electrocatalytic performance of transition-metal-based catalysts. Compared with other methods, Ar plasma treatment is a time-saving and eco-friendly process owing to its strong etching effect. Li *et al.* prepared atomic layer $\text{Co}_3\text{O}_{4-x}$ nanosheets by Ar plasma treatment as air cathode for ZABs ^[133]. The $\text{Co}^{2+}/\text{Co}^{3+}$ ratio of the sample is increased from 1 to 1.3 after plasma treatment, suggesting that oxygen vacancies were generated at the catalyst surfaces. The enhanced electrocatalytic activities of $\text{Co}_3\text{O}_{4-x}$ for OER and ORR and excellent battery performance are ascribed to the increased Co^{2+} species at the tetrahedral sites and the transformation of low-spin $\text{Co}^{3+}(t_{2g}^6e_g^0)$ to high-spin $\text{Co}^{3+}(t_{2g}^4e_g^2)$. Moreover,

hydrogen plasma can also generate oxygen vacancies at the surface of perovskite thin films [134].

Plasma treatment can also be used to dope anions into transition-metal oxides, thus optimizing the surface properties of catalysts and improving their intrinsic activity for oxygen electrocatalysis. Zhang *et al.* successfully synthesized CoN nanowires via the nitridation process by N₂ plasma treatment [135]. The morphologies of nanowires were overall preserved after 60 s of N₂ plasma etching. As a result, the modified CoN nanowires exhibited a low overpotential and excellent stability for OER. Moreover, Liang *et al.* used PH₃ plasma to rapidly convert NiFe double hydroxide into metallic NiFeP which showed excellent electrocatalytic performance for OER [136].

Ar plasma has also been conducted to construct composite structures. In this case, Zhao *et al.* prepared a NiS/NiFe₂O₄ composite inside the defective S-doped NiFe₂O₄ by Ar plasma-induced phase reconfiguration [137]. Due to the strong etch effect of Ar plasma, the long-range order of S-doped NiFe₂O₄ was broken to be partly disordered NiFe₂O₄ structures and exposed sulfides, thus forming short-range ordered NiS structures coupled with intrinsic defects.

2.4 References

- [1] J. Liu, J. Xiao, J. H. Yang, W. Wang, Y. Y. Shao, P. Liu, M. S. Whittingham, The TWh challenge: Next generation batteries for energy storage and electric vehicles, *Next Energy*, 2023, 1, 100015.
- [2] S. Orangi, N. Mabjong, D. P. Clos, L. Usai, O. S. Burheim, A. H. Strømman, Historical and prospective lithium-ion battery cost trajectories from a bottom-up production modeling perspective, *Journal of Energy Storage*, 2024, 76, 109800.
- [3] A. Jilani, Z. Awan, S. A. Taqvi, F. Khan, T. Alshahrani, Recent advances in the development of Li-air batteries, experimental and predictive approaches -prospective, challenges, and opportunities, *ChemBioEng*, 2024, 11, 95-114.

- [4] T. Li, M. Huang, X. Bai, Y. X. Wang, Metal–air batteries: A review on current status and future applications, *Progress in Natural Science: Materials International*, 2023, 33, 151-171.
- [5] W. J. Shao, R. Yan, M. Zhou, L. Ma, C. Roth, T. Ma, S. J. Cao, C. Cheng, B. Yin, S. Li, Carbon-based electrodes for advanced zinc-air batteries: Oxygen-catalytic site regulation and nanostructure design, *Electrochemical Energy Reviews*, 2023, 6, 11.
- [6] E. V. Timofeeva, C. U. Segre, G. S. Pour, M. Vazquez, B. L. Patawah, Aqueous air cathodes and catalysts for metal–air batteries, *Current Opinion in Electrochemistry*, 2023, 38, 101246.
- [7] T. S. Bai, D. P. Li, S. Y. Xiao, F. J. Ji, S. Zhang, C. Wang, J. Y. Lu, Q. Gao, L. J. Ci, Recent progress on single-atom catalysts for lithium–air battery applications, *Energy & Environmental Science*, 2023, 16, 1431-1465.
- [8] Z. Y. Gao, I. Temprano, J. Lei, L. B. Tang, J. J. Li, C. P. Grey, T. Liu, Recent progress in developing a LiOH-based reversible nonaqueous lithium–air battery, *Advanced Materials*, 2023, 35, 2201384.
- [9] Q. Zhang, L. Guo, Y. Huang, R. H. Zhang, A. G. Ritacca, S. L. Leng, X. W. Zheng, Y. C. Yang, A. Singh, Influence of an imidazole-based ionic liquid as electrolyte additive on the performance of alkaline Al-air battery, *Journal of Power Sources*, 2023, 564, 232901.
- [10] N. Chawla, Recent advances in air-battery chemistries, *Materialstoday Chemistry*, 2019, 12, 324-331.
- [11] J. Fu, Z. P. Cano, M. H. Park, A. P. Yu, M. Fowler, Z. W. Chen, Electrically rechargeable zinc–air batteries: Progress, challenges, and perspectives, *Advanced Materials*, 2017, 29, 1604685.
- [12] A. Volta, J. Banks, I. On the electricity excited by the mere contact of conducting substances of different kinds, *Proceedings of the Royal Society of London*, 1832, 1, 27-29.
- [13] L. Maiche, French Patent, 1878, 127, 069.
- [14] Z. G. Zhu, J. M. Zhang, X. M. Peng, Y. Y. Liu, T. L. Cen, Z. F. Ye, D. S. Yuan, Co_3O_4 -

NiCo₂O₄ hybrid nanoparticles anchored on N-doped reduced graphene oxide nanosheets as an efficient catalyst for Zn-air batteries, *Energy & Fuel*, 2021, 5, 35.

[15] S. Askari, D. Mariotti, R. McGlynn, J. Benedikt, Air - cathode with 3D multiphase electrocatalyst interface design for high - efficiency and durable rechargeable zinc - air batteries, *Energy technology*, 2021, 9, 2000999.

[16] Y. N. Zhang, J. B. Wang, M. Alfred, P. F. Lv, F. L. Huang, Y. B. Cai, H. Qiao, Q. F. Wei, Recent advances of micro-nanofiber materials for rechargeable zinc-air batteries, *Energy Storage Materials*, 2022, 51, 181-211.

[17] P. Gu, M. B. Zheng, Q. X. Zhao, X. Xiao, H. G. Xue, H. Pang, Rechargeable zinc-air batteries: a promising way to green energy, *Journal of Materials Chemistry A*, 2017, 5, 7651.

[18] P. Sapkota, H. Kim, Zinc-air fuel cell, a potential candidate for alternative energy, *Journal of Industrial and Engineering Chemistry*, 2009, 15, 445-450.

[19] Y. Kumar, M. Mooste, K. Tammeveski, Recent progress of transition metal-based bifunctional electrocatalysts for rechargeable zinc-air battery application, *Current Opinion in Electrochemistry*, 2023, 38, 101229.

[20] H. Chang, L. N. Shi, Y. H. Chen, P. F. Wang, T. F. Yi, Advanced MOF-derived carbon-based non-noble metal oxygen electrocatalyst for next-generation rechargeable Zn-air batteries, *Coordination Chemistry Reviews*, 2022, 473, 214839.

[21] Q. Liu, X. H. Zou, Y. F. Bu, Z. P. Shao, Structural design of supported electrocatalysts for rechargeable Zn-air batteries, *Energy Storage Materials*, 2023, 55, 166-192.

[22] D. Yang, H. T. Tan, X. H. Rui, Y. Yu, Electrode Materials for Rechargeable Zinc-Ion and Zinc-Air Batteries: Current Status and Future Perspectives, *Electrochemical Energy Review*, 2019, 2, 395-427.

[23] A. K. Worku, D. W. Ayele, N. G. Habtu, M. A. Teshager, Z. G. Workineh, Recent progress in MnO₂-based oxygen electrocatalysts for rechargeable zinc-air batteries, *Materials Today Sustainability*, 2021, 13, 100072.

[24] L. L. Zhang, S. Y. Jiang, W. Ma, Z. Zhou, Oxygen reduction reaction on Pt-based

electrocatalysts: Four-electron vs. two-electron pathway, *Chinese Journal of Catalysis*, 2022, 43, 1433-1443.

[25] Y. R. Li, L. B. Zhang, Y. Han, W. X. Ji, Z. Y. Liu, B. S. Wang, S. M. Zhao, X. K. Wu, L. G. Zhang, R. F. Zhang, Interface engineering of bifunctional oxygen electrocatalysts for rechargeable Zn–air batteries, *Materials Chemistry Frontiers*, 2023, 7, 4281-4303.

[26] P. Anand, M. S. Wong, Y. P. Fu, Perovskite oxide composites for bifunctional oxygen electrocatalytic activity and zinc-air battery application- a mini-review, *Energy Storage Materials*, 2023, 59, 362-380.

[27] D. B. Kumar, W. Nie, Z. Q. Jiang, J. Lee, T. Maiyalagan, Recent progress in transition metal carbides and nitrides based composites as bifunctional oxygen electrocatalyst for zinc air batteries, *Journal of Alloys and Compounds*, 2023, 960, 170828.

[28] Q. Lu, X. H. Zou, Y. F. Bu, Z. P. Shao, Structural design of supported electrocatalysts for rechargeable Zn–air batteries, *Energy Storage Materials*, 2023, 55, 166-192.

[29] A. B. Haruna, E. U. Onoh, K. I. Ozoemena, Emerging high-entropy materials as electrocatalysts for rechargeable zinc–air batteries, *Current Opinion in Electrochemistry*, 2023, 39, 101264.

[30] F. Gao, Y. P. Zhang, Z. Y. Wu, H. M. You, Y. K. Du, Universal strategies to multi-dimensional noble-metal-based catalysts for electrocatalysis, *Coordination Chemistry Reviews*, 2021, 436, 213825.

[31] N. T. Suen, S. F. Hung, Q. Quan, N. Zhang, Y. J. Xu, H. M. Chen, Electrocatalysis for the oxygen evolution reaction: recent development and future perspectives, *Chemical Society Reviews*, 2017, 46, 337-365.

[32] A. V. Miller, V. V. Kaichev, I. P. Prosvirin, V. I. Bukhtiyarov, Mechanistic study of methanol decomposition and oxidation on Pt(111), *The Journal of Physical Chemistry C*, 2013, 117, 8189-8197.

[33] C. Wang, L.J. Jin, H. Y. Shang, H. Xu, Y. Shiraishi, Y. K. Du, Advances in engineering RuO₂ electrocatalysts towards oxygen evolution reaction, *Chinese Chemical Letters*, 2021, 32, 2108-2116.

- [34] J. W. Zhu, S. C. Mu, Defect engineering in the carbon-based electrocatalysts: Insight into the intrinsic carbon defects, *Advanced Functional Materials*, 2020, 30, 2001097.
- [35] H. M. Liu, Q. L. Liu, Y. R. Wang, Y. F. Wang, S. L. Chou, Z. Z. Hu, Z. Q. Zhang, Bifunctional carbon-based cathode catalysts for zinc-air battery: A Review, *Chinese Chemical Letters*, 2022, 33, 683-692.
- [36] J. Pan, X. L. Tian, S. Zaman, Z. H. Dong, H. F. Liu, H. S. Park, B. Y. Xia, Recent Progress on transition metal oxides as bifunctional catalysts for lithium-air and zinc-air batteries, *Batteries & Supercaps*, 2019, 2, 336-347.
- [37] M. Mechili, C. Vaitsis, N. Argirusis, P. K. Pandis, G. Sourkouni, C. Argirusis, Research progress in transition metal oxide based bifunctional electrocatalysts for aqueous electrically rechargeable zinc-air batteries, *Renewable and Sustainable Energy Reviews*, 2022, 156, 111970.
- [38] Y. Z. Wang, Z. Z. Liang, H. Q. Zheng, R. Cao, Recent progress on defect-rich transition metal oxides and their energy-related applications, *Chemistry An Asian Journal*, 2020, 15, 3717-3736.
- [39] F. Fasulo, A. Massaro, A. Pecoraro, A. B. Muñoz-García, M. Pavone, Role of defect-driven surface reconstructions in transition metal oxide electrocatalysis towards OER/ORR: A quantum-mechanical perspective, *Current Opinion in Electrochemistry*, 2023, 42, 101412.
- [40] Z. G. Yang, H. M. Xu, T. Y. Shuai, Q. N. Zhan, Z. J. Zhang, K. Huang, C. L. Dai, G. R. Li, Recent progress in the synthesis of transition metal nitride catalysts and their applications in electrocatalysis, *Nanoscale*, 2023, 15, 11777-11800.
- [41] W. Shen, J. M. Zhu, Y. Hu, J. Yin, Y. Zheng, P. X. Xi, Applications of rare earth promoted transition metal sulfides in electrocatalysis, *Chinese Journal of Chemistry*, 2023, 41, 1740-1752.
- [42] Y. T. Deng, S. T. Xiao, Y. J. Zheng, X. Rong, M. R. Bai, Y. J. Tang, T. Ma, C. Cheng, C. S. Zhao, Emerging electrocatalytic activities in transition metal selenides: synthesis, electronic modulation, and structure-performance correlations, *Chemical Engineering Journal*, 2023, 451, 138514.

- [43] X. Chen, Y. H. Li, X. Y. Zhao, Screening of transition metal-based MOF as highly efficient bifunctional electrocatalysts for oxygen reduction and oxygen evolution, *Surfaces and Interfaces*, 2023, 38, 102821.
- [44] A. K. Ipadeola, K. Eid, A. M. Abdullah, Porous transition metal-based nanostructures as efficient cathodes for aluminum-air batteries, *Current Opinion in Electrochemistry*, 2023, 37, 101198.
- [45] Q. Zhao, Z. H. Yan, C. C. Chen, J. Chen, Spinel: Controlled preparation, oxygen reduction/evolution reaction application, and beyond, *Chemical reviews*, 2017, 117, 10121-10211.
- [46] C. N. Chinnasamy, A. Narayanasamy, N. Ponpandian, K. Chattopadhyay, K. Shinoda, B. Jeyadevan, K. Tohji, K. Nakatsuka, T. Furubayashi, I. Nakatani, Mixed spinel structure in nanocrystalline NiFe_2O_4 , *Physical Review B*, 2001, 63, 184108.
- [47] F. Bosi, Chemical and structural variability in cubic spinel oxides, *Structural Science Crystal Engineering Materials*, 2019, B75, 279-285.
- [48] Y. W. Dai, J. Yu, M. Ni, Z. P. Shao, Rational design of spinel oxides as bifunctional oxygen electrocatalysts for rechargeable Zn-air batteries, *Chemical Physics Reviews*, 2020, 1, 011303.
- [49] A. K. Lebechi, A. K. Ipadeola, K. Eid, A. M. Abdullah, K. I. Ozoemena, Porous spinel-type transition metal oxide nanostructures as emergent electrocatalysts for oxygen reduction reactions, *Nanoscale*, 2022, 14, 10717-10737.
- [50] W. Deeloed, T. Priamushko, J. Čížek, S. Suramitr, F. Kleitz, Defect-engineered hydroxylated mesoporous spinel oxides as bifunctional electrocatalysts for oxygen reduction and evolution reactions, *ACS Applied Materials & Interfaces*, 2022, 14, 23307-23321.
- [51] C. Belkessam, S. Bencherif, M. Mechouet, N. Idiri, J. Ghilane, The effect of heteroatom doping on nickel cobalt oxide electrocatalysts for oxygen evolution and reduction reactions, *ChemPlusChem*, 2020, 85, 1710-1718.
- [52] C. Chen, H. Su, L. N. Lu, Y. S. Hong, Y. Z. Chen, K. Xiao, T. Ouyang, Y. L. Qin, Z. Q. Liu, Interfacing spinel NiCo_2O_4 and NiCo alloy derived N-doped carbon nanotubes for

enhanced oxygen electrocatalysis, *Chemical Engineering Journal*, 2021, 408, 127814.

[53] T. Maiyalagan, K. R. Chemelewski, A. Manthiram, Role of the morphology and surface planes on the catalytic activity of spinel $\text{LiMn}_{1.5}\text{Ni}_{0.5}\text{O}_4$ for oxygen evolution reaction, *ACS Catalysis*, 2014, 4, 421-425.

[54] X. Y. Meng, Y. Yuan, J. G. Feng, C. C. Ma, Y. Z. Sun, J. Zhang, B. L. Pang, Y. J. Chen, L. Y. Yu, L. F. Dong, Design and synthesis of self-supporting FeCoNi- and N-doped carbon fibers/nanotubes as oxygen bifunctional catalysts for solid-state flexible Zn-air batteries, *Chemical Engineering Journal*, 2024, 479, 147648.

[55] J. X. Zheng, R. Sun, D. P. Meng, J. X. Guo, Z. Wang, Boosting oxygen evolution reaction performance via metal defect-induced lattice oxygen redox reactions on spinel oxides, *Journal of Materials Chemistry A*, 2023, 11, 15044-15053.

[56] H. Yuan, J. T. Li, W. Yang, Z. C. Zhuang, Y. Zhao, L. He, L. Xu, X. B. Liao, R. Q. Zhu, L. Q. Mai, Oxygen vacancy-determined highly efficient oxygen reduction in NiCo_2O_4 /hollow carbon spheres, *ACS Applied Materials & Interfaces*, 2018, 10, 16410-16417.

[57] Y. M. Zhu, X. Liu, S. G. Jin, H. J. Chen, W. Lee, M. L. Liu, Y. Chen, Anionic defect engineering of transition metal oxides for oxygen reduction and evolution reactions, *Journal of Materials Chemistry A*, 2019, 7, 5875-5897.

[58] F. Y. Cheng, J. Shen, B. Peng, Y. D. Pan, Z. L. Tao, J. Chen, Rapid room-temperature synthesis of nanocrystalline spinels as oxygen reduction and evolution electrocatalysts, *Nature Chemistry*, 2011, 3, 79-84.

[59] Y. X. Zhao, C. Chang, F. Teng, Y. F. Zhao, G. B. Chen, R. Shi, G. I. N. Waterhouse, W. F. Huang, T. R. Zhang, Defect-engineered ultrathin $\delta\text{-MnO}_2$ nanosheet arrays as bifunctional electrodes for efficient overall water splitting, *Advanced Energy Materials*, 2017, 7, 1700005.

[60] K. Li, R. R. Zhang, R. J. Gao, G. Q. Shen, L. Pan, Y. D. Yao, K. H. Yu, X. W. Zhang, J. Zou, Metal-defected spinel $\text{Mn}_x\text{Co}_{3-x}\text{O}_4$ with octahedral Mn-enriched surface for highly efficient oxygen reduction reaction, *Applied Catalysis B: Environmental*, 2019, 244, 536-545.

- [61] J. X. Zheng, X. F. Peng, Z. Xu, J. B. Gong, Z. Wang, Cationic defect engineering in spinel NiCo_2O_4 for enhanced electrocatalytic oxygen evolution, *ACS Catalysis*, 2022, 12, 10245-10254.
- [62] D. F. Yan, Y. X. Li, J. Huo, R. Chen, L. M. Dai, S. Y. Wang, Defect chemistry of nonprecious-metal electrocatalysts for oxygen reactions, *Advanced Materials*, 2017, 29, 1606459.
- [63] K. L. Ao, J. H. Shi, X. Y. Zhang, W. A. Daoud, Tuning oxygen vacancies in spinel nanosheets for binder-free oxygen cathodes with superior catalytic activity in zinc-air batteries, *Journal of Power Sources*, 2022, 521, 230918.
- [64] S. X. Guo, X. Y. Wang, X. H. Zhou, H. W. Li, X. F. Ding, Tuning oxygen vacancies in Co_3O_4 nanorods through solvent reduction method for enhanced oxygen evolution activity, *Energy & Fuel*, 2023, 37, 5421-5428.
- [65] H. Jiang, D. A. Stewart, Using dopants to tune oxygen vacancy formation in transition metal oxide resistive memory, *ACS Applied Materials & Interfaces*, 2017, 9, 16296-16304.
- [66] L. Xu, Q. Q. Jiang, Z. H. Xiao, X. Y. Li, J. Huo, S. Y. Wang, L. M. Dai, Plasma-engraved Co_3O_4 nanosheets with oxygen vacancies and high surface area for the oxygen evolution reaction, *Angewandte Chemie*, 2016, 128, 5363-5367.
- [67] D. Lim, H. Kong, C. Lim, N. Kim, S. E. Shim, S. H. Baeck, Spinel-type NiCo_2O_4 with abundant oxygen vacancies as a high-performance catalyst for the oxygen reduction reaction, *International Journal of Hydrogen energy*, 2019, 44, 23775-23783.
- [68] Z. H. Xiao, Y. Wang, Y. C. Huang, Z. X. Wei, C. L. Dong, J. M. Ma, S. H. Shen, Y. F. Li, S. Y. Wang, Filling the oxygen vacancies in Co_3O_4 with phosphorus: an ultra-efficient electrocatalyst for overall water splitting, *Energy & Environmental Science*, 2017, 10, 2563-2569.
- [69] L. Y. Cao, B. W. Zhang, S. L. Zhao, Cation-tuning engineering on metal oxides for oxygen electrocatalysis, *Chemistry A European Journal*, 2023, 29, e202202000.
- [70] Y. M. Zhu, X. Liu, S. G. Jin, H. J. Chen, W. Lee, M. L. Liu, Y. Chen, Anionic defect engineering of transition metal oxides for oxygen reduction and evolution reactions, *Journal of Materials Chemistry A*, 2019, 7, 5875-5897.

- [71] X. Chen, M. YU, Z. H. Yan, W. Y. Guo, G. L. Fan, Y. X. Ni, J. D. Liu, W. Zhang, W. Xie, F. Y. Cheng, J. Chen, Boosting electrocatalytic oxygen evolution by cation defect modulation via electrochemical etching , *CCS Chemistry*, 2020, 3, 675-685.
- [72] P. Tan, Z. Wu, B. Chen, H. R. Xu, W. Z. Cai, S. W. Jin, Z. P. Shao, M. Li, Cation-substitution-tuned oxygen electrocatalyst of spinel cobaltite $M\text{Co}_2\text{O}_4$ ($M = \text{Fe}, \text{Co}, \text{and Ni}$) hexagonal nanoplates for rechargeable Zn-air batteries, *Journal of The Electrochemical Society*, 2019, 166, A3448-3455.
- [73] S. Liu, B. S. Zhang, Y. Cao, H. L. Wang, Y. M. Zhang, S. J. Zhang, Y. T. Li, H. C. Gong, S. Z. Liu, Z. X. Yang, J. Sun, Understanding the effect of nickel doping in cobalt spinel oxides on regulating spin state to promote the performance of the oxygen reduction reaction and zinc–air batteries, *ACS Energy Letters*, 2023, 8, 159-168.
- [74] G. Janani, Y. J. Chae, S. Surendran, Y. Sim, W. Park, J. K. Kim, U. Sim, Rational design of spinel oxide nanocomposites with tailored electrochemical oxygen evolution and reduction reactions for zincair batteries, *Applied Sciences*, 2020, 10, 3165.
- [75] J. B. Luo, X. Z. Wang, S. T. Wang, W. L. Li, Y. P. Li, T. Y. Wang, F.Q. Xu, Y. Liu, Y. Zhou, J. Zhang, MOF-derived S-doped NiCo_2O_4 hollow cubic nanocage for highly efficient electrocatalytic oxygen evolution, *Journal of Colloid and Interface Science*, 2024, 656, 297-308.
- [76] J. Yin, Y. X. Li, F. Lv, Q. H. Fan, Y. Q. Zhao, Q. L. Zhang, W. Wang, F. Y. Cheng, P. X. Xi, S. J. Guo, NiO/CoN porous nanowires as efficient bifunctional catalysts for Zn–air batteries, *ACS Nano*, 2017, 11, 2275-2283.
- [77] Z. M. Zhang, H. N. Sun, J. F. Li, Z. H. Shi, M. H. Fan, H. Q. Bian, T. Wang, D. Q. Gao, S-doped CoMo_2O_4 with more high valence metallic cations and oxygen defects for zinc-air batteries, *Journal of Power Source*, 2021, 491, 229584.
- [78] Z. H. Xiao, Y. Wang, Y. C. Huang, Z. X. Wei, C. L. Dong, J. M. Ma, S. H. Shen, Y. F. Li, S. Y. Wang, Filling the oxygen vacancies in Co_3O_4 with phosphorus: an ultra-efficient electrocatalyst for overall water splitting, *Energy & Environmental Science*, 2017, 10, 2563-2569.
- [79] P. W. Menezes, A. Indra, D. González-Flores, N. R. Sahraie, I. Zaharieva, M.

Schwarze, P. Strasser, H. Dau, M. Driess, High-performance oxygen redox catalysis with multifunctional cobalt oxide nanochains: Morphology-dependent activity, *ACS Catalysis*, 2015, 5, 2017-2027.

[80] D. U. Lee, J. Scott, H. W. Park, S. Abureden, J. Y. Choi, Z. W. Chen, Morphologically controlled Co_3O_4 nanodisks as practical bi-functional catalyst for rechargeable zinc–air battery applications, *Electrochemistry Communications*, 2014, 43, 109-112.

[81] J. M. Concalves, M. N. Silva, K. K. Naik, P. R. Martins, D. P. Rocha, E. Nossol, R. A. Munoz, L. Angnes, C. S. Rout, Multifunctional spinel MnCo_2O_4 based materials for energy storage and conversion: a review on emerging trends, recent developments and future perspectives, *Journal of Materials Chemistry A*, 2021, 9, 3095-3124.

[82] Y. He, J. F. Zhang, G. W. He, X. P. Han, X. R. Zheng, C. Zhong, W. B. Hu, Y. D. Deng, Ultrathin Co_3O_4 nanofilm as an efficient bifunctional catalyst for oxygen evolution and reduction reaction in rechargeable zinc–air batteries, *Nanoscale*, 2017, 9, 8623-8630.

[83] S. V. Devaguptapu, S. Hwang, S. Karakalos, S. Zhao, S. Gupta, D. Su, H. Xu, G. Wu, Morphology control of carbon-free spinel NiCo_2O_4 catalysts for enhanced bifunctional oxygen reduction and evolution in alkaline media, *Acs Applied Materials & Interfaces*, 2017, 9, 44567-44578.

[84] Z. Chen, C. X. Kronawitter, B. E. Koel, Facet-dependent activity and stability of Co_3O_4 nanocrystals towards the oxygen evolution reaction, *Physical Chemistry Chemical Physics*, 2015, 17, 29387-29393.

[85] Q. F. Liu, Z. P. Chen, Z. Yan, Y. Wang, E. D. Wang, S. Wang, S. D. Wang, G. Q. Sun, Crystal-plane-dependent activity of spinel Co_3O_4 towards water splitting and oxygen reduction reaction, *ChemElectronChem*, 2018, 5, 1080-1086.

[86] X. Q. Xu, M. Y. Liu, Y. Nie, C. Wang, W. Wang, C. T. Liu, X. Y. Wang, Z. Cai, X. F. Liu, S. C. Huo, B. Liu, J. L. Zou, Modulating electronic structure of interfacial Fe sites in $\text{Fe}_2\text{N}/\text{CoFe}_2\text{O}_4$ nano-heterostructure for enhancing corrosion-resistance and oxygen electrocatalysis in zinc-air battery, *Chemical Engineering Journal*, 2023, 471, 144639.

[87] K. Wang, Z. Wang, Y. G. Liu, J. P. Liu, Z. M. Cui, X. F. Zhang, F. Ciucci, Z. H. Tang, Tailoring the interfacial active center of $\text{MnS}_x\text{O}_{2-x}/\text{MnCo}_2\text{S}_4$ heterostructure to boost the

performance for oxygen evolution reaction and Zn-air batteries in neutral electrolyte, *Chemical Engineering Journal*, 2022, 427, 131966.

[88] Z. P. Hu, S. J. Dong, Q. F. He, Z. H. Chen, D. Yuan, Synergetic nanostructure engineering and electronic modulation of a 3D Hollow heterostructured NiCo₂O₄@NiFe-LDH self-supporting electrode for rechargeable Zn–air batteries, *Inorganic Chemistry*, 2023, 62, 7471-7482.

[89] Z. M. Zhang, X. L. Liang, J. F. Li, J. M. Qian, Y. G. Liu, S. L. Yang, Y. Wang, D. Q. Gao, D. S. Xue, Interfacial engineering of NiO/NiCo₂O₄ porous nanofibers as efficient bifunctional catalysts for rechargeable zinc–air batteries, *ACS Applied Materials & Interfaces*, 2020, 12, 21661-21669.

[90] X. Q. Xu, M. Y. Liu, Y. Nie, C. Wang, W. Wang, C. T. Liu, X. Y. Wang, Z. Cai, X. F. Liu, S. C. Huo, B. Liu, J. L. Zou, Modulating electronic structure of interfacial Fe sites in Fe₂N/CoFe₂O₄ nano-heterostructure for enhancing corrosion-resistance and oxygen electrocatalysis in zinc-air battery, *Chemical Engineering Journal*, 2023, 471, 144639.

[91] C. Rui, T. Zhang, Y. Jiang, D. S. Xie, M. Li, Q. Lu, Y. F. Bu, Highly efficient and stable bifunctional electrocatalyst with Alloy/Oxide heterostructures for a rechargeable zinc–air battery, *Energy & Fuels*, 2022, 36, 12816-12825.

[92] S. Shrestha, B. Wang, P. Dutta, Nanoparticle processing: Understanding and controlling aggregation, *Advances in Colloid and Interface Science*, 2020, 279, 102162.

[93] X. M. Deng, Y. J. Mi, Y. Z. Liu, Y. Sun, Y. S. Cheng, W. Wang, Co, N co-doped carbon nanosheets coupled with NiCo₂O₄ as an efficient bifunctional oxygen catalyst for Zn-air batteries, *International Journal of Hydrogen Energy*, 2023, 48, 13452-13459.

[94] J. L. Liu, D. D. Zhu, Y. Zheng, A. Vasileff, S. Z. Qiao, Self-supported earth-abundant nanoarrays as efficient and robust electrocatalysts for energy-related reactions, *ACS Catalysis*, 2018, 8, 6707-6732.

[95] Y. Y. Ma, W. X. Shang, W. T. Yu, X. H. Chen, W. D. Xia, C. Wang, P. Tan, Synthesis of ultrasmall NiCo₂O₄ nanoparticle-decorated N-doped graphene nanosheets as an effective catalyst for Zn–air batteries, *Energy & Fuels*, 2021, 35, 14188-14196.

[96] Y. X. Zhang, X. Y. Xie, Z. C. Zheng, X. He, P. Du, R. Zhang, L. M. Guo, K. Huang,

Manganese-cobalt spinel nanoparticles anchored on carbon nanotubes as bi-functional catalysts for oxygen reduction and oxygen evolution reactions, *Applied Sciences*, 2023, 13, 12702.

[97] X. Chen, L. Luo, Y. Z. Zhang, Identification of the active sites of NiCo_2O_4 and the support effect with carbon nanotubes for oxygen reduction catalysis, *Langmuir*, 2021, 37, 6330-336.

[98] H. Xu, J. J. Yuan, G. Y. He, H. Q. Chen, Current and future trends for spinel-type electrocatalysts in electrocatalytic oxygen evolution reaction, *Coordination Chemistry Reviews*, 2023, 475, 214869.

[99] Z. Y. Shao, X. T. Wu, X. F. Wu, S. H. Feng, K. K. Huang, Synthesis and advantages of spinel-type composites, *Materials Chemistry Frontiers*, 2023, 7, 5288-5308.

[100] Q. Liu, L. Wang, D. G. Fu, Research progress on the construction of synergistic electrocatalytic ORR/OER self-supporting cathodes for zinc-air batteries, *Journal of Material Chemistry A*, 2023, 11, 4400-4427.

[101] N. N. Xu, J. A. Wilson, Y. D. Wang, T. S. Su, Y. N. Wei, J. L. Qiao, X. D. Zhou, Y. X. Zhang, S. H. Sun, Flexible self-supported bi-metal electrode as a highly stable carbon- and binder-free cathode for large-scale solid-state zinc-air batteries, *Applied Catalysis B: Environmental*, 2020, 272, 118953.

[102] J. Yin, Y. X. Li, F. Lv, Q. H. Fan, Y. Q. Zhao, Q. L. Zhang, W. Wang, F. Y. Cheng, P. X. Xi, S. J. Guo, NiO/CoN porous nanowires as efficient bifunctional catalysts for Zn-air batteries, *ACS Nano*, 2017, 11, 2275-2283.

[103] J. Yin, P. P. Zhou, L. An, L. Huang, C. W. Shao, J. Wang, H. Y. Liu, P. X. Xi, Self-supported nanoporous NiCo_2O_4 nanowires with cobalt-nickel layered oxide nanosheets for overall water splitting, *Nanoscale*, 2016, 8, 1390.

[104] K. T. A. L. Burm, Plasma: The fourth state of matter, *Plasma Chem Plasma Process*, 2012, 32, 401-407.

[105] F. F. Chen, Introduction to plasma physics and controlled fusion, Springer Cham, Online ISBN: 978-3319223094.

[106] M. A. Lieberman, A. J. Lichtenberg, Principles of plasma discharges and materials processing, John Wiley & Sons, Online ISBN: 978-0471724254.

[107] National Academies of Sciences, Engineering, and Medicine, Plasma Science: Enabling Technology, Sustainability, Security, and Exploration. Washington, DC: The National Academies Press, Online ISBN: 978-0309677639.

[108] M. Goossens, Basic plasma properties. In: An Introduction to Plasma Astrophysics and Magnetohydrodynamics. Astrophysics and Space Science Library, Springer, Online ISBN: 978-9400710764.

[109] M. J. Kushner, Hybrid modelling of low temperature plasmas for fundamental investigations and equipment design, Journal of Physics D: Applied Physics, 2029, 42, 194013.

[110] B. M. Penetrante, R. M. Brusasco, B. T. Merritt, G. E. Vogtlin, Environmental applications of low-temperature plasmas, Pure and Applied Chemistry, 1999, 71, 1829-1835.

[111] J. Y. Liu, Y. H. Li, Y. Chen, Y. Y. Zhou, S. S. Wang, Z. Z. Yuan, Z. J. Jin, X. Liu, A review of low-temperature plasma-assisted machining: from mechanism to application, Frontiers of Mechanical Engineering, 2023, 18, 18.

[112] J. Schmitz, Low temperature thin films for next-generation microelectronics, Surface and Coating Technology, 2018, 343, 83-88.

[113] D. Y. Hou, F. N. Bai, P. Dong, J. Chen, Y. T. Zhang, F. M. Meng, Z. H. Zhang, C. X. Zhang, Y. J. Zhang, J. Hu, Recent development of low temperature plasma technology for lithium-ion battery materials, Journal of Power Sources, 2023, 584, 233599.

[114] C. Qin, S. J. Tian, Z. J. Jiang, M. Thandavarayan, Z. Q. Jiang, Low temperature plasma-assisted synthesis and modification of water splitting electrocatalysts, Electrochimica Acta, 2023, 449, 142179.

[115] M. Zelzer, D. Scurr, B. Abdullah, A. J. Urquhart, N. Gadegaard, J. W. Bradley, M. R. Alexander, Influence of the plasma sheath on plasma polymer deposition in advance of a mask and down pores, The Journal of Physical Chemistry B, 2009, 113, 8487-8494.

- [116] S. Y. Lee, C. Kim, H. T. Kim, Difference in chemical reactions in bulk plasma and sheath regions during surface modification of graphene oxide film using capacitively coupled NH_3 plasma, *Journal of Applied Physics*, 2015, 118, 103303.
- [117] S. Wilczek, J. Schulze, R. P. Brinkmann, Z. Donkó, J. Trieschmann, T. Mussenbrock, Electron dynamics in low pressure capacitively coupled radio frequency discharges, *Journal of Applied Physics*, 2020, 127, 1881101.
- [118] M. M. Devadevan, J. Krishnanand, K. B. Shilpa, R. N. Kini, A compact, fast, and efficient plasma cleaner, *IEEE Transactions on Plasma Science*, 2021, 49, 3576-3581.
- [119] Y. Uchida, T. Fukuda, H. Yanazawa, X-ray photoelectron spectroscopic study of surface modification of low-k organic materials by plasma treatment, *Surface and Interface Analysis*, 2024, 36, 677-680.
- [120] T. OH, Comparison between organic thin films deposited by using CCP-CVD and ICP-CVD, *Journal of the Korean Physical Society*, 2009, 55, 1950-1954.
- [121] K. K. Jayapalan, O. H. Chin, C. S. Wong, Radio frequency planar inductively coupled plasma: Fundamentals and applications. In: Rawat, R. (eds) *Plasma Science and Technology for Emerging Economies*. Springer, Singapore. Online ISBN: 978-9811042171.
- [122] D. K. Lee, J. J. Lee, J. Joo, Low temperature TiN deposition by ICP-assisted chemical vapor deposition, *Surface and Coatings Technology*, 2003, 174-175, 1234-1237.
- [123] C. L. Ma, A. Nikiforov, D. Hegemann, N. D. Geyter, R. Morent, M. Ostrikov, Plasma-controlled surface wettability: recent advances and future applications, *International Materials Reviews*, 2023, 68, 82-119.
- [124] A. Yusuf, H. K. Amusa, J. O. Eniola, A. Giwa, O. Pikuda, A. Dindi, M. R. Bilad, Hazardous and emerging contaminants removal from water by plasma-based treatment: A review of recent advances, *Chemical Engineering Journal Advances*, 2023, 14, 100443.
- [125] M. Zhianmanesh, A. Gilmour, M. M. Bilek, B. Akhavan, Plasma surface functionalization: A comprehensive review of advances in the quest for bioinstructive materials and interfaces, *Applied Physics Reviews*, 2023, 10, 021301.

- [126] J. P. Chang, J. W. Coburn, Plasma-surface interactions, *Journal of Vacuum Science & Technology A*, 2003, 21, S145.
- [127] B. D. Wirth, K. Nordlund, D. G. Whyte, D. Xu, Fusion materials modeling: Challenges and opportunities, *MRS Bulletin*, 2011, 36, 216-222.
- [128] C. Steinbrüchel, Ion-surface interactions: from sputtering to reactive ion etching, *Materials Science and Technology*, 1992, 8, 565-573.
- [129] W. Petasch, B. Kegel, H. Schmid, K. Lendenmann, H. U. Keller, Low-pressure plasma cleaning: a process for precision cleaning applications, *Surface and Coating Technology*, 1997, 97, 176-181.
- [130] S. Tang, N. Lu, J. K. Wang, S. K. Ryu, H. S. Choi, Novel effects of surface modification on activated carbon fibers using a low pressure plasma treatment, *The Journal of Physical Chemistry: C*, 2007, 111, 1820-1829.
- [131] L. M. Dai, H. J. Griesser, A. W. Mau, Surface modification by plasma etching and plasma patterning, *The Journal of Physical Chemistry: B*, 1997, 101, 9548-9554.
- [132] R. S. Pessoa, M. A. Fraga, L. V. Santos, N. K. Galvão, H. S. Maciel, M. Massi, Plasma-assisted techniques for growing hard nanostructured coatings: An overview, *Anti-Abrasive Nanocoatings*, Woodhead Publishing, 2015, 455-479.
- [133] M. Li, F. Luo, Q. Zhang, Z.H. Yang, Z.K. Xu, Atomic layer $\text{Co}_3\text{O}_{4-x}$ nanosheets as efficient and stable electrocatalyst for rechargeable zinc-air batteries, *Journal of Catalysis*, 2020, 381, 395-401.
- [134] Y. M. Zhu, X. Zhong, S. G. Jin, H. J. Chen, Z. Y. He, Q. Y. Liu, Y. Chen, Oxygen defect engineering in double perovskite oxides for effective water oxidation, *Journal of Material Chemistry A*, 2020, 8, 10957-10965.
- [135] Y. Q. Zhang, B. Ouyang, J. Xu, G. C. Jia, S. Chen, R. S. Rawat, H. J. Fan, Rapid synthesis of cobalt nitride nanowires: highly efficient and low-cost catalysts for oxygen evolution, *Angewandte Chemie*, 2016, 55, 8670-8674.
- [136] H. F. Liang, A. N. Gandi, D. H. Anjum, X. B. Wang, U. Schwingenschlögl, H. N. Alshareef, Plasma-assisted synthesis of NiCoP for efficient overall water splitting, *Nano*

Letter, 2016, 16, 7718-7725.

[137] Z. Y. Shao, Q. Zhu, Y. Sun, Y. Zhang, Y. L. Jiang, S. Q. Deng, W. Zhang, K. K. Huang, S. H. Feng, Phase-reconfiguration-induced NiS/NiFe₂O₄ composite for performance-enhanced zinc-air batteries, *Advanced Materials*, 2022, 34, 2110172.

会当凌绝顶，一览众山小。

-----杜甫

Try to ascend the mountain's crest;
It dwarfs all peaks under our feet.

----- Fu Du (Translated by Yuanchong Xu)

3

EXPERIMENTAL METHODS AND SETUPS

This chapter briefly introduces the methods and devices used in this thesis. First, the methods and reactors for the material synthesis are introduced. Then, the plasma reactors employed to modify material surfaces are presented. Finally, the characterization methods of plasma and electrocatalysts are introduced.

3.1 Material preparation

3.1.1 Hydrothermal method

The hydrothermal method is commonly applied to synthesize inorganic materials, which has been widely used in the research fields of nanomaterials, biomaterials, and geomaterials [1-3]. This chapter provides a brief introduction to this method, with further details available in the referenced books [4-6].

The term “hydrothermal” was initially used in geology to describe the natural process of water in the earth’s crust under elevated temperature and pressure, resulting in the formation of various rocks and minerals. The first report on the synthesis of crystals by the hydrothermal method was published by Karl Emil von Schafhäütl in 1845. He used silicic acid as a raw material to grow microscopic quartz crystals in a pressure cooker [7]. After nearly two centuries of development, this method has progressed from the simulation of geological ore generation to the synthesis of zeolite molecular sieves and other crystalline materials. Now, the hydrothermal method is defined as the utilization of an aqueous solution as the reaction medium in a special sealed vessel, which is then heated to create a high-temperature (100~1000 °C) and high-pressure (1~100 MPa) reaction environment, thereby facilitating the dissolution and recrystallization of poorly soluble or insoluble precursors.

Compared to other wet-chemical synthesis processes, the hydrothermal method has several advantages as follows:

- (1) Nanomaterials synthesized by the hydrothermal method have high purity, well-developed grains, light agglomeration, and a narrow particle size distribution.
- (2) Avoiding the introduction of impurities and structural defects by post-treatment processes such as high-temperature calcination or ball milling.
- (3) This method allows for the synthesis of single crystals, thin films, and nanoparticles with different morphologies, structures, and even metastable phases.

However, due to the special reaction conditions, the hydrothermal method also has

certain limitations:

- (1) It is difficult to observe the material growth process.
- (2) The high requirements for the reactor which must be able to withstand high temperatures, pressure, and corrosion.
- (3) The hydrothermal synthesis process is inherently unsafe due to the high working pressure.
- (4) The hydrothermal synthesis is not suitable for large-scale production.

In this thesis, the hydrothermal method was employed to synthesize spinel transition-metal oxides as pristine electrocatalysts for oxygen-related reactions and zinc-air batteries.

3.1.2 Equipment for the hydrothermal method

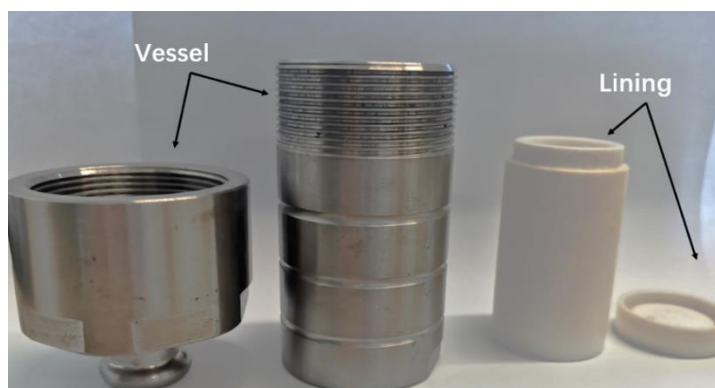


Figure 3.1 the laboratory reactor for the hydrothermal method.

The hydrothermal method for the synthesis of electrocatalysts relies on a suitable reactor. Figure 3.1 shows a typical laboratory reactor, which is comprised of two components, the vessel and the lining. The vessel is constructed from stainless steel and its body and lid are connected by threads to achieve a robust and reliable sealing mechanism. Due to the possible presence of acid or alkaline precursors, a lining is necessary, which is made of polytetrafluoroethylene with excellent corrosion resistance and seal function. Therefore, the working temperature must be below the softening point of polytetrafluoroethylene (250 °C). External heating devices, such as ovens or muffle furnaces, are common heating sources.

Once the reaction has been completed, it is necessary to allow the autoclave to cool fully. This prevents sudden release of pressure and reduces the risk of splashing hot liquid.

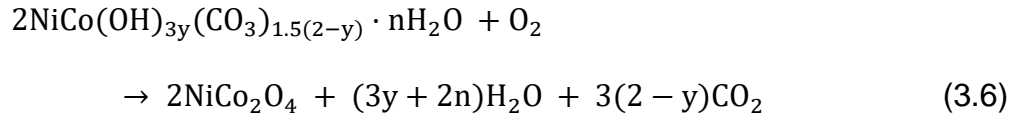
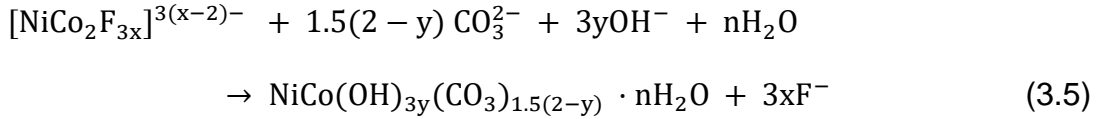
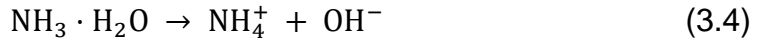
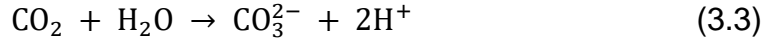
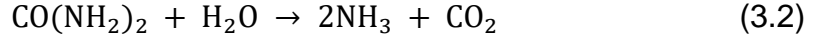
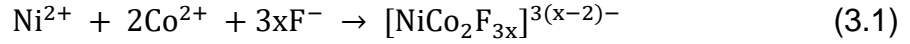
3.1.3 Hydrothermal synthesis of electrocatalysts

As we mentioned before, spinel-oxide-based materials grown on conductive supports have been regarded as promising self-supported bifunctional electrocatalysts to replace these noble-metal-based electrocatalysts in RZABs. In this study, spinel NiCo_2O_4 nanowires were grown on commercial carbon papers by the hydrothermal method followed by an annealing process. The specific steps are as follows:

Step 1: Pre-treatment of carbon paper. Carbon paper offers the advantages of good conductivity, a high specific surface area, excellent flexibility and accepted thermal and acid resistance. These properties make it an ideal substrate for supporting active materials [8-10]. However, the surface of pristine carbon paper is usually hydrophobic, necessitating a pre-treatment process for the surface to generate hydrophilic groups, which facilitate the uniform growth of materials at it.

Step 2: Precursor solution preparation. The transition-metal nitrate hexahydrate with the corresponding atom ratios, urea ($\text{CO}(\text{NH}_2)_2$) and ammonium fluoride (NH_4F) are dissolved into deionized water as the precursor solution. These nitrate hexahydrates control the species of spinel oxides. The alkali source, urea, and the additive, NH_4F , play a key role in the formation of material morphologies [11-12].

Step 3: Material synthesis process. The precursor solution is then transferred into the lining, and one piece of pre-treated carbon paper is vertically placed into the solution. The lining is sealed into the vessel and heated to $120\text{ }^\circ\text{C}$ for 12 h to produce a high-pressure reaction environment for the deposition process. Once the vessel has cooled to room temperature and its inner pressure has returned to atmospheric pressure, open it and take the sample out. The sample is washed with deionized water and dried at $60\text{ }^\circ\text{C}$ overnight. Finally, the as-prepared sample is annealed at $350\text{ }^\circ\text{C}$ in the air for 3 h to fabricate the self-supported electrocatalysts. Take the NiCo_2O_4 as an example to illustrate the possible reactions as follows [12-13]:



Due to the existence of CO_3^{2-} ions, the fabricated NiCo_2O_4 is in the shape of nanowires [12].

3.2 Plasma setups

Although these NiCo_2O_4 nanowires present bifunctional electrocatalytic activities for both OER and ORR, their practical performance remains unsatisfactory owing to their poor conductivity and low intrinsic activity [14-15]. To improve the electrocatalytic performance of the catalysts, two plasma reactors were constructed to modify their surfaces and optimize their properties.

(1) CCP reactor

Figure 3.2 show the CCP reactor and its structural sketch. This device composes of four parts: a power system, a pumping system, a gas supply system and a reactor chamber.

The power system contains a RF power and a matchbox. The RF power is supplied by Dressler Cesar RF power generator at 27.12 MHz with the matching network of Palstar AT4K used for matching the impedance between the RF source and the load.

The pumping system has two vacuum pumps: a pre-pump (Sliding vane vacuum pump, Pfeiffer Vacuum DUO 2.5) and a turbomolecular pump (Pfeiffer vacuum d-35614

asslar). The pre-pump is connected to the turbomolecular pump and pumps the chamber to a low pressure first. When the chamber pressure reaches the operating level of the turbomolecular pump (< 100 Pa), the turbomolecular pump starts pumping the chamber to a final pressure below 5×10^{-3} Pa. A butterfly valve between the turbomolecular pump and the chamber is used to control the desired pressure in the chamber.

The gas supply system contains three mass flow controllers (mks) to precisely control the flow rate of the process gases inserted into the reactor chamber.

The chamber reactor is a glass tube with an inner diameter of 36 mm. Two ring electrodes are placed in the middle outside of the tube and separated by 44 mm. One electrode is connected to the RF power system and another one is grounded. The gas is inserted into the tube at its left side and its right side is connected to the pumping system. During the plasma modification process, the catalyst standing on an electrically isolated substrate holder on a floating potential was positioned between the electrodes in the active plasma zone.

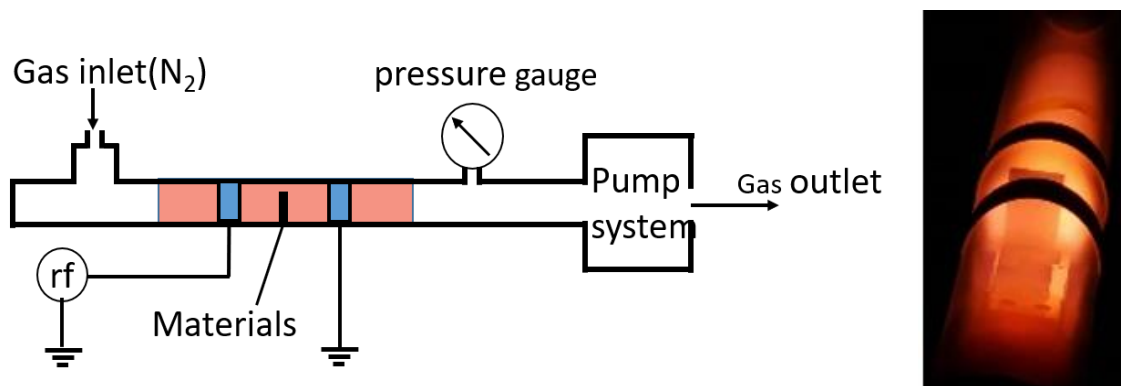


Figure 3.2 the CCP reactor and its structural sketch (same to Figure 2.5(b)).

(2) ICP reactor

Figure 3.3 shows the ICP device and its cross-sectional sketch. This device is a unique device build with inverted electrode geometry, where the small area electrode with the sample is grounded and the reactor wall with large area is biased (DC or RF) to induce the largest voltage drop across the sheath in front of the grounded electrode,

where the substrate and the sampling orifice of the mass spectrometer are placed. The surface area ratio of the chamber wall to the grounded substrate holder is about 20 to ensure a highly asymmetric electrode geometry. This geometry was motivated by the work of Wild and Koidl^[16], where they used the same principle to measure ion energy distribution functions with the help of a retarding field analyzer.

The main inductively coupled plasma is generated with the help of a planar coil with two spiral arms placed in a quartz dome at the top of the chamber. However, the RF-bias itself can be used to ignite capacitively coupled plasma as well. This system is composed of five parts: two power systems, one for the ICP part and one for the bias, a pumping system, a gas supply system and a reactor chamber. This device has a similar main power system, gas supply system and pumping system to the CCP device. The bias is generated either by second RF-power supply with a match box or by a DC power supply. Furthermore, the vacuum chamber is enclosed inside a grounded shielding cage to prevent the radiation of the RF power. More details could be found in the literature^[17].

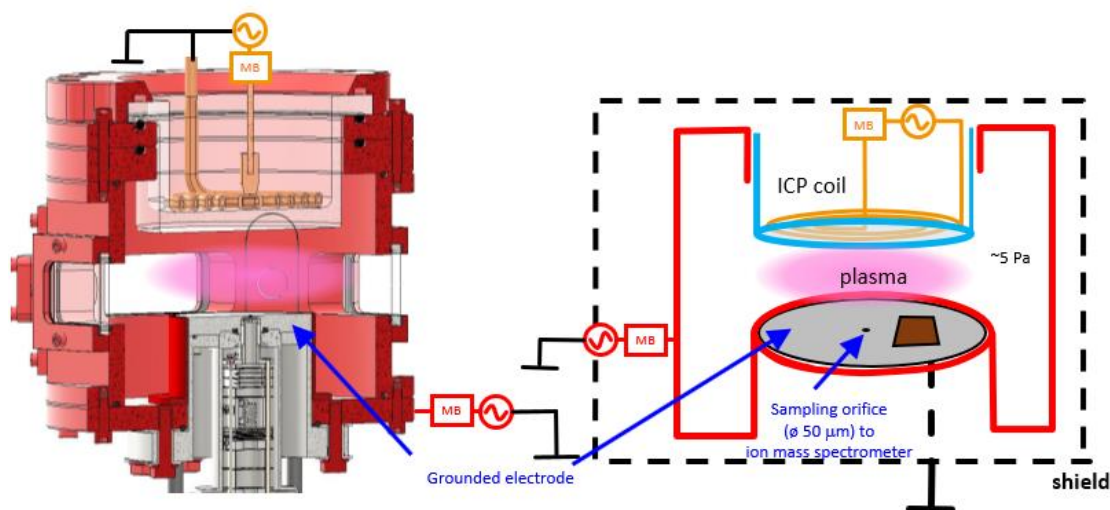


Figure 3.3 the ICP reactor and its structural sketch.

3.3 Plasma characterization

3.3.1 Energy resolved ion mass spectrometry (ERIMS)

Energy resolved ion mass spectrometry (PSM device of Hiden Analytical Ltd.) with Bessel box as the energy filter, Quadrupole as the mass filter and with Channeltron secondary electron multiplier as the detector is used to character the plasma properties. The device also has an electron impact ionizer and enables the analysis of the gas mixture (not used in this thesis).

3.3.2 Plasma characterization by ERIMS

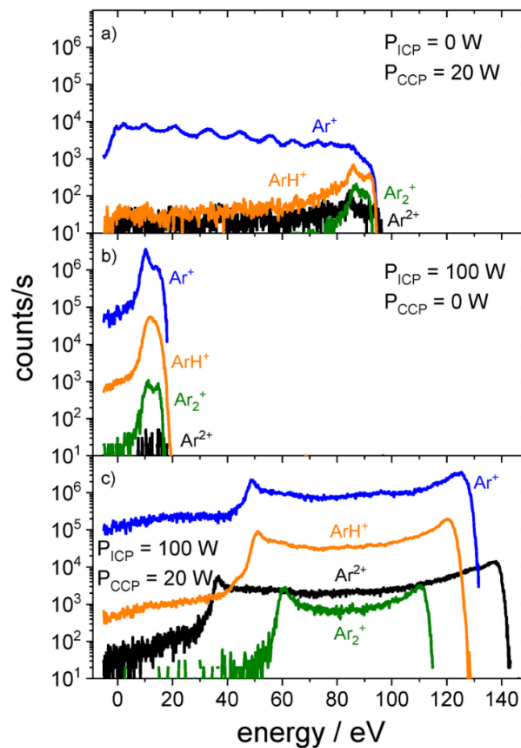


Figure 3.4 IEDFs of argon-related ions in an argon plasma at 5 Pa (a) Only capacitive power coupling to the reactor wall with a power of 20 W. (b) Only inductive coupling with a power of 100 W applied to the planar rf coil. (c) Both inductive and capacitive couplings are applied. ^[17] Copyright 2022 by the authors.

The practical application of ERIMS for plasma characterization in the ICP reactor has been reported by Schulze *et al.* ^[17]. Figure 3.4 shows the Ion flux-energy

distribution functions (IEDFs) for ions originating in ICP and CCP argon plasma at the pressure of 5 Pa. It is clearly visible that the ion flux is much larger from the ICP with ion energy typically below 20 eV. On the contrary, supplying CCP power generates a low-density plasma (two orders of magnitude difference), but the ion energy is much larger close to 100 eV. By combining both the ICP power and CCP power, a plasma with high densities and ion fluxes at high ion energies was generated due to the additional RF bias. Moreover, Figure 3.5 shows the measurement of the typical ions in plasma generated by both constant ICP and varies CCP power. The applied CCP power successfully controlled the sheath voltage and influenced the ion energy in the plasma.

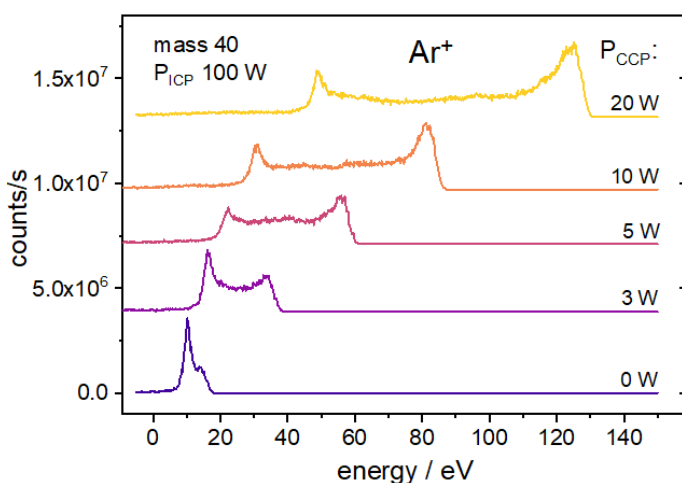


Figure 3.5 IEDFs of Ar⁺ as function of applied power of the capacitively coupled bias on the reactor wall. Argon pressure 5 Pa. ^[17] Copyright 2022 by the authors.

Inspired by these results, N₂ plasma was generated in this system and used to modify the catalyst. The selected catalyst was placed on the sample holder near the sampling orifice connected to the ERIMS that in-situ monitored the composition, energy and flux of ions reaching the catalyst surface. Moreover, a DC bias was connected to the chamber wall and tuned the ion energy of the plasma. The collected results enable better control and understanding of the treatment process.

3.4 Material characterization

A variety of material characterization methods were performed to investigate the catalyst structures and electrocatalytic performance. This chapter will only provide a brief overview of these methods and corresponding setups, more details can be found in the relevant books ^[18-19].

3.4.1 Electrochemical measurement

To evaluate the electrocatalytic performance of catalysts, a series of electrochemical measurements were performed using an electrochemical workstation (Wave Driver 200, Pine Research) with a standard three-electrode system. The samples, an Ag/AgCl (3 M KCl) electrode, a Pt wire, and 1 M KOH solution were applied as the working electrode, the reference electrode, the counter electrode, and the electrolyte, respectively. The working electrode is the research electrode with the catalyst, the reference electrode is employed to measure the potential of the working electrode, and the counter electrode is used to establish a circuit with the working electrode. This section only provides a brief overview of the electrochemical measurements, more details can be found in the relevant books ^[20-21].

(1) Potential scanning method

The potential scanning method, including the cyclic voltammetry (CV) and the linear sweep voltammetry (LSV), is used to study the fundamental properties of the electrochemical reactions at the electrode/electrolyte interface. It is widely employed in many research fields, including the chemical industry, energy, metallurgy, metal corrosion and protection, environmental science and life science.

The potential scanning process is that a triangular waveform pulse voltage is applied to the circuit of the working and counter electrodes, changing the potential at the working electrode/electrolyte interface, and prompting the active substance on the working electrode to undergo oxidation/reduction reactions, thereby generating the response current. The electrode potential and response current are recorded to obtain the corresponding current-voltage curve. In the case of the LSV measurement, the

recording process is only from the starting potential to the end potential in a certain direction. The resulting current-voltage curve is called the LSV curve. For the CV measurement, the recording potential is returned to the starting potential in the reverse direction at the same speed to complete a cycle. The resulting current-voltage curves are called the CV curves. Similarly, multiple cycles can be scanned continuously according to actual needs.

(2) Electrochemical impedance spectroscopy

Electrochemical impedance spectroscopy (EIS) studies the relationship between the electrochemical AC impedance and the frequency by applying a small AC excitation signal according to the sinusoidal law when the electrochemical cell is in a state of equilibrium (open circuit) or under a certain stable DC polarization condition. Since the applied potential signal is under the sinusoidal law, the anode and cathode processes alternate on the electrode. However, the small amplitude perturbation signal will not lead to the cumulative development of polarization phenomena or cumulative changes in the electrode surface state, even if it acts on the electrode system for a long time.

By analyzing the EIS results, various important parameters, including the electrode interface reaction rate, the conductivity of the electrolyte solution, and the electron transfer process can be studied. Moreover, it provides important theoretical and practical guidance for the advancement of electrochemical energy storage and conversion, electrochemical sensors and other related fields.

(3) Stability test

The stability of electrocatalysts is an important property that significantly impacts the practical performance of batteries. chronoamperometry or chronopotentiometry techniques are usually used to evaluate the stability of electrocatalysts. The chronoamperometry stability test employs a control technique to maintain a constant voltage on the working electrode and to measure the change in current over time. In contrast, the chronopotentiometry method is to measure the potential change under a constant current.

3.4.2 Scanning Electron Microscope

The scanning electron microscope (SEM) is a precise instrument for high-resolution micro-region morphology analysis. It provides a comprehensive understanding of the morphology and structure of the sample without significant damage.

The electron beam emitted by the electron gun is focused by the electromagnetic lens and accelerated by the electric field to bombard the sample surface. These electrons interact with the sample nucleus or nuclear electrons and are scattered, changing their movement direction and energy. This process generates various signals, including secondary electrons, backscattered electrons, absorbed electrons, transmitted electrons, Rochelle electrons, electron potentials, cathodoluminescence, and X-rays, which can be used to characterize the physical or chemical properties of the material surfaces.

In this thesis, the SEM devices (Zeiss Ultra 55 Plus and Zeiss EVO 10) was employed to measure the morphologies and structures of the samples. This measurement has been performed under the assistance of Igor Barg, Dr. Haoyi Qiu and Dr. Luka Hansen.

3.4.3 Transmission Electron Microscope

The transmission electron microscope (TEM) is a large microscopic analysis equipment that uses high-energy electron beams as illumination sources to perform surface magnified imaging. It has been widely utilized in various scientific fields, especially in the research of chemistry, physics, biology, medicine, and materials, playing an irreplaceable role.

The TEM device is similar in structure and fundamental principles to the optical microscope. The electron beam emitted by the electron gun is condensed to a sharp, bright, and uniform light spot by collecting the lens illuminated on the sample. The electrons, after passing through the sample, carry the structural information of the sample. The electrons in the same direction converge to one point on the rear focal

plane of the objective lens, forming the electron diffraction patterns. The electrons emitted from the same object point in the sample are brought together again on the objective lens image plane, providing the amplification image of the sample.

In this thesis, the TEM device (Tecnai F30 G2 STwin and JEOL JEM-ARM200F) was employed to measure the morphologies and nanostructures of the samples. This measurement has been performed in the group of Prof. Dr. Lorenz Kienle under the assistance of Dr. Niklas Wolff and Dr. Martin Müller.

3.4.4 Energy Dispersive X-ray spectroscopy

Energy dispersive X-ray spectroscopy (EDS) is an analytical technique for identifying and quantifying the elemental composition of the material surfaces, from B to U in the periodic table. This device is always constructed in SEM or TEM devices.

The electron beam emitted by the electron gun interacts with the sample, transferring parts of its energies to the sample atoms. The electrons in the sample atoms absorb the energy and are stripped from the atomic nuclei. At this time, the vacancies in the electron orbit will be filled by electrons in high-energy orbits, resulting in the generate of X-rays owing to the release of excess energy. For the sample atoms, the energy difference between each energy level is determined, and thus the X-rays produced by exciting the atoms can be used to identify the type of elements present in the sample.

In this thesis, the EDX device (OXFORD Xplore 15) was used to detect the surface composition of the catalyst and measure the element mapping.

3.4.5 X-ray powder diffractometer

X-ray powder diffractometer (XRD) is a characterization device that performs X-ray diffraction on materials and analyzes these diffraction patterns to obtain the material information, including the compositions, structures and physical properties of the material.

The wavelength of X-rays is similar to the distance between the atomic planes

within the crystal, making the crystal a spatial diffraction grating for X-rays to generate diffraction spectra. For crystalline materials, the atoms are arranged in a long-range order in three-dimensional space, which results in enhanced diffraction peaks at specific positions in the diffraction patterns. For amorphous materials, since their structure only shows short-range order within a few atoms, their XRD pattern only exhibits diffuse scattering steamed bun peaks.

In this thesis, the XRD device (Stoe Stadi P diffractometer with Mo K α radiation ($\lambda = 0.7093 \text{ \AA}$)) was used to measure the crystal structure of the catalyst. This measurement has been performed in the group of Prof. Dr. Malte Behrens under the assistance of Dr. Jihao Wang.

3.4.6 Raman spectroscopy

Raman spectroscopy is based on the Raman scattering effect, which was discovered by the Indian scientist C. V. Raman. Analyzing the scattering spectrum with a different frequency from the incident light allows us to obtain information on molecular vibration and rotation, which is applied in molecular structure research.

After passing through the sample, most photons retain their original energy and frequency, undergoing either elastic or Rayleigh scattering. However, a small number of photons present the energy change, undergoing inelastic scattering, that is Raman scattering. Therefore, chemical bonds and achiral molecules in materials all have their specific spectral information, which can be used to identify these molecules by analyzing their Raman spectra.

In this thesis, the device of Raman spectroscopy (532 nm, alpha 300 RA) was used to analyze the crystal structure of the sample. This measurement has been performed in the group of Prof. Dr. Rainer Adelung under the assistance of Dr. Haoyi Qiu.

3.4.7 Specific surface area and pore size distribution

The specific surface area (m^2/g) of the sample is the ratio of its surface area that can contact the air to its weight, including the external surface area and internal

surface area. The pore size distribution provides insight into the size of the pores in the sample. The pore structure has an obvious impact on the specific surface area of the sample.

Brunauer-Emmett-Teller (BET) surface area analysis is based on the BET theory, developed by scientists Brunauer, Emmett and Teller. The inert gas, such as nitrogen, as adsorbent and helium or hydrogen as the carrier gas, mixing in a certain ratio to reach a specified relative pressure, pass continuously over the sample surface and the small gas molecules adsorb on the sample surfaces due to the van der Waals forces. By placing the sample tube in liquid nitrogen for insulation, the nitrogen is physically adsorbed onto the sample surfaces and the adsorption peak will appear. After removing the liquid nitrogen, the sample tube returns to room temperature, and the adsorbed nitrogen is desorbed, forming a desorption peak. Moreover, a known volume of pure nitrogen is injected to obtain a calibration peak. Based on the peak areas of the calibration peak and the desorption peak, the adsorption amount of the sample at that relative pressure is calculated. By changing the mixing ratio of nitrogen and the carrier gas, the adsorption amount under relative pressure is collected, and the specific surface area of the sample is calculated by the BET formula.

In this thesis, the BELSORP-max device was used to analyze the specific surface area and pore size distribution of the sample. This measurement has been performed in the group of Prof. Dr. Malte Behrens under the assistance of Dr. Jihao Wang.

3.5 References

- [1] S. H. Feng, R. R. Xu, New materials in hydrothermal synthesis, *Accounts of Chemical Research*, 2001, 34, 239-247.
- [2] O. Schäf, H. Ghobarkar, P. Knauth, Hydrothermal synthesis of nanomaterials. In: Knauth, P., Schoonman, J. (eds) *Nanostructured Materials. Electronic Materials: Science & Technology*, Springer, Boston, MA. Online ISBN: 978-0306477225.

- [3] R. I. Walton, Perovskite oxides prepared by hydrothermal and solvothermal synthesis: A review of crystallisation, chemistry, and compositions, *Chemistry A European Journal*, 2020, 26, 9041-9069.
- [4] K. Byrappa, M. Yoshimura, *Handbook of hydrothermal technology*, Elsevier, 2006, Online ISBN: 978-0123750907.
- [5] S. H. Feng, G. H. Li, Chapter 4 - Hydrothermal and solvothermal syntheses, *Modern Inorganic Synthetic Chemistry*, 2017, Online ISBN: 978-0444635914.
- [6] A. N. Lobachev, *Crystallization processes under hydrothermal conditions*, Springer, Online ISBN: 978-1468475234.
- [7] Schafhäütl, "Die neuesten geologischen Hypothesen und ihr Verhältniß zur Naturwissenschaft überhaupt" (The latest geological hypotheses and their relation to science in general), *Gelehrte Anzeigen* (published by: die königliche Bayerische Akademie der Wissenschaften (the Royal Bavarian Academy of Sciences)), 1845, 20: 557, 561-567, 569-576, 577-596.
- [8] Z. L. Wang, Y. B. Xia, L. Liu, Y. Zhang, X. Liu, Binder-free one-dimensional NiCo₂O₄ nanowires@carbon papers composite as an anode for lithium-ion batteries, *Energy & Fuel*, 2020, 34, 13111-13117.
- [9] Z. X. Li, S. A. Liu, L. D. Li, W. K. Qi, W. D. Lai, L. Li, X. H. Zhao, Y. C. Zhang, W. M. Zhang, In situ grown MnCo₂O₄@NiCo₂O₄ layered core-shell plexiform array on carbon paper for high efficiency counter electrode materials of dye-sensitized solar cells, *Solar Energy Materials and Solar Cells*, 2021, 220, 110859.
- [10] T. H. Ko, C. S. Kwak, J. G. Seong, Y. H. Cho, D. Y. Lei, W. K. Choi, Y. S. Kuk, M. K. Seo, B. S. Kim, Influence of electrochemically deposited polypyrrole layers on NiCo₂O₄-decorated carbon fiber paper electrodes for high-performance hybrid supercapacitor applications, *Functional Composites and Structures*, 2019, 1, 045003.
- [11] S. C. Li, X. Guo, L. L. Zhao, F. H. Chen, X. Y. Wang, Y. Chu, W. H. Wan, Y. P. Zhu, NiCo₂O₄ nanofiber cluster assisted by NH₄F growing on 3D graphene as a binder-free electrode for lithium-ion batteries, *Energy & Fuel*, 2022, 36, 1072-1080.
- [12] J. X. Wang, Y. Y. Zhang, J. H. Ye, H. M. Wei, J. H. Hao, J. Y. Mu, S. Q. Zhao, S.

Hussain, Facile synthesis of three-dimensional NiCo₂O₄ with different morphology for supercapacitors, RSC Advances, 2016, 6, 70077-70084.

[13] H. W. Wang, X. F. Wang, Growing nickel cobaltite nanowires and nanosheets on carbon cloth with different pseudocapacitive performance, ACS Applied Materials & Interfaces, 2013, 5, 6255-6260.

[14] J. X. Zheng, X. F. Peng, Z. Wang, Plasma-assisted defect engineering of N-doped NiCo₂O₄ for efficient oxygen reduction, Physical Chemistry Chemical Physics, 2021, 23, 6591.

[15] R. D. Zhao, D. Cui, J. Q. Dai, J. Xiang, F. F. Wu, Morphology controllable NiCo₂O₄ nanostructure for excellent energy storage device and overall water splitting, Sustainable Materials and Technologies, 2020, 24, e00151.

[16] C. Wild, P. Koidl, Ion and electron dynamics in the sheath of radio-frequency glow discharges, Journal of Applied Physics, 1991, 69, 2909-2922.

[17] C. Schulze, H. Li, L. Mohn, M. Müller, J. Benedikt, Chamber with inverted electrode geometry for measuring and control of ion flux-energy distribution functions, Plasma, 2022, 5, 295-305.

[18] S. K. Sharma, Handbook of materials characterization, Springer Cham, Online ISBN: 978-3319929552.

[19] Y. Leng, Materials characterization: Introduction to microscopic and spectroscopic methods, John Wiley & Sons, Online ISBN: 978-3527334636.

[20] A. J. Bard, L. R. Faulkner, H. S. White, Electrochemical methods: Fundamentals and applications, John Wiley & Sons, Online ISBN: 978-1119334064.

[21] C. G. Zoski, Handbook of electrochemistry, Elsevier, Online ISBN: 978-0444519580.

穷则独善其身，达则兼善天下。

-----孟子

In poverty, one should still hold himself to a high standard, and when prosperous, one should contribute to the wellbeing of all.

----- Zi Meng



Nitrogen-doped NiCo₂O₄ nanowires on carbon paper as a self-supported air cathode for rechargeable Zn-air batteries

An efficient bifunctional electrocatalyst for oxygen evolution reaction (OER) and oxygen reduction reaction (ORR) is of great importance for the performance of rechargeable zinc-air batteries. Compared to traditional powder electrocatalysts, self-supported electrocatalysts can be directly assembled in the air cathode without additional binders. In this work, a self-supported electrocatalyst of NiCo₂O₄ nanowires grown on commercial carbon papers was synthesized by a hydrothermal method followed an annealing process. To further improve its electrocatalytic performance, N₂ plasma was employed to modify its surfaces and dope N atoms into its structures. As a result, the N-doped catalyst presented enhanced catalytic activities for both OER and ORR due to enhanced electrical conductivity and increased active sites. In addition, a zinc-air battery with the modified catalyst showed a small charge/discharge voltage gap and excellent

cycling stability compared to the batteries with the unmodified catalyst and noble-metal catalyst counterparts.

He Li, Sadegh Askari, Jihao Wang, Niklas Wolff, Malte Behrens, Lorenz Kienle, Jan Benedikt, Nitrogen-doped NiCo₂O₄ nanowires on carbon paper as a self-supported air cathode for rechargeable Zn-air batteries, *International Journal of Hydrogen Energy*, 2023, 48, 26107-26118.

[DOI: 10.1016/j.ijhydene.2023.03.146]

Reproduced with permission of Elsevier Ltd.

Prof. Dr. Jan Benedikt designed the underlying concept, provided experimental funding and reviewed the manuscript. The author of this thesis carried out the experiments and prepared the first draft. Other authors helped with the material characterization and reviewed the manuscript.

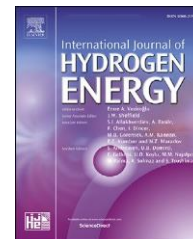


ELSEVIER

Available online at www.sciencedirect.com

ScienceDirect

journal homepage www.elsevier.com/locate/h



Nitrogen-doped NiCo₂O₄ nanowires on carbon paper as a self-supported air cathode for rechargeable Zn-air batteries

He Li ^a, Sadegh Askari ^b, Jihao Wang ^c, Niklas Wolff ^{d,e}, Malte Behrens ^{c,e}, Lorenz Kienle ^{d,e}, Jan Benedikt ^{a,e,*}

^aInstitute of Experimental and Applied Physics, Kiel University, Leibnizstraße 19, D-24098 Kiel, Germany

^bDepartment of Fiber and Polymer Technology, KTH Royal Institute of Technology, SE-10044, Stockholm, Sweden

^cInstitute of Inorganic Chemistry, Kiel University, Max-Eyth-Straße 2, D-24118 Kiel, Germany

^dDepartment of Materials Science, Chair for Synthesis and Real Structure, Faculty of Engineering, Kiel University, Kaiserstraße 2, D-24143 Kiel, Germany

^eKiel Nano, Surface and Interface Science KiNSIS, Kiel University, Christian-Albrechts-Platz 4, D-24118 Kiel, Germany

highlights

N-doped NiCo₂O₄ was prepared by hydrothermal method and N₂ plasma treatment.

Mild plasma treatment leads to efficient N doping in NiCo₂O₄.

NiCo₂O₄ with N₂ plasma treatment of 2 min exhibits excellent OER/ORR performances.

NiCo₂O₄-2 min worked as a binder-free air cathode in Zn-air batteries.

article info

Article history:

Received 10 January 2023

Received in revised form

6 March 2023

Accepted 11 March 2023 Available
online 8 April 2023

Keywords:

Nitrogen-doped NiCo₂O₄

N₂ plasma

Bifunctional oxygen electrocatalyst

Binder-free cathode

Rechargeable zinc-air battery

abstract

A noble-metal-free bifunctional electrocatalyst with outstanding activity and stability is of great importance for the development of rechargeable zinc-air batteries (ZABs). Herein, we employed a facile strategy to fabricate nitrogen-doped NiCo₂O₄ nanostructures on carbon paper as a binder-free air cathode for rechargeable ZABs. An optimized process of nitrogen plasma treatment has enhanced the electrical conductivity of the metal oxide and induced abundant active sites into the crystal structures, resulting in enhanced electrocatalytic activities toward oxygen evolution reaction (OER) and oxygen reduction reaction (ORR). Notably, mild plasma treatment leads to efficient N doping while the morphology and specific surface area of the catalyst both remain unchanged. The air cathode with NiCo₂O₄ doped with nitrogen in 2 min plasma treatment and integrated into a zinc-air battery with liquid electrolyte provided a small charge-discharge voltage gap and distinguished cycling stability superior to the air cathode with noble-metal catalyst counterparts. Furthermore, the solid-state zinc-air battery with this material displays excellent stability with just a small increase of the charge-discharge voltage gap over 20 h of operation. This work illustrates the promising potential of plasma treatment in the fabrication of high-performance catalysts.

© 2023 Hydrogen Energy Publications LLC. Published by Elsevier Ltd. All rights reserved.

* Corresponding author. Institute of Experimental and Applied Physics, Kiel University, Leibnizstraße 19, D-24098 Kiel, Germany. E-mail address:

benedikt@physik.uni-kiel.de (J. Benedikt).

<https://doi.org/10.1016/j.ijhydene.2023.03.146>

0360-3199/© 2023 Hydrogen Energy Publications LLC. Published by Elsevier Ltd. All rights reserved.

4 “Nitrogen-doped NiCo₂O₄ nanowires on carbon paper as a self-supported air cathode for rechargeable Zn-air batteries”

Introduction

With the ever-growing environmental crisis and energy demands in the world, the development of renewable energy conversion and storage systems is becoming increasingly important [1-11]. Among these new technologies, rechargeable zinc-air batteries (ZABs) have made great progress in recent years due to their low-cost, high theoretical energy density and safe nature [12-14]. Nevertheless, the performance of ZABs is still limited by the sluggish kinetics of the oxygen evolution reaction (OER) during the charge process and oxygen reduction reaction (ORR) during the discharge process at the air cathode [15-17]. Noble-metal-based catalysts, such as Pt, Pd, Ir and RuO₂, are state-of-the-art electrocatalysts for the oxygen electrochemistry, but the high cost, unsatisfactory stability and mono-functionality of these catalysts severely hinder their large-scale applications [18,19].

Transition-metal-based materials have been recognized as the promising candidates to replace the noble-metal-based catalysts owing to their low-cost, natural abundance and high stability [20-22]. Importantly, they can provide rich metal oxidation states on the surface which can be modified easily to optimize their electronic structures, thus enhancing their electrocatalytic performance [23-25]. NiCo₂O₄, a typical spinel oxide, has received much attention owing to its unique structure, however, its electrocatalytic performance for oxygen electrocatalysis is still unsatisfactory due to its poor conductivity and low intrinsic activity [26,27]. Additionally, NiCo₂O₄-based catalysts reported before are mostly in powder form, which have to be mixed with a polymer binder and then fixed on the conductive substrates as the air electrode for ZABs. The cathode prepared by this complex preparation process suffers from component maldistribution and particle agglomeration after a long-term operation. Moreover, the polymer binder solution covers the catalyst surfaces, thus blocking some active sites and reducing the charge transport at the multiphase interfaces [28].

Self-supported catalysts from metal oxides directly grown on the current collector and with the designed surface modifications offer an efficient method to address the aforementioned issues. The hydrothermal method has been widely used for the grow of nanostructured metal oxides on various substrates [29,30]. For example, NiCo₂O₄ nanowires grown on carbon fibers were synthesized by the hydrothermal method and then used as a binder-free electrode for water splitting [31]. The electrocatalytic performance of NiCo₂O₄ can be enhanced by heteroatom doping, morphological control, and/ or alloying with other metal oxides [32-34]. Among them, nitrogen doping has been considered a competitive strategy that effectively improves the electrical conductivity and optimizes the adsorption of oxygen intermediates, resulting in an enhanced electrocatalytic activity [34,35]. Annealing with nitrogen-containing precursors such as urea, NH₃ or cyanamide at a high temperature is a common approach for nitrogen doping [36-38]. However, this method introduces other impurities onto the catalyst surface and the exhaust gases generated during the annealing process are hazardous for the environment.

Compared with other methods, plasma processing has been widely used for surface modifications as a time-saving process with minimized precursor consumption and waste generation. Moreover, the morphologies and structures of the nanomaterials remain intact upon generation of surface defects in plasma treatment due to low temperature and highly nonequilibrium conditions during the plasma operation [39-42].

We report a facile route to synthesize nitrogen-doped NiCo₂O₄ nanowires coated on carbon paper as an efficient bifunctional electrocatalyst for ZABs in this article. The superb electrocatalytic performance of the modified catalyst is attributed to the enhanced conductivity and abundant number of active sites on the surface after nitrogen plasma treatment.

Materials and methods

Materials

Ni(NO₃)₂•6H₂O (99.999%), Co(NO₃)₂•6H₂O (99.999%), CO(NH₂)₂ (98%), NH₄F (98%), Zn(CH₃CO₂)₂ (99.99%), KOH(85%), Nitric acid(70%) and Nafion 1100 EW (5 wt%) were purchased from Sigma-Aldrich. Carbon paper (CP, GDL 28AA) was purchased from sgl carbon. All the chemicals were directly used without further purification.

Pretreatment of CP

A piece of CP was immersed in nitric acid and kept at 95 °C for 3 h. After natural cooling down to room temperature, the treated CP was washed with a lot of water until pH neutral, then dried at 60 °C overnight.

Synthesis of NiCo₂O₄ nanowires

Pristine NiCo₂O₄ nanowires were prepared by the hydrothermal method and subsequent annealing process. A mixture of 2 mmol Co(NO₃)₂•6H₂O, 1 mmol Ni(NO₃)₂•6H₂O, 6 mmol of urea and 2 mmol of NH₄F were dissolved in 12 mL of deionized water. After stirring for 30 min, the pink solution was transferred to a 50 mL Teflon-lined stainless autoclave and one piece of as-prepared CP was vertically immersed into the solution. The autoclave was sealed and kept at 120 °C for 12 h. After naturally cooling down to room temperature, the sample was taken out and washed with a lot of deionized water, then dried at 60 °C overnight. Finally, the dried sample was annealed at 350 °C in the air atmosphere for 3 h to obtain NiCo₂O₄ nanowires on the CP.

Nitrogen plasma treatment

The as-obtained NiCo₂O₄ nanowires were directly modified by nitrogen plasma (27.12 MHz RF source, isolated substrate holder on floating potential) with the power of 200 W, N₂ gas flow of 8 sccm, and working pressure of 20 Pa at different irradiation times. The corresponding samples were named as NeNiCo₂O_{4-x}-Y min, where Y indicates irradiation time (1, 2, 3 min).

Characterization

The excited species in plasma emitting in the spectral range from 250 to 900 nm were detected by optical emission spectroscopy (OES, Ocean

4 “Nitrogen-doped NiCo₂O₄ nanowires on carbon paper as a self-supported air cathode for rechargeable Zn-air batteries”

Optics HR4000CG-UV-NIR). The crystalline phases of the prepared samples were characterized by X-ray diffraction (XRD, Stoe Stadi P) with Mo K α radiation ($\lambda = 0.7093 \text{ \AA}$). The morphologies and structures of the samples were tested by field emission scanning electron microscopy (FESEM, Zeiss Ultra 55 Plus). The nanostructure analysis was performed by transmission electron microscope (TEM). The treated NiCo₂O₄ nanowires were carefully scratched off the support onto a carbon-lacey film on a copper grid, and the TEM experiments were conducted on a Tecnai F30 G² STwin and a JEOL JEM-ARM200F microscope performing high-resolution imaging, selected-area electron diffraction (SAED) experiments and energy-dispersive X-ray spectroscopy (EDS) experiments ($2 \times 100 \text{ mm}^2$ active area of silicon drift detectors). The chemical states of elements were measured by X-ray photoelectron spectroscopy (XPS, ESCALAB XI+) and the final data were corrected with C 1s at 284.8 eV. Functional groups in the samples were analyzed by Raman spectroscopy (532 nm, alpha 300 RA). The specific surface area and pore size distribution of the samples were estimated by Brunauer-Emmett-Teller method (BET, BELSORP-max instrument).

Electrochemical measurement

All electrochemical measurements were carried out by an electrochemical workstation (Wave Driver 200, Pine Research) with a conventional three-electrode system. Pt wire, Ag/AgCl electrode and 1 M KOH were used as the counter electrode, the reference electrode and the electrolyte, respectively. All measured potentials were finally converted to the potentials of reversible hydrogen electrode (RHE) according to the Nernst Equation ($E_{\text{RHE}} = E_{\text{Ag/AgCl}} + 0.059 \text{ pH} + 0.197$), and all CV and LSV curves were corrected by iR compensation.

(a) OER Test

The sample (1 cm \times 1 cm) was directly used as the working electrode. Before the test, the cyclic voltammetry (CV) test was executed more than 60 times at a scan rate of 100 mV s⁻¹ to stabilize the catalysts. Linear sweep voltammetry (LSV) curves were collected at a scan rate of 5 mV s⁻¹ from 1.2 to 1.8 V (vs. RHE). Tafel plots were calculated from LSV results. The CV curves were measured from 1.03 to 1.13 V at different scan rates to estimate the electrochemical double-layer capacitance (C_{dl}). The electrochemical surface area (ECSA) was calculated according to the equation: $\text{ECSA} = C_{\text{dl}}/C_s$, where C_s is the specific capacitance of transition oxide surface in 1 M KOH as 0.04 mF cm⁻². The operational stability test was carried out at 10 mA cm⁻² by the chronopotentiometry method. The cycling stability was also analyzed after 1000 CV cycles.

(b) ORR Test

The catalyst powders were carefully scraped off from the carbon paper. Then, 5 mg of catalyst, 40 mL Nafion solution and 1 mL isopropanol were mixed together and sonicated for 30 min to obtain a homogeneous catalyst ink. Subsequently, 12 μL of the catalyst ink was dropped onto the polished glassy carbon electrode (\varnothing 6 mm) and dried at 65 °C in the furnace (the loading amount is about 0.2 mg cm⁻²).

Before the start of each measurement, the CV scans were executed more than 60 times at a scan rate of 100 mV s⁻¹ to stabilize the catalysts, then measured in the O₂ saturated and N₂ saturated 1 M KOH electrolyte at a rotation rate of 1600 rpm. Electrochemical impedance spectroscopy (EIS) measurements were conducted at 0 V vs. Ag/AgCl from 100 kHz to 1 Hz. All LSV curves were collected at a scan rate of 5 mV s⁻¹ at different rotation rates (400-2500 rpm). The electron transfer number (n) was calculated by the Kentucky-Levich (K-L) equations:

$$1/j = 1/j_k + 1/(B\omega^{1/2})$$

$$B = 0.2nFC_0D_0^{2/3}\nu^{-1/6}$$

where j and j_k are the measured current density and the kinetic current density, ω is the electrode rotation rate (rpm), B is the slope of the K-L plots, F is the Faraday constant (96485 C mol⁻¹), C_0 is the bulk concentration of O₂ ($0.83 \times 10^3 \text{ mol L}^{-1}$ in 1 M KOH), D_0 is the diffusion coefficient of O₂ ($1.76 \times 10^5 \text{ cm}^2 \text{ s}^{-1}$), and ν is the kinetic viscosity ($0.095 \text{ cm}^2 \text{ s}^{-1}$). The operational stability was investigated by the chronoamperometric method at -0.4 V vs. Ag/AgCl. The cycling stability was also analyzed after 1000 CV cycles.

Battery test

(a) Liquid Battery

A custom-made rechargeable zinc-air battery was assembled to evaluate the electrochemical performance of the samples. The sample was directly used as the air cathode in the cell, the polished Zn plate was used as the anode, and the electrolyte was the solution of 6 M KOH and 0.2 M Zn(Ac)₂. All battery measurements were conducted by an electrochemical workstation (Wave Driver 200, Pine Research) except for discharge-charge cycling tests which were performed by a LAND testing system.

For comparison, commercial Pt/C þ RuO₂ (1:1) with the loading mass of 1 mg cm⁻² was used as a reference.

(b) Solid-state Battery

The PVA gel electrolyte for the solid-state zinc-air battery was prepared as follows: 1 g PVA was dissolved in 10 mL deionized water at 100 °C under stirring for around 2 h, then 2 mL 18 M KOH with 0.2 M Zn(Ac)₂ was slowly added in the above solution. After stirring at 90 °C for 0.5 h, the mixed solution becomes uniform, then frozen at -20 °C overnight.

The carbon paper with catalysts and zinc foil were cut into 1 \times 2 cm², and used as the air cathode and the anode, respectively. The air cathode and the anode were attached to the two sides of solid electrolyte, then two pieces of aluminum foil with the plastic film were used to seal the cell. A small hole was opened at the air cathode side.

All measurements of the solid-state batteries are the same as the measurements of batteries with liquid electrolyte.

4 “Nitrogen-doped NiCo₂O₄ nanowires on carbon paper as a self-supported air cathode for rechargeable Zn-air batteries”

Results and discussion

Scheme 1 illustrates the synthesis process of the nitrogen-doped NiCo₂O₄ nanowires. The pristine NiCo₂O₄ nanowires were synthesized by the hydrothermal method at 120 C for 12 h, followed by the annealing process at 350 C for 3 h. After that, N₂ plasma was employed to induce surface defects and N element to the surface of the nanowires. The samples with different treatment times were labeled as N-NiCo₂O_{4-x}-1 min, N-NiCo₂O_{4-x}-2 min and N-NiCo₂O_{4-x}-3 min.

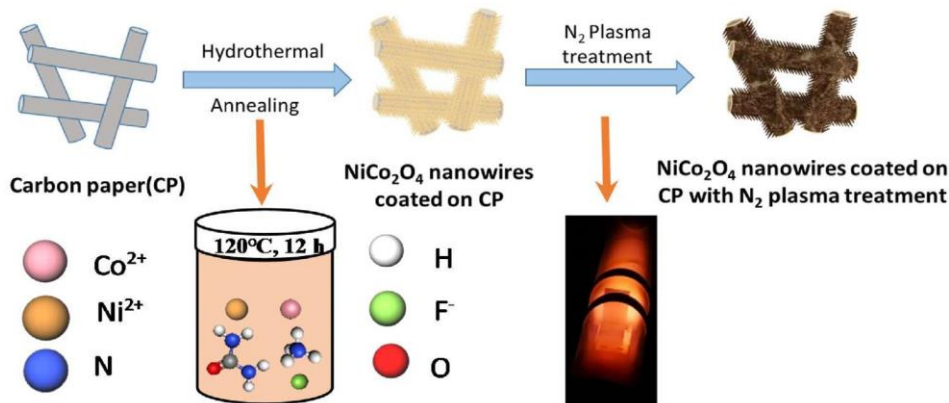
The excited species emitting in the spectral range from 250 to 900 nm and possibly contributing to the plasma functionalization of NiCo₂O₄ nanowires were detected by OES during N₂ plasma treatment. In Fig. S1, the spectrum of N₂ plasma consists of various nitrogen emission features. The spectrum is dominated by the first positive system of neutral nitrogen molecules (N₂(FPS)) in the range of 478-900 nm. As shown in Fig. S1(b), several lines were observed in the range from 316 to 406 nm, corresponding to the second positive system of neutral nitrogen molecules (N₂(SPS)). In addition, two lines at 391 nm and 427 nm are assigned to the first negative transitions of N₂⁺ molecular ions [43]. These excited molecular nitrogen species are due to their high internal energy the probable source of the N doping at the catalyst surface. Additional sources could be atomic nitrogen atom (N) and ions (N⁺), which are, unfortunately, not emitting in the studied spectral range. Study of the role of N₂⁺ and N⁺ ions is being prepared at another plasma reactor equipped with energy resolved ion mass spectrometry diagnostics [44], but this is out of the scope of this article.

The crystal structures of NiCo₂O₄ nanowires before and after N₂ plasma treatment were characterized by X-ray diffraction (XRD). Fig. S2(a) shows that the main reflections from the NiCo₂O₄-based catalysts are consistent with the cubic NiCo₂O₄ (PDF #20-0781). The main reflections at 8.6°, 14.1°, 16.6°, 20.0°, 24.6°, 26.1°, 28.5° and 33.4° are assigned to the typical (111), (220), (311), (400), (422), (511), (440) and (533) planes of NiCo₂O₄ and the reflections at 12.1° and 33.5° belong to the graphitic carbon support (Fig. S2(b), Supporting Information). After N₂ plasma treatment, no structural decomposition into binary metal nitrides such as CoN and NiN is detected, which is probably due to the high dispersity of the N atoms.

These results indicate that N₂ plasma treatment was not changing the crystal structure of NiCo₂O₄.

The morphology and structure of NiCo₂O₄ nanowires before and after N₂ plasma treatment observed by scanning electron microscopy (SEM) are shown in Fig. 1(a-d). It can be seen that the morphology of nanowires grown uniformly on the carbon paper remained unchanged after N₂ plasma treatment, indicating that the plasma modification did not cause severe structural damage to the macroscopic surface morphology. Notably, the 3D structure of long needle-shaped rods provides a large surface area and abundant active sites for the triple-phase catalytic reaction (Fig. S3, Supporting Information). Furthermore, the catalysts firmly grown on the carbon fibers are effectively protected against aggregation and corrosion during operation and can be, therefore, used as the binder-free air cathode for ZABs.

The electrocatalytic performance of all samples was evaluated in 1 M KOH solution by a conventional three-electrode system. For the OER measurement, commercial RuO₂ catalyst loading on carbon paper (1 mg cm⁻²) was used as a reference. Fig. 2(a and b) shows the LSV profiles of the samples, in which the overpotential at a current density of 10 mA cm⁻² (E_{j = 10}) has been used to compare the OER activity. It can be seen that the plasma treated NiCo₂O₄ samples exhibit the lower overpotentials than pristine NiCo₂O₄ and even the commercial RuO₂. In addition, N-NiCo₂O_{4-x}-2 min shows the lowest overpotential (300 mV) which is lower than that of N-NiCo₂O_{4-x}-1 min (305 mV) and N-NiCo₂O_{4-x}-3 min (310 mV), indicating its highest OER performance. Fig. 2(c) shows the Tafel slopes of the catalysts. The Tafel slope of N-NiCo₂O_{4-x}-2 min is 64.3 mV dec⁻¹, which is smaller than that of other samples, revealing that N-NiCo₂O_{4-x}-2 min has the fastest reaction rate constant and electrocatalytic kinetics. Fig. 2(d) and S4 show the results obtained for double-layer capacitance (C_{dl}) of the samples which could be used to evaluate the electrochemical surface area (ECSA). The C_{dl} of N-NiCo₂O_{4-x}-2 min is 21.3 mF cm⁻² which is larger than that of N-NiCo₂O_{4-x}-1 min (19.6 mF cm⁻²) and N-NiCo₂O_{4-x}-3 min (20.0 mF cm⁻²) and all of them are higher than that of pristine NiCo₂O₄ (17.4 mF cm⁻²). Correspondingly, in Fig. S5(a), NiCo₂O₄ samples after N₂ plasma treatment show increased ECSA values



Scheme 1 - Schematic illustration of the preparation process of the catalysts.

4 "Nitrogen-doped NiCo₂O₄ nanowires on carbon paper as a self-supported air cathode for rechargeable Zn-air batteries"

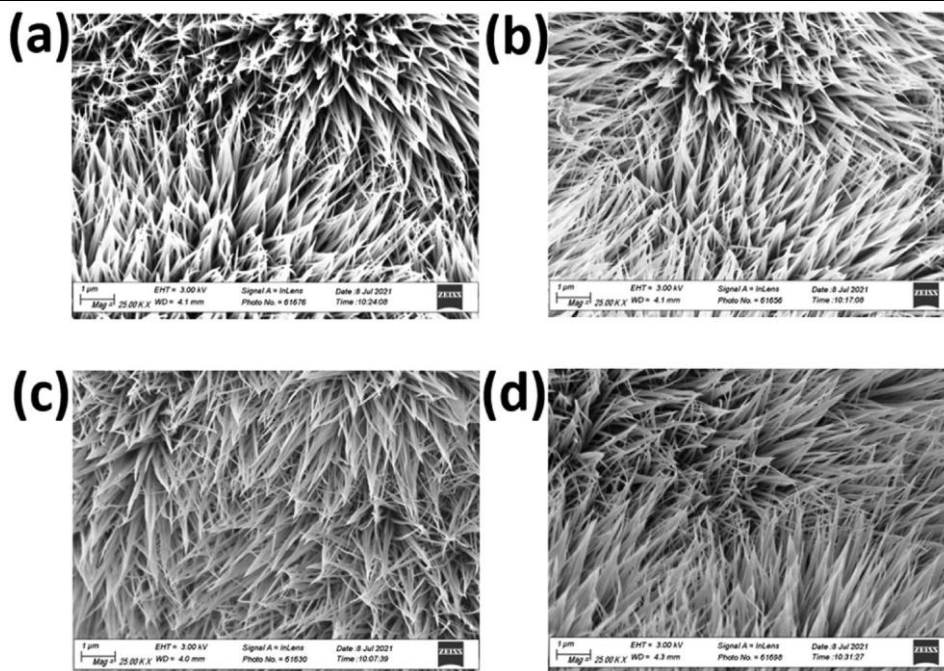


Fig. 1 - SEM images of (a) NiCo₂O₄, (b) N-NiCo₂O_{4-x}-1 min, (c) N-NiCo₂O_{4-x}-2 min, (d) N-NiCo₂O_{4-x}-3 min.

compared to pristine one, indicating that more active sites are available for OER. As shown in Fig. S5(b), the polarization curves were normalized by the ECSAs to estimate the intrinsic activities of all samples,

where again the N-NiCo₂O_{4-x}-2 min one exhibits the highest OER performance. Stability is another essential parameter of any catalyst. Fig. S6(a) shows the operational stability of the N-NiCo₂O_{4-x}-2 min

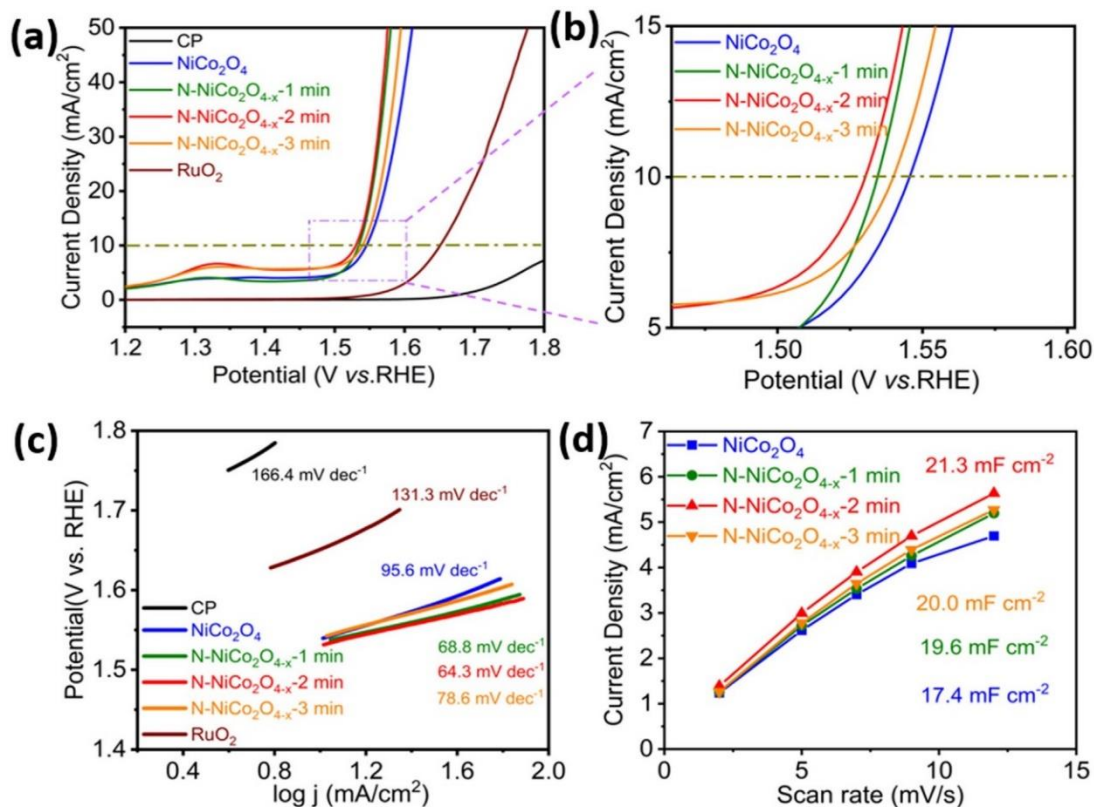


Fig. 2 - (a, b) LSV polarization curves, (c) Tafel plots, (d) the estimation of C_{dl} of all samples for OER in 1 M KOH.

4 “Nitrogen-doped NiCo₂O₄ nanowires on carbon paper as a self-supported air cathode for rechargeable Zn-air batteries”

and RuO₂ samples at 10 mA cm⁻² as measured by chronopotentiometry, where much better stability was observed for N-NiCo₂O_{4-x-2} min after 18 h test. In addition, the morphology and composition of the N-NiCo₂O_{4-x-2} min sample were conserved very well after this long-term test (Fig. S6 (b, c)). Moreover, as shown in Fig. S6(d), the OER LSV curve of N-NiCo₂O_{4-x-2} after the 1000 CV cycles presents only a negligible shift, further illustrating its excellent cycling durability.

To evaluate the ORR performance of the samples, the cyclic voltammetry (CV) measurements were performed in N₂- and O₂-saturated 1 M KOH solutions at a rotating speed of 1600 rpm. In Fig. S7(a), N-NiCo₂O_{4-x-2} min shows an obvious oxygen reduction peak at around 0.70 V in O₂-saturated electrolyte compared to the flat curve in N₂-saturated electrolyte. Fig. 3(a) exhibits the CV curves of all samples in O₂-saturated 1 M KOH, in which N-NiCo₂O_{4-x-2} min displays the most positive potentials at different current densities than that of pristine NiCo₂O₄, N-NiCo₂O_{4-x-1} min and N-NiCo₂O_{4-x-3} min, demonstrating its best ORR electrocatalytic performance. Linear sweep voltammetry (LSV) was also conducted in the O₂-saturated electrolyte. As shown in Fig. 3(b), N-NiCo₂O_{4-x-2} min exhibits an onset potential (E_{onset}) of 0.85 V and a halfwave potential (E_{1/2}) of 0.75 V, which is better than pristine NiCo₂O₄ (E_{onset} = 0.79 V, E_{1/2} = 0.69 V), N-NiCo₂O_{4-x-1} min (E_{onset} = 0.79 V, E_{1/2} = 0.70 V) and N-NiCo₂O_{4-x-3} min (E_{onset} = 0.84 V, E_{1/2} = 0.74 V), and close to Pt/C (E_{onset} = 0.95 V, E_{1/2} = 0.86 V). Meanwhile, the Tafel slope of N-NiCo₂O_{4-x-2} min is 109.4 mV dec⁻¹, lower than that of the other three NiCo₂O₄-based catalysts. These results illustrate that N-NiCo₂O_{4-x-2} min provides the highest ORR performance, verifying the positive influence of the N₂ plasma treatment on ORR activity.

Fig. S7(b) shows the electrochemical impedance spectroscopy (EIS) of all samples. N-NiCo₂O_{4-x-2} min exhibits the smallest semicircle which indicates the lowest charge transfer resistance at the catalytic interface, suggesting that N₂ plasma treatment could efficiently enhance the conductivity of transition metal oxides and improve charge transfer during the ORR process. The electron transfer number (n) of N-NiCo₂O_{4-x-2} min is calculated by LSV measurements at different rotating rates according to Koutecky-Levich (K-L) equation. As shown in Fig. 3(d) and Fig. S7(c), the calculated n of N-NiCo₂O_{4-x-2} min is about 3.97 at the potential of 0.4-0.6 V, indicating the four electrons reduction pathway for ORR process. Fig. S8(a) presents the operational stability tests of N-NiCo₂O_{4-x-2} min and commercial Pt/C coated on carbon paper by the chronoamperometry method. It can be seen that, N-NiCo₂O_{4-x-2} min maintains a 94.58% retention in current density after operation at 0.4 V vs. Ag/AgCl for 7200 s, which is superior to commercial Pt/C (88.84%). In addition, Fig. S8(b) shows that the ORR LSV curve of N-NiCo₂O_{4-x-2} after the 1000 CV cycles results only in a negligible shift, indicating its excellent ORR cycling durability. Obviously, these results demonstrate that the proper N₂ plasma treatment time can optimize the ORR activity of NiCo₂O₄. The catalyst should have both excellent OER and ORR activity as an air cathode for rechargeable ZABs. Therefore, the gap potential (ΔE) between E_{j=10} for OER and E_{1/2} for ORR is used to evaluate the bifunctional performance of the measured catalysts. It can be seen from Fig. 3(e) that N-NiCo₂O_{4-x-2} min shows a low gap potential of 0.78 V, which is the same as for commercial Pt/C and RuO₂ combination and some similar electrocatalysts reported recently (Table S1).

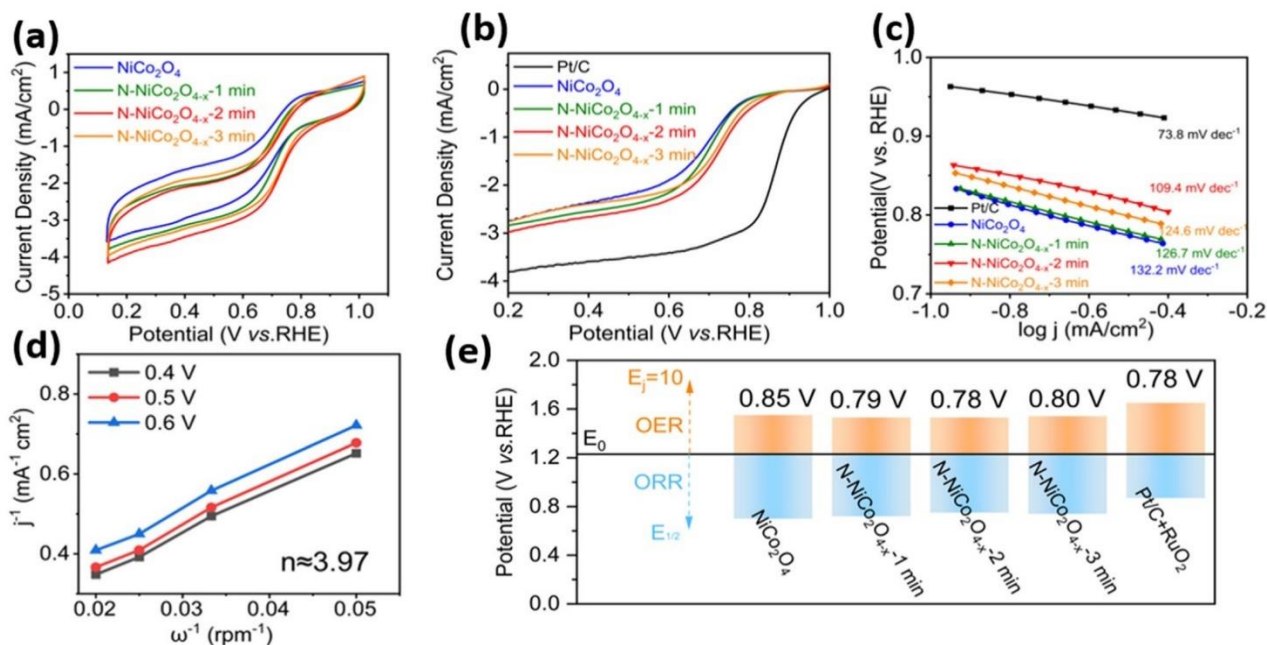


Fig. 3- (a) CV curves, (b) LSV polarization curves and (c) Tafel plots of all catalysts tested in O₂-saturated 1 M KOH, (d) K-L plots at different potentials, (e) Gap potentials for OER and ORR of all samples in 1 M KOH.

4 “Nitrogen-doped NiCo₂O₄ nanowires on carbon paper as a self-supported air cathode for rechargeable Zn-air batteries”

It could be found that, at first, the electrocatalytic performances improved with the increase of N₂ plasma treatment time due to the increased active sites and the enhanced conductivity. The optimal treatment time is 2 min. The weak electrocatalytic activity of N-NiCo₂O_{4-x}-3 min could be attributed to the reduced conductivity and ECSA by the overtreatment of N₂ plasma [45]. The exact mechanism leading to the deterioration of the catalyst performance after prolonged plasma treatments is not known.

The nanostructure and morphology of N-NiCo₂O_{4-x}-2 min sample were further characterized by transmission electron microscopy (TEM), see Fig. 4. The TEM image in Fig. 4(a) shows several nanowires with a polycrystalline structure and abundant nanopores providing a large surface area. The NiCo₂O₄ phase is evidenced by HRTEM analysis, showing one exemplary nanocrystal in Fig. 4(b) with an interplanar d-spacing of 0.46 nm referenced to the (111) plane of the cubic structure. Selected-area electron diffraction (SAED) patterns of these nanostructures show intensity maxima distributed on discrete rings typical for polycrystalline material, see Fig. 4(c). A plot of the rotationally integrated diffracted intensity is presented in Fig. 4(d) and compared to the reflection position of the spinel-type structure of NiCo₂O₄. A very good agreement of the reflection maxima with the reference corresponding to the (111), (220), (311), (400), (511) and (440) planes is observed. Additionally, SAED experiments on single nanowire structures revealed the presence of a preferred crystalline texture of the individual nanocrystals discussed in Fig. S9. However, not all ternary phase nanowire structures exhibited such a nanocrystalline texture, and occasionally nanowires consisting of binary oxides of CoO and NiO were observed which might be due to the N₂ plasma treatment or minor failure of the synthesis process [46]. No decomposition into metal nitrides such as CoN and NiN was observed by the TEM investigation, fully corresponding to the XRD results. Further, STEM-EDS measurements and elemental mapping were performed on single nanowires to confirm N-doping and phase stability after plasma treatment. As shown in Fig. S10, the presented elemental maps of Co and Ni show the homogenous distribution of the ternary phase across all mapped nanowire crystals and EDS measurements on such nanowires yield a stoichiometric

Ni:Co ratio of 1:2. Subtle N-doping of the nanowire is indicated by the EDS spectra showing a small X-ray signal of nitrogen.

The surface chemical compositions and elemental states of pristine NiCo₂O₄ and N-NiCo₂O_{4-x}-2 min were also investigated by X-ray photoelectron spectroscopy (XPS). Fig. 5(a) shows the full spectrum of pristine NiCo₂O₄ and N-NiCo₂O_{4-x}-2 min with the co-existence of Ni, Co, O. However, nitrogen can only be detected in the N-NiCo₂O_{4-x}-2 min which also proves the successful doping of N atom after N₂ plasma treatment, corresponding with STEM-EDS results. As shown in the high-resolution Co 2p (Fig. 5(b)), there are two dominating peaks for Co 2p_{1/2} and Co 2p_{3/2} located at around 796.9 eV and 781.1 eV, respectively. In addition, two satellites are also detected at around 803.5 eV and 785.8 eV. Notably, the N-NiCo₂O_{4-x}-2 min catalyst shows a higher atomic ratio of Co²⁺/Co³⁺, which is attributed to the N₂ plasma treatment. Likewise, the Ni 2p spectra also consists of two main peaks of Ni 2p_{1/2} and Ni 2p_{3/2} with two satellites (Fig. 5(c)). Notably, compared to pristine NiCo₂O₄, the Co 2p peaks and Ni 2p peaks of N-NiCo₂O_{4-x}-2 min shift to lower energies, suggesting the increased electron density around the metal atoms owing to the partial replacement of lattice O by N [47,48]. Furthermore, in Fig. 5(d), the N doping could also be confirmed by the N 1s spectra, which is deconvoluted into three peaks at 400.4 eV, 398.4 eV and 397.3 eV, corresponding to Graphitic-N, Metal-N and Pyridinic-N. Functional groups in the samples were further characterized by Raman spectroscopy. As shown in Fig. S11, two broad peaks at around 1334 and 1581 cm⁻¹ are assigned to the D and G bands of carbon substrates, respectively. The I_D/I_G ratio in N-NiCo₂O_{4-x}-2 min is larger than that of NiCo₂O₄, suggesting that more defects in its carbon structure arose due to N doping. In addition, two peaks at 321 and 511 cm⁻¹ are attributed to the vibrations of Metal-O bands. Interestingly, these peaks in the N-NiCo₂O_{4-x}-2 min shift to lower wavenumbers which is mainly attributed to the substitution of N atoms. Furthermore, a new peak at 638 cm⁻¹ was observed in the spectrum of N-NiCo₂O_{4-x}-2 min, which belongs to the Metal-N band [49,50]. These results indicate the formation of N-doped NiCo₂O₄ nanowires.

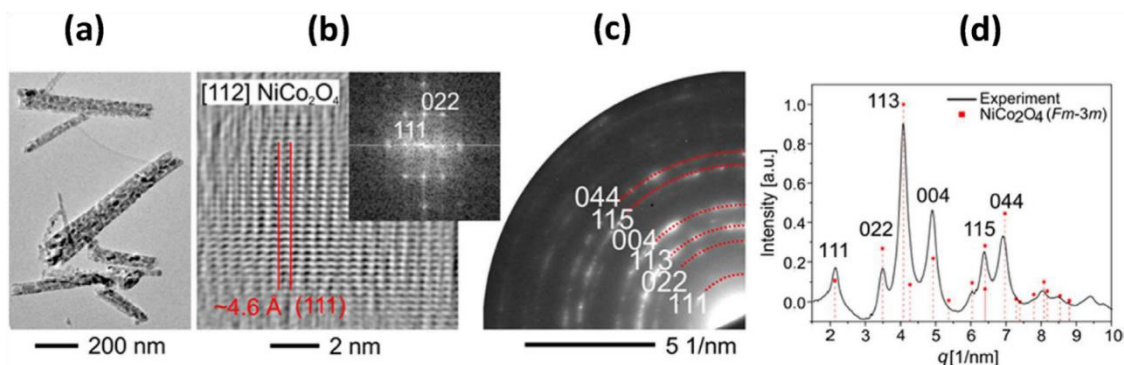


Fig. 4 - TEM analysis of the N-NiCo₂O_{4-x}-2 min sample. (a) TEM image showing multiple polycrystalline nanowires dispersed on the carbon support film. (b) HRTEM micrograph of an individual nanocrystal as part of a nanowire and its FFT identified as ternary phase NiCo₂O₄ with spinel-type structure. (c) SAED pattern with discrete rings of intensity belonging to the indicated lattice planes of NiCo₂O₄ and (d) the corresponding radially integrated intensity distribution.

4 “Nitrogen-doped NiCo₂O₄ nanowires on carbon paper as a self-supported air cathode for rechargeable Zn-air batteries”

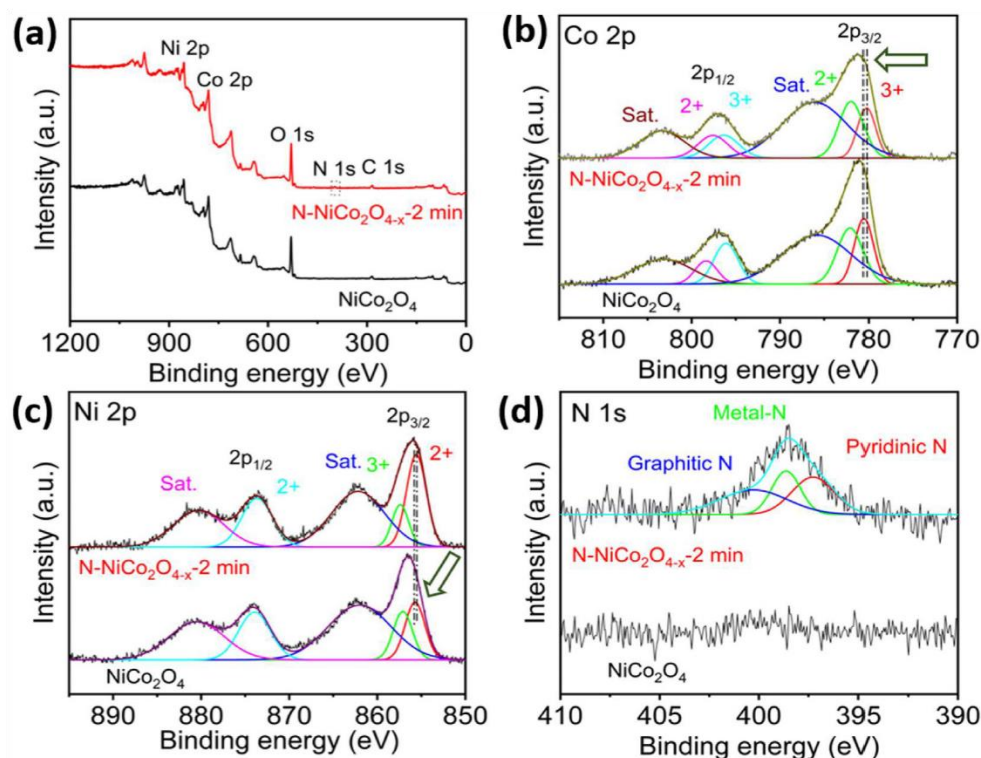


Fig. 5 - (a) The XPS full spectra of pristine NiCo₂O₄ and N-NiCo₂O_{4-x}-2 min. High-resolution XPS spectra of (b) Co 2p, (c) Ni 2p and (d) N 1s.

The specific surface area and pore distribution of pristine NiCo₂O₄ and N-NiCo₂O_{4-x}-2 min were analyzed by Brunauer-Emmett-Teller (BET) measurements. In Fig. S12(a), these two samples show similar results which possess type-IV isotherm with the mesoporous structure. The N-NiCo₂O_{4-x}-2 min exhibits the calculated specific surface area of 54.4 m² g⁻¹, which is slightly higher than that of NiCo₂O₄ (52.8 m² g⁻¹). In Fig. S12(b), the NiCo₂O₄ and N-NiCo₂O_{4-x}-2 min also display a similar pore size distribution based on the Barrett-Joyner-Halenda model. These results are different from results of Ar plasma treatments reported in the literature, where the improved properties have been explained by the significant increase of the specific surface area [27,51]. Our results indicate that only weak etching process of the metal oxide structures take place in N₂ plasma used here, allowing us to analyze the contribution of N₂ plasma induced modifications (defects, doping) of NiCo₂O₄ surface to its electrocatalytic performance.

Based on the all obtained characterizations and electrocatalytic results, the factors enhancing the catalytic performance of NiCo₂O₄ after N₂ plasma treatment could be summarized as follows: (1) enhanced electrical conductivity; (2) more exposed active sites; (3) high atomic ratio of Co²⁺/Co³⁺ and Ni²⁺/Ni³⁺. For the OER process, the Co²⁺ and Ni²⁺ sites could be oxidized at the onset of OER to form (Co, Ni)-OOH species as the active sites [51-55]. In our work, more Co²⁺ and Ni²⁺ species have been formed

after N₂ plasma treatment, providing more active sites for OER and enhancing, therefore, the OER performance of NiCo₂O₄. For the ORR process, the formation of metal-N, pyridinic-N and graphitic-N could participate in the ORR process as active sites, thus increasing the ORR activity of NiCo₂O₄ [56]. Notably, the fact that N-NiCo₂O_{4-x}-2 min has more active sites compared to the pristine sample, but without an increase in the sample specific surface area, emphasizes the significance of N doping for electrocatalysis. Moreover, the electron transfer is accelerated during the electrocatalytic reaction owing to the doping of the N element in oxides to form hetero-nanostructures [32]. The synergetic effect from these advancements endows the excellent electrocatalytic performance of N-NiCo₂O_{4-x}-2min.

In order to test the catalyst in practice, a rechargeable Zn-air battery was assembled (Fig. S13). The schematic diagram of the battery is shown in Fig. 6(a). Zinc plates, the air cathodes with prepared catalysts and 6 M KOH + 0.2 M Zn(Ac)₂ were used as anode, cathode and electrolyte, respectively. Fig. 6(b) presents the discharge and charge polarization curves of pristine NiCo₂O₄, N-NiCo₂O_{4-x}-2 min and Pt/C + RuO₂. It can be seen that N-NiCo₂O_{4-x}-2 min exhibits a higher discharge voltage and a lower charge voltage than that of pristine NiCo₂O₄ at the same current density. Additionally, the charge voltage is even better than the one of the mixed commercial noble-catalyst, corresponding well with the

4 “Nitrogen-doped NiCo₂O₄ nanowires on carbon paper as a self-supported air cathode for rechargeable Zn-air batteries”

above OER and ORR results. As shown in Fig. 6(c), the battery with N-NiCo₂O_{4-x}-2 min has a peak power density of 52 mW cm⁻², which surpassed the battery with the pristine NiCo₂O₄ (44 mW cm⁻²) and is close to the battery with Pt/C + RuO₂ (71 mW cm⁻²). In addition, the battery with N-NiCo₂O_{4-x}-2 min also presents a higher voltage of 1.18 V, 1.13 V, 1.08

V and 1.01 V at the current densities of 2, 5, 10 and 20 mA cm⁻², respectively (Fig. 6(d)). Additionally, it recovered to 1.20 V when the current density decreases from 20 mA cm⁻² to 2 mA cm⁻². These results indicate the excellent discharge rate performance and reversibility. Fig. 6(e) shows the charging-discharging performance of the catalysts at a

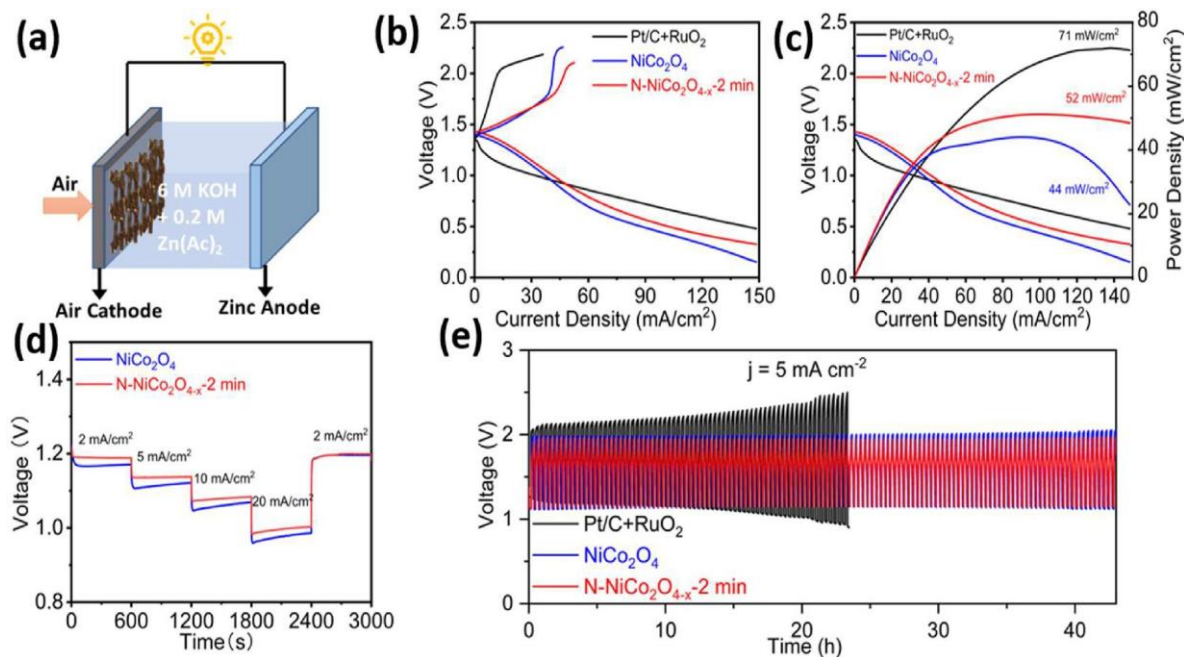


Fig. 6 e (a) Schematic diagram of zinc-air battery, (b) charge-discharge curve, (c) discharge curves and corresponding power densities of the rechargeable zinc-air batteries, (d) discharge voltages at different current densities, (e) long-term cycling test at 5 mA cm⁻².

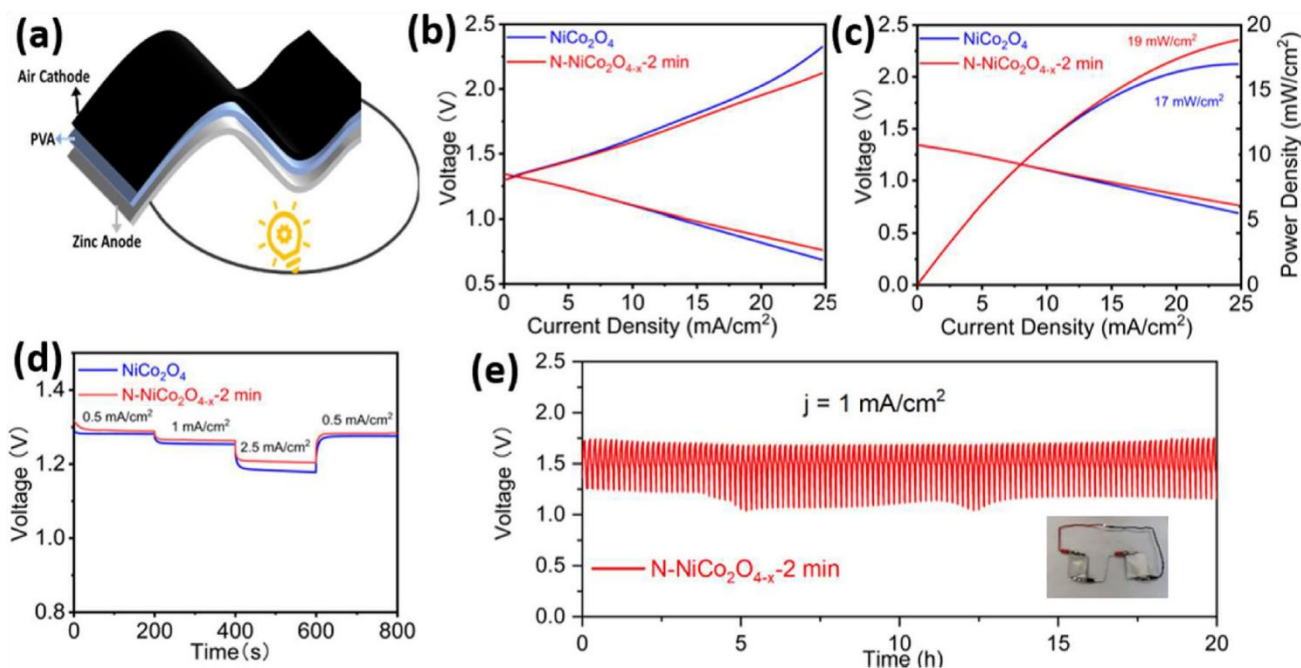


Fig. 7 e (a) Schematic diagram of all-solid-state zinc-air battery, (b) charge-discharge curve, (c) discharge curves and corresponding power densities of the zinc-air batteries, (d) discharge voltages at different current densities, (e) long-term cycling test at 1 mA cm⁻². The inset shows two batteries powering an LED.

4 “Nitrogen-doped NiCo₂O₄ nanowires on carbon paper as a self-supported air cathode for rechargeable Zn-air batteries”

current density of 5 mA cm⁻². The battery with N-NiCo₂O_{4-x}-2 min delivers an initial charge and discharge voltage of 1.95 V and 1.13 V, and the gap voltage and conversion efficiency are calculated to be 0.82 V and 57.9%, respectively. Initially, the gap voltage is reduced slightly due to the initial activation process. But after further cycling for 45 h, the gap voltage and conversion efficiency are not considerably changed, demonstrating the charge-discharge durability of the cathode which is better than that of other recently reported binder-free catalysts (Table S2). For comparison, the battery with Pt/C + RuO₂ exhibits the drop of the gap voltage and conversion efficiency from initial 0.92 V and 56.6% to 1.56 V and 37.6% after 23 h, indicating its poor durability.

Inspired by the fast development of wearable electronic devices, a homemade all-solid-state zinc-air battery was also assembled to expand the practical application of the modified catalyst. Fig. 7(a) displays the schematic diagram of the solid-state battery. Fig. 7(b) shows the discharge and charge polarization curves of pristine NiCo₂O₄ and N-NiCo₂O_{4-x}-2 min. Compared with pristine NiCo₂O₄, N-NiCo₂O_{4-x}-2 min has a higher discharge voltage and lower charge voltage at the same current density which is the same as for the battery with liquid electrolyte. It also shows a slightly higher peak power density (19 mW cm⁻²). Moreover, as shown in Fig. 7(d), the battery with N-NiCo₂O_{4-x}-2 min exhibits a better discharge performance at identical current densities, and good reversibility when the current density decreases from 2.5 to 0.5 mA cm⁻². All these results confirm that N-NiCo₂O_{4-x}-2 min possesses a better bifunctional catalytic activity. Stability was also tested by the charge-discharge cycling at a current density of 1 mA cm⁻². It can be seen from Fig. 7(e), the N-NiCo₂O_{4-x}-2 min based all solid-state zinc-air battery exhibits excellent durability with a small increase of the gap voltage after 20 h. Two solid-state zinc-air batteries were employed as a power source for lighting an LED (see inset in Fig. 7(e)).

Conclusions

In summary, nitrogen-doped NiCo₂O₄ nanowires coated on carbon paper have been successfully prepared in a facile process as a binder-free air cathode for rechargeable ZABs. Compared with pristine NiCo₂O₄, N-doped NiCo₂O₄ present better OER and ORR performance with a lower overpotential at 10 mA cm² for OER and a higher half-wave potential for ORR. Our results show that the enhanced electrocatalytic performance is attributed to the enhanced conductivity and availability of more active sites after nitrogen plasma treatment. Moreover, the best electrocatalytic activity of N-NiCo₂O_{4-x}-2 min with a similar specific surface area as the pristine NiCo₂O₄ further emphasize the important effect of N doping. As expected, the liquid zinc-air battery assembled with N-NiCo₂O_{4-x}-2 min as the binder-free air cathode exhibits a small charge/discharge voltage gap and long-

time cycling stability. Significantly, the excellent stability is greater than that of noble metal-based battery. Furthermore, N-NiCo₂O_{4-x}-2 min can also be employed in the solid-state zinc-air battery which displays excellent stability with a small increase of gap voltage after running for 20 h. This work illustrates the promising potential of plasma technology in the development of high-performance catalysts.

Declaration of competing interest

The authors declare that they have no known competing financial interests or personal relationships that could have appeared to influence the work reported in this paper.

Acknowledgements

H.L. thanks the China Scholarship Council (CSC) for the support through the project 202009110110. N.W. and L.K. thank the German Research Foundation (DFG) for funding through the collaborative research center 1261 in project A6.

Appendix A. Supplementary data

Supplementary data to this article can be found online at <https://doi.org/10.1016/j.ijhydene.2023.03.146>.

REFERENCES

- [1] Kang Y, Wang W, Li J, Mi Y, Gong H, Lei Z. 3D Rosa centifolia-like CeO₂ encapsulated with N-doped carbon as an enhanced electrocatalyst for Zn-air batteries. *J Colloid Interface Sci* 2020;578:796e804. <https://doi.org/10.1016/j.jcis.2020.06.040>.
- [2] Li H, Mu ZX, Sha Q. Ag/AgCl coupled with WO₃ films on glass slides and enhanced photocatalysis performance under visible light. *Mater Res Express* 2019;6:096421. <https://doi.org/10.1088/2053-1591/ab2e5b>.
- [3] Anjali J, Jose VK, Lee J-M. Carbon-based hydrogels: synthesis and their recent energy applications. *J Mater Chem* 2019;7:15491-518. <https://doi.org/10.1039/C9TA02525A>.
- [4] Gao LQ, Xiao ML, Jin Z, Liu CP, Zhu JB, Ge JJ, et al. Correlating Fe source with Fe-NC active site construction: guidance for rational design of high-performance ORR catalyst. *J Energy Chem* 2018;27(6):1668-73. <https://doi.org/10.1016/j.jechem.2018.06.008>.
- [5] Zhang K, Cen Z, Yang F, Xu KB. Rational construction of NiCo₂O₄@Fe₂O₃ core-shell nanowire arrays for high-performance supercapacitors. *Prog. Nat. Sci-Mater.* 2021;31:19-24. <https://doi.org/10.1016/j.pnsc.2020.12.001>.
- [6] Rauf M, Wang JW, Wang SH, Zhou ZY, Lqbal W, Khan SA, et al. Highly stable N-containing polymer-based Fe/N_x/C electrocatalyst for alkaline

4 “Nitrogen-doped NiCo₂O₄ nanowires on carbon paper as a self-supported air cathode for rechargeable Zn-air batteries”

- anion exchange membrane fuel cell applications. *Prog. Nat. Sci-Mater.* 2022;32:27-33. <https://doi.org/10.1016/j.pnsc.2021.10.016>.
- [7] Liu A, Liang XY, Ren XF, Guan WX, Ma TL. Recent progress in MXene-based materials for metal-sulfur and metal-air batteries: potential high-performance electrodes. *Electrochem. Energy Rev.* 2022;5:112-44. <https://doi.org/10.1007/s41918-021-00110-w>.
- [8] Zhang SM, Chen MH, Zhao X, Cai JL, Yan W, Yen JC, et al. Advanced noncarbon materials as catalyst supports and non-noble electrocatalysts for fuel cells and metal-air batteries. *Electrochem. Energy Rev.* 2021;4:336-81. <https://doi.org/10.1007/s41918-020-00085-0>.
- [9] Zhang ZC, Xi BJ, Ma XJ, Chen WH, Feng JK, Xiong SL. Recent progress, mechanisms, and perspectives for crystal and interface chemistry applying to the Zn metal anodes in aqueous zinc-ion batteries. *SusMat* 2022;2:114-41. <https://doi.org/10.1002/sus2.53>.
- [10] Wu MJ, Zhang GX, Chen N, Chen WF, Qiao JL, Sun SH. A self-supported electrode as a high-performance binder- and carbon-free cathode for rechargeable hybrid zinc batteries. *Energy Storage Mater* 2020;24:272-80. <https://doi.org/10.1016/j.ensm.2019.08.009>.
- [11] Wan L, Wang PC. Recent progress on self-supported two-dimensional transition metal hydroxides nanosheets for electrochemical energy storage and conversion. *Int J Hydrogen Energy* 2021;46:8356e-76. <https://doi.org/10.1016/j.ijhydene.2020.12.061>.
- [12] Askari S, Mariotti D, Brunet P, Vahl A, Benedikt J. Iron-doped nanoflakes of layered double hydroxide of nickel for high-performance hybrid zinc batteries. *Mater Today Energy* 2021;22:100879. <https://doi.org/10.1016/j.mtener.2021.100879>.
- [13] Lee S, Choi J, Kim M, Park J, Park M, Cho J. Material design and surface chemistry for advanced rechargeable zinc-air batteries. *Chem Sci* 2022;13:6159-80. <https://doi.org/10.1039/D1SC07212A>.
- [14] Wu MJ, Zhang GX, Chen N, Hu YF, Regier T, Rawach D, et al. Self-reconstruction of Co/Co₂P heterojunctions confined in N-doped carbon nanotubes for zinc-air flow batteries. *ACS Energy Lett* 2021;6:1153-61. <https://doi.org/10.1021/acseenergylett.1c00037>.
- [15] Mathur A, Halder A. One-step synthesis of bifunctional iron-doped manganese oxide nanorods for rechargeable zinc-air batteries. *Catal Sci Technol* 2019;9:1245-54. <https://doi.org/10.1039/C8CY02498G>.
- [16] Liu WJ, Bao J, Xu L, Guan ML, Lei YC. Chromium-modulated multifunctional electrocatalytic activities of spinel oxide for Zn-air batteries and overall water splitting. *J Power Sources* 2020;479:229099. <https://doi.org/10.1016/j.jpowsour.2020.229099>.
- [17] Ibupoto ZH, Tahira A, Shah AA, Aftab U, Solangi MY, Leghari JA, et al. NiCo₂O₄ nanostructures loaded onto pencil graphite rod: an advanced composite material for oxygen evolution reaction. *Int J Hydrogen Energy* 2022;47:6650-65. <https://doi.org/10.1016/j.ijhydene.2021.12.024>.
- [18] Seong A, Kim J, Kwon O, Jeong HY, Gorte RJ, Vohs JM, et al. Self-reconstructed interlayer derived by in-situ Mn diffusion from La_{0.5}Sr_{0.5}MnO₃ via atomic layer deposition for an efficient bi-functional electrocatalyst. *Nano Energy* 2020;71:104564. <https://doi.org/10.1016/j.nanoen.2020.104564>.
- [19] Wu HH, Zeng M, Li ZY, Zhu X, Tian CC, Xia CG, et al. Coupling FeNi alloys and hollow nitrogen-enriched carbon frameworks leads to high-performance oxygen electrocatalysts for rechargeable zinc-air batteries. *Sustain Energy Fuels* 2019;3:136. <https://doi.org/10.1039/C8SE00362A>.
- [20] Liu C, Zhou W, Zhang JF, Chen ZL, Liu SL, Zhang Y, et al. Air-assisted transient synthesis of metastable nickel oxide boosting alkaline fuel oxidation reaction. *Adv Energy Mater* 2020;10:2001397. <https://doi.org/10.1002/aenm.202001397>.
- [21] Cui BH, Hu Z, Liu C, Liu SL, Chen FS, Hu S, et al. Heterogeneous lamellar-edged Fe-Ni(OH)₂/Ni₃S₂ nanoarray for efficient and stable seawater oxidation. *Nano Res* 2021;14:1149-55. <https://doi.org/10.1007/s12274-020-3164-3>.
- [22] Cui BH, Liu C, Zhang JF, Lu JJ, Liu SL, Chen FS, et al. Waste to wealth: defect-rich Ni-incorporated spent LiFePO₄ for efficient oxygen evolution reaction. *Sci. China, Mater.* 2021;64:2710-8. <https://doi.org/10.1007/s40843-021-1682-0>.
- [23] Liu Y, Yang F, Yang GW. Co₂P@NiCo₂O₄ bi-functional electrocatalyst with low overpotential for water splitting in wide range pH electrolytes. *J Colloid Interface Sci* 2019;534:55-63. <https://doi.org/10.1016/j.jcis.2018.09.017>.
- [24] Askari S, Mariotti D, McGlynn R, Benedikt J. Air-cathode with 3D multiphase electrocatalyst interface design for high-efficiency and durable rechargeable zinc-air batteries. *Energy Technol* 2021;9:2000999. <https://doi.org/10.1002/ente.202000999>.
- [25] Matthews T, Dolla TH, Gwebu SS, Mashola TA, Dlamini LT, Carleschi E, et al. Mn-Ni-Co-O spinel oxides towards oxygen reduction reaction in alkaline medium: Mn_{0.5}Ni_{0.5}Co₂O₄/C synergism and cooperation. *Catalysts* 2021;11:1059. <https://doi.org/10.3390/catal11091059>.
- [26] Liu Y, Liu P, Qin W, Wu X, Yang G. Laser modification-induced NiCo₂O₄-d with high exterior Ni³⁺/Ni²⁺ ratio and substantial oxygen vacancies for electrocatalysis. *Electrochim Acta* 2019;297:623-32. <https://doi.org/10.1016/j.electacta.2018.11.111>.
- [27] Lin JH, Yan YT, Xu TX, Qu CQ, Li J, Cao J, et al. S doped NiCo₂O₄ nanosheet arrays by Ar plasma: an efficient and bifunctional electrode for overall water splitting. *J Colloid Interface Sci* 2020;560:34-9. <https://doi.org/10.1016/j.jcis.2019.10.056>.
- [28] Chen X, Yan ZH, Yu M, Sun HM, Liu FM, Zhang QY, et al. Spinel oxide nanoparticles embedded in nitrogen-doped carbon nanofibers as a robust

4 “Nitrogen-doped NiCo₂O₄ nanowires on carbon paper as a self-supported air cathode for rechargeable Zn-air batteries”

- and self-standing bifunctional oxygen cathode for Zn-air batteries. *J Mater Chem* 2019;7:24868-76. <https://doi.org/10.1039/C9TA09873A>.
- [29] Yang F, Chu J, Cheng YP, Gong JF, Wang XQ, Xiong SX. Hydrothermal synthesis of NiCo-layered double hydroxide nanosheets decorated on biomass carbon skeleton for high performance supercapacitor. *Chem Res Chin Univ* 2021;37:772-7. <https://doi.org/10.1007/s40242-020-0333-6>.
- [30] Xu J, Ruan CH, Li PX, Xie YB. Excessive nitrogen doping of tin dioxide nanorod array grown on activated carbon fibers substrate for wire-shaped microsupercapacitor. *Chem Eng J* 2019;378:122064. <https://doi.org/10.1016/j.cej.2019.122064>.
- [31] Yin J, Zhou PP, An L, Huang L, Shao CW, Wang J, et al. Self-supported nanoporous NiCo₂O₄ nanowires with cobalt-nickel layered oxide nanosheets for overall water splitting. *Nanoscale* 2016;8:1390. <https://doi.org/10.1039/C5NR06197K>.
- [32] Zhu ZG, Zhang JM, Peng XM, Liu YY, Cen TL, Ye ZF, et al. Co₃O₄NiCo₂O₄ hybrid nanoparticles anchored on N-doped reduced graphene oxide nanosheets as an efficient catalyst for Zn-air batteries. *Energy Fuel* 2021;5:35. <https://doi.org/10.1021/acs.energyfuels.0c04079>.
- [33] Zhao RD, Cui D, Dai JQ, Xiang J, Wu FF. Morphology controllable NiCo₂O₄ nanostructure for excellent energy storage device and overall water splitting. *Sustain. Mater. Technol.* 2020;24:e00151. <https://doi.org/10.1016/j.susmat.2020.e00151>.
- [34] Yin J, Li YX, Lv F, Fan QH, Zhao YQ, Zhang QH, et al. NiO/CoN porous nanowires as efficient bifunctional catalysts for Zn-air batteries. *ACS Nano* 2017;11:2275-83. <https://doi.org/10.1021/acsnano.7b00417>.
- [35] J Bian J, Cheng XP, Meng XY, Wang J, Zhou JG, Li SQ, et al. Nitrogen-doped NiCo₂O₄ microsphere as an efficient catalyst for flexible rechargeable zinc-air batteries and self-charging power system. *ACS Appl Energy Mater* 2019;2:2296-304. <https://doi.org/10.1021/acsaem.9b00120>.
- [36] Lu JF, Zhang QW, Wang J, Saito F, Uchida M. Synthesis of N-Doped ZnO by grinding and subsequent heating ZnO-urea mixture. *Powder Technol* 2006;162:33-7. <https://doi.org/10.1016/j.powtec.2005.12.007>.
- [37] Choi K, Moon IK, Oh J. An efficient amplification strategy for N-doped NiCo₂O₄ with oxygen vacancies and partial Ni/Co-nitrides as a dual-function electrode for both supercapacities and hydrogen electrocatalysis. *J Mater Chem* 2019;7:1468-78. <https://doi.org/10.1039/C8TA07210H>.
- [38] Fischer A, Makowski P, Muller JO, Antonietti M, Thomas A, Goettmann F. High surface area TiO₂ and TiN as catalysts for the C-C coupling of alcohols and ketones. *ChemSusChem* 2008;5:444-9. <https://doi.org/10.1002/cssc.200800019>.
- [39] He H, Huang D, Pang W, Sun D, Wang Q, Tang Y, et al. Plasma-induced amorphous shell and deep cation-site S doping endow TiO₂ with extraordinary sodium storage performance. *Adv Mater* 2018;30:1801013. <https://doi.org/10.1002/adma.201801013>.
- [40] Li H, Mu ZX, Guang SG, Zhang JL. Effect of the deposition conditions on the properties of photocatalytic WO₃ thin films prepared by mid-frequency magnetron sputtering. *Mater Sci Semicond Process* 2019;99:99-105. <https://doi.org/10.1016/j.mssp.2019.04.011>.
- [41] Askari S, Machhadani H, Benedikt J, Helmersson U. Plasmabased processes for planar and 3D surface patterning of functional nanoparticles. *J Nano Res* 2019;21:223. <https://doi.org/10.1007/s11051-019-4674-3>.
- [42] Askari S, Mariotti D, Stehr JE, Benedikt J, Keraudy J, Helmersson U. Low-loss and tunable localized mid-infrared plasmons in nanocrystals of highly fegenerate InN. *Nano Lett* 2018;18(9):5691-5687. <https://doi.org/10.1021/acs.nanolett.8b02260>.
- [43] Dey A, Ghosh P, Bowen J, St N, Braithwaite J, Krishnamurthy S. Engineering work function of graphene oxide from p to n type using a low power atmospheric pressure plasma jet. *Phys Chem Chem Phys* 2020;22:7685-98. <https://doi.org/10.1039/C9CP06174F>.
- [44] Schulze C, Li H, Mohn L, Müller M, Benedikt J. Chamber with inverted electrode geometry for measuring and control of ion flux-energy distribution functions. *Plasma* 2022;5:295. <https://doi.org/10.3390/plasma5030023>.
- [45] Zhang YQ, Ouyang B, Xu J, Jia GC, Chen S, Rawat RS, et al. Rapid synthesis of cobalt nitride nanowires: highly efficient and low-cost catalysts for oxygen evolution. *Angew Chem Int Ed* 2016;55:8670-4. <https://doi.org/10.1002/ange.201604372>.
- [46] Zheng JX, Peng XF, Wang Z. Plasma-assisted defect engineering of N-doped NiCo₂O₄ for efficient oxygen reduction. *Phys Chem Chem Phys* 2021;23:6591. <https://doi.org/10.1039/D1CP00525A>.
- [47] Wang ZC, Xu WJ, Chen XK, Peng YH, Song YY, Lv CX, et al. Defect-rich nitrogen doped Co₃O₄/C porous nano-cubes enable high-efficiency bifunctional oxygen electrocatalysis. *Adv Funct Mater* 2019;29:1902875. <https://doi.org/10.1002/adfm.201902875>.
- [48] Wang MX, Fan LS, Sun X, Guan B, Jiang B, Wu X, et al. Nitrogen-doped CoSe₂ as a bifunctional catalyst for high areal capacity and lean electrolyte of LiS battery. *ACS Energy Lett* 2020;5:3041-50. <https://doi.org/10.1021/acscenergylett.0c01564>.
- [49] Sammed KA, Pan LJ, Farid A, Javid M, Yang ST, Asif M. Carbon nano-coil-supported three-dimensional structure of nickel-cobalt nitrides as the electrode material for supercapacitors. *ACS Appl Energy Mater* 2021;4:6678-87. <https://doi.org/10.1021/acsaem.1c00745>.
- [50] Meganathan MD, Mao S, Huang TZ, Sun GX. Reduced graphene oxide intercalated Co₂C or Co₄N nanoparticles as an efficient and durable fuel cell catalyst for oxygen reduction. *J Mater Chem* 2017;5:2972. <https://doi.org/10.1039/c6ta09729d>.
- [51] Xu L, Jiang QQ, Xiao ZH, Li XY, Hao J, Wang SY, et al. Plasma-engraved Co₃O₄ nanosheets with oxygen vacancies and high surface area

4 “Nitrogen-doped NiCo₂O₄ nanowires on carbon paper as a self-supported air cathode for rechargeable Zn-air batteries”

- for the oxygen evolution reaction. *Angew Chem, Int Ed* 2016;55:5277-81.
<https://doi.org/10.1002/anie.201600687>.
- [52] Budiyo E, Yu MQ, Chen MM, Debeer S, Rüdiger O, Tu`ysu`z H. Tailoring morphology and electronic structure of cobalt iron oxide nanowires for electrochemical oxygen evolution reaction. *ACS Appl Energy Mater* 2020;3:8583-94. <https://doi.org/10.1021/acsaem.0c01201>.
- [53] Liu GG, Li P, Zhao GX, Wang X, Kong JT, Liu HM, et al. Promoting active species generation by plasmon-induced hot-electron excitation for efficient electrocatalytic oxygen evolution. *J Am Chem Soc* 2016;138(29):9128-36. <https://doi.org/10.1021/jacs.6b05190>.
- [54] Xiang WK, Yang NT, Li XP, Linnemann J, Hagemann U, Ruediger O, et al. 3D atomic-scale imaging of mixed Co-Fe spinel oxide nanoparticles during oxygen evolution reaction. *Nat Commun* 2022;13:179. <https://doi.org/10.1038/s41467021-27788-2>.
- [55] Sun Y, Wu J, Xie Y, Wang X, Ma KK, Tian Z, et al. Dynamics of both active phase and catalysis pathway for spinel water-oxidation catalysts. *Adv Funct Mater* 2022;2207116. <https://doi.org/10.1002/adfm.202207116>.
- [56] Peng MG, Liu P, Li ZJ, Li Z, Wen JM, Yan CB, et al. Construction of Co/N-doped porous rose-like structure for efficient oxygen reduction reaction catalyst and Zn-air battery. *Appl Surf Sci* 2021;566:150665. <https://doi.org/10.1016/j.apsusc.2021.150665>.

天门中断楚江开，碧水东流至此回。

-----李白

Breaking Mount Heaven's Gate, the great River rolls through,
Its east-flowing green billows, hurled back here, turn north.

----- Bai Li (Translated by Yuanchong Xu)

5

Plasma-engineering of oxygen vacancies on NiCo₂O₄ nanowires with enhanced bifunctional electrocatalytic performance for rechargeable zinc-air battery

Oxygen vacancies, as a type of surface defect, have been demonstrated to be an effective approach to tailoring the surface properties of transition-metal-oxide catalysts and optimizing their electrocatalytic performances. The surface modification via Ar plasma can introduce oxygen vacancies on the catalyst surfaces with a short duration and minimize the consumption of energy and chemical precursors. However, the strong etching effect of Ar plasma also limits the electrocatalytic performance of catalysts due to the over-treatment effect. In this work, the self-support NiCo₂O₄ nanowires reported in Chapter 4 were selected

as the pristine electrocatalysts. The plasma based on a mixed gas of Ar and H₂ was used to modify the catalyst surfaces. As a result, the H₂/Ar plasma treatment generated more oxygen vacancies on the surfaces of NiCo₂O₄ nanowires, which exhibited enhanced electrocatalytic activities for both OER and ORR compared to the catalyst after Ar plasma treatment. Moreover, the performance of zinc-air batteries with the H₂/Ar plasma-modified catalyst was also evaluated.

He Li, Jihao Wang, Tim Tjardts, Igor Barg, Haoyi Qiu, Martin Müller, Jan Krahmer, Sadegh Askari, Salih Veziroglu, Cenk Aktas, Lorenz Kienle, Jan Benedikt, Plasma-engineering of oxygen vacancies on NiCo₂O₄ nanowires with enhanced bifunctional electrocatalytic performance for rechargeable zinc-air battery, *Small*, 2024, 20, 2310660.

[DOI: 10.1002/smll.202310660]

This is an open access article under the terms of the Creative Commons Attribution-NonCommercial-NoDerivs License, which permits use and distribution in any medium, provided the original work is properly cited, the use is non-commercial and no modifications or adaptations are made.

Prof. Dr. Jan Benedikt designed the underlying concept, provided experimental funding and reviewed the manuscript. The author of this thesis carried out the experiments and prepared the first draft. Other authors helped with the material characterization and reviewed the manuscript.

Plasma-Engineering of Oxygen Vacancies on NiCo₂O₄ Nanowires with Enhanced Bifunctional Electrocatalytic Performance for Rechargeable Zinc-air Battery

He Li, Jihao Wang, Tim Tjardts, Igor Barg, Haoyi Qiu, Martin Müller, Jan Krahmer, Sadegh Askari, Salih Veziroglu, Cenk Aktas, Lorenz Kienle, and Jan Benedikt*

Designing an efficient, durable, and inexpensive bifunctional electrocatalyst toward oxygen evolution reactions (OER) and oxygen reduction reactions (ORR) remains a significant challenge for the development of rechargeable zinc-air batteries (ZABs). The generation of oxygen vacancies plays a vital role in modifying the surface properties of transition-metal-oxides (TMOs) and thus optimizing their electrocatalytic performances. Herein, a H₂/Ar plasma is employed to generate abundant oxygen vacancies at the surfaces of NiCo₂O₄ nanowires. Compared with the Ar plasma, the H₂/Ar plasma generated more oxygen vacancies at the catalyst surface owing to the synergic effect of the Ar-related ions and H-radicals in the plasma. As a result, the NiCo₂O₄ catalyst treated for 7.5 min in H₂/Ar plasma exhibited the best bifunctional electrocatalytic activities and its gap potential between $E_{j=10}$ for OER and $E_{1/2}$ for ORR is even smaller than that of the noble-metal-based catalyst. In situ electrochemical experiments are also conducted to reveal the proposed mechanisms for the enhanced electrocatalytic performance. The rechargeable ZABs, when equipped with cathodes utilizing the aforementioned catalyst, achieved an outstanding charge–discharge gap, as well as superior cycling stability, outperforming batteries employing noble-metal catalyst counterparts.

1. Introduction

To better exploit renewable energies, the development of efficient energy storage and conversion systems is of utmost importance.^[1–4] Among these novel technologies, rechargeable zinc-air batteries (ZABs) have been considered promising candidates for applications in electricity storage systems and next-generation electric devices due to their high energy density, low cost, intrinsic safety, and environmental friendliness.^[5–8] The performance of these batteries is highly related to the activity of the oxygen evolution reaction (OER) during the charging process and the oxygen reduction reaction (ORR) during the discharge process at their air cathode.^[9–12] Therefore, designing an appropriate catalyst assembled into the air cathode capable of efficiently accelerating these two oxygen-involved reactions is crucial for the development of rechargeable ZABs.

H. Li, J. Benedikt
Institute of Experimental and Applied Physics
Kiel University
Leibnizstraße 19, D-24098 Kiel, Germany
E-mail: benedikt@physik.uni-kiel.de
J.Wang, J.Krahmer
Institute of Inorganic Chemistry
Kiel University
Max-Eyth-Straße 2/Otto-Hahn-Platz 6, D-24118 Kiel, Germany
T.Tjardts, I.Barg, S.Veziroglu, C.Aktas
Chair for Multicomponent Materials
Department of Materials Science
Faculty of Engineering
Kiel University
Kaiserstraße 2, D-24143 Kiel, Germany



The ORCID identification number(s) for the author(s) of this article can be found under <https://doi.org/10.1002/sml.202310660>

© 2024 The Authors. Small published by Wiley-VCH GmbH. This is an open access article under the terms of the [Creative Commons Attribution-NonCommercial-NoDerivs](https://creativecommons.org/licenses/by-nc/4.0/) License, which permits use and distribution in any medium, provided the original work is properly cited, the use is non-commercial and no modifications or adaptations are made.

DOI: 10.1002/sml.202310660

H. Qiu
Chair for Functional Nanomaterials
Department of Materials Science
Faculty of Engineering
Kiel University
Kaiserstraße 2, D-24143 Kiel, Germany
M. Müller, L. Kienle
Chair for Synthesis and Real Structure
Department of Materials Science
Faculty of Engineering
Kiel University
Kaiserstraße 2, D-24143 Kiel, Germany
S. Askari
Department of Fiber and Polymer Technology
KTH Royal Institute of Technology Stockholm
SE-10044, Sweden
S. Veziroglu, L. Kienle, J. Benedikt
Kiel Nano
Surface, and Interface Science KiNSIS
Kiel University
Christian-Albrechts-Platz 4, D-24118 Kiel, Germany

The current benchmarks for OER and ORR are noble-metal based materials such as Pt, Ir, and RuO₂. However, their high cost and scarcity severely hinder their commercial applications in rechargeable ZABs.^[13,14]

Recently, transition metal oxides (TMOs) have been widely used as active bifunctional catalysts to replace these noble-metal based catalysts owing to their low cost, high stability, and rich redox chemistry.^[15–17] Particularly, the spinel-structured NiCo₂O₄ with a distinct electronic structure has received widespread attention.^[18–21] However, the electrocatalytic performance of bulk NiCo₂O₄ for OER and ORR is still unsatisfactory because of its poor conductivity and low intrinsic activity. The generation of oxygen vacancies at TMOs surfaces has been proven to be an effective strategy for enhancing the electrocatalytic performance of TMOs by modifying their electronic structures and optimizing the adsorption and dissociation of the reactants and reaction intermediates during electrocatalysis reactions.^[22–26] Moreover, the delocalized electrons of metal atoms near oxygen vacancies could also improve the conductivity of TMOs and accelerate their charge transfer.^[23,24] However, some studies also demonstrated that excessive oxygen vacancies damaged the structure integrity of the catalyst, thus reducing the transport of charge carriers during reactions and leading to performance degradation.^[23,27,28] Therefore, finding a facile and reliable approach to easily generate and precisely control the content of oxygen vacancies is still crucial for TMOs to realize their optimal bifunctional electrocatalytic performances.

Various strategies have been developed to generate oxygen vacancies at the TMOs surfaces, including thermal treatment,^[20,24] solution reduction,^[29,30] cation/anion doping,^[31,32] and plasma treatment.^[33,34] Compared with other methods, plasma treatment is an efficient approach for surface modification with a short duration, low temperature, and minimized energy and precursor consumption.^[35,36] More importantly, the content of oxygen vacancies at the TMOs surfaces is easily controllable by tuning the plasma parameters, such as applied power, pressure, operation time, and gas mixture.^[37] Among the numerous types of plasma, argon plasma is a common tool to generate oxygen defects at TMOs surfaces by the physical etching process.^[34,38,39] However, the electrocatalytic performances of TMOs after Ar plasma treatment are limited and unsatisfactory due to the over etching effect of Ar atoms.^[34,40] Previous reports have shown that the plasma with an H₂/Ar gas mixture introduced more oxygen vacancies than the pure Ar plasma at the surface of graphene oxides owing to the existence of hydrogen radicals which can chemically remove oxygen atoms and significantly reduce the treatment duration.^[41] So far, a limited amount of research has been conducted on the electrocatalytic performance of TMOs after H₂/Ar plasma treatment.

Herein, NiCo₂O₄ nanowires were first coated on carbon paper by the hydrothermal method. Subsequently, the prepared samples were modified by plasma to generate oxygen vacancies at their surface. Compared with pure Ar plasma treatment, more oxygen vacancies have been generated at the surface of NiCo₂O₄ nanowires by H₂/Ar plasma treatment. Electrochemical tests have shown that the generation of oxygen vacancies at the catalyst surface leads to more available active sites, higher conductivity, and better intrinsic activities, resulting in the enhanced electrocatalytic performance of NiCo₂O₄ nanowires for OER and ORR.

2. Results and Discussion

The synthesis process of NiCo₂O₄ nanowires with abundant oxygen vacancies is schematically illustrated in **Figure 1**. In this work, commercial carbon paper (CP) with 3D microstructure provided a large surface area to grow NiCo₂O₄ nanowires and its good conductivity also accelerated the charge transfer during electrocatalytic reactions.^[42–44] Firstly, NiCo₂O₄ nanowires were prepared by the hydrothermal method and the following annealing process (350 °C, 3 h).^[45] As shown in **Figure 2a,b**, dense arrays of nanowires with a length of ≈4 μm and a diameter of ≈50 nm are vertically grown on the surface of CP, forming a 3D hedgehog-like nanostructure. Subsequently, the as-prepared samples were modified by pure Ar and H₂/Ar plasmas for different durations. As illustrated in **Figure 2c,d**, the morphology of the nanowires does not show any change after Ar plasma treatment. By contrast, the tips of the nanowires became distorted after H₂/Ar plasma treatment (**Figure 2e,f**). Meanwhile, similar results were also detected from the samples after H₂/Ar plasma treatment for 2.5 and 12.5 min as shown in **Figure S1** (Supporting Information), suggesting that the hydrogen-based species in the H₂/Ar plasma were responsible for this morphological change, see our discussion later. However, the macroscopic hedgehog-like structure was overall preserved after plasma treatment which offered fast charge transfer channels, large surface area as well as abundant active sites for the following surface catalytic reactions.

The XRD patterns shown in **Figure 2g** and **Figure S1 g** (Supporting Information) confirm the successful synthesis of NiCo₂O₄ on the CPs. The reflections at 2θ = 8.6°, 14.1°, 16.6°, 20.0°, 24.6°, 26.1°, 28.5°, and 33.4° match well with the (111), (220), (311), (400), (422), (511), (440), and (533) planes of the cubic spinel-type structure of NiCo₂O₄ (JCPDS #20-0781) and reflections at 2θ = 12.1°, 19.1°, and 24.5° are assigned to the graphitic carbon substrates, respectively. Notably, in the XRD patterns of H-NCO-7.5 and H-HCO-12.5, two additional reflections at 2θ = 19.3° and 27.3° are assigned to the CoNiO₂ (PDF #100188), which is also an excellent bifunctional catalyst, indicating the partial reduction from NiCo₂O₄ to CoNiO₂ at the material surface.^[46,47] These results suggest that the H₂/Ar plasma presented a higher reductivity for NiCo₂O₄ nanowires than the pure Ar plasma.

The TEM bright-field image of the H-NCO-7.5 catalyst shown in **Figure 3a** verifies the nano-porous microstructure of the nanowire. In **Figure 3b**, the selected area electron diffraction (SAED) patterns show discrete rings, which are assigned to the (111), (220), (311), (400), (511), and (440) planes of NiCo₂O₄, respectively, corresponding to XRD results. **Figure 3c** exhibits the element mapping images of the H-NCO-7.5 catalyst, demonstrating that Ni, Co, and O elements are uniformly distributed throughout the nanowire. In addition, the energy-dispersive X-ray spectroscopy (EDS) results shown in **Figure S2** (Supporting Information) confirm qualitatively that the O content of the HNCO-7.5 catalyst is much lower than that of the NCO catalyst, indicating the decrease of surface oxygen groups and the generation of oxygen vacancies at the catalyst surface after H₂/Ar plasma treatment.

The XPS measurement was conducted to investigate the valence states of the elements at the sample surfaces. As shown in **Figure 3d**, the survey spectra of all samples show the presence

5 “Plasma-engineering of oxygen vacancies on NiCo₂O₄ nanowires with enhanced bifunctional electrocatalytic performance for rechargeable zinc-air battery”

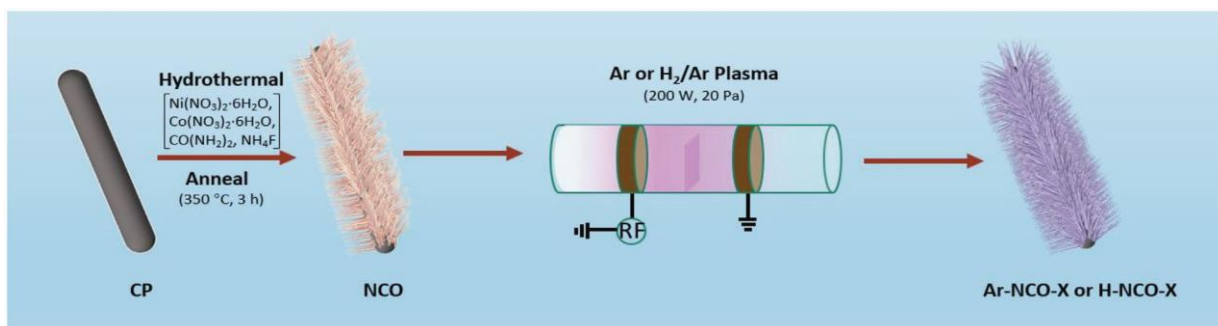


Figure 1. Schematic illustration for preparation of NiCo₂O₄ nanowires with oxygen vacancies generated by the plasma treatment.

of Ni, Co, and O elements, corresponding to the above results. Figure 3e shows the Ni 2p high-resolution spectra, including two primary peaks corresponding to Ni 2p_{3/2} and Ni 2p_{1/2} and two broad peaks belonging to shake-up satellites. The deconvoluted peaks at around 855.29 and 872.79 eV correspond to Ni²⁺ and the peaks at around 856.78 and 879.97 eV belong to Ni³⁺.^[48,49] In Figure 3f, the Co 2p high-resolution spectra also exhibit two dominant peaks of Co 2p_{3/2} and Co 2p_{1/2} with two broader shakeup satellites. The peaks at ≈780.09 and ≈796.22 eV belong to Co³⁺ and the peaks at around 782.06 and around 797.99 eV belong to Co²⁺.^[50,51] In general, the formation of oxygen vacancies is accompanied by the reduction of transition-metal valence states to maintain the charge balance.^[52,53] Therefore, higher ratio values of Ni²⁺/Ni³⁺ and Co²⁺/Co³⁺ at

the surfaces of the Ar-NCO7.5 sample and the H-NCO-7.5 sample, as shown in Table S1 (Supporting Information), suggest that a relatively large amount of oxygen vacancies were formed after plasma treatment, which could also be confirmed by the O 1s high-resolution spectra. The O 1s spectra shown in Figure 3g present three deconvoluted peaks at around 533.55, 531.57, and 529.77 eV, corresponding to the hydroxyl groups (O₁), the oxygen species chemisorbed at oxygen vacancies (O₂), and the metal-O bands (O₃), respectively.^[54-56] As clearly shown in Figure 3h, the content of O₂ for ArNCO-7.5 and H-NCO-7.5 are obviously increased than that for the pristine NiCo₂O₄, confirming the generation of oxygen vacancies after plasma treatment. Notably, the H-NCO-7.5 sample presents a higher

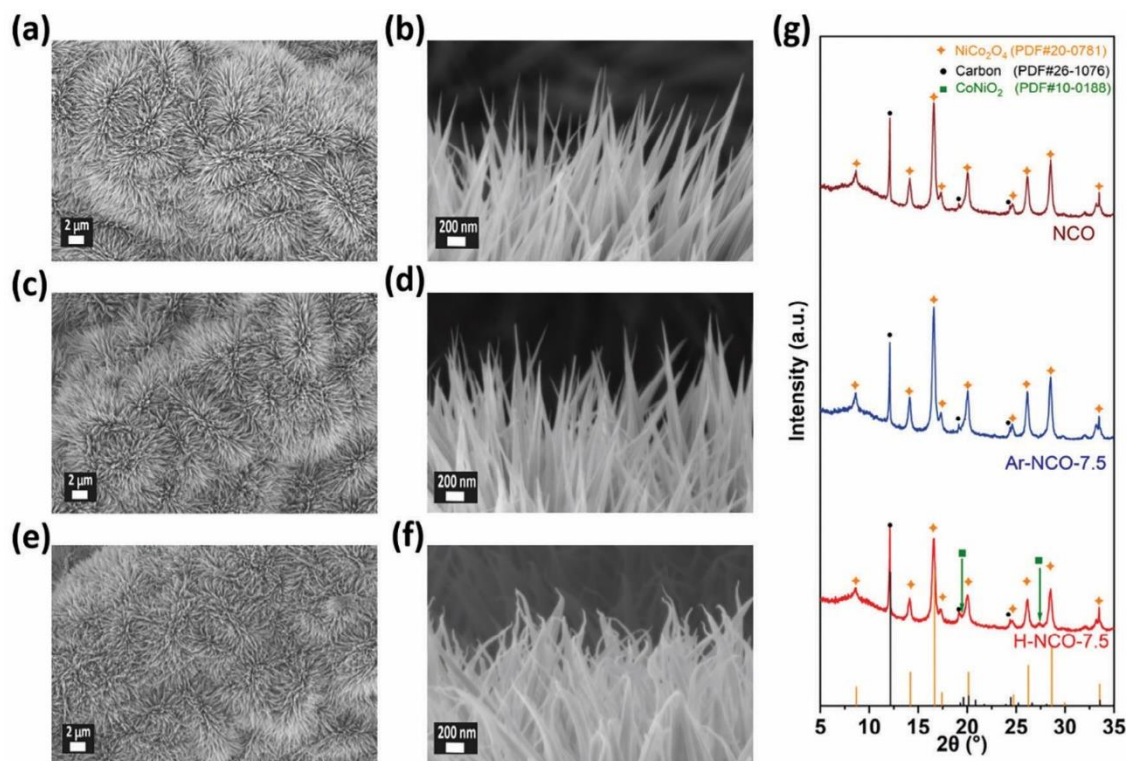


Figure 2. SEM images of (a, b) NCO, (c, d) Ar-NCO-7.5, and (e, f) H-NCO-7.5 samples. g) XRD patterns of NCO, Ar-NCO-7.5, and H-NCO-7.5 samples.

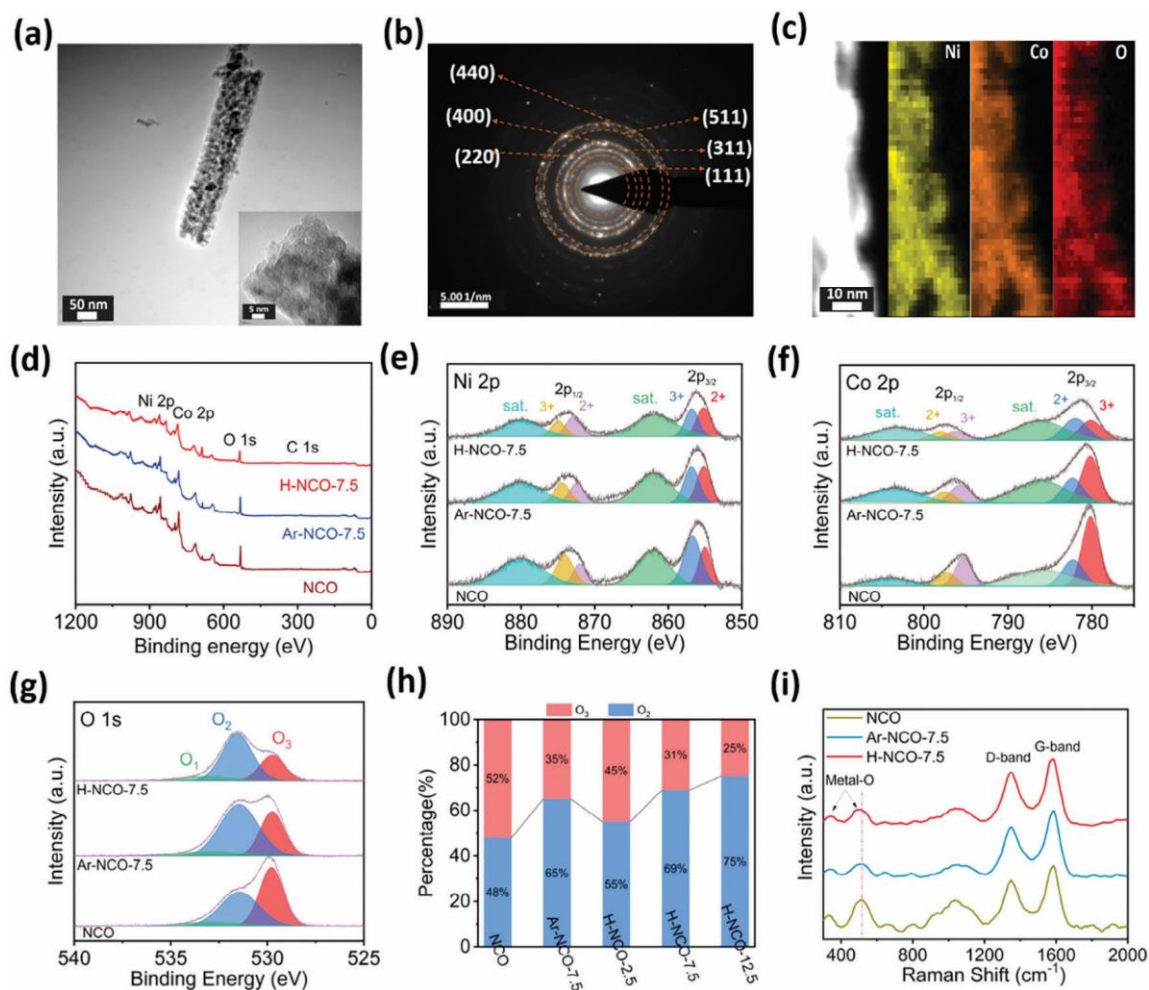


Figure 3. a) TEM image, b) SAED pattern, and c) element mapping of the H-NCO-7.5 sample. XPS results of NCO, Ar-NCO-7.5, and H-NCO-7.5 samples and corresponding d) full spectra, e) Ni 2p, f) Co 2p, and g) O 1s features. h) the ratio of the O₂ peak and O₃ peak in all samples. i) Raman spectra of NCO, Ar-NCO-7.5, and H-NCO-7.5 samples.

percentage of O₂, thus indicating that H₂/Ar plasma is more efficient in producing oxygen vacancies than Ar plasma for the same treatment time. Moreover, the content of oxygen vacancies is further increased when the treatment time reaches up to 12.5 min (see Figure S3, Supporting Information). Furthermore, Raman spectroscopy was performed to analyze the electronic structure of the samples. As shown in Figure 3i, two intense peaks located at 1346 and 1580 cm⁻² are assigned to the D band and G band of carbon substrates, respectively.^[57] In addition, the peaks at around 343 and 507 cm⁻² belong to the vibrations of metal-O bands and these peaks in the H-NCO-7.5 catalyst have an obvious red shift owing to the generation of oxygen vacancies at its surface.^[58,59]

The specific surface area of the prepared samples was investigated by the BET method to determine whether there were any significant changes in the surface area after plasma treatment. As shown in Figure S4 (Supporting Information), all samples show similar type-IV N₂ adsorption/desorption isotherms with mesoporous architectures, further verifying a mild etching effect of plasma for the macroscopic structures of NiCo₂O₄ nanowires. The specific surface area of H-NCO-7.5 is 42.2 m² g⁻¹, which is slightly larger than that of NCO (38.9 m² g⁻¹) but lower than that

of Ar-NCO-7.5 (45.1 m² g⁻¹). These results suggest that the Ar related ions with high energy in plasma are mainly responsible for the increased surface area of the samples.

The excited species emitting in the plasma were detected by the OES to better understand the plasma properties and surface reduction process. Figure 4a shows the OES spectra of Ar and H₂/Ar plasma generated under the power of 200 W and the pressure of 20 Pa. The intense lines observed in the range from 700 to 800 nm are the emission lines of excited Ar atoms. H₂/Ar plasma shows a lower intensity of these lines due to lower argon density and plasma power adsorbed by molecular H₂ gas. Moreover, the emission band near 601.2 nm and the line at 656.3 nm were detected only in the spectrum of H₂/Ar plasma, which corresponds to the Fulcher-transition of the excited H₂ molecule (Figure 4b)^[60] and the H_α Balmer series line of atomic hydrogen (Figure 4c),^[61] respectively. These results confirm that the H atoms and H excited species were produced in the H₂/Ar plasma. Due to the existence of H atoms and different excited species, the H₂/Ar plasma represented different deoxygenation processes than the Ar plasma. For pure Ar plasma treatment, the Ar-related ions with higher energies

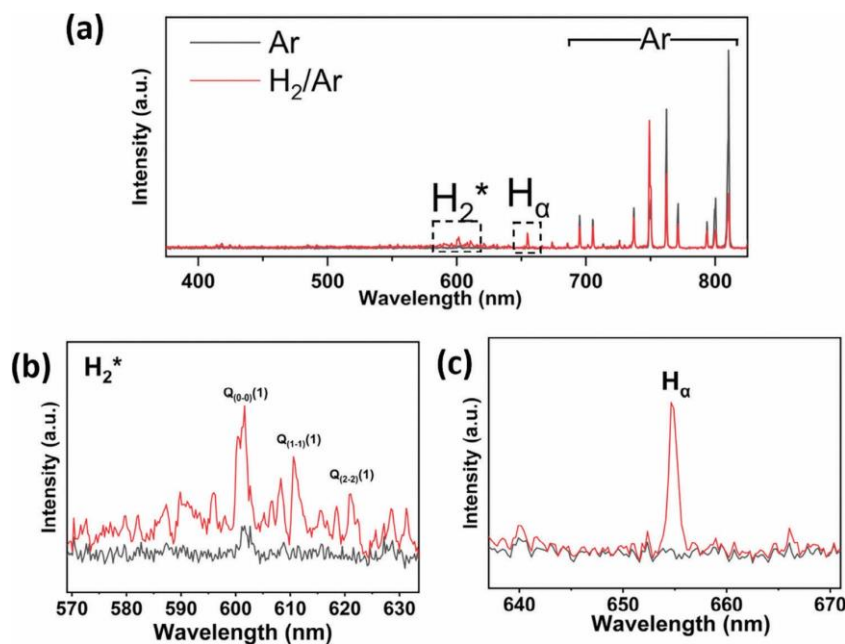


Figure 4. OES results for Ar and H₂/Ar plasma in the spectral range a) from 350 to 850 nm, b) from 568 to 635 nm with Fulcher transitions of excited H₂ molecule, and c) from 637 to 672 nm with H_α Balmer series line.

were very likely responsible for the deoxygenation reaction by physical bombardment, leading to the increase in the specific surface area and the generation of oxygen vacancies. The typical floating potential in the Ar RF-driven plasma is around few tens of eVs. The sheath around the floating substrate demonstrates collisional environment for Ar⁺ ions due to large cross-section of the resonant charge transfer collisions with Ar atoms at the pressure of 20 Pa, but the sheath for doubly ionized Ar²⁺ or other typical Ar-related ions (ArH⁺ and Ar₂⁺) is still remaining collision-less and especially the Ar²⁺ ions can reach the surface with kinetic energies above the threshold for physical sputtering.^[62,63]

Regarding H₂/Ar plasma treatment, the H atoms, excited H₂ molecules, and hydrogen ions can now chemically react with the surface oxides to form volatile species, such as H₂O, which absorb from the surface easily and leave oxygen vacancies behind. Moreover, the energetic ions can still contribute to the generation of oxygen vacancies as described above, but they will also accelerate the desorption of volatile species from the material surface. Therefore, abundant oxygen vacancies were generated at the catalyst surface by H₂/Ar plasma owing to this combined effect of ions, hydrogen atoms, and excited hydrogen molecules. The lower surface area of the H-NCO-7.5 sample in comparison with the Ar-NCO-7.5 sample as determined by BET diagnostics indicates that the physical sputtering is reduced in the H₂/Ar plasma compared to the pure Ar plasma treatment.

The morphological changes of the nanowire tips as observed in Figure 2f are very probably caused by the heating of the tips by recombination reactions of ions and H atoms at the nanowire surface. The temperature increases and any thermal effects are the largest at the tips because the nanowires have the largest surface-to-volume ratio there. It is the same heating process as the selective heating of silicon nanoparticles with

diameters of just a few nanometers observed in Ar/SiH₄(/H₂) plasmas.^[64]

The ORR performances of the samples were measured in 1 M KOH solution via a standard three-electrode system, where the catalyst-coated glassy carbon electrode (GCE), the Ag/AgCl electrode, and the Pt wire were used as the working electrode, the reference electrode and the counter electrode, respectively. The commercial Pt/C powder(20wt.%) was also coated on GCE as the benchmark. As shown in Figure S5a (Supporting Information), the H-NCO-7.5 catalyst presents a distinct reduction peak in the oxygen-saturated electrolyte, indicating its catalytic capability for ORR. Meanwhile, in Figure S5b (Supporting Information), the reduction peak of the H-NCO-7.5 catalyst in the oxygen-saturated electrolyte also appears at a more positive potential of 0.71 V than that of the NCO catalyst (0.64 V) and the Ar-NCO-7.5 catalyst (0.68 V). Figure 5a shows the LSV curves of samples and the H-NCO-7.5 catalyst exhibits an early-onset potential (E_{onset}) of 0.84V and a positive half-wave potential ($E_{1/2}$) of 0.76 V, outperforming that of the NCO catalyst (E_{onset} of 0.80 V, $E_{1/2}$ of 0.73 V) and the Ar/NCO catalyst (E_{onset} of 0.83 V, $E_{1/2}$ of 0.75 V) and closing to that of the Pt/C catalyst (E_{onset} of 0.95 V, $E_{1/2}$ of 0.87 V). Moreover, the H-NCO-7.5 catalyst is also proven to be the better ORR catalyst than NiCo₂O₄ after H₂/Ar plasma treatment for other duration times (Figure S6, Supporting Information). In Figure 5b and Figure S7 (Supporting Information), the H-NCO-7.5 catalyst also exhibits a fast ORR kinetics with a small Tafel slope of 91.8 mV dec⁻¹ and a low charge transfer resistance. These results confirm the positive effect of the H₂/Ar plasma treatment on the ORR performance of NiCo₂O₄. The catalyst with the best performance has been obtained after the treatment duration of 7.5 min indicating that too long treatment leads either to

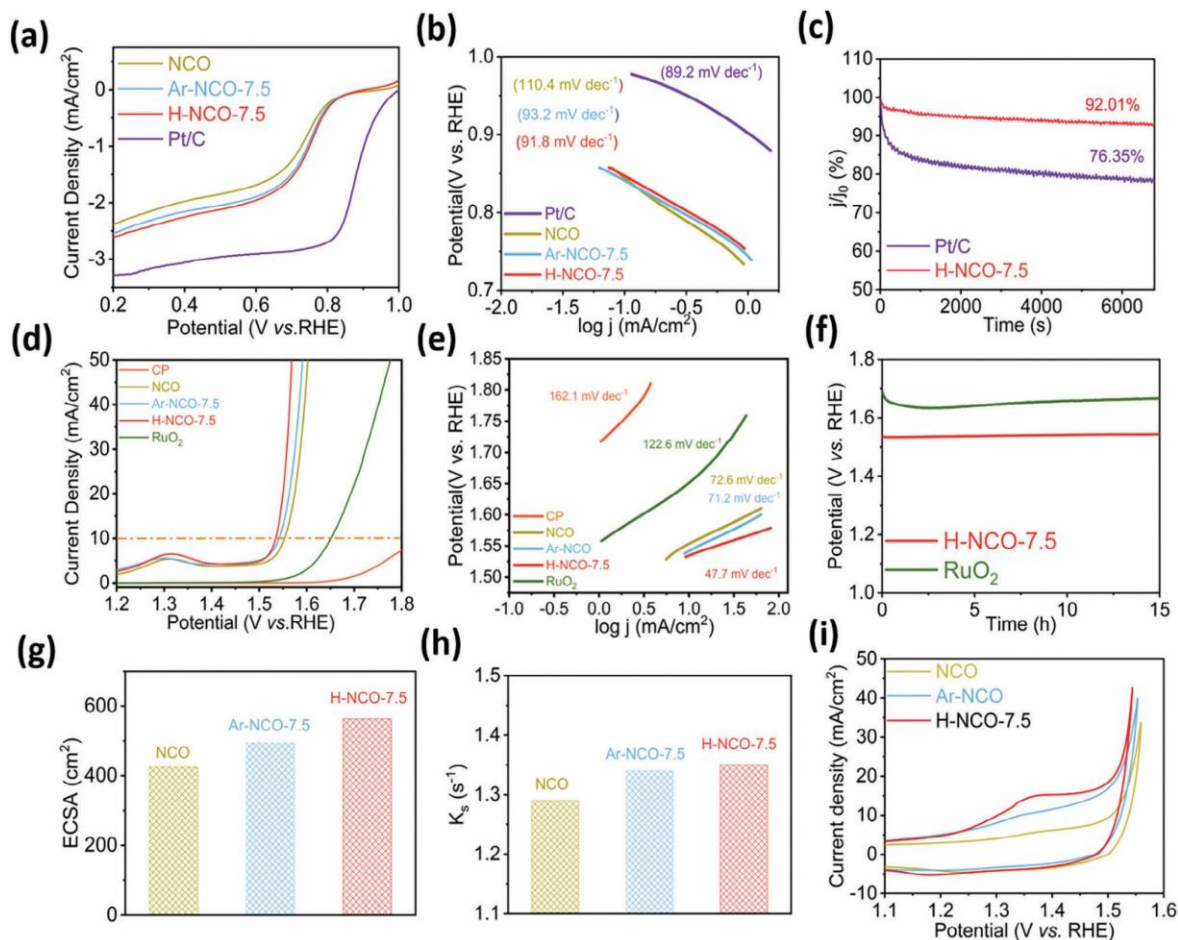


Figure 5. a) LSV curves and b) corresponding Tafel plots of the selected samples. c) The stability test of H-NCO-7.5 and Pt/C in O₂ saturated 1 m KOH for ORR. d) LSV curves and e) corresponding Tafel plots of the selected samples. f) The stability test of H-NCO-7.5 and RuO₂ in 1 m KOH for OER. g) ECSA values, h) K_s values, and i) the first CV curves of NCO, Ar-NCO-7.5, and H-NCO-7.5 samples.

large surface density of oxygen vacancies or to the damage of the surface structure by the prolonged interaction with energetic ions.

Since the catalyst running a 2e⁻ catalytic pathway in the ORR process could produce several corrosive intermediates, the catalyst following a 4e⁻ catalytic pathway for ORR is crucial for its stability as well as its battery performance.^[65,66] The electron transfer number (n) in the ORR process was evaluated by the LSV curves under various rotating rates. As shown in Figure S8 (Supporting Information), the calculated n of the H-NCO-7.5 catalyst is about 3.68, suggesting a 4e⁻ pathway-dominated ORR process by this catalyst. Figure 5c shows the stability tests of the H-NCO-7.5 and Pt/C catalysts using the chronoamperometric method for 7200 s, where the H-NCO-7.5 catalyst exhibits a current retention of 92.01%, superior to the Pt/C catalyst of 76.35%. The preferred 4e⁻ catalytic pathway and excellent stability of the H-NCO-7.5 catalyst suggest that it could be a promising candidate to replace the commercial Pt/C catalyst for ORR.

To evaluate the OER performance of the catalysts, commercial RuO₂ directly coated on carbon paper (1 mg cm⁻²) was used as the reference catalyst. Figure 5d shows the LSV curves of these catalysts and the H-NCO-7.5 exhibits the lowest overpotential of 304 mV at a current density of 10 mA cm⁻² (E_{j=10}) than that of the NCO (323 mV), Ar-NCO-7.5 (313 mV) as well as commercial RuO₂ catalysts (424 mV), suggesting its most

outstanding OER activity. Notably, the E_{j=10} value of the H-NCO-7.5 catalyst is also lower than that of NiCo₂O₄ for other duration times (Figure S9, Supporting Information). Meanwhile, in Figure 5e, the H-NCO-7.5 catalyst also presents the smallest Tafel slope of 47.7 mV dec⁻¹, indicating its outstanding reaction kinetics for OER. The stability of the catalyst was also evaluated by the chronopotentiometric method. As shown in Figure 5f, the H-NCO-7.5 catalyst exhibits excellent stability with just 18 mV increment in potential after 15 h of operation, which is better than the RuO₂ catalyst with 37 mV increment. The SEM image in Figure S10 (Supporting Information) shows that the morphology of the H-NCO-7.5 catalyst after this long-term operation is well preserved, further confirming its outstanding stability. A good air cathode should have both excellent OER and ORR performance. Therefore, the voltage gap (ΔE) between the E_{1/2} of ORR and the E_{j=10} of OER is used to evaluate the bifunctional catalytic performance of each studied sample. Figure S11 (Supporting Information) shows that the H-NCO-7.5 catalyst has the smallest ΔE of 0.77 V, which is better than that of NCO (0.83 V), Ar-NCO-7.5 (0.79 V), Pt/C + RuO₂ (0.78 V) and most of similar bifunctional catalysts reported recently (Table S2, Supporting Information). In addition, the electrocatalytic performance of NiCo₂O₄ with 5 min of plasma treatment was also tested and the H-NCO-5 catalyst also exhibited a better

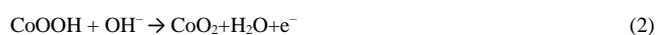
5 “Plasma-engineering of oxygen vacancies on NiCo₂O₄ nanowires with enhanced bifunctional electrocatalytic performance for rechargeable zinc-air battery”

bifunctional catalytic performance than the catalyst of NiCo₂O₄ after Ar plasma treatment for 5 min (Figure S12, Supporting Information). These results strongly confirm that H₂/Ar plasma treatment could be an efficient way to enhance the catalytic performance of NiCo₂O₄.

To better understand the reasons for the increased electrocatalytic activity, we further investigated the changes in electrochemical properties of NiCo₂O₄ nanowires after H₂/Ar plasma treatment. The ECSA of the samples, which are highly related to the number of available active sites, were calculated based on the linear relationship between ECSA and the double-layer capacitance (C_{dl}). As shown in Figure S13 (Supporting Information), the H-NCO-7.5 catalyst presents a higher C_{dl} of 22.5 mF cm⁻² than that of the NCO catalyst (17.0 mF cm⁻²), and the Ar-NCO7.5 catalyst (19.8 mF cm⁻²). Correspondingly, the ECSA values of the samples are illustrated in Figure 5g and the H-NCO-7.5 one also presents the largest ECSA of 563 cm², indicating its more exposed active sites for oxygen catalytic reactions. It should be noticed that the H-NCO-7.5 catalyst shows a lower specific surface area but higher ECSA than that of the Ar-NCO-7.5 catalyst, indicating that H₂/Ar plasma is more efficient for the creation of active sites compared to pure Ar plasma. In addition, the polarization curves of the catalysts were normalized by the values of ECSA to evaluate their intrinsic activities, where the H-NCO-7.5 catalyst still exhibits the highest OER performance (Figure S14, Supporting Information).

The increased intrinsic activities at the catalyst surfaces could be explained based on the Laviron analysis, which is used to investigate the adsorption affinity of HO⁻ ions during the catalytic reactions.^[67,68] As displayed in Figure S15 (Supporting Information), the redox peak current densities of NiCo₂O₄ before and after plasma treatment all show a linear relationship with the square root of the scanning rates increased from 5 to 25 mV s⁻¹, indicating that these redox reactions were controlled by the mass diffusion from the electrolyte to the catalyst surfaces. Therefore, in the alkaline electrolyte, the appropriate affinity for the adsorbed HO⁻ ions are important for the catalytic performance of the catalysts. The redox constant (K_s) of the catalysts was calculated by the Laviron equation^[69] and is shown in Figure 5h. The H-NCO-7.5 catalyst presents the larger K_s (1.35 s⁻¹) than that of NCO (1.29 s⁻¹) and Ar-NCO-7.5 (1.34 s⁻¹). The relatively large K_s indicate the preferential HO⁻ adsorption at the surface of the H-NCO-7.5 catalyst, resulting in its best intrinsic activities.

The best performance of the catalyst after Ar/H₂ plasma treatment can be further explained by CV curves. As shown in Figure S16 (Supporting Information), the broad oxidation peak (A₁) in the first CV cycle from 1.2 to 1.4 V belongs to the M²⁺/M³⁺ (M = Ni and Co) redox couples, and the peak (A₂) at ≈1.50 V corresponds to the Co³⁺/Co⁴⁺ oxidation process. The whole process is described by the following reactions:^[70,71]



The H-NCO-7.5 catalyst exhibits the highest oxidation current during the anodic sweep, indicating that more Co²⁺ and Ni²⁺ sites are presented at the

surface of NiCo₂O₄ after H₂/Ar plasma treatment (Figure 5i)). This result also confirms that the largest amount of oxygen vacancies is generated at the H-NCO7.5 surface, corresponding to the previous characterizations. Previous works have revealed that the Co²⁺ and Ni²⁺ sites were oxidized to CoOOH and NiOOH as the active sites for oxygen electrocatalysis.^[45,70-75] On the other hand, the cathodic sweep from 1.6 to 1.1 V also exhibits a broad peak (C₁) at ≈1.44 V and a small peak (C₂) at ≈1.18 V, which are identified as the reduction of Co⁴⁺ to Co³⁺ and M³⁺ to M²⁺, respectively. It is clearly shown in Figure S17 (Supporting Information) that the C₂ peak for M³⁺ to M²⁺ is negligible, and meanwhile, the A₁ peak for M²⁺ to M³⁺ in the second and followed CV curves are much lower than that in the first CV curves, suggesting that the pre-oxidation of M²⁺ to M³⁺ in the first anodic sweep is an irreversible reaction, which provides a stable catalytic surface for the oxygen electrocatalysis. Therefore, after H₂/Ar plasma treatment, NiCo₂O₄ nanowires with abundant Co²⁺ and Ni²⁺ sites exhibit excellent electrocatalytic performances for ORR and OER owing to the more available active sites and stable catalytic surfaces, corresponding to the ECSA and SEM results.

Based on the above characterizations and electrochemical analyses, the excellent bifunctional electrocatalytic performance of the H-NCO-7.5 catalyst arises from the factors as follows: 1) The 3D hedgehog-like structure provides a large surface area and optimal mass-transfer channels for the surface electrocatalysis. 2) Abundant active sites for ORR and OER are produced by plasma treatment. 3) The modest content of oxygen vacancies increased the electrical conductivity and the intrinsic activity of NiCo₂O₄.

Inspired by their excellent bifunctional performance for ORR and OER, NiCo₂O₄ catalysts before and after plasma treatment were directly used in the air cathode and assembled into rechargeable ZABs with liquid electrolyte (Figure 6a). For comparison, a commercial Pt/C + RuO₂ (1 mg cm⁻², 1:1) catalyst coated on CP was employed as the reference. Figure 6b shows the charging/discharging polarization curves of the samples, where the battery based on the H-NCO-7.5 catalyst exhibits a smaller gap voltage than that of the NCO catalyst. Notably, the charging potential of the H-NCO-7.5 cathode is even lower than that of the Pt/C + RuO₂ cathode, corresponding to the OER results. In Figure 6c, the H-NCO-7.5-based battery presents a maximum peak power density of 54 mW cm⁻², which is higher than that of the NCO one (46 mW cm⁻²) and close to the Pt/C + RuO₂ one (71 mW cm⁻²). Moreover, the H-NCO-7.5-based battery presents voltage plateaus of 1.18, 1.10, 1.04, and 0.98 V at the current density of 2, 5, 10, and 20 mA cm⁻², respectively, which are clearly higher than that of the NCO-based battery (Figure 6d). The rechargeability of the batteries was evaluated at a constant current density of 5 mA cm⁻² with 20 min per cycle. As shown in Figure 6e, the battery with the H-NCO-7.5 catalyst delivers charging and discharging potential of 1.94 and 1.10 V, respectively, at the first cycle with a small gap voltage of 0.84 V and conversion efficiency of 57%, better than the battery with the NCO catalyst (0.87 V and 55%) and close to the battery with the Pt/C + RuO₂

5 "Plasma-engineering of oxygen vacancies on NiCo₂O₄ nanowires with enhanced bifunctional electrocatalytic performance for rechargeable zinc-air battery"

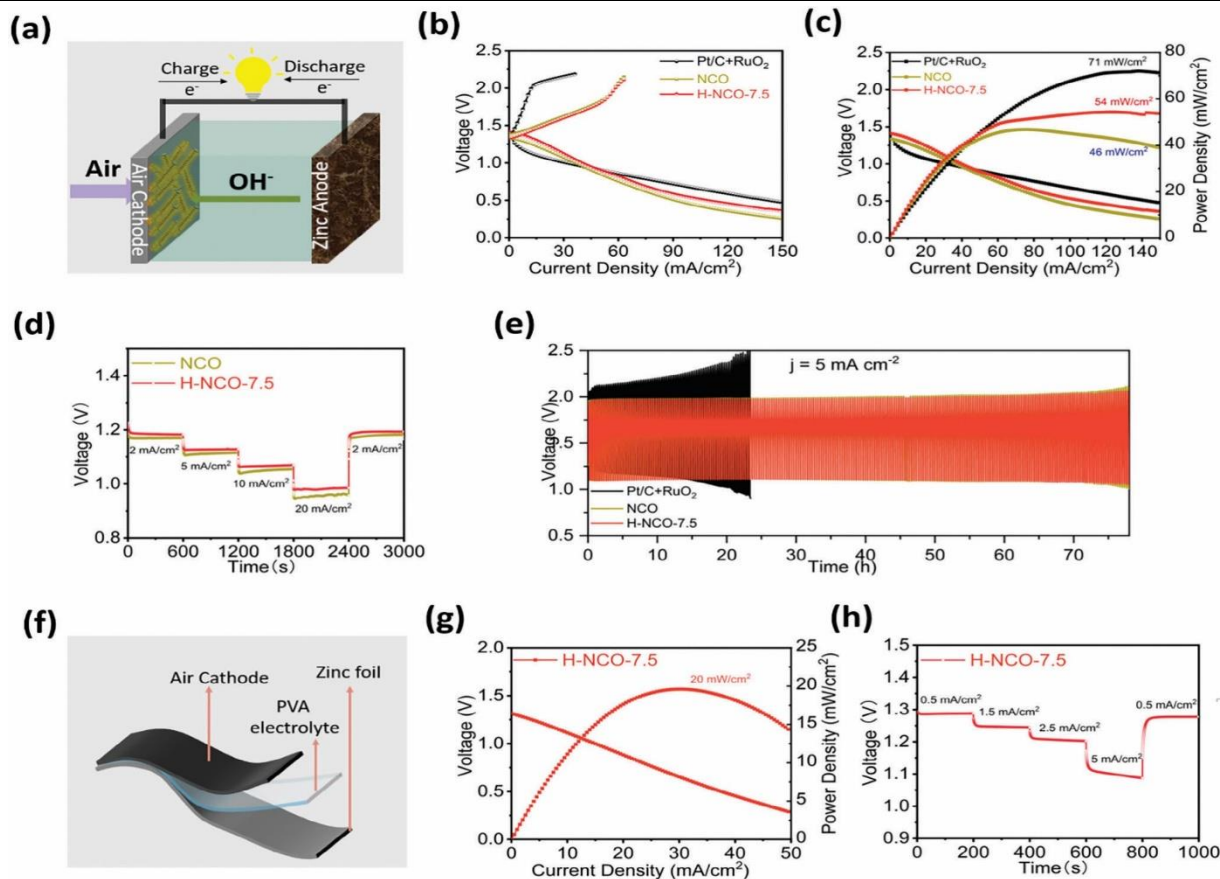


Figure 6. a) Schematic diagram, b) charging-discharging polarization curves, c) power density and discharging curves, d) galvanostatic discharge test at different current densities, and e) galvanostatic charging-discharging cycling test of the zinc-air battery with liquid electrolyte. f) Schematic diagram, g) power density and discharging curves, h) galvanostatic discharge test at different current densities of the zinc-air battery with a solid electrolyte.

catalyst (0.80 V and 61%). Remarkably, the batteries with NiCo₂O₄-based catalysts show negligible potential attenuation after 75 h cycling test, while the battery with Pt/C + RuO₂ only worked for 23 h. Combined, these results confirm that H₂/Ar plasma treatment can be used to enhance the bifunctional catalytic activity of NiCo₂O₄ as a high-performance air cathode in rechargeable ZABs.

The H-NCO-7.5 catalyst was also assembled into solid-state ZABs with PVA gel electrolyte (Figure 6f). As shown in Figure S18a (Supporting Information) and Figure 6g, the prepared battery presents superior charging and discharging potentials and a maximum peak power density of 20 mW cm⁻². Moreover, it also exhibits voltage plateaus of 1.28, 1.24, 1.20, and 1.09 V at the current density of 0.5, 1.5, 2.5, 5 mA cm⁻², respectively. Notably, when the current density recovered from 5 to 0.5 mA cm⁻², the discharging potential could also recover back to 1.27 V, indicating the excellent reversibility of the battery (Figure 6h). Figure S18b (Supporting Information) shows the stability of the battery in a charging-discharging cycling test at the current density of 1 mA cm⁻², where the H-NCO-7.5-based solid-state battery has a stable performance for at least 7 h.

3. Conclusion

In this work, low-pressure H₂/Ar plasma treatment was used to modify hydrothermally grown NiCo₂O₄ nanowires catalyst generating material with abundant oxygen vacancies and superior properties as an efficient and durable bifunctional electrocatalyst for rechargeable ZABs. Compared to pure Ar plasma treatment, H₂/Ar plasma was more effective in reducing the chemical states of the metals and generating oxygen vacancies at the catalyst surface, thus modulating the electronic structure and increasing the surface conductivity of NiCo₂O₄ nanowires. Compared to other NiCo₂O₄-based catalysts, the NiCo₂O₄ nanowires after H₂/Ar plasma treatment for 7.5 min presented the best electrocatalytic performance for ORR and OER. The longer treatment times led to deterioration of the catalyst performance demonstrating that the treatment time has to be carefully selected. The H-NCO-7.5 catalyst was directly used as the air cathode in the rechargeable ZABs with superior stability better than the Pt/C + RuO₂-based battery and its performance was also tested in rechargeable ZABs with solid-state electrolyte. This work provides clear evidence that H₂/Ar plasma treatment is an efficient approach for introducing oxygen vacancies to the TMOs surfaces, and that the research of plasma interaction with these materials is

5 “Plasma-engineering of oxygen vacancies on NiCo₂O₄ nanowires with enhanced bifunctional electrocatalytic performance for rechargeable zinc-air battery”

opening a new avenue to design efficient bifunctional electrocatalysts for rechargeable ZABs.

Experimental Section

Materials: Carbon paper (CP, GDL 28AA) was purchased from SGL Carbon, Germany. The chemicals of Ni(NO₃)₂·6H₂O (98%), Co(NO₃)₂·6H₂O (98%), CO(NH₂)₂ (98%), NH₄F (98%), Zn(CH₃CO₂)₂ (99.99%), KOH(85%), nitric acid(70%), and Nafion 1100EW (5 wt.%) were obtained from Sigma–Aldrich and all of them were used in this work without further purification. H₂ gas (99.999%) was produced by Messer Schweiz AG and Ar gas (99.999%) was purchased from Air Liquid.

Synthesis of NiCo₂O₄ Nanowires on Carbon Paper: NiCo₂O₄ nanowires were synthesized following the method presented in previous work.^[45] First, CP was immersed in the nitric acid at 95 °C for 3 h, then washed with deionized water and dried at 60 °C overnight. Next, NiCo₂O₄ nanowires were grown on the pretreated CP by the hydrothermal method and the followed annealing process. In brief, Ni(NO₃)₂·6H₂O (1 mmol), Co(NO₃)₂·6H₂O (2 mmol), urea (6 mmol), and NH₄F (2 mmol) were dissolved into 12 mL deionized water and stirred for 30 min. The well-mixed solution was poured into a 50 mL Teflon-lined stainless autoclave and one piece of pretreated CP was then vertically immersed into the solution. Afterward, the autoclave was sealed carefully and put into an electric oven at 120 °C for 12 h. After fully cooling down to room temperature, the sample was taken out, rinsed with deionized water several times, dried at 60 °C overnight, and finally annealed at 350 °C in the air for 3 h. The pristine NiCo₂O₄ catalyst on carbon paper was named NCO in this work.

Plasma Treatment: The NCO sample was transferred into a glass tube reactor for plasma treatment. Before treatment, the glass tube chamber (inner diameter 36 mm) was pumped to a base pressure of 5×10^{-3} Pa and then a working gas was injected at 40 sccm controlled by mass flow controllers. The discharge source was an RF power supply (27.12 MHz) that was applied to two ring electrodes separated by 44 mm. The generator power was 200 W and the working pressure was maintained at 20 Pa. An electrically isolated substrate holder for floating potential was positioned between the electrodes in the active plasma zone. The NiCo₂O₄ nanowires with abundant oxygen vacancies were prepared by plasma treatments under two gas sources (pure Ar and H₂/Ar(1:1)) and various treatment durations (0, 2.5, 5, 7.5, 10, 12.5 min). The final samples after Ar and H₂/Ar plasma treatment were named Ar-NCO-X and H-NCO-X (X indicates the treatment time), respectively.

Characterization: The plasma spectra generated by pure Ar gas and H₂/Ar gas were measured by optical emission spectroscopy (OES, Ocean Optics

HR4000CG-UV-NIR). The X-ray diffraction (XRD) patterns were recorded by a Stoe Stadi P diffractometer with Mo K α radiation ($\lambda = 0.7093$ Å). The scanning electron microscopy (SEM) images were measured by a Zeiss Ultra 55 Plus electron microscope. The transmission electron microscope (TEM) images, selected-area electron diffraction (SAED) patterns, and energy-dispersive X-ray spectroscopy (EDS) results were obtained by applying Tecnai F30 G² STwin and JEOL JEM-ARM200F microscopes. The X-ray photoelectron spectroscopy (XPS) results were obtained from an XPS UHV system from PREVAC Sp. z o. o. (Al-anode, 300 W) and the final data were corrected with C 1s at 284.8 eV. The electronic structure of the samples was characterized by Raman spectroscopy (532 nm, alpha 300 RA). The Brunauer–Emmet–Teller results were tested by a BELSORP-max device (Microtrac Retsch GmbH).

Electrochemical Measurement: The electrocatalytic performances of the samples for OER and ORR were performed by the electrochemical workstation (Wave Driver 200, Pine Research) with a three-electrode system. A Pt wire, an Ag/AgCl (3 m KCl) electrode, and 1 m KOH were used as the counter electrode, the reference electrode, and the electrolyte, respectively. All obtained potentials (vs Ag/AgCl) were finally converted to the potentials of reversible hydrogen electrode (vs RHE) using the Nernst equation ($E_{\text{RHE}} = E_{\text{Ag/AgCl}} + 0.059 \text{ pH} + 0.197$). All cyclic voltammetry (CV) and linear sweep voltammetry (LSV) curves in this work were shown after the iR compensation.

For the ORR test, the polished glassy carbon electrode (GCE, ϕ 6 mm) doped with the catalyst ink was used as the working electrode. To prepare the catalyst ink, the catalyst powder (5 mg) was carefully scraped off from the carbon paper, and then mixed with Nafion solution (40 μ L) and Isopropanol (1 mL). After sonicated for 30 min, the catalyst ink became homogeneous and 12 μ L of the ink was dropped onto the GCE surface. The loading amount of the catalyst was maintained at 0.2 mg cm⁻². First, CV scans were performed for 60 cycles to stabilize the electrocatalytic performance of the samples and then measured in nitrogen-saturated and oxygen-saturated electrolytes from 1.2 to 0.2 V (vs RHE) at a scan rate of 100 mV s⁻¹ and a rotation rate of 1600 rpm. Subsequently, LSV curves were recorded from 1.2 to 0.2 V (vs RHE) at a scan rate of 5 mV s⁻¹ and a rotation rate of 1600 rpm. Electrochemical impedance spectroscopy (EIS) results were recorded at 0 V versus Ag/AgCl from 100 kHz to 1 Hz. To calculate the electron transfer numbers (n) during the ORR process, LSV curves were also collected from 1.2 to 0.2 V (vs RHE) at a scan rate of 5 mV s⁻¹ and different rotation rates from 400 to 2500 rpm by the Koutecky–Levich (K–L) equation (described in Supporting Information). The chronoamperometric test was used to evaluate the ORR stability of the catalysts at –0.4 V versus Ag/AgCl.

For the OER test, the as-prepared catalysts (1 cm \times 1 cm) were directly

5 “Plasma-engineering of oxygen vacancies on NiCo₂O₄ nanowires with enhanced bifunctional electrocatalytic performance for rechargeable zinc-air battery”

used as the working electrode. First, CV scans were performed for 60 cycles from 1.2 to 1.8 V (vs RHE) at a scan rate of 100 mV s⁻¹ to stabilize the electrocatalytic performance of the samples. Subsequently, LSV curves were recorded from 1.2 to 1.8 V (vs RHE) at a scan rate of 5 mV s⁻¹. The Chrono potentiometric test was used to evaluate the OER stability of the catalysts under 10 mA cm⁻². The electrochemical surface area (ECSA) was calculated by the equation: $ECSA = C_{dl}/C_s$, where C_{dl} was the electrochemical double-layer capacitance calculated from the CV curves from 1.03 to 1.13 V (vs RHE) at different scan rates and C_s is the specific capacitance of the transition-metal-based catalysts of 0.04 mF cm⁻². In order to understand the OER process, more detailed CV curves were also recorded for the first 5 cycles from 1.0 to 1.5 V (vs RHE) at a scan rate of 10 mV s⁻¹ without the stabilization process. After that, a series of CV curves were also collected from 1.0 to 1.8 V (vs RHE) at different scan rates of 2–30 mV s⁻¹.

Battery Test: For aqueous rechargeable ZAB, a polished Zn plate and a mixed solution of 6 m KOH and 0.2 m Zn(Ac)₂ were employed as the anode and the electrolyte, respectively. The air cathode was a sandwich structure with the order of an as-prepared sample, a waterproof layer, and a current collector. The performance of these batteries was evaluated by an electrochemical workstation (Wave Driver 200, Pine Research), and the stability was tested by a LAND battery tester.

For solid-state rechargeable ZABs, the PVA-gel electrolyte was prepared following the method presented in our previous work⁴⁵. The as-prepared sample and a Zn plate were cut to 1 cm × 2 cm as the cathode and the anode, respectively, and then fixed on the two sides of the gel electrolyte. The sandwich cell was sealed, and a hole was created at the cathode side as the channel for the air. The battery measurement procedure of solid-state ZABs was the same as that of aqueous ZABs.

Supporting Information

Supporting Information is available from the Wiley Online Library or from the author.

Acknowledgements

H.L. thanks the China Scholarship Council (CSC) for the support through the project 202009110110. The authors also thank Prof. Dr. Rainer Adelung at Kiel University for the assistance with Raman spectrum measurement.

Open access funding enabled and organized by Projekt DEAL.

Conflict of Interest

The authors declare no conflict of interest.

Data Availability Statement

The data that support the findings of this study are available on request from the corresponding author. The data are not publicly available due to privacy or ethical restrictions.

Keywords

bifunctional electrocatalysts, H₂/Ar plasma, NiCo₂O₄ nanowires, oxygen vacancies, rechargeable zinc-air battery

Received: November 21, 2023

Revised: December 17, 2023

Published online:

- [1] C. Zhong, B. Liu, J. Ding, X. Liu, Y. Zhong, Y. Li, C. Sun, X. Han, Y. Deng, N. Zhao, W. Hu, *Nat. Energy* **2020**, *5*, 440.
- [2] Y. Sun, X. Liu, Y. Jiang, J. Li, J. Ding, W. Hu, C. Zhong, *J. Mater. Chem. A* **2019**, *7*, 18183.
- [3] J. Lai, Y. Xing, N. Chen, L. Li, F. Wu, R. Chen, *Angew. Chem., Int. Ed.* **2019**, *59*, 2974.
- [4] L. Peng, L. Shang, T. Zhang, G. I. N. Waterhouse, *Adv. Energy Mater.* **2020**, *10*, 2003018.
- [5] Y. Hao, F. Hu, Y. Chen, Y. Wang, J. Xue, S. Yang, S. Peng, *Adv. Fiber Mater.* **2022**, *4*, 185.
- [6] M. Luo, W. Sun, B. B. Xu, H. Pan, Y. Jiang, *Adv. Energy Mater.* **2021**, *11*, 2002762.
- [7] W. Sun, F. Wang, B. Zhang, M. Zhang, V. Küpers, X. Ji, C. Theile, P. Bieker, K. Xu, C. Wang, M. Winter, *Science* **2021**, *371*, 46.
- [8] R. Khezri, S. Rezaei Motlagh, M. Etesami, A. A. Mohamad, F. Mahlendorf, A. Somwangthanaroj, S. Kheawhom, *Chem. Eng. J.* **2022**, *449*, 137796.
- [9] S. Lee, J. Choi, M. Kim, J. Park, M. Park, J. Cho, *Chem. Sci.* **2022**, *13*, 6159.
- [10] N. Batool, N. Ahmad, J. Liu, X.-F. Han, T.-H. Zhang, W.-T. Wang, R. Yang, J.-H. Tian, *Mater. Chem. Front.* **2021**, *5*, 2950.
- [11] J. Song, Y. Chen, H. Huang, J. Wang, S.-C. Huang, Y.-F. Liao, A. E. Fetohi, F. Hu, H.-Y. Chen, L. Li, X. Han, K. M. El-Khatib, S. Peng, *Adv. Sci.* **2022**, *9*, 2104522.
- [12] J. Song, S. Qiu, F. Hu, Y. Ding, S. Han, L. Li, H.-Y. Chen, X. Han, C. Sun, S. Peng, *Adv. Funct. Mater.* **2021**, *31*, 2100618.
- [13] T. Reier, M. Oezaslan, P. Strasser, *ACS Catal.* **2012**, *2*, 1765.

5 "Plasma-engineering of oxygen vacancies on NiCo₂O₄ nanowires with enhanced bifunctional electrocatalytic performance for rechargeable zinc-air battery"

- [14] S. Sui, X. Wang, X. Zhou, Y. Su, S. Riffat, C.-J. Liu, *J. Mater. Chem. A* **2017**, *5*, 1808.
- [15] J. Pan, X. L. Tian, S. Zaman, Z. Dong, H. Liu, H. S. Park, B. Y. Xia, *Batteries Supercaps* **2019**, *2*, 336.
- [16] M. Mechili, C. Vaitsis, N. Argirusis, P. K. Pandis, G. Sourkouni, C. Argirusis, *Renew. Sust. Energ. Rev.* **2022**, *156*, 111970.
- [17] Y. Wang, Z. Liang, H. Zheng, R. Cao, *Chem. Asian J.* **2020**, *15*, 3717.
- [18] J. Zheng, X. Peng, Z. Wang, *Phys. Chem. Chem. Phys.* **2021**, *23*, 6591.
- [19] R. D. Zhao, D. Cui, J. Q. Dai, J. Xiang, F. F. Wu, *Sustain. Mater. Techno.* **2020**, *24*, e00151.
- [20] P. Zhang, S. Xie, P. Deng, S. Huang, Y. Li, Z. Liu, Y.-J. Wang, X. Lu, *J. Mater. Res.* **2022**, *37*, 2185.
- [21] K.-L. Bao, J.-Y. Xu, N.-F. Yu, J.-B. Kuang, Z.-T. Yang, H. Chen, J.-L. Ye, Y.-P. Wu, *Energy Fuels* **2022**, *36*, 6542.
- [22] H. Huang, A. Huang, D. Liu, W. Han, C.-H. Kuo, H.-Y. Chen, L. Li, H. Pan, S. Peng, *Adv. Mater.* **2023**, *35*, 2303109.
- [23] Y. Tian, X. Liu, L. Xu, D. Yuan, Y. Dou, J. Qiu, H. Li, J. Ma, Y. Wang, D. Su, S. Zhang, *Adv. Funct. Mater.* **2021**, *31*, 2101239.
- [24] J. Bao, X. Zhang, B. Fan, J. Zhang, M. Zhou, W. Yang, X. Hu, H. Wang, B. Pan, Y. Xie, *Angew. Chem., Int. Ed.* **2015**, *54*, 7399.
- [25] Y. Zhu, X. Zhong, S. Jin, H. Chen, Z. He, Q. Liu, Y. Chen, *J. Mater. Chem. A* **2020**, *8*, 10957.
- [26] Z. Xiao, Y. Wang, Y.-C. Huang, Z. Wei, C.-L. Dong, J. Ma, S. Shen, Y. Li, S. Wang, *Energy Environ. Sci.* **2017**, *10*, 2563.
- [27] K. Zhu, F. Shi, X. Zhu, W. Yang, *Nano Energy* **2020**, *73*, 104761.
- [28] Y. Zhao, C. Chang, F. Teng, Y. Zhao, G. Chen, R. Shi, G. I. N. Waterhouse, W. Huang, T. Zhang, *Adv. Energy Mater.* **2017**, *7*, 1700005. [29] S. Peng, F. Gong, L. Li, D. Yu, D. Ji, T. Zhang, Z. Hu, Z. Zhang, S. Chou, Y. Du, S. Ramakrishna, *J. Am. Chem. Soc.* **2018**, *140*, 13644.
- [30] X.-Q. Zhang, J.-B. Chen, C.-W. Wang, A.-Z. Liao, X.-F. Su, *Nanotechnology* **2015**, *26*, 175705.
- [31] Z. He, R. Zhao, X. Chen, H. Chen, Y. Zhu, H. Su, S. Huang, J. Xue, J. Dai, S. Cheng, M. Liu, X. Wang, Y. Chen, *ACS Appl. Mater. Interfaces* **2018**, *10*, 42524.
- [32] L. Chen, Y. Zhang, D. Li, Y. Wang, C. Duan, *J. Mater. Chem. A* **2018**, *6*, 18378.
- [33] R. Liu, Y. Wang, D. Liu, Y. Zou, S. Wang, *Adv. Mater.* **2017**, *29*, 1701546.
- [34] L. Xu, Q. Jiang, Z. Xiao, X. Li, J. Huo, S. Wang, L. Dai, *Angew. Chem., Int. Ed.* **2016**, *55*, 5277.
- [35] S. Duo, L. Tao, R. L. Wang, S. E. Hankari, R. Chen, S. Y. Wang, *Adv. Mater.* **2018**, *30*, 1705850.
- [36] N. Kohlmann, L. Hansen, C. Lupan, U. Schürmann, A. Reimers, F. Schütt, R. Adelung, H. Kersten, L. Kienle, *ACS Appl. Mater. Interfaces* **2021**, *13*, 61758.
- [37] A. Badreldin, A. E. Abusrafa, A. Abdel-Wahab, *ChemSusChem* **2021**, *14*, 10.
- [38] Y.-B. Li, Y.-P. Liu, J. Wang, Y.-L. Guo, K. Chu, *Inorg. Chem. Front.* **2020**, *7*, 455.
- [39] Z. Li, X. Liu, M. Zhou, S. Zhang, S. Cao, G. Lei, C. Lou, J. Zhang, *J. Hazard. Mater.* **2021**, *415*, 125757.
- [40] D. Xiao, Q. Ruan, D.-L. Bao, Y. Luo, C. Huang, S. Tang, J. Shen, C. Cheng, P. K. Chu, *Small* **2020**, *16*, 2001470.
- [41] J. Li, C. Chen, J. Wei, J. Li, X. Wang, *J. Phys. Chem. C* **2014**, *118*, 28440.
- [42] Z. Wang, Y. Xia, L. Liu, A. Wang, Y. Zhang, X. Liu, *Energy Fuels* **2020**, *34*, 13111.
- [43] L. Huang, D. Chen, Y. Ding, S. Feng, Z. L. Wang, M. Liu, *Nano Lett.* **2013**, *13*, 3135.
- [44] Y. Liu, X. Chi, Q. Han, Y. Du, J. Yang, Y. Liu, *J. Alloy Compd.* **2019**, *772*, 693.
- [45] H. Li, S. Askari, J. Wang, N. Wolff, M. Behrens, L. Kienle, J. Benedikt, *Int. J. Hydrogen Energy* **2023**, *48*, 26107.
- [46] C. Liu, P. Zuo, Y. Jin, X. Zong, D. Li, Y. Xiong, *J. Power Sources* **2020**, *473*, 228604.
- [47] Y.-Z. Jin, Z. Li, J.-Q. Wang, R. Li, Z.-Q. Li, H. Liu, J. Mao, C.-K. Dong, J. Yang, S.-Z. Qiao, X.-W. Du, *Adv. Energy Mater.* **2018**, *8*, 1703469.
- [48] P. Dubey, N. Kaurav, R. S. Devan, G. S. Okram, Y. K. Kuo, *RSC Adv.* **2018**, *8*, 5882.
- [49] Y.-T. Liu, D.-D. Han, L. Wang, G.-R. Li, S. Liu, X.-P. Gao, *Adv. Energy Mater.* **2019**, *9*, 1803477.
- [50] Z. Li, P. Li, X. Meng, Z. Lin, R. Wang, *Adv. Mater.* **2021**, *33*, 2102338.
- [51] Q. Huang, J. Zhang, Z. He, P. Shi, X. Qin, W. Yao, *Chem. Eng. J.* **2017**, *313*, 1088.
- [52] S. Chen, D. Huang, D. Liu, H. Sun, W. Yan, J. Wang, M. Dong, X. Tong, W. Fan, *Appl. Catal. B* **2021**, *291*, 120065.
- [53] Z. Wang, R. Lin, Y. Huo, H. Li, L. Wang, *Adv. Funct. Mater.* **2022**, *32*, 2109503.
- [54] S. Chen, H. Wang, Z. Kang, S. Jin, X. Zhang, X. Zheng, Z. Qi, J. Zhu, B. Pan, Y. Xie, *Nat. Commun.* **2019**, *10*, 788.
- [55] X. Xiao, X. Zhang, Z. Zhang, J. You, S. Liu, Y. Wang, *Microchim. Acta* **2020**, *187*, 64.
- [56] H. Wang, D. Yong, S. Chen, S. Jiang, X. Zhang, W. Shao, Q. Zhang, W. Yan, B. Pan, Y. Xie, *J. Am. Chem. Soc.* **2018**, *140*, 1760. [57] A. Jorio, R. Saito, *J. Appl. Phys.* **2021**, *129*, 021102.

- [58] Q. Chang, H. Liang, B. Shi, X. Li, Y. Zhang, L. Zhang, H. Wu, *J. Colloid Interf. Sci.* **2021**, *588*, 336.
- [59] B. Wei, J. Wu, G. Mei, Z. Qi, W. Hu, Z. Wang, *Int. J. Hydrogen Energy* **2019**, *44*, 6612.
- [60] S. V. Avtaeva, T. M. Lapochkina, *Plasma Phys. Rep.* **2007**, *33*, 774.
- [61] E. J. D. Mahoney, S. Mushtaq, M. N. R. Ashfold, Y. A. Mankelevich, *J. Phys. Chem. A* **2019**, *123*, 2544.
- [62] C. Schulze, H. Li, L. Mohn, M. Müller, J. Benedikt, *Plasma* **2022**, *5*, 295.
- [63] C. Schulze, Z. Donkó, J. Benedikt, *Plasma Sources Sci. Technol.* **2022**, *31*, 105017.
- [64] L. Mangolini, U. Kortshagen, *Phys. Rev. E* **2009**, *79*, 026405.
- [65] D. B. Sepa, M. V. Vojnovic, A. Damjanovic, *Electrochim. Acta* **1981**, *26*, 781.
- [66] L. Peng, L. Shang, T. Zhang, G. I. N. Waterhouse, *Adv. Energy Mater.* **2020**, *10*, 2003018.
- [67] J. Wang, L. Gan, W. Zhang, Y. Peng, H. Yu, Q. Yan, X. Xia, X. Wang, *Sci. Adv.* **2018**, *4*, eaap7970.
- [68] T. Zhao, X. Shen, Y. Wang, R. K. Hocking, Y. Li, C. Rong, K. Dastafkan, Z. Su, C. Zhao, *Adv. Funct. Mater.* **2021**, *31*, 2100614.
- [69] E. Laviron, *J. Electroanal. Chem.* **1979**, *100*, 263.
- [70] J. Seong, A. M. Patil, S. B. Roy, J. Lee, S. C. Jun, *Int. J. Energy Res.* **2022**, *46*, 24501.
- [71] D. Yan, W. Wang, X. Luo, C. Chen, Y. Zeng, Z. Zhu, *Chem. Eng. J.* **2018**, *334*, 864.
- [72] W. Xiang, N. Yang, X. Li, J. Linnemann, U. Hagemann, O. Ruediger, M. Heidelmann, T. Falk, M. Aramini, S. Debeer, M. Muhler, K. Tschulik, T. Li, *Nat. Commun.* **2022**, *13*, 179.
- [73] J. Kwon, H. Han, S. Jo, S. Choi, K. Y. Chung, G. Ali, K. Park, U. Paik, T. Song, *Adv. Energy Mater.* **2021**, *11*, 2100624.
- [74] A. Karmakar, K. Karthick, S. Kumaravel, S. S. Sankar, S. Kundu, *Inorg. Chem.* **2021**, *60*, 2023.
- [75] Q. Wang, Y. Luo, R. Hou, S. Zaman, K. Qi, H. Liu, H. S. Park, B. Y. Xia, *Adv. Mater.* **2019**, *31*, 1905744.

但愿人长久，千里共婵娟。

-----苏轼

So let us wish that man will live long as he can!

Though miles apart, we'll share the beauty she displays.

----- Shi Su (Translated by Yuanhong Xu)

6

Plasma-engineering of Pt-decorated NiCo₂O₄ nanowires with rich oxygen vacancies for enhanced oxygen electrocatalysis and zinc-air battery performance

Platinum-based materials now remain the most efficient catalysts for the ORR process. However, the commercial Pt/C catalyst presents high cost, poor OER catalytic activity and insufficient stability. Anchoring Pt particles on conductive supports is a facile

and effective approach to preparing highly active and low-cost Pt-based catalysts. Previous works have demonstrated that NiCo₂O₄ nanowires coated on carbon paper could be a promising support material for Pt-based ORR catalysts due to their large surface area and high stability. In this work, a high-efficiency bifunctional low-Pt catalyst was developed. The NiCo₂O₄ nanowires were firstly modified by Ar plasma treatment to generate oxygen vacancies at their surfaces and simultaneously increase their specific surface area. The high-dispersed Pt nanoparticles were coated on the nanowire surfaces by an impregnation-plasma reduction process. The prepared composite catalyst shows excellent OER and ORR electrocatalytic performance under alkaline conditions.

Prof. Dr. Jan Benedikt designed the underlying concept, provided experimental funding and reviewed the manuscript. The author of this thesis carried out the experiments and prepared the first draft. Other authors helped with the material characterization and reviewed the manuscript.

Plasma-engineering of Pt-decorated NiCo₂O₄ nanowires with rich oxygen vacancies for enhanced oxygen electrocatalysis and zinc-air battery performance

He Li¹, Luka Hansen^{1,2}, Ainura Aliyeva³, Jihao Wang⁴, Haoyi Qiu⁵, Martin Müller⁶, Cenk Aktas³,
Lorenz Kienle^{2,6}, Jan Benedikt^{1,2*}

¹ Institute of Experimental and Applied Physics, Kiel University, Leibnizstraße 19, D-24098 Kiel, Germany

² Kiel Nano, Surface and Interface Science KiNSIS, Kiel University, Christian-Albrechts-Platz 4, D-24118 Kiel, Germany

³ Chair for Multicomponent Materials, Department of Materials Science, Faculty of Engineering, Kiel University, Kaiserstraße 2, D-24143 Kiel, Germany

⁴ Institute of Inorganic Chemistry, Kiel University, Max-Eyth-Straße 2, D-24118 Kiel, Germany

⁵ Chair for Functional Nanomaterials, Department of Materials Science, Faculty of Engineering, Kiel University, Kaiserstraße 2, D-24143 Kiel, Germany

⁶ Chair for Synthesis and Real Structure, Department of Materials Science, Faculty of Engineering, Kiel University, Kaiserstraße 2, D-24143 Kiel, Germany

*Corresponding author.

Abstract:

A low-cost and efficient bifunctional catalyst is urgently required to achieve high-performance rechargeable zinc-air batteries. In this study, we report a composite material comprising Pt-decorated NiCo₂O₄ nanowires enriched with abundant oxygen vacancies, designed as a highly efficient bifunctional electrocatalyst for both the oxygen evolution reaction and the oxygen reduction reaction. The introduction of Pt atoms and oxygen vacancies onto the NiCo₂O₄ nanowires was achieved with the assistance of plasma treatment. This approach led to the resulting catalyst benefiting from the presence of a higher number of active sites and increased surface conductivity and exhibiting significantly improved electrocatalytic activity compared to the pristine NiCo₂O₄ nanowires. Moreover, the zinc-air battery based on this composite catalyst exhibits a narrower charge/discharge voltage gap and superior stability when compared to batteries employing commercial noble-metal-based catalysts. This work provides a rational strategy for the construction of high-active and cost-effective Pt-based electrocatalysts.

Keyword: Plasma engineering, NiCo₂O₄ nanowires, oxygen vacancies, Pt atoms, bifunctional electrocatalysts, rechargeable zinc-air battery

Introduction:

The ever-increasing energy crisis and related environmental concerns are driving the development of efficient energy conversion and storage systems [1-5]. Among these novel technologies, rechargeable zinc-air batteries (RZABs) have attracted considerable attention due to their low cost, inherent safety and large theoretical energy density [6-9]. However, the practical performance of RZABs remains unsatisfactory due to the sluggish kinetics of the oxygen reduction reaction (ORR) during the discharge process and the oxygen evolution reaction during the charge process [10-11]. Although noble-metal-based catalysts, such as Pt/C, Ir/C and RuO₂, exhibit excellent catalytic activities for these oxygen-related reactions, their high costs and inferior stability still hinder them in commercial applications [12-13]. Therefore, it is urgent to explore low-cost and efficient catalysts with outstanding bifunctionality and stability for ORR and OER.

Recently, transition-metal-based materials with unique electronic properties have been regarded as promising candidates to replace noble-metal-based catalysts for RZABs [14-16]. Among these, spinel NiCo₂O₄-type catalysts exhibit promising bifunctional catalytic performance, attributed to their rich redox couples and excellent stability [17-19]. In particular, NiCo₂O₄ catalysts with high number of oxygen vacancies present outstanding OER catalytic performance, even surpassing that of the noble-metal-based catalysts [20-21]. However, further improvement is necessary to enhance their unsatisfactory ORR activity. To date, Pt-based materials are still the most efficient catalysts for the ORR process [22-23]. Anchoring Pt onto a conductive substrate is an effective method for reducing the dosage of Pt and enhancing their stability [24-26]. Accordingly, a novel self-supported bifunctional catalyst is designed by combining the excellent OER performance of transition-metal oxides with the outstanding ORR activity of Pt.

Herein, we employed plasma treatment, for the first time, to synthesize Pt-decorated NiCo₂O₄ with rich oxygen vacancies as an efficient bifunctional catalyst in RZABs. Taking spinel-type NiCo₂O₄ nanowires grown on carbon paper (CP) as the pristine catalyst, oxygen vacancies were first generated on the catalyst surfaces by Ar plasma treatment. To improve their ORR activity, Pt atoms were anchored on NiCo₂O₄ nanowires via a novel impregnation-plasma reduction method. Consequently, the

resulting catalyst delivers excellent bifunctional electrocatalytic performance and outstanding stability, even surpassing noble-metal-based catalysts. Moreover, the zinc-air battery assembled with the developed catalyst in the cathode exhibits encouraging charge-discharge potentials and stability.

Results and Discussion:

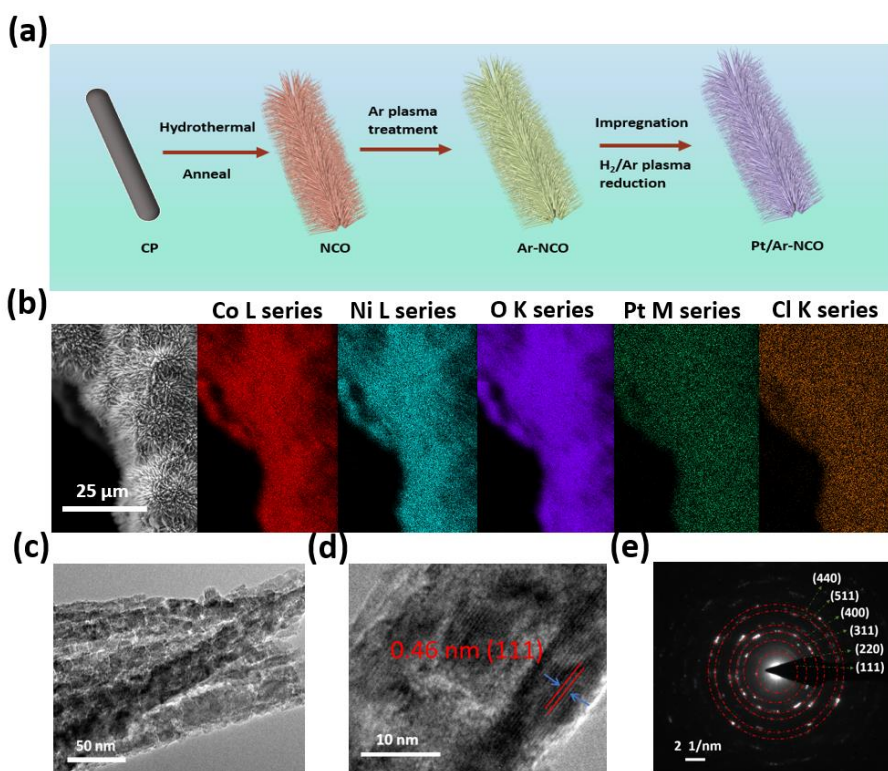


Figure 1. (a) Schematic illustration for the synthesis of the Pt/Ar-NCO catalyst, (b) the elemental mapping by SEM-EDX, (c) TEM image, (d) HRTEM image and (e) SAED pattern of the Pt/Ar-NCO catalyst.

Figure 1(a) provides a schematic illustration of the fabrication process for the Pt/Ar-NCO catalyst. Firstly, NiCo₂O₄ nanowires were directly grown on the commercial CP via the hydrothermal method and an annealing process as described in our previous work (Figure S1(a, b) in SI) [17, 27]. Then, the as-prepared sample was placed in a plasma tube reactor and modified by radio frequency (27.12 MHz) Ar plasma (pressure 20 Pa, power 200 W, duration 7.5 min) to generate abundant oxygen vacancies on the

nanowire surfaces. As shown in Figure S1 (c, d) (SI), the macrostructure of these nanowires was preserved after Ar plasma treatment. Finally, Pt atoms were anchored on these plasma-modified nanowires by an impregnation-plasma reduction method (Figure S1 (g, h) in SI). For comparison, Pt atoms were also anchored on pristine NiCo₂O₄ nanowires without Ar plasma pretreatment via the same steps (Figure S1 (e, f) in SI). It is remarkable that all samples have a similar hedgehog-like nanostructure which offers a large surface area and abundant active sites for the oxygen-related reactions. Moreover, the inner-connected structure that nanowires were directly grown on fibers of carbon papers also provides channels to accelerate charge transfer during the oxygen electrocatalysis process. The scanning electron microscopy-energy dispersive X-ray spectroscopy (SEM-EDS) results confirm the presence of Pt at the nanowire surfaces (Figure S2 in SI). More importantly, the Pt/Ar-NCO sample seems to present a higher Pt content than the Pt/NCO sample owing to the increased surface area of nanowires after Ar plasma treatment which provided more sites to anchor Pt [27]. The uniform distribution of Pt atoms on the NiCo₂O₄ nanowires was also confirmed by the elemental mapping result shown in Figure 1(b). These results are evidence that Pt was successfully deposited on the surface of the NiCo₂O₄ nanowires.

The morphology and microstructure of the samples were further observed by transmission electron microscopy (TEM) measurements. As shown in Figure 1(c) and Figure S3 (SI), the nanowires with a porous microstructure were retained after the Ar plasma treatment and Pt deposition processes. In the high-resolution TEM image of the Pt/Ar-NCO sample (Figure 1d), the nanocrystal with an interplanar d-spacing of 0.46 nm belongs to the (111) plane of NiCo₂O₄. However, no discernible Pt nanoparticles or any additional layer is visible at the nanowire surfaces, indicating that the Pt is highly dispersed on the surface in form of very small clusters, corresponding with the elemental mapping result. The selected-area electron diffraction (SAED) patterns in Figure 2(e) also confirms the successful synthesis of NiCo₂O₄ nanowires. As shown in Figure S4 (SI), the TEM-EDS result performed on a single nanowire also indicates the presence of Pt on NiCo₂O₄ nanowires.

The X-ray photoelectron spectroscopy (XPS) measurements were performed to study the elemental states on the sample surfaces. As shown in Figure S5(a) (SI), Ni,

Co, O and C elements were detected at all sample surfaces. After the Pt deposition process, a new peak corresponding to the Cl element and a tiny peak, close to the detection limit, belonging to the Pt element emerged in the spectra of the Pt/NCO and Pt/Ar-NCO catalysts, suggesting the successful deposition of Pt (Figure S5(b) in SI). In the high-resolution spectra of Pt 4f, the deconvoluted peaks at the binding energies of 71.4 and 74.6 eV ascribed to the metallic Pt⁰ and the peaks at the binding energies of 72.9 and 76.3 eV corresponding to the Pt²⁺ ions (Figure 2(a)) [28-29]. In Figure 2(b), the O 1s spectra exhibit three deconvoluted peaks at 529.8, 531.6 and 533.3 eV, belonging to the metal-O bands (O1), the oxygen species near oxygen vacancies (O2) and the surface hydroxyl oxygen (O3), respectively [27, 30]. The area ratio of the O2/O1 peak is increased on the surface of the Ar-NCO catalyst, indicating the generation of oxygen vacancies after Ar plasma treatment. After Pt deposition, the O2/O1 ratio is further increased owing to the reduction process by the acid and H₂/Ar plasma treatment [27, 31].

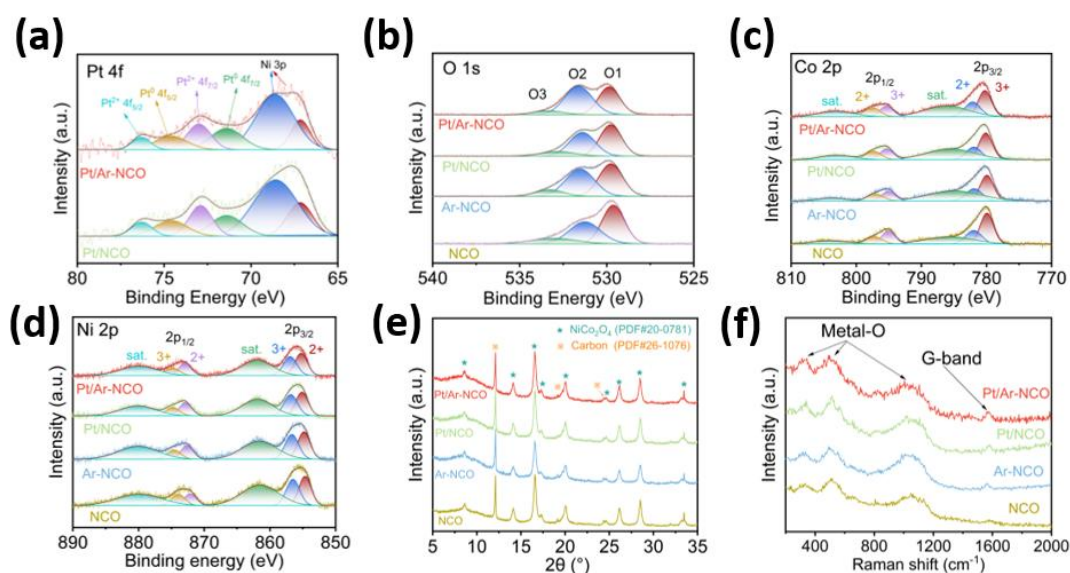


Figure 2. XPS results of the samples and corresponding (a) Pt 4f, (b) O 1s, (c) Co 2p and (d) Ni 2p. (e) XRD patterns, (f) Raman spectra of the samples.

Figure 2(c) shows the high-resolution spectra of Co 2p on sample surfaces. The deconvoluted peaks at 780.1 and 795.2 eV are assigned to Co³⁺ and the peaks at around 782.0 and 797.4 eV belong to Co²⁺, with their satellite peaks at around 786.0 and 803.0 eV [32-33]. Similarly, in Figure 2(d), the Ni 2p spectra can also be deconvoluted into six peaks corresponding to Ni³⁺, Ni²⁺ and satellite peaks, respectively [34-35]. As

shown in Table S1 (SI), the relative atomic ratios of Co²⁺/Co³⁺ and Ni²⁺/Ni³⁺ are increased after Ar plasma and Pt deposition, further indicating the generation of oxygen vacancies on the sample surfaces.

The X-ray diffraction (XRD) patterns in Figure 2(e) show that the as-prepared samples are of the cubic spinel-type structure of NiCo₂O₄ (PDF #20-0781) grown on graphitic carbon support (PDF #26-1076) [36-37]. Raman spectra of the samples also suggest the successful synthesis of NiCo₂O₄ nanowires on carbon materials, as shown in Figure 2(f). The peaks located at around 327, 510 and 1024 cm⁻¹ correspond to the vibrations of metal-O bands in NiCo₂O₄ and the peak at around 1575 cm⁻¹ belongs to the G band of the carbon substrate, respectively [38-40]. In Figure S6 (SI), the metal-O peak in the Pt/Ar-NCO catalyst has obvious red shifted compared to that of the NCO catalyst, further confirming the generation of oxygen vacancies at its surface [41-42]. Because of its low content and high dispersion, no new characteristic intensities corresponding to Pt are detected in either XRD or Raman spectra results.

The ORR performance of the catalysts was investigated in the 1 M KOH electrolyte and the commercial Pt/C powder (20 wt%) was used as the benchmark sample. Figure S7(a) (SI) shows that the Pt/Ar-NCO catalyst exhibits an obvious oxygen reduction peak at 0.69 V in the O₂-saturated electrolyte, indicating its capability for facilitating the ORR process. Moreover, in Figure S7(b) (SI), the reduction peak of the Pt/Ar-NCO catalyst is also the most positive among all the catalysts tested. As shown in Figure 3(a), linear sweep voltammetry (LSV) curves of the catalysts were also measured to evaluate their ORR performance, where the Pt/Ar-NCO catalyst shows the most positive onset potential (E_{onset}) of 0.89 V and half-wave potential ($E_{1/2}$) of 0.78 V, demonstrating its better ORR catalytic ability than the NCO catalyst (0.85 V and 0.74 V), the Ar-NCO catalyst (0.87 V and 0.75 V) and the Pt-NCO catalyst (0.87 V and 0.76 V), closing to the Pt/C catalyst (0.96 V and 0.85 V). In Figure S7(c) (SI), the Pt/Ar-NCO catalyst also presents a low Tafel slope of 125.5 mV dec⁻¹, suggesting its fast ORR kinetics. These results verify the positive effect of Pt atoms on the ORR activity of NiCo₂O₄ nanowires. Based on the Koutecky–Levich equation, the electron transfer number (n) of the Pt/Ar-NCO catalyst during the ORR process was determined by the LSV curves under different rotating rates (Figure S8, SI) [17]. In Figure 3(b), the calculated slop of the Pt/Ar-

NCO catalyst is close to the line of $n = 4$ in the potential range of 0.4-0.6 V, demonstrating its preferred four-electron reduction pathway for ORR.

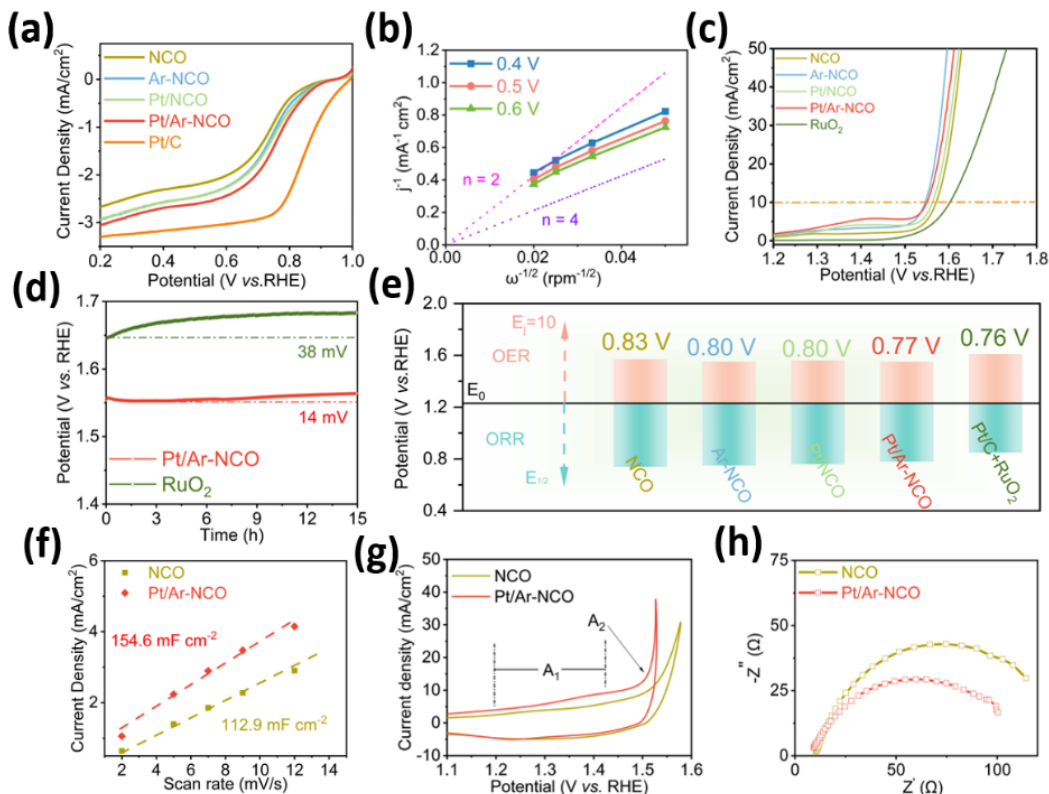


Figure 3. (a) LSV curves of the catalysts for ORR, (b) the electron transfer number of the Pt/Ar-NCO catalyst at different potentials, (c) LSV curves of the catalysts for OER, (d) The stability test of the Pt/Ar-NCO catalyst and the RuO₂ catalyst, (e) Voltage gap of catalysts (ΔE) between the $E_{1/2}$ for ORR and the $E_{j=10}$ for OER, (f) The determination of the corresponding C_{dl} values, (g) the first CV curves, (h) EIS Nyquist plots of NCO and Pt/Ar-NCO catalysts.

The OER electrocatalytic activity of the catalysts was also evaluated by LSV curves from 1.2 to 1.8 V (vs. RHE). As shown in Figure 3(c), the Pt/Ar-NCO catalyst exhibits an excellent OER activity with an overpotential of 321 mV at a current density of 10 mA cm⁻² ($E_{j=10}$), which is better than that of the NCO catalyst (342 mV) and the Pt-NCO catalyst (333 mV), but worse than that of the Ar-NCO catalyst (317 mV). In Figure S9(a) (SI), the Pt/Ar-NCO catalyst also has a small Tafel slope of 83.5 mV dec⁻¹, indicating its fast OER kinetics. The stability of the catalysts was also tested by the chronopotentiometric method at the current density of 10 mA cm⁻², where the Pt/Ar-NCO catalyst presents a negligible increment of 14 mV in potential after 15 h of operation, better than the benchmark RuO₂ catalyst with 38 mV increment (Figure 3(d)). Moreover, in Figure S9(b) (SI), the LSV curve of the Pt/Ar-NCO catalyst after the stability test exhibits only a

negligible shift of 5 mV in $E_{j=10}$, and these nanowires are well preserved, further illustrating its excellent cycling durability (Figure S10 in SI). The bifunctional electrocatalytic performance of the catalysts was evaluated by the voltage gap (ΔE) between the $E_{1/2}$ of ORR and the $E_{j=10}$ of OER. In Figure 3(e), although its OER activity is not the best, the Pt/Ar-NCO catalyst still has the smallest ΔE of 0.77 V, lower than that of other NiCo₂O₄-based catalysts here and close to the Pt/C + RuO₂ catalyst. These results strongly support that the Pt/Ar-NCO catalyst could be a promising candidate to replace noble-metal-based catalysts in RZABs.

To elucidate the reasons behind their enhanced electrocatalytic activity, various electrochemical measurements were conducted to investigate changes in the electrochemical properties of NiCo₂O₄ nanowires after the modification process. Firstly, the electrocatalytic performance of the catalyst is closely linked to the electrochemical surface area (ECSA), which correlates linearly with the double-layer capacitance (C_{dl}). As shown in Figure 3(f) and Figure S11 (SI), the Pt/Ar-NCO catalyst presents a higher C_{dl} of 154.6 mF cm⁻² than the NCO catalyst, indicating that it has more available active sites for oxygen electrocatalysis reactions. Secondly, the curve for the first cyclic voltammetry (CV) cycle is also analyzed to study the surface properties of the catalysts. As shown in Figure 3(g), the broad peak from 1.2 to 1.4 V belongs to the oxidation peak (A_1) of M^{2+}/M^{3+} ($M = Ni$ and Co) and the peak from ~1.5 V is assigned to the oxidation peak (A_2) of M^{3+}/M^{4+} . The Pt/Ar-NCO catalyst exhibits a higher A_1 than the NCO catalyst, indicating that more M^{2+} ions are presented in the Pt/Ar-NCO catalyst, corresponding to the XPS results. These M^{2+} sites in NiCo₂O₄ could be oxidized to MOOH, which are recognized as active sites for oxygen electrocatalysis [17, 30]. However, the degraded OER performance of the Pt/Ar-NCO catalyst with a high ratio of M^{2+}/M^{3+} to that of the Ar-NCO catalyst is likely attributed to the presence of Cl⁻ ions at the catalyst surface [43-44]. Finally, in Figure 3(h), the Pt/Ar-NCO catalyst also shows a lower surface resistance than the NCO catalyst.

A density functional theory (DFT) calculation was also performed to further explore the effect of Pt atoms on the ORR electrocatalytic activity of the spinel NiCo₂O₄. Based on the material characterization results described earlier, the optimal configuration of NiCo₂O₄ models with oxygen vacancies (NCO or Ar-NCO) or Pt deposition (Pt/Ar-NCO)

was constructed. The ORR process of catalysts involves four steps and the formation reactions of the intermediates on the active sites are graphically shown in Figure 4(a) and Figure S12 (SI). The adsorption energies of intermediates were obtained by DFT results and then the Gibbs free energy change (ΔG) for each step is also calculated, which is the key factor to evaluate the electrocatalytic performance of catalysts. Figures 4(b, c) show the ΔG of catalysts at different voltages ($U = 0$ and 1.23 V). When $U = 0$ V, the free energy change of the Pt/Ar-NCO catalyst decreases stepwise, indicating exothermic ORR reactions facilitated by this catalyst. For the NCO catalyst, the reduction of $\ast\text{OH}$ is an endothermic and thermodynamically unfavorable process, hindering the ORR process. When increasing to $U = 1.23$ V, the last step of the $\ast\text{OH}$ reduction is the rate-determining step for both the NCO and Pt/Ar-NCO catalysts. The ΔG_4 value of the Pt/Ar-NCO catalyst (0.27 eV) is smaller than that of the NCO catalyst (3.04 eV), indicating that $\ast\text{OH}$ is easier to release at the surface of the Pt/Ar-NCO catalyst. In summary, Pt atom deposition can significantly reduce the energy barrier of the ORR process, resulting in a better ORR performance of the Pt/Ar-NCO catalyst than the NCO catalyst.

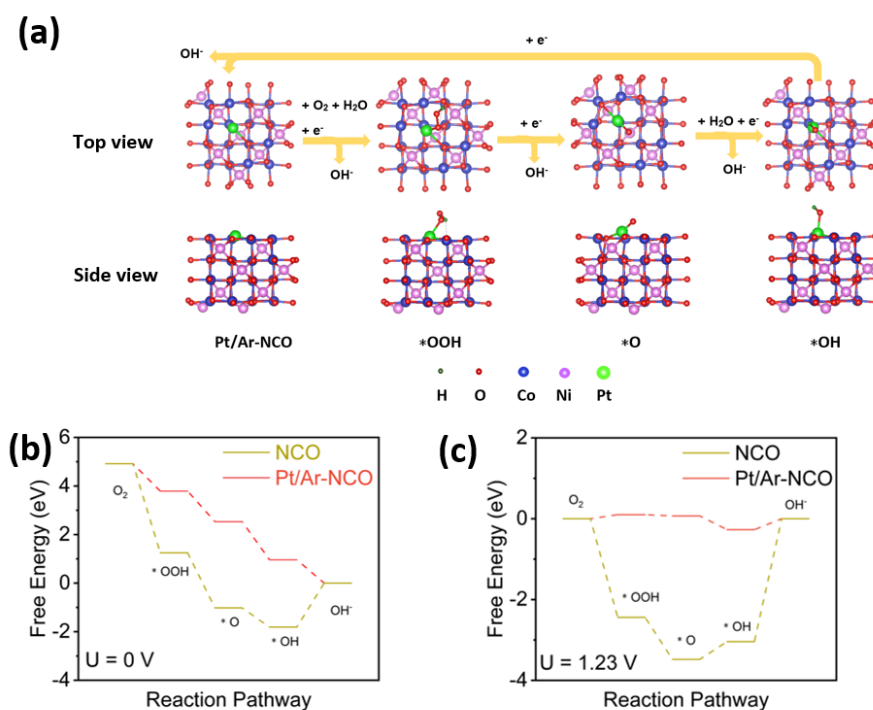


Figure 4. (a) Schematic illustration of the proposed electrochemical ORR pathway by the Pt/Ar-NCO catalyst. Energy profiles of the NCO and Pt/Ar-NCO catalysts for ORR (b) at $U = 0$ V, (c) at $U = 1.23$ V.

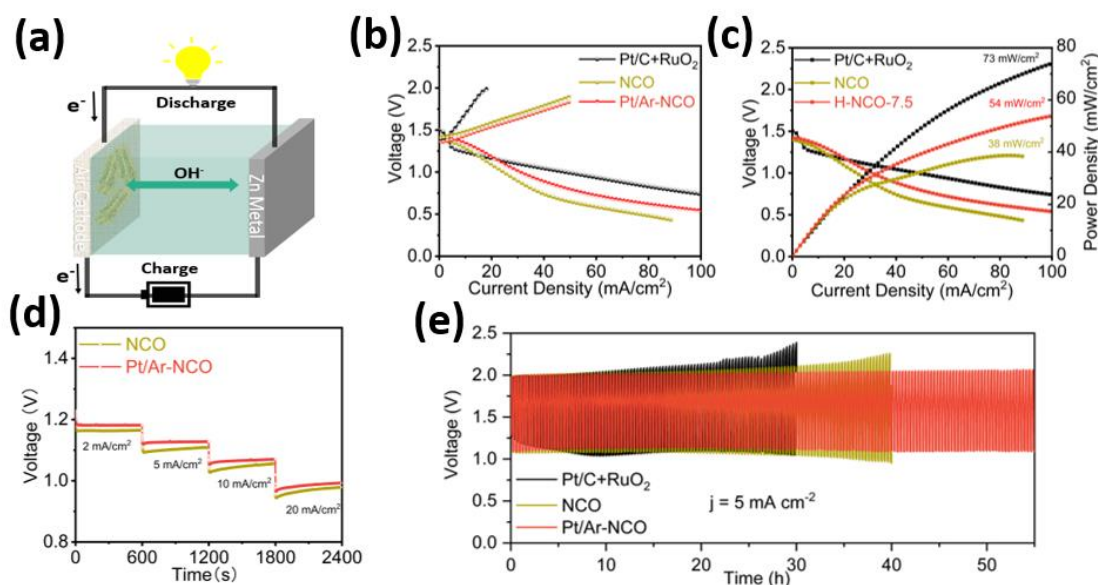


Figure 5. (a) Schematic diagram of the the aqueous zinc-air battery, (b) charging and discharge polarizations curves, (c) discharge curves and powder density, (d) galvanostatic discharge test, (e) rechargeability of the battery with catalysts.

To assess their practical application, the NCO and Pt/Ar-NCO catalysts were directly integrated into air cathodes for RZABs (Figure 5(a)). Figure 5(b) illustrates that the battery employing the Pt/Ar-NCO catalyst exhibits lower charge potentials and higher discharge potentials compared to the NCO catalyst, aligning with the OER and ORR performance results. Additionally, as shown in Figure 5(c), the Pt/Ar-NCO catalyst-based battery exhibits a peak power density of 54 mW cm⁻², higher than that of the NCO catalyst and close to the mixed noble metal catalysts. Moreover, the practical discharge potentials were also measured under different current densities. As shown in Figure 5(d), the Pt/Ar-NCO catalyst-based battery shows higher discharge voltages at current densities of 2, 5, 10 and 20 mA cm⁻², further confirming its better ORR performance than the NCO catalyst. The rechargeability of the batteries was also tested at the current density of 5 mA cm⁻² for 20 min/cycle. As shown in Figure 5(e), at the initial stage, the battery with the Pt/Ar-NCO catalyst presents an excellent charge potential of 1.97 V and an acceptable discharge potential of 1.10 V, outperforming the NCO catalyst. More importantly, even after 30 hours of operation, the Pt/Ar-NCO based battery shows only a negligible potential attenuation, compared to the noble-metal-based battery. These results further suggest that the Pt/Ar-NCO catalyst could be a

promising candidate for replacing these noble-metal-based catalysts in RZAB applications.

Conclusions

In this work, plasma engineering was used to synthesize Pt-decorated NiCo₂O₄ nanowires enriched with oxygen vacancies, creating a self-supported catalyst with an excellent bifunctional electrocatalytic performance for RZABs. Compared to pristine NiCo₂O₄ nanowires, these treated with Ar plasma treatment exhibited higher level of oxygen vacancies and then loaded more Pt atoms in the impregnation process involving plasma reduction. As a result, the final catalyst exhibits enhanced electrocatalytic activity for OER and ORR, compared to the pristine NiCo₂O₄ nanowires, owing to more available active sites and increased surface conductivity. DFT simulation results also confirm the positive effect of Pt atoms on the ORR performance of NiCo₂O₄. Correspondingly, the zinc-air battery assembled with this composite catalyst displays an outstanding charge/discharge voltage gap and high stability. This work presents a novel synthesis route for the development of low-cost, high-active, and stable bifunctional electrocatalysts with significant potential for further improvements through the optimization of both the Ar plasma treatment of the NiCo₂O₄ nanowires and the plasma-based reduction process of Pt.

Acknowledgements

H.L. thanks the China Scholarship Council (CSC) for the support through the project 202009110110. We also thank Prof. Dr. Rainer Adelung at the University of Kiel for the help with Raman spectrum measurement.

Reference:

- [1] F. Liu, Z. X. Fan, Defect engineering of two-dimensional materials for advanced energy conversion and storage, *Chem. Soc. Rev.*, 2023,52, 1723-1772.
- [2] S. Sikiru, T. L. Oladosu, S. Y. Kolawole, L. A. Mubarak, H. Soleimani, L. O. Afolabi, A. O. Toyin, Advance and prospect of carbon quantum dots synthesis for energy conversion and storage application: A comprehensive review, *J. Energy Storage*, 2023, 60, 106556.
- [3] S. Venkateshalu, G. M. Tomboc, S. P. Nagalingam, J. Kim, T. Sawaira, K. Sehar, B. G. Pollet, J. Y. Kim, A. N. Grace, K. Lee, Synergistic MXene/LDH heterostructures with extensive interfacing as emerging energy conversion and storage materials, *J. Mater. Chem. A*, 2023,11, 14469-14488.
- [4] T. He, Y. L. Zhao, Covalent organic frameworks for energy conversion in photocatalysis, *Angew. Chem. Int. Edit.*, 2023, 62, e202303086.
- [5] J. M. Chen, Y. P. Lin, H. Wang, J. M. Li, S. J. Liu, J. M. Lee, Q. Zhao, 2D molybdenum compounds for electrocatalytic energy conversion, *Adv. Funct. Mater.*, 2023, 33, 2210236.
- [6] P. Zhang, K. Chen, J. Y. Li, M. M. Wang, M. Li, Y. Q. Liu, Y. Pan, Bifunctional single atom catalysts for rechargeable zinc–air batteries: from dynamic mechanism to rational design, *Adv. Mater.*, 2023, 35, 2303243.
- [7] A. Kundu, T. Kuila, N. C. Murmu, P. Samanta, S. Das, Metal–organic framework-derived advanced oxygen electrocatalysts as air-cathodes for Zn–air batteries: recent trends and future perspectives, *Mater. Horiz.*, 2023,10, 745-787.
- [8] P. Anand, M. S. Wong, Y. P. Fu, Perovskite oxide composites for bifunctional oxygen electrocatalytic activity and zinc-air battery application- a mini-review, *Energy Storage Mater.*, 2023, 58, 362-380.
- [9] Y. Kumar, M. Mooste, K. Tammeveski, Recent progress of transition metal-based bifunctional electrocatalysts for rechargeable zinc–air battery application, *Curr. Opin. Electroche.*, 2023, 38, 101229.
- [10] H. X. Li, G. Li, Novel palladium-based nanomaterials for multifunctional ORR/OER/HER electrocatalysis, *J. Mater. Chem. A*, 2023,11, 9383-9400.
- [11] E. V. Rebrov, P. Z. Gao, Molecular catalysts for OER/ORR in Zn–air batteries, *Catalysts*, 2023,13, 1289.
- [12] X. N. Ma, M. Y. Liu, Q. Li, X. D. Xiao, J. N. Liu, X. Q. Xu, Y. H. Yin, P. Z. Qiao, L. M. Zhang, X. Y. Zou, R. H. Wang, B. J. Jiang, Associating Co single atoms with RuO₂ nanoparticles anchor on nitrogen-doped ultrathin porous carbon nanosheets as effective bifunctional oxygen electrocatalysts for rechargeable Zn–air batteries, *J. Mater. Chem. A*, 2023,11, 16889-16899.
- [13] S. Y. Zhao, T. Liu, Y. W. Dai, J. Wang, Y. Wang, Z. J. Guo, J. Yu, I. T. Bello, M. Ning, Pt/C as a bifunctional ORR/iodide oxidation reaction (IOR) catalyst for Zn-air batteries with unprecedentedly

high energy efficiency of 76.5%, *Appl. Catal. B-Environ.*, 2023, 320, 121992.

[14] D. B. Kumar, W. Nie, Z. Q. Jiang, J. Lee, T. Maiyalagan, Recent progress in transition metal carbides and nitrides based composites as bifunctional oxygen electrocatalyst for zinc air batteries, *J. Alloy Compd.*, 2023, 960, 170828.

[15] G. Dias, J. M. Costa, A. F. Neto, Transition metal chalcogenides carbon-based as bifunctional cathode electrocatalysts for rechargeable zinc-air battery: An updated review, *Adv. Colloid. Interfac.*, 2023, 315, 102891.

[16] Y. T. He, X. C. Zhou, Y. F. Jia, H. T. Li, Y. Wang, Y. N. Liu, Q. Tan, Advances in transition-metal-based dual-atom oxygen electrocatalysts, *Small*, 2023, 19, 2206477.

[17] H. Li, S. Askari, J. H. Wang, N. Wolff, M. Behrens, L. Kienle, J. Benedikt, Nitrogen-doped NiCo₂O₄ nanowires on carbon paper as a self-supported air cathode for rechargeable Zn-air batteries, *Int. J. Hydrogen. Energ.*, 2023, 48, 26107-26118.

[18] W. Q. Tang, J. Y. Tang, K. M. Liao, Z. P. Shao, Self-reconstruction of highly active NiCo₂O₄ with triple-continuous transfer of electrons, ions, and oxygen for Zn-air batteries, *Chem. Eng. J.*, 2023, 455, 140855.

[19] J. Yin, H. B. Liu, B. L. Huang, M. Lu, J. Y. Li, H. W. Liu, H. Zhang, Y. Peng, P. X. Xi, C. H. Yan, NiCo₂O₄-based nanosheets with uniform 4 nm mesopores for excellent Zn–air battery performance, *Adv. Mater.*, 2020, 32, 2001651.

[20] S. Chen, D. M. Huang, D. Y. Liu, H. Z. Sun, W. J. Yan, J. C. Wang, M. Dong, X. L. Tong, W. B. Fan, Hollow and porous NiCo₂O₄ nanospheres for enhanced methanol oxidation reaction and oxygen reduction reaction by oxygen vacancies engineering, *Appl. Catal. B-Environ.*, 2021, 291, 120065.

[21] B. Rashid, K. Mala, M. Ali, U. Rafiq, M. Quereshi, P. Ahmad, M. Dar, M. Wahid, Temperature ramp strategy for regulating oxygen vacancies in NiCo₂O₄ nanoneedles towards enhanced electrocatalytic water splitting, *ChemPhysChem*, 2023, 24, e202300013.

[22] M. L. Liu, Z. P. Zhao, X. F. Duan, Y. Huang, Nanoscale structure design for high-performance Pt-based ORR catalysts, *Adv. Mater.*, 2019, 31, 1802234.

[23] Y. Wang, D. S. Wang, Y. D. Li, A fundamental comprehension and recent progress in advanced Pt-based ORR nanocatalysts, *SmartMat*, 2021, 2, 56-75.

[24] J. T. Zhang, M. Y. Wang, T. T. Wan, H. T. Shi, A. J. Lv, W. Xiao, S. Q. Jiao, Novel (Pt-O_x)-(Co-O_y) nonbonding active structures on defective carbon from oxygen-rich coal tar pitch for efficient HER and ORR, *Adv. Mater.*, 2022, 34, 2206960.

[25] N. Logeshwaran, S. Ramakrishnan, S. S. Chandrasekaran, M. Vinothkannan, A. R. Kim, S. Sengodan, D. B. Velusamy, P. Varadhan, J. H. He, D. J. Yoo, An efficient and durable trifunctional electrocatalyst for zinc–air batteries driven overall water splitting, *Appl. Catal. B-Environ.*, 2021, 297,

120405.

[26] J. X. Han, X. Y. Meng, L. Lu, Z. L. Wang, C. W. Sun, Triboelectric nanogenerators powered electrodepositing tri-functional electrocatalysts for water splitting and rechargeable zinc-air battery: A case of Pt nanoclusters on NiFe-LDH nanosheets, *Nano Energy*, 2020, 72, 104669.

[27] H. Li, J. H. Wang, T. Tjardts, I. Barg, H. Y. Qiu, M. Müller, J. Krahmer, S. Askari, S. Veziroglu, C. Aktas, L. Kienle, J. Benedikt, Plasma-engineering of oxygen vacancies on NiCo₂O₄ nanowires with enhanced bifunctional electrocatalytic performance for rechargeable zinc-air battery, *Small*, 2024, 2310660.

[28] Y. Xing, L. X. Zhang, C. T. Li, Y. Y. Yin, L. J. Bie, Pt decoration and oxygen defects synergistically boosted xylene sensing performance of polycrystalline SnO₂ nanosheet assembled microflowers, *Sensor Actuat. B-Chem.*, 2022, 354, 131220.

[29] H. Xiao, X. M. Yang, M. Zhao, R. Zhang, Y. Y. Jing, L. Zhang, Y. L. He, H. S. Wu, J. F. Jia, Revealing promotion of interfacial Pt–O–Fe oxygen bridge structure in PtFe/graphene synthesized by a four-electrode electrochemical system on water splitting, *Int. J. Hydrogen Energ.*, 2023, 48, 38728-38741.

[30] X.C. Xiao, X.M. Zhang, Z.Y. Zhang, J.D. You, S.R. Liu, Y.D. Wang, Macro-/meso-porous NiCo₂O₄ synthesized by template-free solution combustion to enhance the performance of a nonenzymatic amperometric glucose sensor, *Microchim. ACTA*, 2020, 187, 64.

[31] Y. Wang, W. Z. Si, Y. Peng, J. J. Chen, Y. WANG, D. L. Chen, Z. B. Tian, J. Wang, J. H. Li, Oxygen vacancy engineering on copper-manganese spinel surface for enhancing toluene catalytic combustion: A comparative study of acid treatment and alkali treatment, *Appl. Catal. B-Environ. Energy*, 2024, 340, 123142.

[32] Z. L. Li, P. Y. Li, X. P. Meng, Z. Lin, R. H. Wang, The interfacial electronic engineering in binary sulfiphilic cobalt boride heterostructure nanosheets for upgrading energy density and longevity of lithium-sulfur batteries, *Adv. Mater.*, 2021, 33, 2102338.

[33] Rebekah, C. Viswanathan, N. Ponpandian, NiCo₂O₄ nanoparticles inlaid on sulphur and nitrogen doped and co-doped rGO sheets as efficient electrocatalysts for the oxygen evolution and methanol oxidation reactions, *Nanoscale Adv.*, 2021, 3, 3216-3231.

[34] W. H. Zhang, Y. H. Tang, L. M. Yu, X. Y. Yu, Activating the alkaline hydrogen evolution performance of Mo-incorporated Ni(OH)₂ by plasma-induced heterostructure, *Appl. Catal. B-Environ. Energy*, 2020, 260, 118154.

[35] X. Y. Lei, S. C. Ge, T. Y. Yang, Y. L. Lu, Y. L. Chueh, B. Xiang, Ni–Mo–S@Ni–P composite materials as binder-free electrodes for aqueous asymmetric supercapacitors with enhanced performance, *J. Power Sources*, 2020, 477, 229022.

[36] D. M. Cai, Q. H. Cao, J. J. Du, Y. Liu, F. Bu, Y. H. Yan, X. H. Lu, Q. H. Xia, D. Zhou, Y. D. Xia,

Oxygen vacancies enhanced NiCo₂O₄ nanoarrays on carbon cloth as cathode for flexible supercapacitors with excellent cycling stability, *Batteries Supercaps*, 2022, 5, e202100344.

[37] Z. L. Wang, Y. B. Xia, L. Liu, A. N. Wang, Y. Zhang, X. Liu, Binder-free one-dimensional NiCo₂O₄ nanowires@carbon papers composite as an anode for lithium-ion batteries, *Energy Fuels* 2020, 34, 10, 13111-13117.

[38] A. Jorio, R. Saito, Raman spectroscopy for carbon nanotube applications, *J. Appl. Phys.*, 2021, 129, 021102.

[39] Q. Chang, H. S. Liang, B. Shi, X. L. Li, Y. T. Zhang, L. M. Zhang, H. J. Wu, Ethylenediamine-assisted hydrothermal synthesis of NiCo₂O₄ absorber with controlled morphology and excellent absorbing performance, *J. Colloid. Interf. Sci.*, 2021, 588, 336-345.

[40] B. B. Wei, J. Wu, G. Wei, Z. B. Qi, W.S. Hu, Z. C. Wang, NiCo₂O₄ nanowire arrays rich in oxygen deficiencies for hydrogen evolution reaction, *Int. J. Hydrogen Energ.*, 2019, 44, 6612-6617.

[41] S. Z. Yao, H. S. Wei, Y. Zhang, X. R. Zhang, Y. Wang, J. Q. Liu, H. H. Tan, T. Xie, Y. C. Wu, Controlled growth of porous oxygen-deficient NiCo₂O₄ nanobelts as high-efficiency electrocatalysts for oxygen evolution reaction, *Catal. Sci. Technol.*, 2021, 11, 264-271.

[42] Q. Chang, H. S. Liang, B. Shi, X. L. Li, Y. T. Zhang, L. M. Zhang, H. J. Wu, Ethylenediamine-assisted hydrothermal synthesis of NiCo₂O₄ absorber with controlled morphology and excellent absorbing performance, *J. Colloid. Interf. Sci.*, 2021, 588, 336-345.

[43] J. G. Vos, Z. C. Liu, F. D. Speck, N. Perini, W. T. Fu, S. Cherevko, M. T. M. Koper, Selectivity trends between oxygen evolution and chlorine evolution on iridium-based double perovskites in acidic media, *ACS Catal.*, 2019, 9, 8561-8574.

[44] H. Jung, J. Song, Y. C. Lee, H. S. Jung, K. J. Noh, H. Im, Y. Lee, T. Y. Kim, O. Seo, T. Watanabe, L. S. R. Kumara, D. Matsumura, S. Park, J. W. Han, Computational discovery of optimal dopants for nickel iron oxyhydroxide to enhance OER activity and saline water compatibility, *ACS Energy Lett.*, 2024, 9, 2162-2172.

人间四月芳菲尽，山寺桃花始盛开。

-----白居易

All flowers in late spring have fallen far and wide, but peach blossoms are full-blown on this mountainside.

-----Wei Wang (Translated by Yuanhong Xu)



Mass spectrometry facilitates the precise control of N₂ plasma surface modification

Plasma surface treatment has been regarded as an efficient and environmentally friendly method for modifying the catalyst surfaces and optimizing their surface properties, thereby increasing their catalytic performance. However, most plasma-related material research focused on the operating parameters of the plasma and the characterization of the materials. Regrettably, these optimal operating parameters are not universally applicable to other devices. Therefore, a novel setup was constructed, as described in Section 3.2, which enabled in-situ monitoring of plasma parameters during the plasma modification process. In this work, single-layer graphene was first treated by N₂ plasma under a variation of reactor pressure. Second, commercial-available carbon paper as a model example and was chosen as a pristine catalyst and its ORR electrocatalytic performances were improved by N₂ plasma treatment. The ion composition, density, energy distribution and impurities of the N₂ plasma reaching the catalyst surface during the modification process were studied. These plasma properties

during the treatment help us to better understand and control the treatment process.

Prof. Dr. Jan Benedikt designed the underlying concept, provided experimental funding and reviewed the manuscript. The author of this thesis carried out the experiments and prepared the first draft. Other authors helped with the material characterization and reviewed the manuscript.

Mass spectrometry facilitates the precise control of N₂ plasma surface modification

He Li¹, Martin Müller², Christian Schulze¹, Haoyi Qiu³, Jan Benedikt^{1,4*}

¹ Institute of Experimental and Applied Physics, Kiel University, Leibnizstraße 19, D-24098 Kiel, Germany

² Chair for Synthesis and Real Structure, Department of Materials Science, Faculty of Engineering, Kiel University, Kaiserstraße 2, D-24143 Kiel, Germany

³ Chair for Functional Nanomaterials, Department of Materials Science, Faculty of Engineering, Kiel University, Kaiserstraße 2, D-24143 Kiel, Germany

⁴ Kiel Nano, Surface and Interface Science KiNSIS, Kiel University, Christian-Albrechts-Platz 4, D-24118 Kiel, Germany

*Corresponding author.

Abstract:

Plasma technology is offering a green and efficient process for nanomaterial synthesis and treatment. Many studies of plasma modification of materials, particularly catalysts, are however primarily focused on the characterization of the induced material changes after using plasma just as a black box tool for the treatment, where the plasma properties such as plasma density, ion composition and ion-flux energy distribution functions are not known. In this study, plasma treatments are performed with a novel reactor that combines RF inductively coupled plasma with DC or RF bias at the chamber wall to control the ion flux and ion energy at the grounded electrode independently. First, the capability of the system to treat sensitive materials is demonstrated on the N₂ plasma treatment of single-layer graphene under variation of reactor pressure. Second, catalyst treatment is studied using carbon paper as a model example of a pristine catalyst. Its treatment with capacitively coupled N₂ plasma at a rather high pressure of 20 Pa has significantly improved its ORR performance. To reveal the treatment mechanism and ion energies, carbon paper was also treated in the novel reactor. The composition and energy distribution of ions arriving at the grounded electrode with the treated substrate is measured during both single-layer graphene and carbon paper plasma treatments by an energy-selective ion mass spectrometer. These measurements demonstrated in the first case that the defects in single-layer graphene are formed with ions with energy as low as 23 eV and that 30 s of treatment with the ion energy of 28 eV resulted in the partial graphene removal. In the second case, carbon paper ORR performance improvement could not be reproduced with ion energy as high as 83 eV. Applying RF bias on the wall of the novel reactor allowed to simulate the treatment conditions in capacitive plasma at 20 Pa and the measurement of ion-flux energy distribution function has shown that particularly N⁺ ions with energy as high as the RF voltage amplitude can reach the substrate at this pressure, being very probably responsible for the observed ORR improvement. Additional experiments are being planned to confirm this result. The presented results clearly demonstrate that both plasma properties and the properties of the treated material play important roles in plasma treatment.

1. Introduction

Plasma surface modification as an effective and economical technique for material preparation is gaining popularity [1-4]. The abundant ionized and excited species in the plasma area present high chemical reactivities and are easily used to optimize the surface properties of materials [5]. Moreover, plasma surface modification also has several advantages, such as short treatment duration, energy efficiency and low-heating effect, which cannot change the bulk properties of materials obviously [6-7].

Electrode materials, especially electrocatalysts for accelerating energy conversation reactions, play a key role in developing novel energy conversion and storage systems [8-12]. As a facile method, plasma surface treatment has been extensively applied to synthesize highly efficient and low-cost electrocatalysts [13-17]. For example, Zhang *et al.* employed N₂ plasma to fabricate the Mn-CoN-1.5 catalyst for zinc-air batteries and Zhao *et al.* prepared a composite catalyst of NiS/NiFe₂O₄ by Ar plasma-induced phase reconfiguration [18-19]. However, in these published studies, plasma technology is merely regarded as a black box tool for modifying catalysts, and they only investigated the relationship between the change of material properties and plasma operating parameters, such as the treatment time, power supply as well as working pressure [20-23]. Although the best operating parameters have been provided, they are not universally applicable to different devices due to differences in reactor structures, which seriously hinders the development of plasma technology. In fact, the energetic ions in the plasma with their energy distribution, are often the most important factor in optimizing material properties and affecting the catalyst performance. Therefore, to better develop and understand this promising technology, it is necessary to monitor the ion properties of plasma during the surface treatment and finally correlate these data with the changes in material properties.

This work utilizes a new plasma reactor with inverted electrode geometry, which we have introduced recently, for assembling an energy-selective mass spectrometer at the grounded substrate holder. By this reactor, the ion properties in plasma, such as the composition and energy distribution of the ions (including the ions originating from the impurities or from material sputtering), can be monitored during the modification

process at the very same electrode, where the plasma treatment takes place. The first treatment example is a model study of the graphene treatment at pressure variation as a control of the ion-flux energy distribution function (IEDF). Additionally, using commercially available carbon paper as the pristine catalyst, N₂ plasma is applied to optimize its surface properties and improve its ORR performance. The surface properties of the catalyst after plasma treatment were also investigated and correlated with the measured plasma data, which can be used to facilitate the precise control of N₂ plasma surface modification.

2. Experimental apparatus and materials

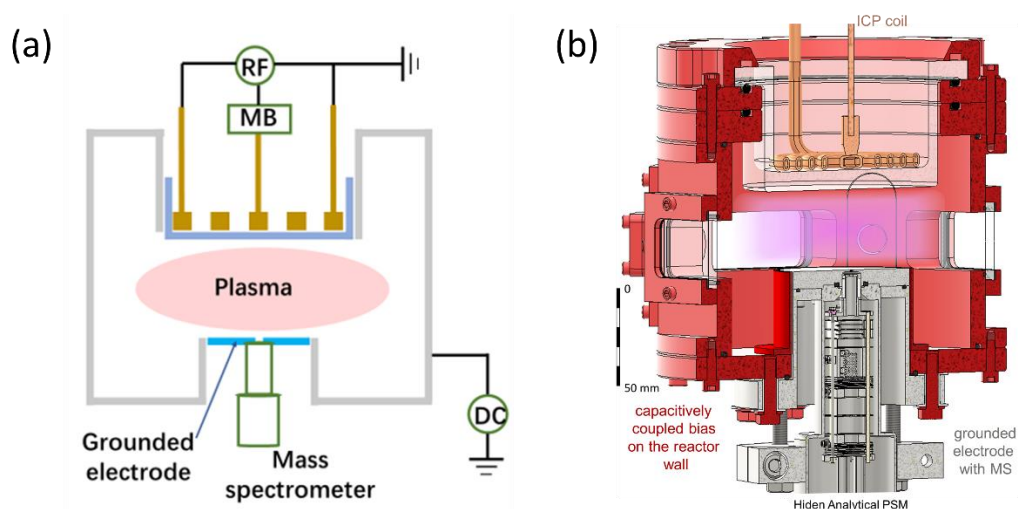


Figure 1. (a) Sketch of the experimental setup. (b) The reactor 3D cross section drawing showing the ICP coil (orange) in quartz dome, grounded electrode with the integrated PSM ion mass spectrometer (grey), and biased reactor walls (red color).

Setup: Figure 1 shows the sketch of the 3D cross-section drawing of the experimental setup. In brief, this plasma reactor consists of an inductively coupled plasma (ICP) power source (RF power, 13.56 MHz), a direct current (DC) bias power source, a large chamber, a grounded substrate holder and an energy-selective mass spectrometer. The plasma is generated and sustained by the ICP power, while the DC bias connecting to the large chamber wall is conducted to control the ion energy of the plasma. DC bias was used, because the treated samples are conductive and their

charging is, therefore, not a problem. But RF bias can be used as well as demonstrated before^[24]. During plasma treatment, an energy-selective mass spectrometer integrated at the grounded substrate holder precisely measured the ion properties of the plasma. More details about the setup are shown in the reference ^[24]. Another way to control energy and ion density is through chamber pressure. As the pressure increases, the number of collisions of charged ions with neutral atoms increases and the mean free path of the ions decreases, thus decreasing the energy with which they reach the mass spectrometer at the level of the grounded electrode or the surface of the sample being processed.

The results provided in this work focus on the N₂ plasma as an example of non-oxidizing plasma and it has been applied to single-layer graphene and carbon paper as two model carbon-based materials. Interaction with polycrystalline monolayer graphene films has been studied recently for example by Stafford et al. revealing the effects of argon ions, VUV photons, and metastables on the formation of defects and their self-healing at grain boundaries, enhanced by phonons excited due to graphene interaction with metastables ^[25-26]. Other authors have studied the treatment of graphene with electron-beam generated plasma ^[27], its plasma-induced hydrogen coverage ^[28], or measured and simulated the behavior of implanted noble gas atoms in graphene stacks ^[29]. The large amount of available literature, the level of knowledge about plasma-graphene interaction, and the availability of graphene with defined properties as commercial product (e.g., in the form of suspended graphene on TEM grids) allow to use graphene as a model material in experimental studies of the plasma-surface interaction.

Carbon paper is a non-woven porous material composed of carbon fibers and is commonly used as a conductive and gas-permeable support substrate for catalysts in many applications owing to its high conductivity and excellent chemical/thermal stability ^[30-32]. For example, Bhandary *et al.* prepared Mn-Fe oxide nanopetals on carbon paper as an excellent self-supported electrocatalyst ^[33]. However, the electrochemical performance of carbon paper itself is poor due to the lack of active sites. Previous studies show that rational surface engineering could activate the surface of the carbon paper and improve its electrochemical performance, which makes it possible to be a

self-supporting electrocatalyst [34-35].

N₂ plasma surface treatment of single layer graphene: Single layer graphene were synthesized on copper substrate by CVD method (provided by Olexander Volochanskyj in the group of Prof. Dr. Martin Kalbáč, J. Heyrovský Institute of Physical Chemistry) [36-37]. The sample was loaded to the substrate holder of the plasma chamber and pumped down to the base pressure of 1.5×10^{-3} Pa. Then N₂ gas was introduced to the chamber with a flow rate of 2.5 sccm and the pressure was controlled in range of 1.5 - 20 Pa using a throttle valve. The ICP power of 100 W was applied to the coil on top of the plasma chamber and no additional DC bias was used. The ion energy and flux were measured simultaneously during the graphene treatment and controlled solely by adjusting the pressure.

N₂ plasma surface treatment of carbon paper: Carbon papers (CP, 28AA) were purchased from slg carbon, Germany. The N₂ plasma treatment was carried out by the plasma reactor mentioned before. Firstly, The CP was put onto the substrate holder. After that, the chamber was pumped by a two-stage pumping system to the base pressure. The flow rate of N₂ gas was 2.5 sccm and the working pressure was 2.5 Pa. Then, N₂ plasma was generated and sustained by the ICP power of 100 W and the ion energy was controlled by the DC bias.

Materials characterization: Graphene samples were analyzed by Raman spectroscopy (532nm, alpha 300 RA).

Electrochemical measurements: The ORR performance of the catalysts was evaluated by an electrochemical workstation (Wave Driver 200, Pine Research) with a three-electrode system, where the Pt wire, the Ag/AgCl electrode and the rotating disk electrode ($\varnothing = 6$ mm) attached by the modified catalysts (4 mm x 4 mm) were used as the counter electrode, the reference electrode and the working electrode, respectively. The Linear sweep voltammetry (LSV) curves were measured at a sweep rate of 5 mV s^{-1} and a rotation rate of 1600 rpm in the O₂-saturated electrolyte of 1 M KOH and all the potentials were converted to the potentials of reversible hydrogen electrode (vs. RHE) and corrected by the iR compensation.

3. Results and discussion

3.1 Plasma treatment of single layer graphene

The effect of plasma on the single-layer graphene, and especially the effect of ion energy has been studied as a function of pressure variation between 1.5 Pa and 20 Pa. The IEDFs of N₂⁺ ions are shown in Figure 2(a) on a linear and logarithmic scale. The lowest pressure results in a dominant ion signal centered at 28 eV with a relatively small contribution of low-energy ions. Increasing the pressure makes the plasma sheath in front of the grounded electrode more and more collisional and the low-energy ions start to dominate the spectrum. The maximum energy is also reduced to below 25 eV at higher pressure as a result of changing experimental conditions. The highest pressures result in most of the ions being with energy below 5 eV.

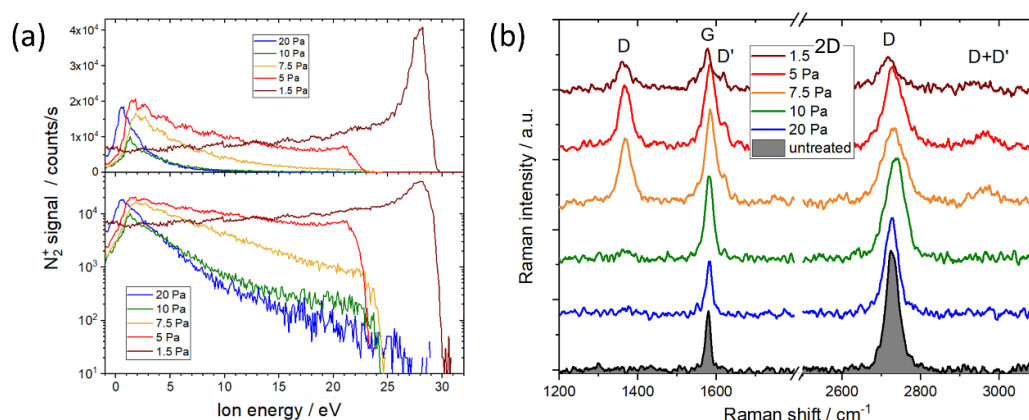


Figure 2: (a) Linear and logarithmic plots of measured IEDF of N₂⁺ ions in an ICP plasma by pressure variation. Applied ICP power: 100 W. (b) Raman spectra of untreated graphene and graphene treated for 30 s at the grounded electrode and at the given plasma pressure. The baseline of each spectrum is subtracted and the curves are shifted along the y-axis for better visibility.

Figure 2(b) compares the Raman spectra of treated graphene with that of untreated substrate. The results clearly demonstrate that the low energy ion treatment at 20 Pa and 10 Pa does not change the Raman spectra or results only in the broadening of the 2D peak in the case of 10 Pa treatment. Starting with 7.5 Pa pressure, where larger fluxes of ions with energy up to ~24 eV appear, the treatment results in the appearance of additional D and D' peaks in the spectrum and the reduction of the intensity of the original D peak. The highest ion energy and flux of energetic ions at the lowest pressure results in a clear reduction of the signal intensity of all peaks indicating

partial graphene destruction or removal.

These measurements confirm that single-layer graphene can withstand N₂ plasma treatment without damage when the sheath is collisional and the ions have energy below 5 eV and that mainly the energetic ions with energy 10 to 23 eV are inducing the defects in its structure. The ion flux dominated by ions with 28 eV energy was already leading to removal of graphene and reduction of the Raman signal.

3.2 Plasma treatment of carbon paper

Carbon materials with heteroatom dopants have been extensively applied as electrode materials. Previous literature has indicated that the ORR performance of carbon papers can be improved by N doping owing to the generation of nitrogen-based functional species [38-40]. Inspired by these results, the main part of this work is the treatment of a commercial carbon paper as the pristine catalyst in an N₂ plasma. The first treatment was performed in a CCP reactor (see chapter 3) at pressure of 20 Pa, N₂ flow of 8 sccm, applied power of 200 W, treatment time of 10 minutes and CP being mounted on the floating substrate holder. The LSV results in Figure 3 clearly show that the ORR performance of the CP is significantly improved after 10 minutes of the CCP treatment, The onset potential increases from 0.80 V to 0.86 V and a half-wave potential from 0.71 V to 0.76 V.

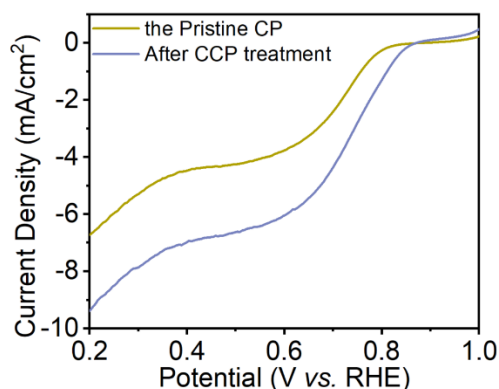


Figure 3: ORR performances of CPs before and after CCP treatment.

The floating potential of the substrate in a capacitively coupled plasma is given by:

$$\phi_{f,RF} = \frac{kT_e}{e} \left[\frac{1}{2} \ln \left(\frac{2\pi m}{M} \right) - \ln \left(I_0 \left(\frac{eV_a}{kT_e} \right) \right) \right] \quad (3.2.1)$$

where m and M are electron and ion masses, respectively, V_a is the applied voltage

amplitude and $I_0(x)$ is the zero-order modified Bessel function [41]. The direct measure of the V_a with a high voltage probe has provided the value of 295 V. Because the V_a is much larger than T_e , the resulting floating potential is only very weakly dependent on it and the Equation 3.2.1 provides the value 294 V. The ions arriving at the substrate of the CP can, therefore, reach kinetic energy at this level or even higher when plasma potential is considered as well. On the other hand, the relatively large pressure of 20 Pa could result in a highly collisional sheath and the ion energy of the majority of the ions should be much lower as seen in the example of graphene treatment, see the comparison of IEDFs in Figure 2(a).

To be able to estimate the ion energies in the CCP reactor and to reveal the role of ion energy in this promising N₂ CCP treatment of the CP, new experiments were performed in the ICP reactor with inverted electrode geometry with controlled ion energy. Again, an energy-selective ion mass spectrometer connecting to the substrate holder measured the ion properties of the N₂ plasma during the treatment process. First, the effect of base pressure before the plasma treatment on the ion composition is studied in the chamber without the inserted carbon paper substrate. This study was necessary, because our chamber has currently no load-lock installed and the possible effect of impurities on the plasma composition after substrate insertion with the whole chamber being pressurized, can be, therefore, large.

3.2.1 Ion composition of inductively coupled N₂ plasma

The ion composition of the plasma is one of the most important parameters for the surface treatment process. Firstly, the ion mass spectrum of the ICP was measured under the specified working parameters several minutes after evacuating the chamber and at the ion energy corresponding to the sheath potential drop of 23.3 eV (see the next section).

As shown in Figure 4(a), various nitrogen-positive ions were detected in the N₂ plasma, including N^+/N_2^{2+} ($m/z = 14$), N_2^+ ($m/z = 28$), N_3^+ ($m/z = 42$) and N_4^+ ($m/z = 56$). Among them, molecular N_2^+ ions were generated by a single electron impact following the process: $N_2 + e^- \rightarrow N_2^+ + 2e^-$ (15.6 eV). Atomic N^+ ions were produced by a

dissociative ionization step: $N_2 + e^- \rightarrow N^+ + N + 2e^-$ (24.3 eV) [42-43]. It should be noted that the N^+ ions may also be generated by the step: $N + e^- \rightarrow N^+ + 2e^-$ (14.5 eV). In addition, the N_3^+ and N_4^+ ions were formed by the combination of N^+ and N_2^+ ions and the N_2 molecular [44-45]. During plasma treatment, these generated nitrogen ions enter the plasma sheath near the grounded substrate holder and are accelerated by the sheath potential, finally reaching the catalyst surface.

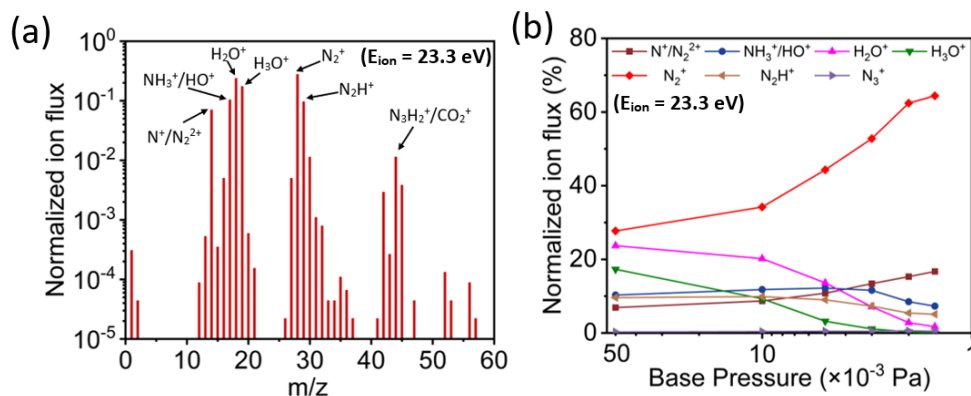


Figure 4: (a) Positive ion mass spectrum in N₂ plasma. Plasma parameters: N₂ gas flow 2.5 sccm, pressure 2.5 Pa, power 100 W, chamber base pressure before experiment 5×10⁻² Pa. (b) The content change of positive ions under reduction of the chamber base pressures resulting from the prolonged chamber evacuation ranging from minutes up to more than a day.

However, several impurities were also detected in N₂ plasma, including HO^+ , H_2O^+ and CO_2^+ , which were mainly formed by ionizing the adsorbed species at the reactor wall [46]. These impurities not only dissipated the input energy but also reacted with nitrogen-related ions to form hydro-nitrogen ions, thus reducing the concentration of pure nitrogen ions. More importantly, they are highly reactive and can damage the surface integrity of the catalyst and generate some undesirable defects on its surface during the surface modification process. One common approach to efficiently remove these impurities is to reduce the base pressure of the chamber. Figure 4(b) shows the effect of the base pressure on the intensities of dominant impurity peaks. Among them, the H_2O^+ content exhibits a notable decline from 23.7% to 1.7% as the base pressure decreased from 5 × 10⁻² Pa to 1.5 × 10⁻³ Pa. Additionally, the H_3O^+ ions present a near-complete disappearance when the base pressure is below 3 × 10⁻³ Pa. Moreover, we speculate that the HO^+ ions also disappeared at low base pressures, and the ions at

$m/z = 17$ are mainly NH_3^+ . The reduction in these hydroxide ions was accompanied by a slight decline in the formation of NH_3^+ and N_2H^+ ions. Conversely, the proportions of N^+/N_2^{2+} and N_2^+ increased from 6.9% and 27.7% to 16.7% and 64.4%, respectively. The data presented here demonstrate that pumping the chamber to a lower base pressure was an effective method for reducing impurities and increasing the content of nitrogen ions.

3.2.2 Ion-flux energy distribution functions and ion energy control

Figure 5(a) shows the ion energies and fluxes of nitrogen ions (the N^+/N_2^{2+} , N_2^+ , N_2H^+ and N_3^+ ions were used for the energy analysis). It can be observed that the ions in the plasma exhibit a similar peak energy of approximately 23.3 eV used previously for the ion mass spectra measurements. Following the result of the previous discussion, the chamber base pressure before following measurements of the ion-flux energy distribution spectra was controlled to be at or below 2×10^{-3} Pa.

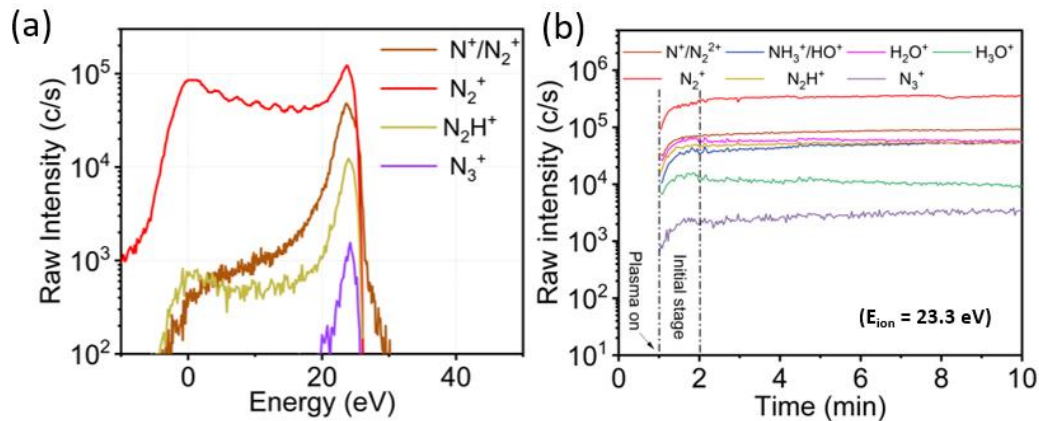


Figure 5: (a) the ion energies and fluxes of nitrogen-related ions (N^+/N_2^{2+} , N_2^+ , N_2H^+ and N_3^+) under the ICP power of 100 W, (b) time evolution of ion fluxes during plasma modification.

The low-energy part is observed mainly at N_2^+ ion due to the large cross-section for the resonant charge transfer with the N_2 molecules. The cross sections of non-resonant charge transfer of other ions with N_2 are smaller and result mainly in the formation of the N_2^+ ion and therefore they are not observed at lower energies.

The ion densities at the peak energy of 23.3 eV were also measured as a function of time after plasma ignition. As shown in Figure 5(b), the steady-state signals are

reached after an initial development time period of about 1 min, during which the densities of all ions exhibited a rapid increase within the first 20 seconds followed by slower levelling of the signals. During this period, the peak densities of the H_2O^+ and H_3O^+ ions were observed due to the desorption of water from the chamber wall. Still, the N_2^+ ion was the dominant positive ion in the plasma at any time and the densities of nitrogen-based ions, N^+/N_2^{2+} and N_2^+ , were maintained at a constant level, while the concentrations of H-based impurities decreased slowly as the discharge time increased, indicating that the rest water impurity is being removed. This is an expected behavior of this kind of plasma discharge.

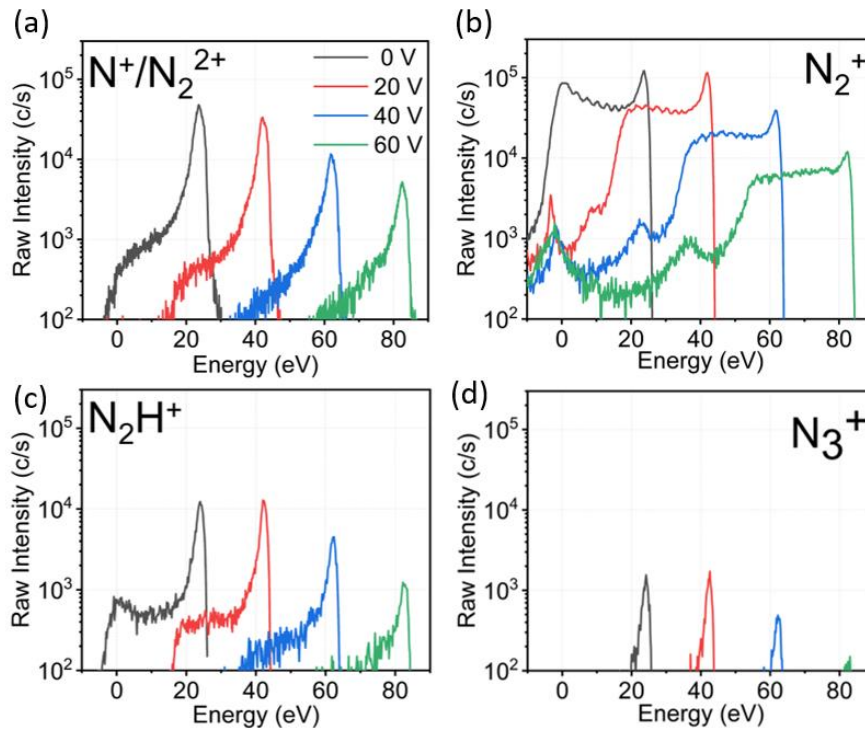


Figure 6: The IEDFs of nitrogen-related ions under different DC bias voltages (a) N^+/N_2^{2+} , (b) N_2^+ , (c) N_2H^+ and (d) N_3^+

To control the ion energy, a positive DC bias was applied to the chamber wall, shifting the plasma potential correspondingly to the higher values and increasing hence the voltage drop across the sheath in front of the grounded electrode. Figure 6 shows the IEDFs of the dominant ions under different DC biases. It can be seen that the same ions exhibit similar flux-energy distribution functions, but the peak energies increase linearly with the DC bias voltage.

Table 1: DC bias voltages and their corresponded plasma modification durations. Sample names: CP stays for pristine carbon paper, N-CP-1 to N-CP-4 stay for the four treatments with the N₂ plasma.

Sample Name	DC bias voltages (V)	Peak ion energy (eV)	Durations (Min)
CP	/	/	/
N-CP-1	0	23.3	2.5
N-CP-2	20	43.2	2.75
N-CP-3	40	63.3	10
N-CP-4	60	83.1	25

Nonlinear is the behavior of the measured signal intensities with increasing bias. 20 V bias results in a very small reduction of the signal intensities of the N^+/N_2^{2+} and N_2^+ ions, without any clear effect on the N_2H^+ and N_3^+ ion signal intensities. Additional bias increases to 40 V and 60 V results, however, in a decrease of measured ion intensities roughly with factor three in each step. This decrease is probably caused by changing plasma properties due to the increasing sheath thickness, but no visible changes in the plasma appearance were observed. This reduction is very probably not caused by the changes in the transmission function of the mass spectrometer (e.g. changes in the acceptance angle), because these effects are expected to play a role at smaller energies and they should result more probably in the increase of the ion signal with increasing ion energy. To compensate for this decreasing ion flux, the treatment times at different applied biases were adjusted in the way that the time-integrated ion flux is the same for all treatments, see the treatment durations given in Table 1.

3.2.3 Effect of N₂ plasma treatment on CP properties

The CP catalysts were then modified by N₂ ICP with different DC bias voltages and time durations as given before in Table 1. Figure 7(a) shows the ORR performance of the catalysts. Additionally, the result obtained after CCP treatment already shown in Figure 3 is included here as well. Surprisingly, there is only a small change in the ORR performance, which is slightly increasing with increasing ion peak energy. At an ion peak energy of 83.1 eV, the N-CP-4 catalyst shows an onset potential of 0.82 V and a half-wave potential of 0.72 V compared to the pristine CP catalyst (0.79 V and 0.69 V).

These values are significantly behind the ORR performance of the CP after CPP treatment with an onset potential of 0.86 V and a half-wave potential of 0.76 V.

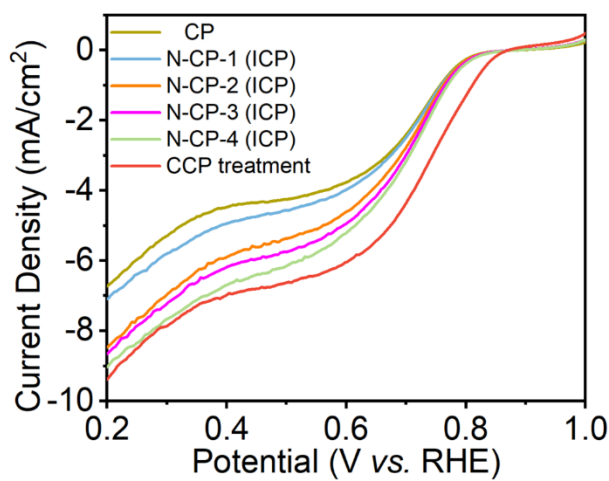


Figure 7: The ORR performances of CPs before and after N₂ plasma treatment.

The fact that our CCP treatment is more effective than the ICP treatment is rather surprising. The significantly higher pressure and lower plasma density in a CCP compared to ICP, even if the power is twice as large, should result in a smaller flux of ions probably at lower energies due to the high pressure of 20 Pa. The IEDFs cannot be measured in our CCP system due to the limits given by the glass tube and the absence of any internal electrodes, where the sampling orifice can be placed. However, the CCP plasma can also be ignited in the chamber with inverted geometry when the RF voltage is applied to the reactor wall and the ICP plasma stays turned off. The RF power supply (13.56 MHz in this case) and matchbox have been used for this experiment, where the voltage amplitude was monitored directly at the reactor chamber with a high-voltage probe. Figure 8 provides the IEDF of the same ions as in Figure 6 at four RF voltage amplitudes from 50 V to 200 V. The largest amplitude that could be achieved was 200 V at 180 W applied power. Larger powers and voltage amplitudes have resulted in the disturbance of the electronic units of the turbomolecular pumps and mass spectrometer and could not be, therefore, applied here.

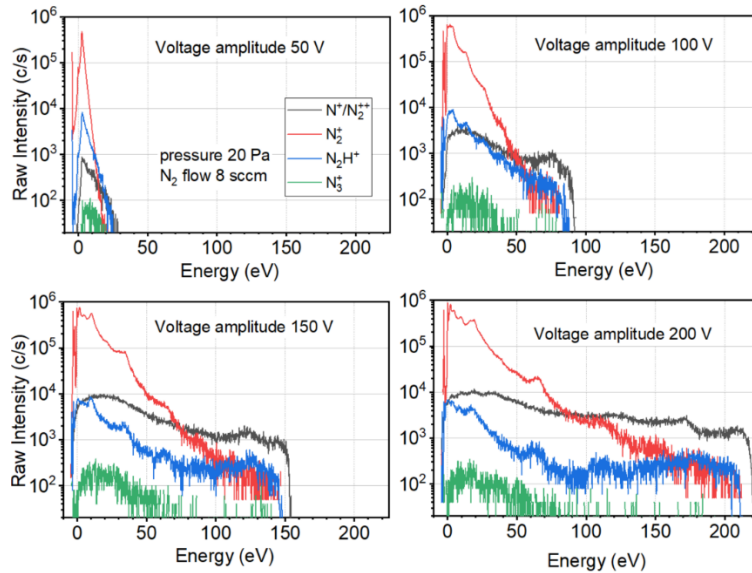


Figure 8: IEDFs as measured at masses 14, 28, 29 and 42 amu. RF voltage amplitude was changed between 50 and 200 V.

The measured IEDFs in Figure 8 confirm that most of the ions are slowed down through collisions in the sheath and their energy is below 83 eV used in our previous experiment. However, a small fraction of ions reaches the energy at or slightly higher than the applied voltage amplitude. Especially the contribution of the N^+ (or N_2^{2+}) ions pathing the rf sheath without collisions is increasing with increasing voltage amplitude (increasing applied power). This is caused by increasing plasma density with increased power, which results in decreased sheath width and therefore lower collision probability. These experimental conditions are not perfectly comparable to the conditions in the tube CCP reactor, but they indicate that the very high energy ions ($E_{\text{ion}} > 83$ eV) are responsible for the CP modifications.

4 Conclusion

In this work, the low-pressure N₂ treatments of single-layer graphene and carbon paper as model materials were studied in a novel plasma reactor with tunable plasma density through the inductive plasma coupling and controllable ion energy at the grounded substrate through DC or RF bias at the reactor wall. The main plasma

diagnostic was the energy-selective ion mass spectrometry. First, the variation of reactor pressure has been used to change the ion-flux energy distribution function of N₂ ICP plasma used for 30 s to treat single-layer graphene. The Raman measurements demonstrate that the N₂ plasma at 20 Pa with ion energy below 5 eV doesn't result in the modification of the single-layer graphene. Pressure reduction and ion energy increase to 23 eV induced the appearance of defects seen through the presence of additional D and D' peaks in the spectrum. The treatment at the lowest pressure of 1.5 Pa resulted in the decrease of the Raman spectra intensity indicating the graphene removal from the substrate. The highest ion-flux and highest ion energy of 28 eV are responsible for this result.

Carbon paper as a model pristine catalyst was treated in the second example of N₂ plasma treatment of carbon-based materials. This study was motivated by capacitively coupled N₂ plasma treatment at a rather high pressure of 20 Pa, which has significantly improved carbon paper's ORR performance. The CP treatment with controlled ion energies revealed that ion energy as high as 83 eV could not reproduce the ORR performance boost. Applying RF bias on the reactor wall allowed to simulate the treatment conditions in capacitive plasma at 20 Pa and the measurement of ion-flux energy distribution function has shown that ions with energy as high as the RF voltage amplitude can reach the substrate even at the pressure of 20 Pa. Particularly the N⁺ ion-flux energy distribution function contains a high portion of the ions close to the maximum possible energy, mainly due to their lower non-resonant charge transfer cross section in collisions with N₂ molecules. The RF voltage amplitude of 295 eV was measured at the CCP electrodes and N⁺ ions with energy up to this value are reaching the floating substrate in the CCP treatment. These energetic ions are very probably responsible for the observed ORR improvement. Additional experiments are being planned to confirm this result.

Acknowledgements

H.L. thanks the China Scholarship Council (CSC) for the support through the project 202009110110. DFG is acknowledged for the financial support through the project BE4349/8-1 (project number 530936824).

References

- [1] M. Kaseem, S. Fatimah, N. Nashrah, Y. G. Ko, Recent progress in surface modification of metals coated by plasma electrolytic oxidation: Principle, structure, and performance, *Prog. Mater. Sci.*, 2021, 117, 100735. <https://doi.org/10.1016/j.pmatsci.2020.100735>
- [2] C. L. Ma, A. Nikiforov, D. Hegemann, N. D. Geyter, R. Morent, K. Ostrikov, Plasma-controlled surface wettability: recent advances and future applications, *Int. Mater. Rev.*, 2023, 68, 82-119. <https://doi.org/10.1080/09506608.2022.2047420>
- [3] D. Y. Hou, F. N. Bai, P. Dong, J. Chen, Y. T. Zhang, F. M. Meng, Z. H. Zhang, C. X. Zhang, Y. J. Zhang, J. Hu, Recent development of low temperature plasma technology for lithium-ion battery materials, *J. Power Sources*, 2023, 584, 233599. <https://doi.org/10.1016/j.jpowsour.2023.233599>
- [4] K. K. Yeboah, I. K. Bique, X. C. Qiao, Advances of non-thermal plasma discharge technology in degrading recalcitrant wastewater pollutants. A comprehensive review, *Chemosphere*, 2023, 320, 138061. <https://doi.org/10.1016/j.chemosphere.2023.138061>
- [5] S. Dou, L. Tao, R. L. Wang, S. E. Hankari, R. Chen, S. Y. Wang, Plasma-assisted synthesis and surface modification of electrode materials for renewable energy, *Adv. Mater.*, 2018, 30, 1705850. <https://doi.org/10.1002/adma.201705850>
- [6] H. Li, S. Askari, J. H. Wang, N. Wolff, M. Behrens, L. Kienle, J. Benedikt, Nitrogen-doped NiCo₂O₄ nanowires on carbon paper as a self-supported air cathode for rechargeable Zn-air batteries, *Int. J. Hydrogen. Energ.*, 2023, 48, 26107-26118. <https://doi.org/10.1016/j.ijhydene.2023.03.146>
- [7] Y. Q. Zhang, B. Ouyang, G. K. Long, H. Tan, Z. Wang, Z. Zhang, W. B. Gao, R. S. Rawat, H. J. Fan, Enhancing bifunctionality of CoN nanowires by Mn doping for long-lasting Zn-air batteries, *Sci. China Chem.*, 2020, 63, 890-896.

<https://doi.org/10.1007/s11426-020-9739-2>

[8] J. Sun, N. Wang, Z. Z. Qiu, L. X. Xing, L. Du, Recent progress of non-noble metal catalysts for oxygen electrode in Zn-air batteries: A mini review, *Catalysts*, 2022, 12, 843.

<https://doi.org/10.3390/catal12080843>

[9] H. C. Xu, X. Y. Li, W. X. Hu, Z. H. Yu, H. R. Zhou, Y. M. Zhu, L. F. Lu, C. L. Si, Research progress of highly efficient noble metal catalysts for the oxidation of 5-hydroxymethylfurfural, *ChemSusChem*, 2022, 15, e202200352.

<https://doi.org/10.1002/cssc.202200352>

[10] K. Loza, M. Heggen, M. Epple, Synthesis, structure, properties, and applications of bimetallic nanoparticles of noble metals, *Adv. Funct. Mater.*, 2020, 30, 1909260.

<https://doi.org/10.1002/adfm.201909260>

[11] P. F. Oliveira, R. M. Torresi, F. Emmerling, P. H. Camargo, Challenges and opportunities in the bottom-up mechanochemical synthesis of noble metal nanoparticles, *J. Mater. Chem. A*, 2020, 8, 16114-16141. <https://doi.org/10.1039/D0TA05183G>

[12] H. Y. Chang, Z. J. Liang, L. Wang, C. Wang, Research progress in improving the oxygen evolution reaction by adjusting the 3d electronic structure of transition metal catalysts, *Nanoscale*, 2022, 14, 5639-5656. <https://doi.org/10.1039/D2NR00522K>

[13] X. Q. Xu, R. Wang, C. Feng, X. Zhang, N. N. Wang, Q. Zhang, M. Xie, Y. C. Xu, Y. Jiao, J. R. Chen, Controlling the electronic structure of Fe-MOF electrocatalyst for enhanced water splitting and urea oxidation: A plasma-assisted approach, *J. Colloid. Interf. Sci.*, 2023, 650, 1290-1300.

<https://doi.org/10.1016/j.jcis.2023.07.034>

[14] J. H. Park, K. Kim, X. Y. Wang, M. Huda, Y. Sawada, Y. Matsuo, N. Saito, M. Kawasumi, Highly durable graphene-encapsulated platinum-based electrocatalyst for oxygen reduction reactions synthesized by solution plasma process, *J. Power Sources*, 2023, 580, 233419.

<https://doi.org/10.1016/j.jpowsour.2023.233419>

[15] J. Ding, W. Y. Li, Q. Q. Chen, J. F. Liu, S. Tang, Z. W. Wang, L. W. Chen, H. M. Zhang, Sustainable ammonia synthesis from air by the integration of plasma and electrocatalysis techniques, *Inorg. Chem. Front.*, 2023, 10, 5762-5771.

<https://doi.org/10.1039/D3QI00915G>

[16] Y. Luo, Y. H. Wu, C. Huang, C. Menon, S. P. Feng, P. K. Chu, Plasma modified and tailored defective electrocatalysts for water electrolysis and hydrogen fuel cells, *EcoMat*, 2022, 4, e12197.

<https://doi.org/10.1002/eom2.12197>

[17] V. S. Gharahshiran, Y. Zheng, Sustainable ammonia synthesis: An in-depth review of non-thermal plasma technologies, *J. Energy Chem.*, 2024, 96, 1-38.

<https://doi.org/10.1016/j.jechem.2024.04.018>

[18] Y.Q. Zhang, B. Ouyang, G.K. Long, H. Tan, Z. Wang, Z. Zhang, W.B. Gao, R.S. Rawat, H.J. Fan, Enhancing bifunctionality of CoN nanowires by Mn doping for long-lasting Zn-air batteries, *Sci. China Chem.*, 2020, 63, 890-896.

<https://doi.org/10.1007/s11426-020-9739-2>

[19] Z.Y. Shao, Q. Zhu, Y. Sun, Y. Zhang, Y.L. Jiang, S.Q. Deng, W. Zhang, K.K. Huang, S.H. Feng, Phase-reconfiguration-induced NiS/NiFe₂O₄ composite for performance-enhanced zinc-air batteries, *Adv. Mater.*, 2022, 34, 2110172.

<https://doi.org/10.1002/adma.202110172>

[20] H. Li, J. H. Wang, T. Tjardts, I. Barg, H. Y. Qiu, M. Müller, J. Krahmer, S. Askari, S. Veziroglu, C. Aktas, L. Kienle, J. Benedikt, Plasma-engineering of oxygen vacancies on NiCo₂O₄ nanowires with enhanced bifunctional electrocatalytic performance for rechargeable zinc-air battery, *Small*, 2024, 2310660.

<https://doi.org/10.1002/sml.202310660>

[21] R. Q. Cheng, F. Wang, M. Jiang, K. Q. Li, T. S. Zhao, P. Y. Meng, J. Yang, C. P. Fu, Plasma-assisted synthesis of defect-rich O and N codoped carbon nanofibers with manganese oxides as an efficient oxygen reduction electrocatalyst for aluminum–air batteries, *ACS Appl. Mater. Interfaces*, 2021, 13, 37123-37132.

<https://doi.org/10.1021/acsami.1c09067>

[22] R. Kulkarni, L.P. Lingamdinne, R.R. Karri. Z.H. Momin, J.R. Koduru, Y.Y. Chang, Catalytic efficiency of LDH@carbonaceous hybrid nanocomposites towards water splitting mechanism: Impact of plasma and its significance on HER and OER activity, *Coordin. Chem. Rev.*, 2023, 497, 215460. <https://doi.org/10.1016/j.ccr.2023.215460>

[23] Y.B. Liu, Z.Q. Jiang, Z.J. Jiang, Plasma-assisted formation of oxygen defective NiCoO/NiCoN heterostructure with improved ORR/OER activities for highly durable all-solid-state zinc-air batteries, *Adv. Funct. Mater.*, 2023, 33, 2302883.

<https://doi.org/10.1002/adfm.202302883>

[24] C. Schulze, H. Li, L. Mohn, M. Müller, J. Benedikt, Chamber with inverted electrode geometry for measuring and control of ion flux-energy distribution functions, *Plasma*, 2022, 5, 295-305.

<https://doi.org/10.3390/plasma5030023>

[25] P. Vinchon, X. Glad, G. R. Bigras, A. Sarkissian, R. Martel, L. Stafford, Plasma–graphene interactions: combined effects of positive ions, vacuum-ultraviolet photons, and metastable species, *J. Phys. D: Appl. Phys.*, 2021, 54, 295202.

<https://doi.org/10.1088/1361-6463/abfe3b>

[26] P. Vinchon, X. Glad, G. R. Bigras, R. Martel, L. Stafford, Preferential self-healing at grain boundaries in plasmatreated graphene, *Nat. Mater.*, 2021, 20, 49-54.

<https://doi.org/10.1038/s41563-020-0738-0>

[27] S. G. Walton, S. C. Hernández, D. R. Boris, T. B. Petrova, G. M. Petrov, Electron beam generated plasmas for the processing of graphene, *J. Phys. D: Appl. Phys.*, 2017, 50, 354001.

<https://doi.org/10.1088/1361-6463/aa7d12>

[28] F. Zhao, Y. Raitses, X. Yang, A. Tan, C. G. Tully, High hydrogen coverage on graphene via low temperature plasma with applied magnetic field, *Carbon*, 2021, 177, 244-251.

<https://doi.org/10.1016/j.carbon.2021.02.084>

[29] A. A. Shiryayev, A. L. Trigub, E. N. Voronina, K. O. Kvashnina, V. L. Bukhovets, Behavior of implanted Xe, Kr and Ar in nanodiamonds and thin graphene stacks: experiment and modeling, *Phys. Chem. Chem. Phys.*, 2021, 23, 21729-21737.

<https://doi.org/10.1039/D1CP02600C>

[30] A. Arabsaebi, P. Akbarian, M. Kheirmand, Carbon fiber paper based on composites of carbon and polyacrylonitrile for fuel cell application, *Carbon Trends*, 2024, 14, 100335.

<https://doi.org/10.1016/j.cartre.2024.100335>

[31] G. F. Tang, B. Wang, H. T. Wang, J. J. Zhang, J. H. Jin, S. L. Yang, G. Li, Z. G. Shen, Optimal fabrication of carbon paper by different lengths of chopped carbon fibers and its enhanced performance in proton exchange membrane fuel cell, *Int. J. Hydrogen. Energ.*, 2024, 50, 897-907.

<https://doi.org/10.1016/j.ijhydene.2023.09.150>

[32] M. Fontana, R. Ramos, A. Morin, J. Dijon, Direct growth of carbon nanotubes forests on carbon fibers to replace microporous layers in proton exchange membrane fuel cells, *Carbon*, 2021, 172, 762-771.

<https://doi.org/10.1016/j.carbon.2020.10.049>

[33] N. Bhandary, P. P. Ingole, S. Basu, Electrosynthesis of Mn-Fe oxide nanopetals on carbon paper as bi-functional electrocatalyst for oxygen reduction and oxygen evolution reaction, *Int. J. Hydrogen. Energ.*, 2018, 43, 3165-3171.

<https://doi.org/10.1016/j.ijhydene.2017.12.102>

[34] C. M. Liu, C. X. Sun, Y. J. Gao, W. J. Lan, S. W. Chen, Improving the electrochemical properties of carbon paper as cathodes for microfluidic fuel cells by the electrochemical activation in different solutions, *ACS Omega*, 2021, 6, 19153-19161.

<https://doi.org/10.1021/acsomega.1c02507>

[35] H. Q. Ji, M. F. Wang, S. S. Liu, H. Sun, J. Liu, T. Qian, C. L. Yan, Pyridinic and graphitic nitrogen-enriched carbon paper as a highly active bifunctional catalyst for Zn-air batteries, *Electrochimica Acta*, 2020, 334, 135562.

<https://doi.org/10.1016/j.electacta.2019.135562>

[36] V. L. P. Guerra, V. Valeš, J. Mikšátko, J. Pišek, K. A. Drogowska-Horná, O. Volochanskyia, M. Kalbáč, The use of sample positioning to control defect creation by oxygen plasma in isotopically labelled bilayer graphene membranes, *RSC Advances*, 2021, 11, 10316-10322.

<https://doi.org/10.1039/D1RA01249E>

[37] M. Müller, M. Bouša, Z. Hájková, M. Ledinský, A. Fejfar, K. Drogowska-Horná, M. Kalbáč, O. Frank, Transferless Inverted Graphene/Silicon Heterostructures Prepared by Plasma-Enhanced Chemical Vapor Deposition of Amorphous Silicon on CVD Graphene, *nanomaterials*, 2020, 10, 589.

<https://doi.org/10.3390/nano10030589>

[38] H. Jiang, J. X. Gu, X. S. Zheng, M. Liu, X. Q. Qiu, L. B. Wang, W. Z. Li, Z. F. Chen, X. B. Ji, J. Li, Defect-rich and ultrathin N doped carbon nanosheets as advanced trifunctional metal-free electrocatalysts for the ORR, OER and HER, *Energy Environ. Sci.*, 2019, 12, 322-333.

<https://doi.org/10.1039/C8EE03276A>

[39] G. Massaglia, A. Sacco, M. Castellino, A. Chiodoni, F. Frascella, S. Bianco, C.F. Pirri, M. Quaglio, N-doping modification by plasma treatment in polyacrylonitrile derived carbon-based nanofibers for oxygen reduction reaction, *Int. J. Hydrogen. Energ.*, 2021, 46, 13845-13854.

<https://doi.org/10.1016/j.ijhydene.2020.09.149>

[40] B. Ouyang, Y. Q. Zhang, Y. Wang, Z. Zhang, H. J. Fan, R. S. Rawat, Plasma surface functionalization induces nanostructuring and nitrogen-doping in carbon cloth with enhanced energy storage performance, *J. Mater. Chem. A*, 2016, 4, 17801.

<https://doi.org/10.1039/C6TA08155J>

[41] P. Chabert, N. Braithwaite, *Physics of Radio-Frequency Plasmas*, Cambridge University Press, ISBN: 978-0-521-76300-4.

<https://doi.org/10.1017/CBO9780511974342>

[42] K. H. Bai, D. S. Lee, H. Y. Chang, H. S. Uhm, Control and analysis of ion species in N₂ inductively coupled plasma with inert gas mixing, *Appl. Phys. Lett.*, 2002, 80, 3907-3909.

<https://doi.org/10.1063/1.1479452>

[43] M. Wang, X.F. Gao, R. Su, P. He, Y. Y. Cheng, K. Li, D. B. Mi, X. P. Zhang, X. L. Zhang, H. W. Chen, R. G. Cooks, Abundant production of reactive water radical cations under ambient conditions, *CCS Chem.*, 2022, 4, 1224-1231.

<https://doi.org/10.31635/ccschem.021.202101427>

[44] L. L. Alves, L. Marques, C. D. Pintassilgo, G. Wattieaux, E. Es-sebbar, J. Berndt, E. Kovacević, N. Carrasco, L. Boufendi, G. Cernogora, Capacitively coupled radio-frequency discharges in nitrogen at low pressures, *Plasm Sources Sci. Technol.*, 2012, 21, 045008.

<https://doi.org/10.1088/0963-0252/21/4/045008>

[45] V. G. Anicich, D. B. Milligan, D. A. Fairley, M. J. McEwan, Termolecular ion–molecule reactions in titan's atmosphere, I: Principal ions with principal neutrals, *Icarus*, 2000, 146, 118-124.

<https://doi.org/10.1006/icar.2000.6353>

[46] S. K. Tang, W. C. Wang, J. H. Liu, X. F. Yang, Y. Wu, Diagnosis of positive ions from the near-

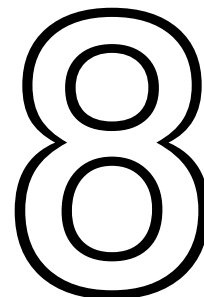
cathode region in a high-voltage pulsed corona discharge N₂ plasma, J. Vac. Sci. Technol. A, 2000, 18, 2213-2216. <https://doi.org/10.1116/1.1286362>

无边落木萧萧下，不尽长江滚滚来。

-----杜甫

The boundless forest sheds its leaves shower by shower;
The endless river rolls its waves hour after hour.

-----Fu DU (Translated by Yuanzhong Xu)



CONCLUSION

In this thesis, plasma surface modification was conducted to synthesize highly efficient, eco-friendly and low-cost bifunctional electrocatalysts for both OER and ORR at air cathodes in rechargeable zinc-air batteries. The self-supported material of NiCo₂O₄ nanowires grown on commercial carbon paper was used as the pristine electrocatalyst which was synthesized by a hydrothermal method followed by an annealing process. Plasma technologies were employed to enhance the electrocatalytic performance of the catalyst by the strategies of defect engineering, heteroatom doping, and interface engineering.

Firstly, the pristine catalyst was modified by N₂ plasma with varying durations. The N₂ plasma modification successfully introduced the N atoms into the NiCo₂O₄ structure without causing any significant changes to its morphology or special surface area. Electrochemical results show that the N-doped catalyst exhibits better OER and ORR performance than the pristine catalyst due to the increased active sites and enhanced surface conductivity. Moreover, the optimal treatment duration was determined to be 2 min and the over-treatment of N₂ plasma reduced the

electrocatalytic performance of the catalyst.

Secondly, H₂/Ar plasma was used to modify NiCo₂O₄ nanowires. Compared to Ar plasma, the plasma based on a mixed gas of H₂ and Ar (1:1) generated more oxygen vacancies at the catalyst surfaces owing to the combined effect of Ar-related ions and H-radicals present in the plasma. Following the generation of oxygen vacancies, more Co²⁺ and Ni²⁺ ions were found at the NiCo₂O₄ surfaces, which have been accepted as active sites for OER and ORR. As a result, the optimal treatment time for H₂/Ar plasma on NiCo₂O₄ nanowires was 7.5 min and the longer treatment duration has led to a decline in catalyst performance.

Thirdly, although the self-supported NiCo₂O₄-based catalyst presented excellent OER performance, its ORR performance is still unsatisfactory. To improve its ORR performance, high-dispersion Pt nanoparticles were coated on its surfaces by an impregnation-plasma reduction process. The results demonstrate that NiCo₂O₄ nanowires treated with Ar plasma can anchor more Pt nanoparticles on their surfaces owing to the increased oxygen vacancies and specific surface area. The electrochemical results show that NiCo₂O₄ nanowires after Ar plasma treatment and Pt deposition exhibited excellent bifunctional electrocatalytic activities, even exceeding that of noble-metal-based catalysts.

Finally, to gain greater insight into the treatment process by plasma, a novel setup was constructed and an energy-selective mass spectrometer was connected to the substrate holder near the sample and used to monitor the plasma properties during the modification process. First, single-layer graphene was treated by N₂ ICP under the variation of reactor pressures. A lower pressure results in a higher ion energy, while increasing the pressure makes the plasma sheath more and more collisional and reduces the ion energy. Raman results demonstrate that the N₂ plasma at high reactor pressures, 10 Pa and 20 Pa, with dominant ion energy below 5 eV cannot obviously modify the single-layer graphene. Starting with 7.5 Pa pressure, the treatment results in defect generation on the graphene surface. The treatment at the lowest pressure of 1.5 Pa removed the graphene from the substrate. Second, carbon papers were selected as the pristine ORR catalysts. The application of a DC

bias to the chamber wall successfully controlled the ion energy of N₂ plasma. The electrochemical results revealed that the ion energy as high as 83 eV could not reproduce the ORR performance boost.

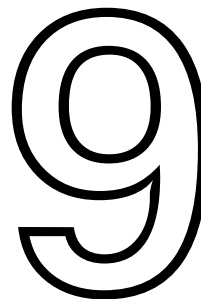
For further research, some advanced characterization techniques, such as in-situ TEM, FTIR, and XAFS, can be applied to gain a deeper understanding of the redox mechanism of the catalyst in the real electrochemical catalytic process. Moreover, in Chapter 7, a higher ion energy in the ICP reactor is necessary to further study the treatment process by N₂ plasma.

海内存知己，天涯若比邻。

-----王勃

When one has a close friend in this world, the far ends of
heaven are like next door.

-----Bo Wang (Translated by Yuanchong Xu)



Appendix

9.1 Nitrogen-doped NiCo₂O₄ nanowires on carbon paper as a self-supported air cathode for rechargeable Zn-air batteries

Supporting Information for

Nitrogen-doped NiCo₂O₄ nanowires on carbon paper as a self-supported air cathode for rechargeable Zn-air batteries

He Li¹, Sadegh Askari², Jihao Wang³, Niklas Wolff^{4,5}, Malte Behrens^{3,5}, Lorenz Kienle^{4,5}, Jan Benedikt^{1,5*}

¹ Institute of Experimental and Applied Physics, Kiel University, Leibnizstraße 19, D-24098 Kiel, Germany

² Department of Fiber and Polymer Technology, KTH Royal Institute of Technology, SE-10044, Stockholm, Sweden

³ Institute of Inorganic Chemistry, Kiel University, Max-Eyth-Straße 2, D-24118 Kiel, Germany

⁴ Department of Materials Science, Chair for Synthesis and Real Structure, Faculty of Engineering, Kiel University, Kaiserstraße 2, D-24143 Kiel, Germany

⁵ Kiel Nano, Surface and Interface Science KiNSIS, Kiel University, Christian-Albrechts-Platz 4, D-24118 Kiel, Germany

*Corresponding author.

Supplementary Figures

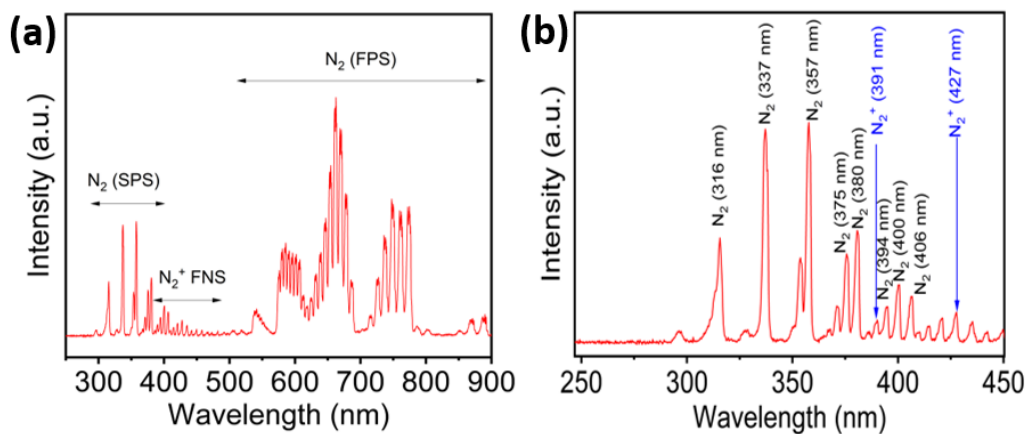


Fig. S1 (a) Optical emission spectra of N_2 plasma in the spectral range (a) from 250 to 900 nm, (b) from 250 to 450 nm. Plasma power 200 W, pressure 20 Pa, frequency 27.12 MHz, gas flow 8 sccm of N_2 gas.

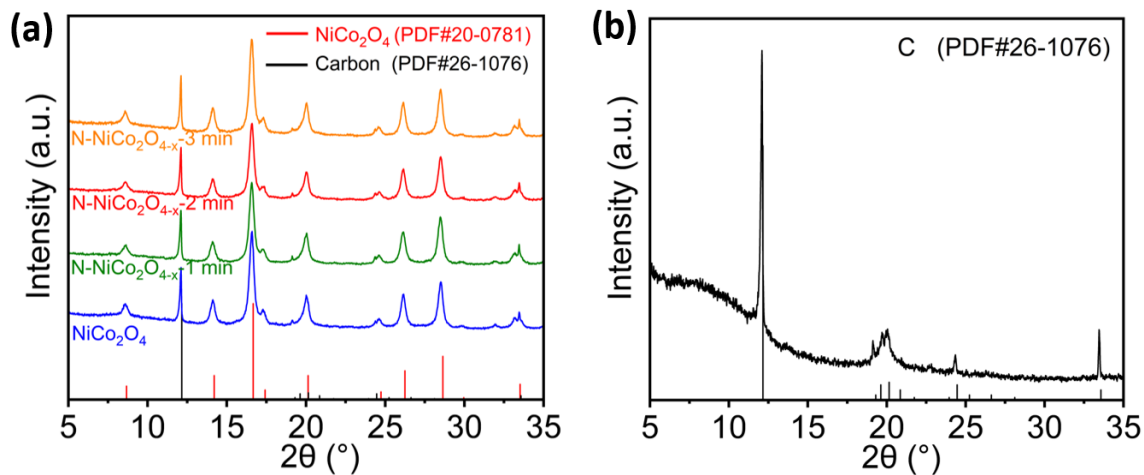


Fig. S2 (a) XRD diffractograms of $NiCo_2O_4$ nanowires before and after N_2 plasma treatment. (b) XRD pattern of carbon paper.

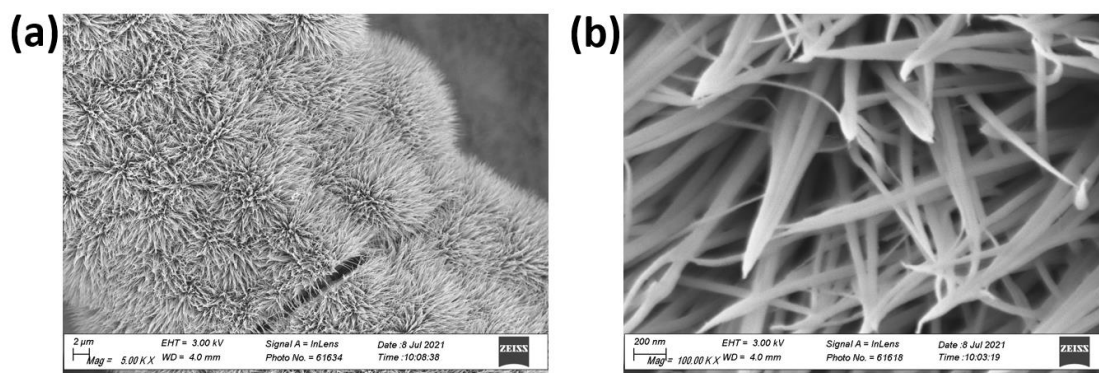


Fig. S3 SEM images of N-NiCo₂O_{4-x}-2 min, (a) Low-magnification, (b) High-magnification.

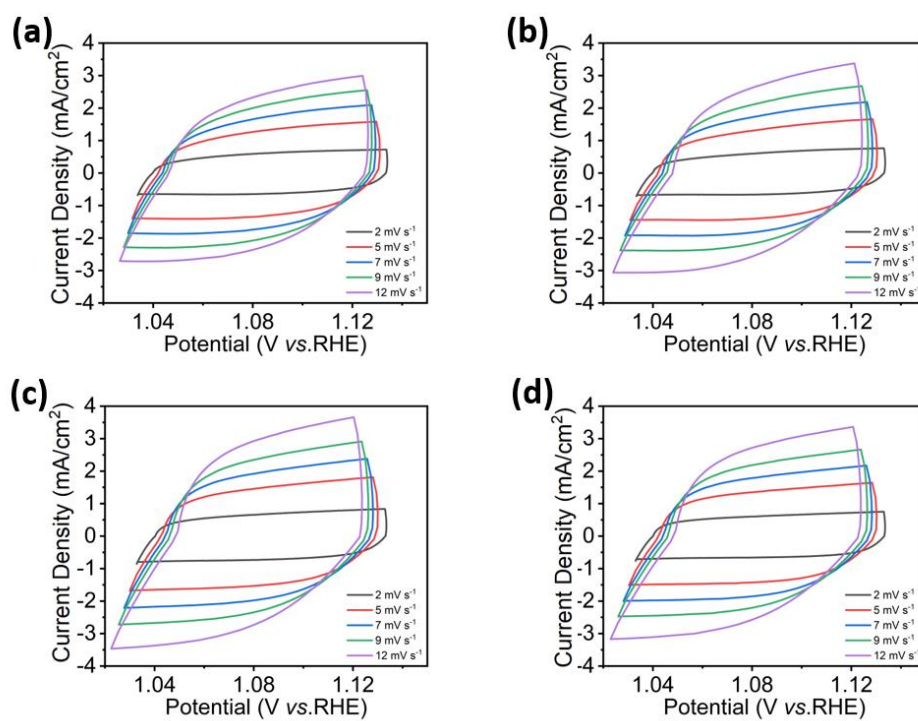


Fig. S4 CV curves from 1.03 to 1.13 V at different scan rates of (a) NiCo₂O₄, (b) N-NiCo₂O_{4-x}-1 min, (c) N-NiCo₂O_{4-x}-2 min, (d) N-NiCo₂O_{4-x}-3 min.

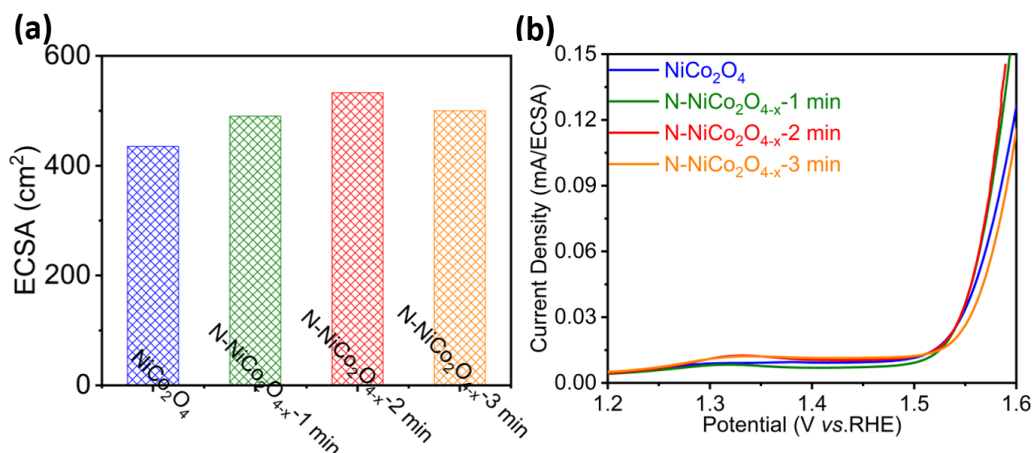


Fig. S5 (a) The ECSA values and (b) polarization curves normalized to ECSA for all samples.

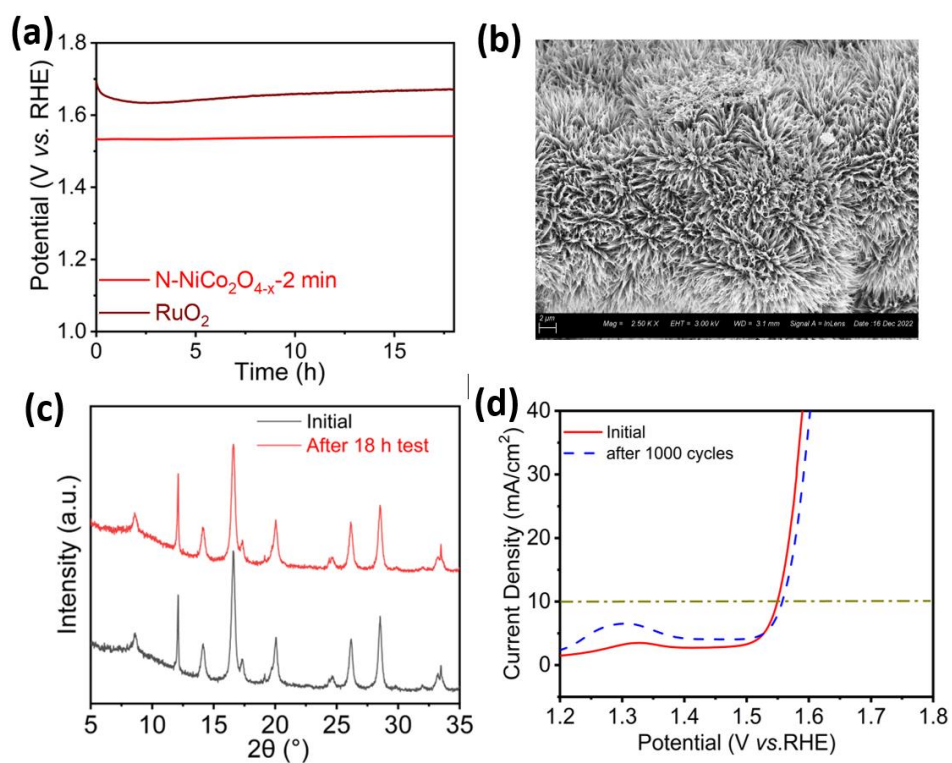


Fig. S6 (a) Stability test of the $\text{N-NiCo}_2\text{O}_{4-x}$ -2 min and RuO_2 samples at 10 mA cm^{-2} for OER in 1 M electrolyte, (b) SEM images of $\text{N-NiCo}_2\text{O}_{4-x}$ -2 min sample after 18 h test, (c) XRD diffractograms of $\text{N-NiCo}_2\text{O}_{4-x}$ -2 min after 18 h test, (d) OER LSV plots of $\text{N-NiCo}_2\text{O}_{4-x}$ -2 min before and after 1000 CV cycles.

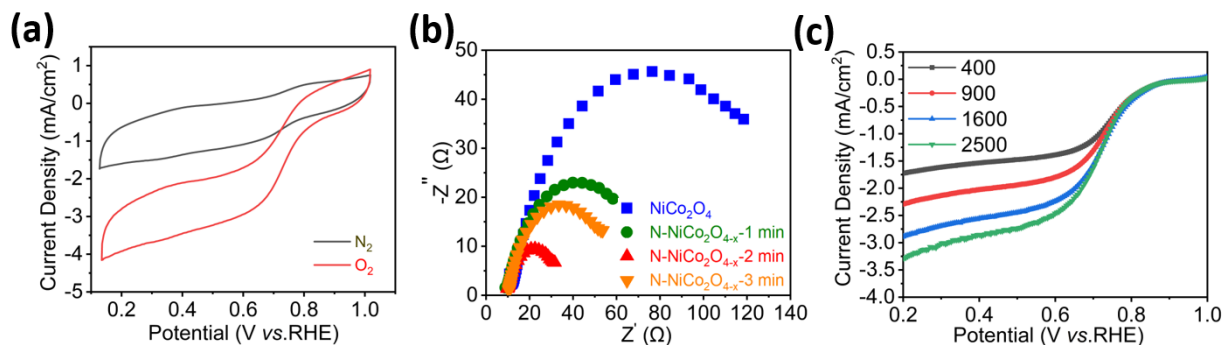


Fig. S7 (a) CV curves of N-NiCo₂O_{4-x}-2 min tested in N₂- and O₂-saturated 1 M KOH, (b) EIS plots of all catalysts tested in O₂-saturated 1 M KOH, (c) LSV of N-NiCo₂O_{4-x}-2 min at different rotation speeds,

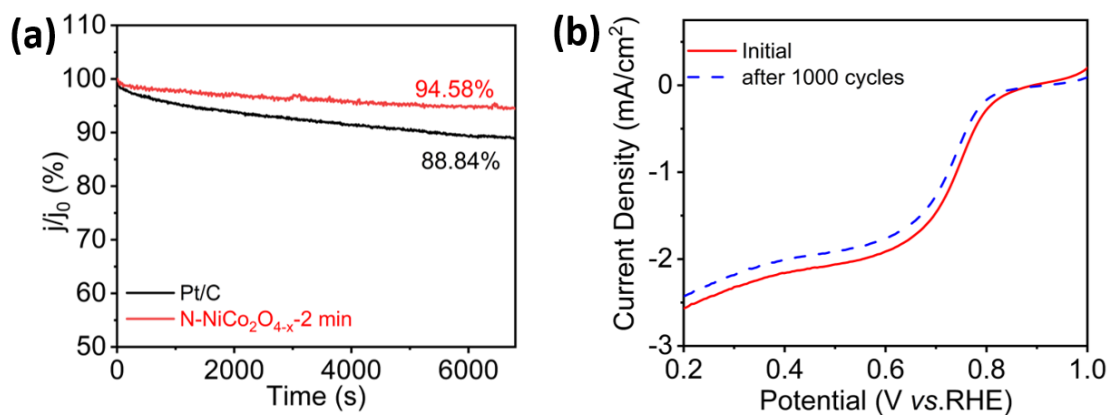


Fig. S8 (a) Stability test of Pt/C and N-NiCo₂O_{4-x}-2 min for ORR in 1 M electrolyte, (b) ORR LSV plots of N-NiCo₂O_{4-x}-2 min before and after 1000 CV cycles.

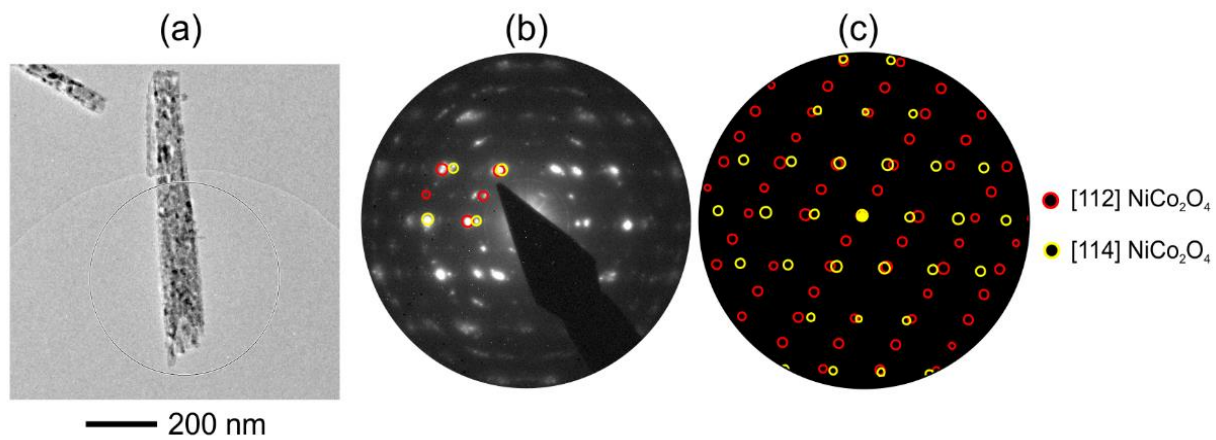


Fig. S9 Evidence for nanoscale crystalline texture. (a) TEM image of a single polycrystalline nanowire. (b) SAED pattern of this nanowire. The pattern shows discrete reflection spots indicating a preferred orientation of the individual nanosized crystals. (c) Simulation of the spot patterns identifies two of at least three major crystalline components as NiCo₂O₄ phase with [112] and [114] orientations.

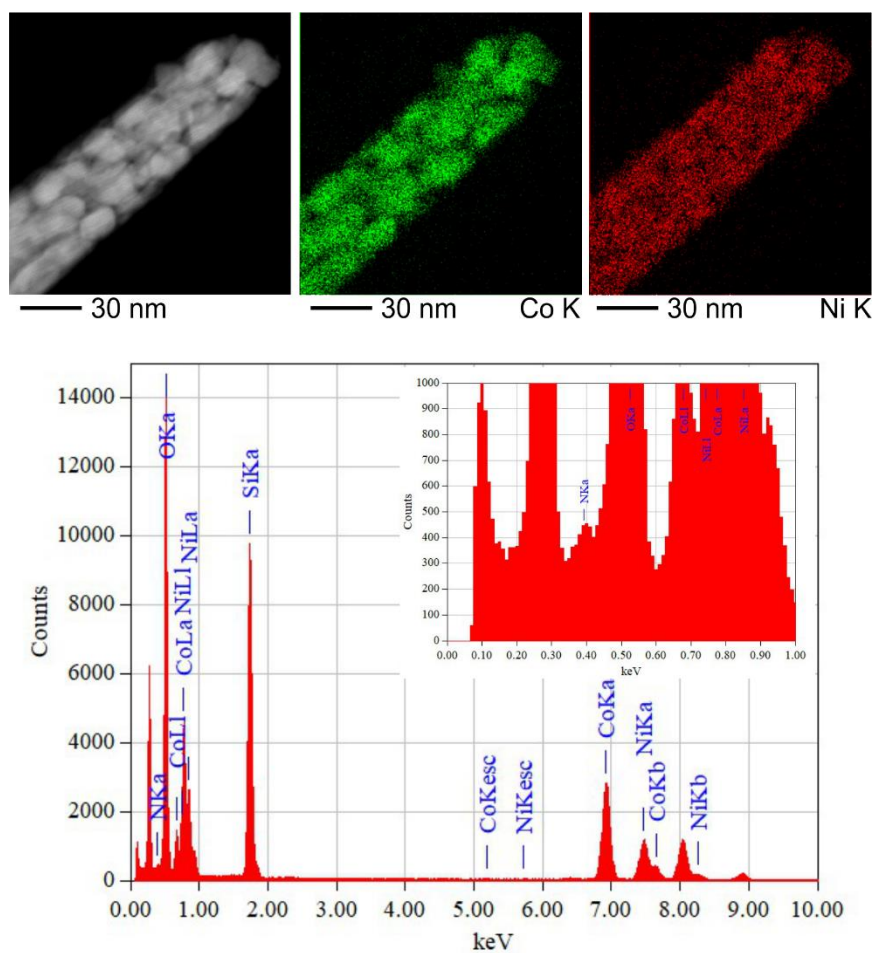
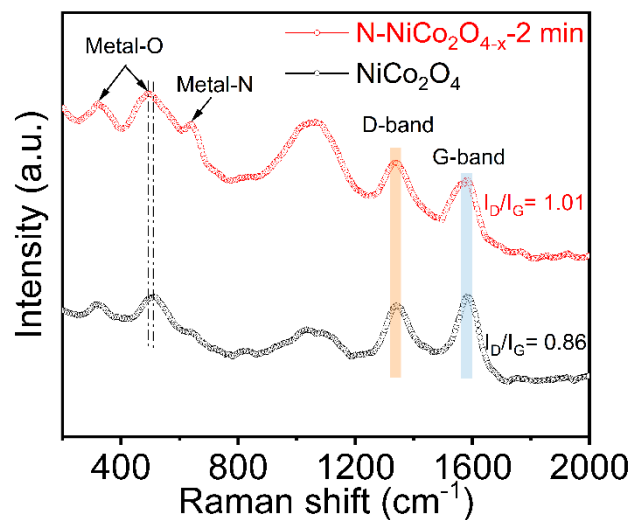
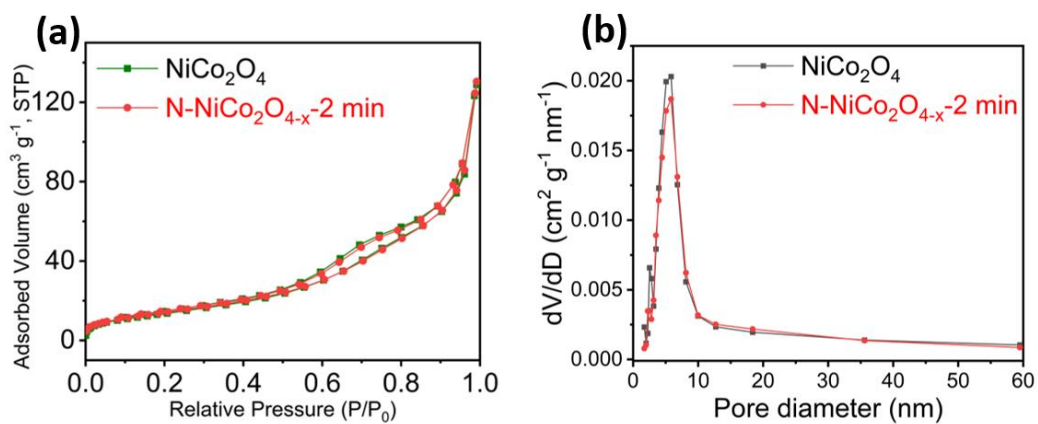


Fig. S10 STEM EDS mapping of a single N-NiCo₂O_{4-x}-2 min nanowire. The elemental maps of Co and Ni reveal a homogenous distribution consistent with the ternary phase compound. The corresponding EDS sum spectrum shows a low intensity peak of collected X-ray signals of nitrogen which is indicating subtle doping of the nanowire structures.

Fig. S11 Raman spectra of NiCo₂O₄ and N-NiCo₂O_{4-x}-2 min.Fig. S12 N₂ adsorption-desorption isotherms and (b) pore size distribution of NiCo₂O₄ and N-NiCo₂O_{4-x}-2

min.



Fig. S13 The primary zinc-air battery of N-NiCo₂O_{4-x}-2 min.

9 Appendix

Table S1 Comparison of the bifunctional electrocatalytic performances of our work and other similar reported catalysts

Catalysts	$E_{j=10}$ (V vs. RHE)		$E_{1/2}$ (V vs. RHE)		ΔE (V)	Refs.
	^a 0.1 M KOH		^a 0.1 M KOH			
	^b 1 M KOH		^b 1 M KOH			
NiCo ₂ O ₄	^b 1.55	^b 0.70	0.85	This work		
N-NiCo ₂ O _{4-x} -1 min	^b 1.53	^b 0.72	0.79	This work		
N-NiCo ₂ O _{4-x} -2 min	^b 1.53	^b 0.75	0.78	This work		
N-NiCo ₂ O _{4-x} -3 min	^b 1.54	^b 0.74	0.80	This work		
porous-Ni/NiO	^a 1.49	^a 0.75	0.74	[S1]		
NiCo ₂ S ₄	^a 1.60	^a 0.80	0.80	[S2]		
NiO/CoN	^b 1.53	^a 0.68	0.85	[S3]		
N-NiCo ₂ O ₄	^a 1.65	^a 0.63	1.02	[S4]		
CoMn ₂ O ₄	^b 1.57	^a 0.83	0.74	[S5]		
CoMn _{2-x} Cr _x O ₄	^b 1.65	^a 0.82	0.83	[S6]		
Mn-CoN-1.5	^a 1.63	^a 0.65	0.98	[S7]		
Fe ₃ Co ₇ /N-CNTs@CC	^a 1.64	^a 0.78	0.86	[S8]		
Zn _{0.4} Ni _{0.6} Co ₂ O ₄ /NCNTs	^a 1.64	^a 0.78	0.86	[S9]		
N-NiO	^b 1.50	^a 0.69	0.81	[S10]		

9 Appendix

Table S2 Comparison of zinc-air batteries of our work and other binder-free catalysts

Catalysts	Electrolyte	Peak power density (mW cm ⁻²)	Charge/discharge Current (mA cm ⁻²)	Stability (h)	Refs.
N-NiCo ₂ O _{4-x} -2 min	6.0 M KOH + 0.2 M ZnAc	67	5	45	This work
NiO/CoN	6.0 M KOH	79.6	Charge: 50 Discharge: 1	8	S3
NiCo ₂ O ₄ @FeNi LDH	6.0 M KOH + 0.2 M ZnAc	130	10	35	S11
NiCo ₂ O ₄ nanosheets	6.0 M KOH + 0.2 M ZnAc	102	10	30	S12
Mn _{0.5} Ni _{0.5} Co ₂ O ₄ 3DOM	6.0 M KOH + 0.2 M ZnAc	117	10	21	S13
NCFPO-350	6.0 M KOH + 0.2 M ZnAc	74.6	10	30	S14
N, S-CC	6.0 M KOH + 0.2 M ZnAc	42	20	40	S15

Supplementary References

[S1] P.T. Liu, J.Q. Ran, B.R. Xia, S.B. Xi, D.Q. Gao, J. Wang, Bifunctional oxygen electrocatalyst of mesoporous Ni/NiO nanosheets for flexible rechargeable Zn-air batteries, *Nano-Micro Lett.*, 2020, 12, 68. <https://doi.org/10.1007/s40820-020-0406-6>

[S2] X.P. Han, X.Y. Wu, C. Zhong, Y.D. Deng, N.Q. Zhao, W.B. Hu, NiCo₂S₄ nanocrystals anchored on nitrogen-doped carbon nanotubes as a highly efficient bifunctional electrocatalyst for rechargeable zinc-air batteries. *Nano Energy*, 2017, 31, 541-550. <https://doi.org/10.1016/j.nanoen.2016.12.008>

[S3] J. Yin, Y.X. Li, F. Lv, Q.H. Fan, Y.Q. Zhao, Q.H. Zhang, W. Wang, F.Y. Cheng, P.X. Xi, S.J. Guo, NiO/CoN porous nanowires as efficient bifunctional catalysts for Zn-air batteries, *ACS Nano*, 2017, 11, 2275-2283. <https://doi.org/10.1021/acsnano.7b00417>

[S4] J.J. Bian, X.P. Cheng, X.Y. Meng, J. Wang, J.G. Zhou, S.Q. Li, Y.F. Zhang, C.W. Sun, Nitrogen-doped NiCo₂O₄ microsphere as an efficient catalyst for flexible rechargeable zinc-air batteries and self-charging power system, *ACS Appl. Energy Mater.*, 2019, 2, 2296-2304. <https://doi.org/10.1021/acsaem.9b00120>

[S5] X. Chen, Z.H. Yan, M. Yu, H.M. Sun, F.M. Liu, Q.Y. Zhang, F.Y. Cheng, J. Chen, Spinel oxide nanoparticles embedded in nitrogen-doped carbon nanofibers as a robust and self-standing bifunctional oxygen cathode for Zn-air batteries, *J. Mater. Chem. A*, 2019, 7, 24868. <https://doi.org/10.1039/C9TA09873A>

[S6] W.J. Liu, J. Bao, L. Xu, M.L. Guan, Y.C. Lei, Chromium-modulated multifunctional electrocatalytic activities of spinel oxide for Zn-air batteries and overall water splitting, *J. Power Sources*, 2020, 479, 229099. <https://doi.org/10.1016/j.jpowsour.2020.229099>

[S7] Y.Q. Zhang, B. Ouyang, G.K. Long, H. Tan, Z. Wang, Z. Zhang, W.B. Gao, R.S. Rawat, H.J. Fan, Enhancing bifunctionality of CoN nanowires by Mn doping for long-lasting Zn-air batteries. *Sci China Chem*, 2020, 63, 890-896. <https://doi.org/10.1007/s11426-020-9739-2>

[S8] Z.Y. Li, H.Q. Yang, H. Sun, S. Liang, G.L. Lu, Z.N. Liu, S.Q. Kou, Highly nitrogen-doped carbon nanotube nanoarrays as self-supported bifunctional electrocatalysts for rechargeable and flexible zinc-air batteries, *ACS Sustainable Chem. Eng.*, 2021, 9, 4498-4508. <https://doi.org/10.1021/acssuschemeng.0c08727>

[S9] X.T. Wang, T. Ouyang, L. Wang, J.H. Zhong, Z.Q. Liu, Surface reorganization on electrochemically-induced Zn-Ni-Co spinel oxides for enhanced oxygen electrocatalysis, *Angew. Chem. Int. Ed.* 2020, 59, 6492-6499. <https://doi.org/10.1002/anie.202000690>

[S10] J.M. Qian, X.W. Bai, S.B. Xi, W. Xiao, D.Q. Gao, J.L. Wang, Bifunctional electrocatalytic activity of nitrogen-doped NiO nanosheets for rechargeable zinc-air batteries, *ACS Appl. Mater. Interfaces* 2019, 11, 30865-30871. <https://doi.org/10.1021/acscami.9b08647>

[S11] L. Wan, Z.H. Zhao, X.X. Chen, P.F. Liu, P.C. Wang, Z. Xu, Y.Q. Li, B.G. Wang, Controlled synthesis of bifunctional NiCo₂O₄@FeNi LDH core-shell nanoarray air electrodes for rechargeable zinc-air batteries, *ACS Sustainable Chem. Eng.* 2020, 8, 30, 11079-11087. <https://doi.org/10.1021/acssuschemeng.0c00442>

[S12] W.J. Liu, J. Bao, L. Xu, M.L. Guan, Z.L. Wang, J.X. Qiu, Y.P. Huang, J.X. Xia, Y.C. Lei, H.M. Li, NiCo₂O₄ ultrathin nanosheets with oxygen vacancies as bifunctional electrocatalysts for Zn-air battery, *Appl. Surf. Sci.* 2019, 478, 552-559. <https://doi.org/10.1016/j.apsusc.2019.01.243>

[S13] J. Béjar, L. Álvarez-Contreras, F. Espinosa-Magaña, J. Ledesma-García, N. Arjona, L. G. Arriaga, Zn-air battery operated with a 3DOM trimetallic spinel (Mn_{0.5}Ni_{0.5}Co₂O₄) as the oxygen electrode,

Electrochimica Acta, 2021, 391, 138900. <https://doi.org/10.1016/j.electacta.2021.138900>

[S14] D.S. Pan, P. Chen, L.L. Zhou, J.H. Liu, Z.H. Guo, J.L. Song, Self-template construction of 2D amorphous N-doped CoFe-mesoporous phosphate microsheets for zinc-air batteries, J. Power Sources, 2021, 498, 229859. <https://doi.org/10.1016/j.jpowsour.2021.229859>

[S15] Z. Zhao, Z.K. Yuan, Z.S. Fang, J.H. Jian, J. Li, M.J. Yang, C.S. Mo, Y. Zhang, X.H. Hu, P. Li, S.Y. Wang, W. Hong, Z.K. Zheng, G.F. Ouyang, X.D. Chen, D.S. Yu, In situ activating strategy to significantly boost oxygen electrocatalysis of commercial carbon cloth for flexible and rechargeable zn-air batteries, Adv. Sci., 2018, 5, 1800760. <https://doi.org/10.1002/advs.201800760>

9.2 Plasma engineering of oxygen vacancies on NiCo₂O₄ nanowires with enhanced bifunctional electrocatalytic performance for rechargeable zinc-air batteries

NANO · MICRO
small

Supporting Information

for *Small*, DOI 10.1002/smll.202310660

Plasma-Engineering of Oxygen Vacancies on NiCo₂O₄ Nanowires with Enhanced Bifunctional Electrocatalytic Performance for Rechargeable Zinc-air Battery

*He Li, Jihao Wang, Tim Tjardts, Igor Barg, Haoyi Qiu, Martin Müller, Jan Krahmer, Sadegh Askari, Salih Veziroglu, Cenk Aktas, Lorenz Kienle and Jan Benedikt**

Supporting Information for

Plasma-engineering of Oxygen Vacancies on NiCo₂O₄ Nanowires with Enhanced Bifunctional Electrocatalytic Performance for Rechargeable Zinc-air Battery

He Li¹, Jihao Wang², Tim Tjardts³, Igor Barg³, Haoyi Qiu⁴, Martin Müller¹, Jan Krahmer², Sadegh Askari², Salih Veziroglu^{3,3}, Cenk Aktas³, Lorenz Kienle^{5,7}, Jan Benedikt^{1,7*}

¹ Institute of Experimental and Applied Physics, Kiel University, Leibnizstraße 19, D-24098 Kiel, Germany

² Institute of Inorganic Chemistry, Kiel University, Max-Eyth-Straße 2/Otto-Hahn-Platz 6, D-24118 Kiel, Germany

³ Chair for Multicomponent Materials, Department of Materials Science, Faculty of Engineering, Kiel University, Kaiserstraße 2, D-24143 Kiel, Germany

⁴ Chair for Functional Nanomaterials, Department of Materials Science, Faculty of Engineering, Kiel

¹ Chair for Synthesis and Real Structure, Department of Materials Science, Faculty of Engineering, Kiel University, Kaiserstraße 2, D-24143 Kiel, Germany

² Department of Fiber and Polymer Technology, KTH Royal Institute of Technology, SE-10044, Stockholm, Sweden

³ Kiel Nano, Surface and Interface Science KiNSIS, Kiel University, Christian-Albrechts-Platz 4, D-24118 Kiel, Germany

*Corresponding author.

University, Kaiserstraße 2, D-24143 Kiel, Germany

Supplementary Figures

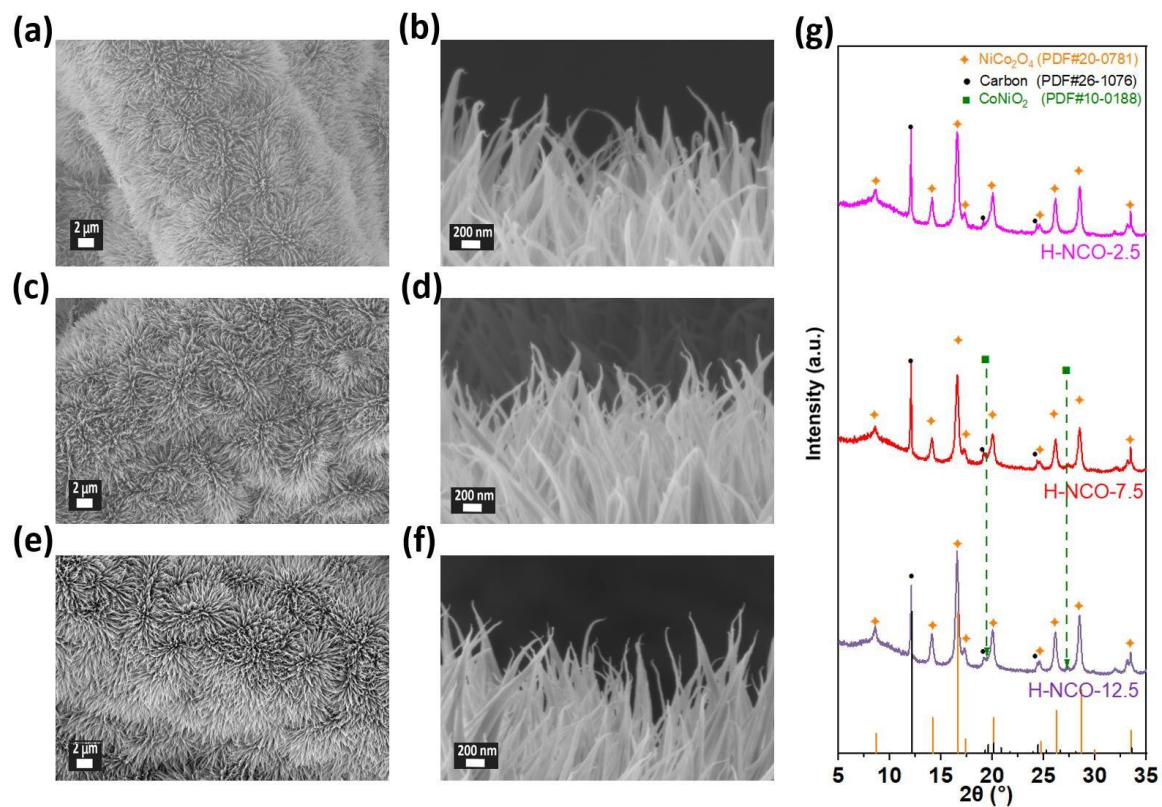


Figure S1. SEM images of (a, b) H-NCO-2.5, (c, d) H-NCO-7.5 (the same data in Figure 2), (e, f) H-NCO-12.5 samples. (g) XRD patterns of H-NCO-2.5, H-NCO-7.5 (the same data in Figure 2) and H-NCO-12.5 samples.

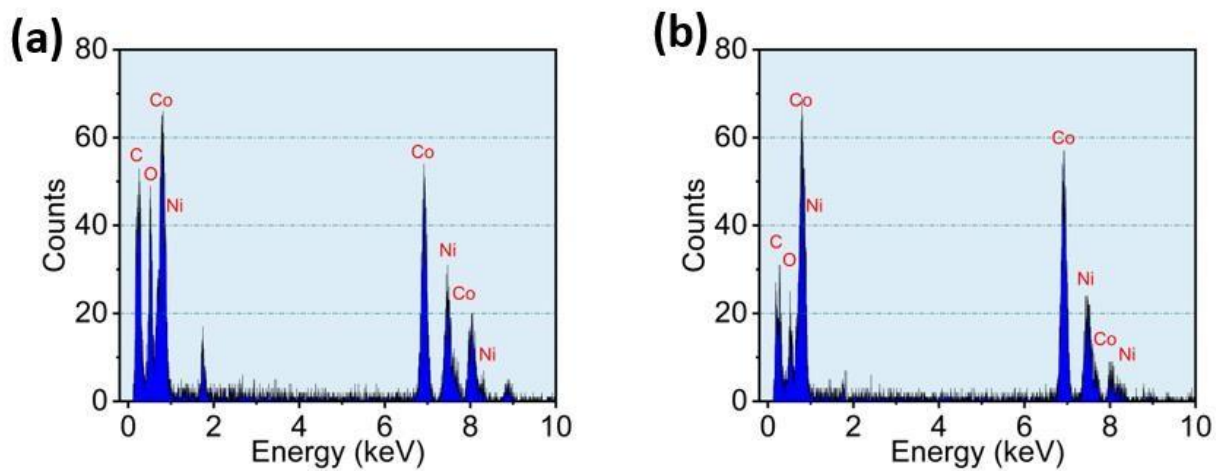


Figure S2. EDS analysis of (a) NCO and (b) H-NCO-7.5 samples.

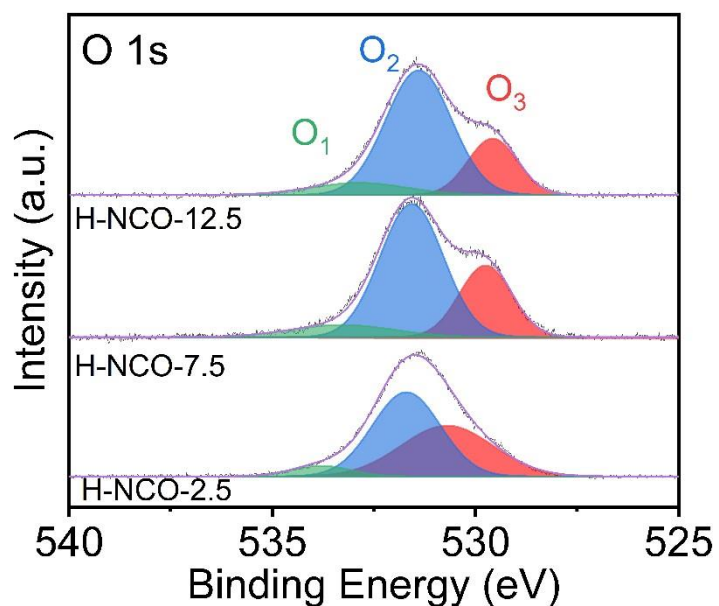


Figure S3. O 1s spectrum of H-NCO-2.5, H-NCO-7.5 (the same data in Figure 2) and H-NCO-12.5 samples.

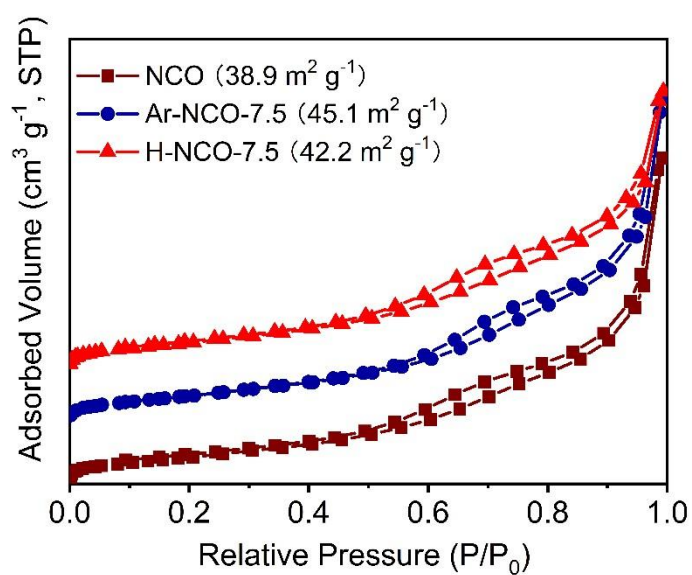


Figure S4. BET results for of H-NCO-2.5, H-NCO-7.5 and H-NCO-12.5 samples (the measured curved have

been shifted in vertical direction for better visibility).

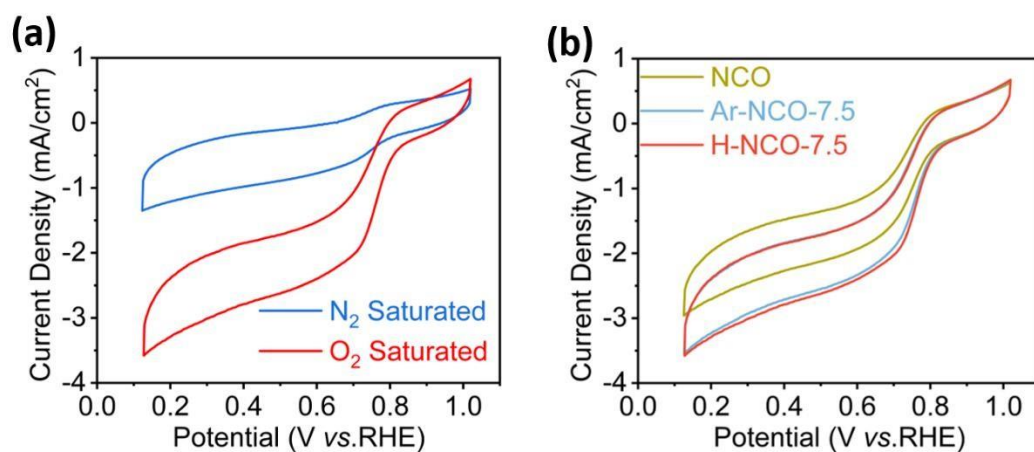


Figure S5. (a) CV curves of H-NCO-7.5 in N_2 - and O_2 saturated 1 M KOH for ORR. (b) CV curves of the samples in O_2 saturated 1 M KOH for ORR.

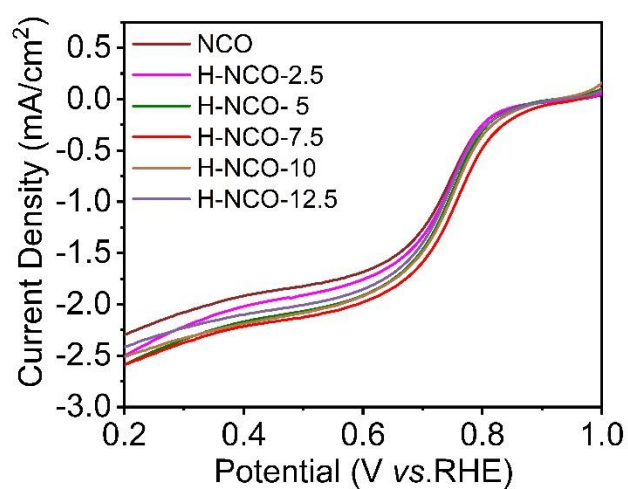


Figure S6. LSV curves of NiCo_2O_4 nanowires under different H_2 plasma treatment times in O_2 saturated 1 M KOH for ORR.

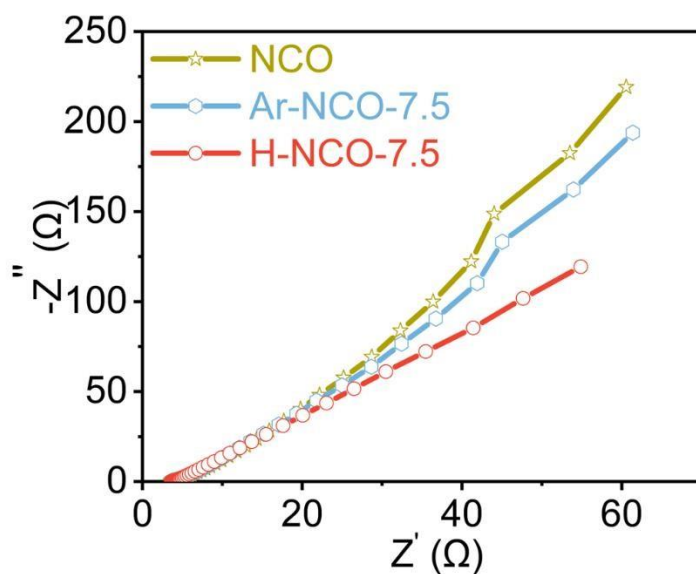


Figure S7. EIS Nyquist plots of NCO, Ar-NCO-7.5 and H-NCO-7.5 in O_2 saturated 1 M KOH for ORR.

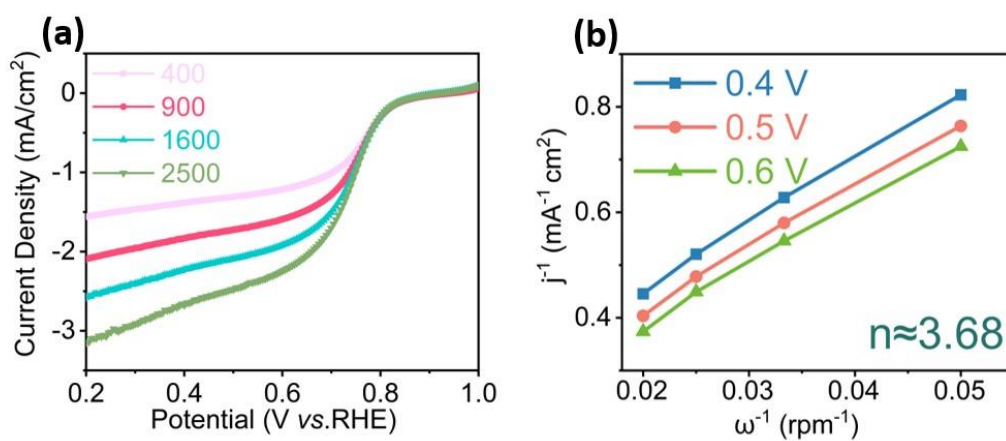


Figure S8. (a) ORR LSV curves of H-NCO-7.5 in O_2 saturated 1 M KOH under different rotation rates. (b) the corresponding K-L plots at different potentials.

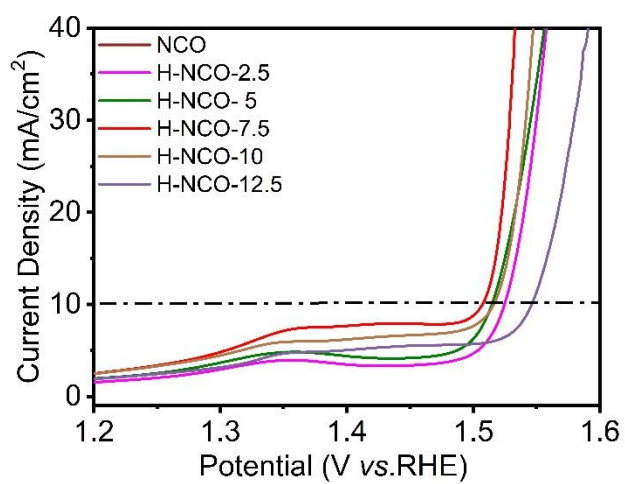


Figure S9. LSV curves of NiCo₂O₄ nanowires under different H₂ plasma treatment times in 1 M KOH for OER.

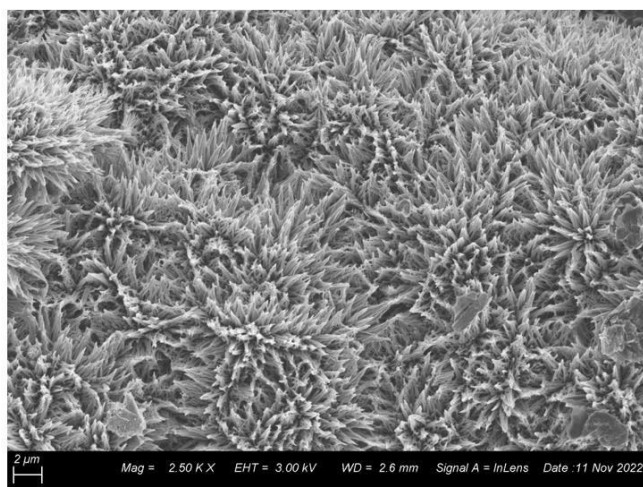


Figure S10. SEM images of the H-NiCo₂O₄-7.5 nanowires after 15 h of operation.

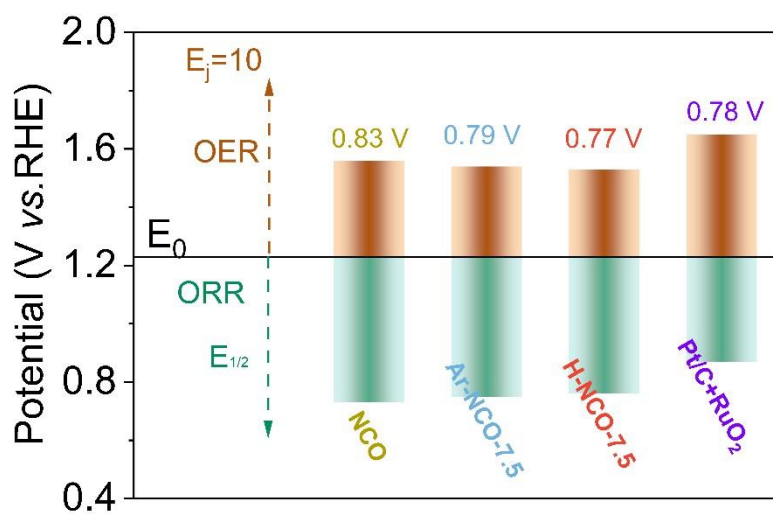


Figure S11. Voltage gap (ΔE) between the $E_{1/2}$ of ORR and the $E_{j=10}$ of OER of the studied catalysts.

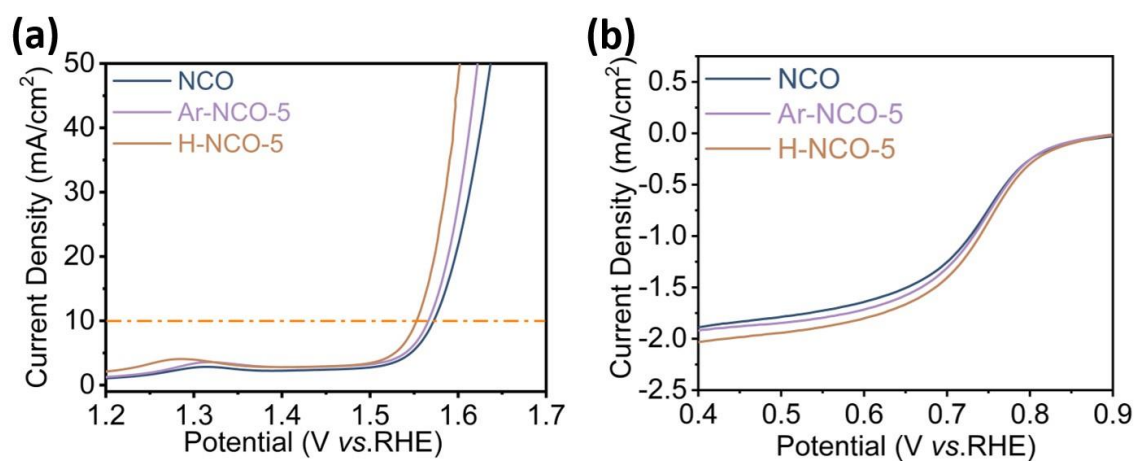


Figure S12. LSV curves of the samples with 5 min of plasma treatment (a) for OER, and (b) for ORR.

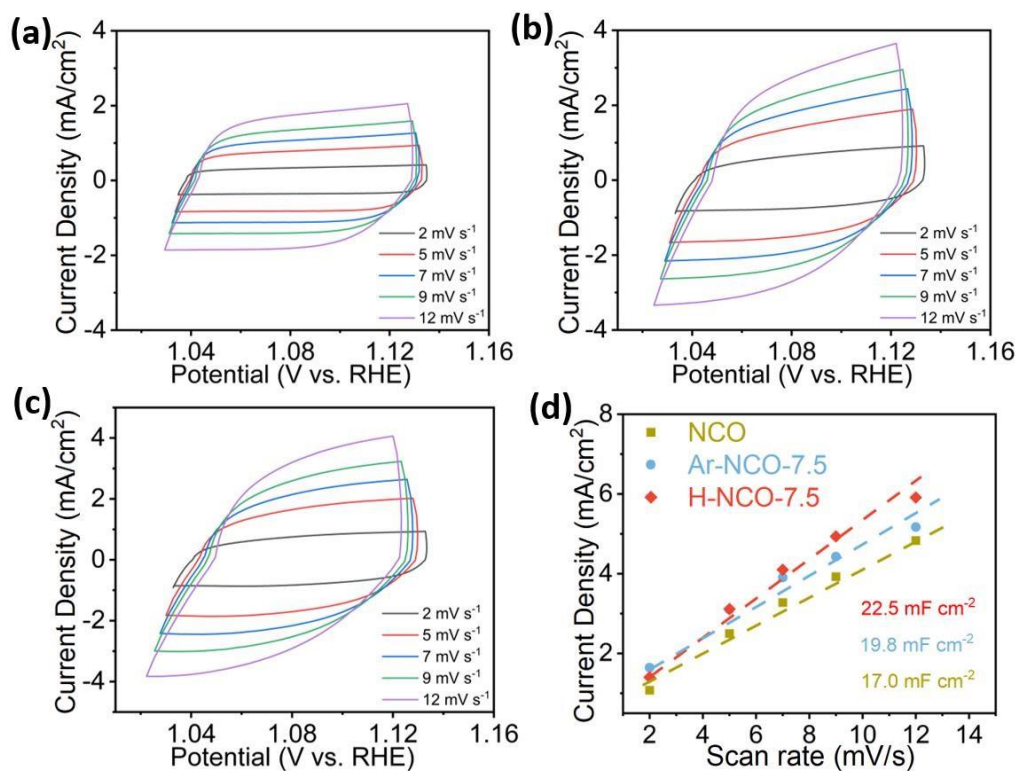


Figure S13. The CV curves of (a) NCO, (b) Ar-NCO-7.5 and (c) H-NCO-7.5 at different scan rates in 1 M KOH. (d) The determination of the corresponding C_{dl} values.

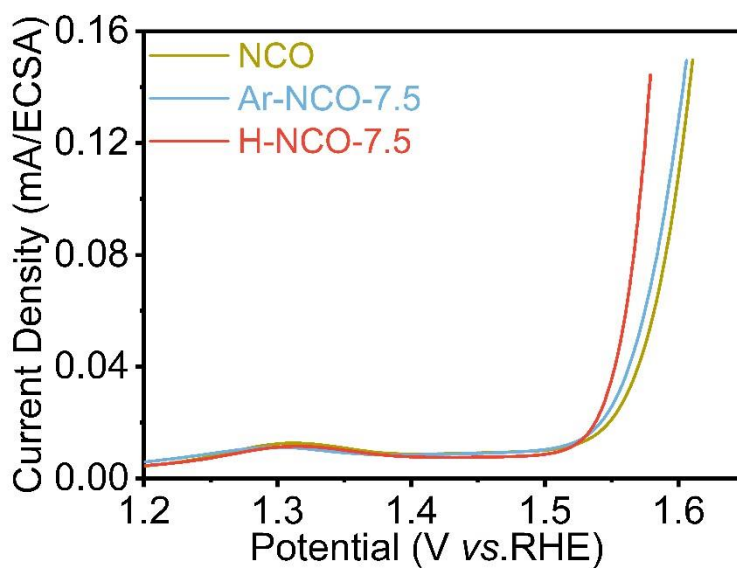


Figure S14. LSV curves of the samples normalized to ECSA.

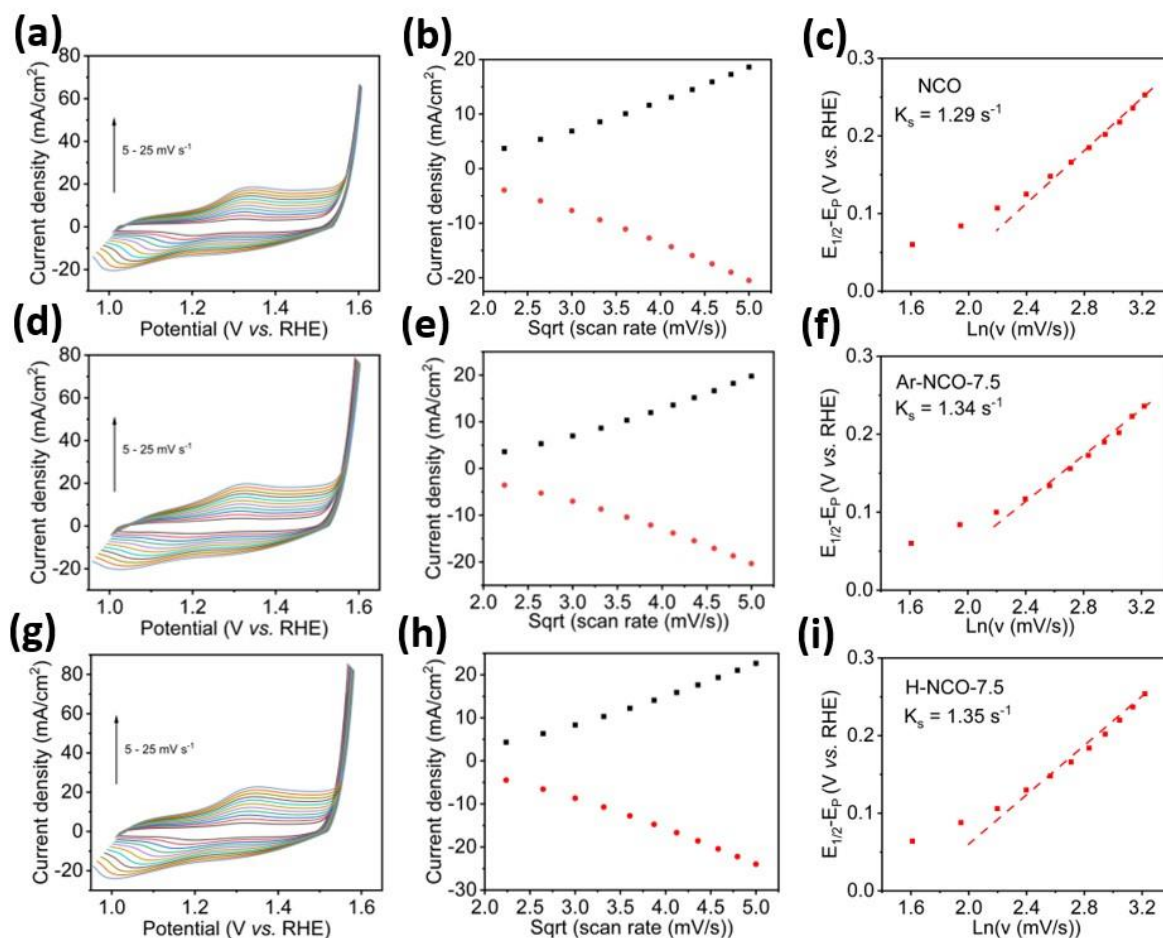


Figure S15. Analysis of the catalysts by Laviron equation. CVs of (a) NCO, (d) Ar-NCO-7.5 and (g) H-NCO-7.5 with scan rates from 5 to 25 mV s^{-1} . The plot of the redox peak current densities versus the square root of scan rates for (b) NCO, (e) Ar-NCO-7.5 and (h) H-NCO-7.5 samples. The plot of the anode peak potentials versus the logarithm of scan rates for (c) NCO, (f) Ar-NCO-7.5 and (i) H-NCO-7.5 samples.

Note:

Laviron equation

$$E_p = E_{1/2} + \frac{RT}{\alpha nF} \times \ln(RTK_s/\alpha nF) - \frac{RT}{\alpha nF} \times \ln(v)$$

where E_p is the reduction potential of metal redox, $E_{1/2}$ is the formal potential of metal redox, R is the universal gas constant, T is the temperature in kelvin, n is the number of electrons transferred, α is the transfer coefficient, K_s is the rate constant of metal redox, and v is the scan rate in the CV measurements.

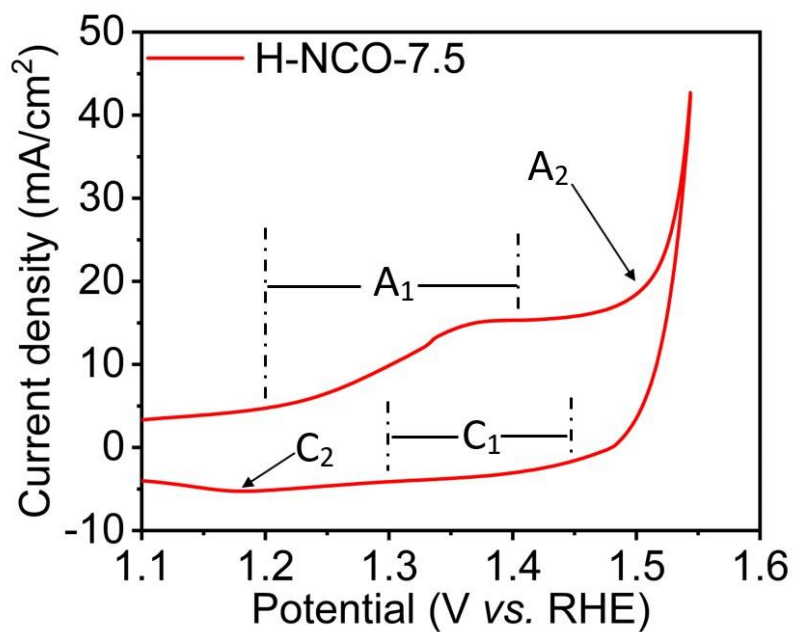


Figure S16. First CV cycle of the H-NCO-7.5 sample.

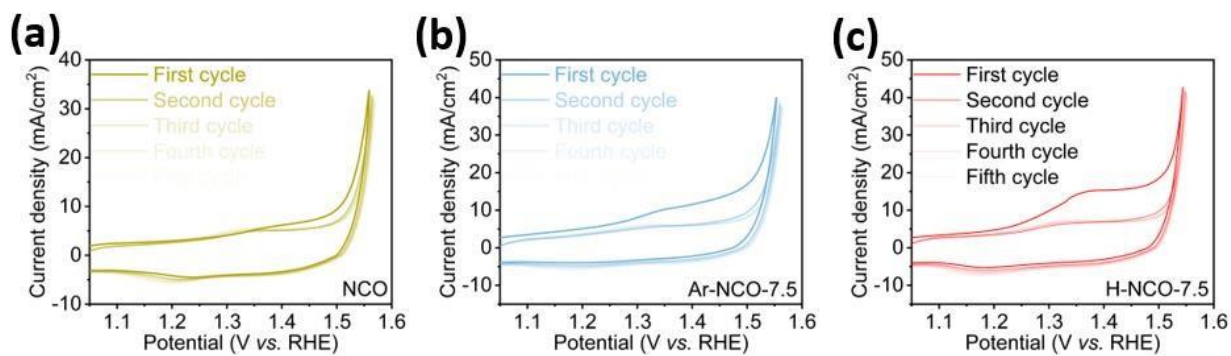


Figure S17. First five CV cycles of (a) NCO, (b) Ar-NCO-7.5 and (c) H-NCO-7.5 samples.

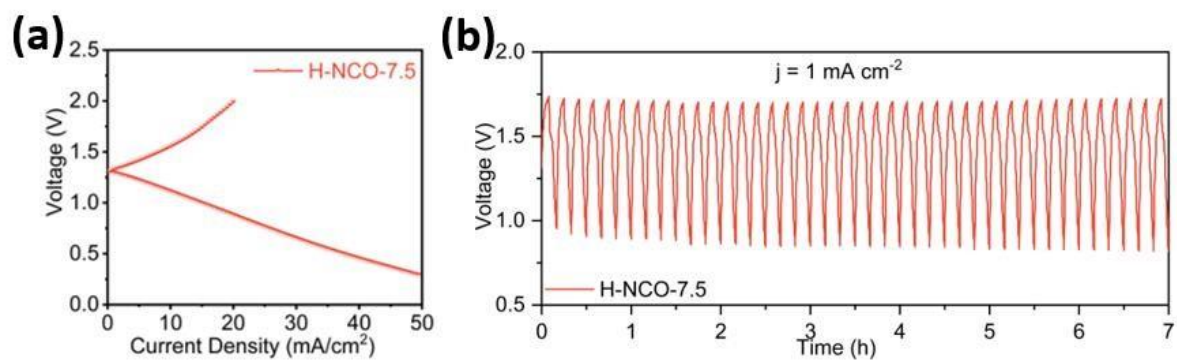


Figure S18. (a) Charging-discharging polarization curves, and (b) galvanostatic charging-discharging cycling test of the zinc-air battery with solid electrolyte.

Table S1. The properties of NiCo₂O₄ nanowires before and after plasma treatment

Catalysts	Specific Surface Area (m ² g ⁻¹)	Ni ₂₊ /Ni ₃₊	Co ₂₊ /Co ₃₊	O ₂ /O ₃
NCO	38.9	0.60	0.47	0.92
Ar-NCO-7.5	45.1	0.93	0.60	1.86
H-NCO-7.5	42.2	1.63	0.80	2.23

Table S2. Comparison of the OER and ORR performance of the NiCo₂O₄-based catalysts for this work with some recently reported catalysts

Catalysts	OER Overpotential (mV) @10 mA cm ⁻²	Durability (h)	ORR E _{1/2} (V)	Electrolyte	ΔE (V)	Ref.
H-NCO-7.5	304	15 h @ 1.53 V	0.76	1 M KOH	0.77	This work
Ar-NCO-7.5	312	----	0.75	1 M KOH	0.79	This work
NCO	324	----	0.73	1 M KOH	0.83	This work
N-NiCo ₂ O ₄ -2 min	300	18 h @ 1.53 V	0.75	1 M KOH	0.78	S1
NiCo ₂ S ₄ /N-CNT	370	-----	0.80	0.1 M KOH	0.80	S2
Zn _{0.4} Ni _{0.6} Co ₂ O ₄ /NCNTs	410	20 h @ 1.64 V	0.78	0.1 M KOH	0.86	S3
N-NiCo ₂ O ₄	419	2.8 h @ 1.65 V	0.63	0.1 M KOH	1.02	S4
NiO/NiCo ₂ O ₄	357	----	0.73	0.1 M KOH	0.86	S5
NiCo ₂ O ₄ -CN-180	383	----	0.81	OER: 1 M KOH ORR: 0.1 M KOH	0.80	S6
NiCo ₂ O ₄ /NCNTs/NiCo	350	32 h @ -0.6 V	0.83	OER: 1 M KOH ORR: 0.1 M KOH	0.75	S7
CoFe/C	430	----	0.85	0.1 M KOH	0.81	S8
ZnCo ₂ Se ₄ @rGO	290	50 h	0.80	0.1 M KOH	0.72	S9
MnCo ₂ O ₄ /NCNTs	363	----	0.76	0.1 M KOH	0.83	S10

Supplementary References

[S1] H. Li, S. Askari, J.H. Wang, N. Wolff, M. Behrens, L. Kienle, J. Benedikt, Nitrogen-doped NiCo₂O₄ nanowires on carbon paper as a self-supported air cathode for rechargeable Zn-air batteries, *Int. J. Hydrogen. Energ.*, 2023, 48, 26107-26118.

[S2] X.P. Han, X.Y. Wu, C. Zhong, Y.D. Deng, N.Q. Zhao, W.B. Hu, NiCo₂S₄ nanocrystals anchored on nitrogen-doped carbon nanotubes as a highly efficient bifunctional electrocatalyst for rechargeable zinc– air batteries. *Nano Energy*, 2017, 31, 541-550.

[S3] X.T. Wang, T. Ouyang, L. Wang, J.H. Zhong, Z.Q. Liu, Surface reorganization on electrochemically induced Zn–Ni–Co spinel oxides for enhanced oxygen electrocatalysis, *Angew. Chem. Int. Ed.* 2020, 59, 6492–6499.

[S4] J.J. Bian, X.P. Cheng, X.Y. Meng, J. Wang, J.G. Zhou, S.Q. Li, Y.F. Zhang, C.W. Sun, Nitrogen-doped NiCo₂O₄ microsphere as an efficient catalyst for flexible rechargeable zinc-air batteries and self-charging power system, *ACS Appl. Energy Mater.*, 2019, 2, 2296-2304.

[S5] Z.M. Zhang, X.L. Liang, J.F. Li, J.M. Qian, Y.G. Liu, S.L. Yang, Y. Wang, D.Q. Gao, D.S. Xue, Interfacial engineering of NiO/NiCo₂O₄ porous nanofibers as efficient bifunctional catalysts for rechargeable zinc–air batteries, *ACS Appl. Mater. Interfaces*, 2020, 12, 21661-21669.

[S6] Y. Li, Z.H. Zhou, G. Cheng, S.B. Han, J.L. Zhou, J.K. Yuan, M. Sun, L. Yu, Flower-like NiCo₂O₄–CN as efficient bifunctional electrocatalyst for Zn-Air battery, *Electrochim. Acta*, 2020, 341, 135997.

[S7] C. Chen, H. Su, L.N. Lu, Y.S. Hong, Y.Z. Chen, K. Xiao, Y. Ouyang, Y.L. Qin, Z.Q. Liu, Interfacing spinel NiCo₂O₄ and NiCo alloy derived N-doped carbon nanotubes for enhanced oxygen electrocatalysis, *Chem. Eng. J.*, 2021, 408, 127814.

[S8] M.L. Jiao, Q. Zhang, C.L. Ye, R.H. Gao, L.X. Dai, G.M. Zhou, H.M. Cheng, Isolating contiguous Fe atoms by forming a Co–Fe intermetallic catalyst from spent lithium-ion batteries to regulate activity for zinc–air batteries, *ACS Nano*, 2022, 16, 13223-13231.

[S9] R.S. Kumar, S. Prabhakaran, S. Ramakrishnan S.C. Karthikeyan, A.R. Kim, D.H. Kim. D.J. Yoo, Developing outstanding bifunctional electrocatalysts for rechargeable Zn-air batteries using high-purity spinel-type ZnCo₂Se₄ nanoparticles, *Small*, 2023, 2207096.

[S10] Z.P. Wang, J.H. Huang, L. Wang, Y.Y. Liu, W.H. Liu, S.L. Zhao, Z.Q. Liu, Cation-tuning induced d-band center modulation on Co-based spinel oxide for oxygen reduction/evolution reaction, *Angew. Chem. Int. Edit.*, 2022, 61, e202114696.

9.3 Plasma-engineering of Pt-decorated NiCo₂O₄ nanowires with rich oxygen vacancies for enhanced oxygen electrocatalysis and zinc-air battery performance

Supporting Information for

Plasma-engineering of Pt-decorated NiCo₂O₄ nanowires with rich oxygen vacancies for enhanced oxygen electrocatalysis and zinc-air battery performance

He Li¹, Luka Hansen^{1,2}, Ainura Aliyeva³, Jihao Wang⁴, Haoyi Qiu⁵, Martin Müller⁶, Cenk Aktas³, Lorenz Kienle^{2,6}, Jan Benedikt^{1,2*}

¹ Institute of Experimental and Applied Physics, Kiel University, Leibnizstraße 19, D-24098 Kiel, Germany

² Kiel Nano, Surface and Interface Science KiNSIS, Kiel University, Christian-Albrechts-Platz 4, D-24118 Kiel, Germany

³ Chair for Multicomponent Materials, Department of Materials Science, Faculty of Engineering, Kiel University, Kaiserstraße 2, D-24143 Kiel, Germany

⁴ Institute of Inorganic Chemistry, Kiel University, Max-Eyth-Straße 2, D-24118 Kiel, Germany

⁵ Chair for Functional Nanomaterials, Department of Materials Science, Faculty of Engineering, Kiel University, Kaiserstraße 2, D-24143 Kiel, Germany

⁶ Chair for Synthesis and Real Structure, Department of Materials Science, Faculty of Engineering, Kiel University, Kaiserstraße 2, D-24143 Kiel, Germany

*Corresponding author.

Supplementary Methods:

Materials: Commercial carbon paper (CP) was purchased from sgl carbon, Germany. $\text{Ni}(\text{NO}_3)_2 \cdot 6\text{H}_2\text{O}$ (98%), $\text{Co}(\text{NO}_3)_2 \cdot 6\text{H}_2\text{O}$ (98%), NH_4F (98%), $\text{CO}(\text{NH}_2)_2$ (98%), $\text{Zn}(\text{CH}_3\text{CO}_2)_2$ (99.99%), KOH (85%), nitric acid (70%), H_2PtCl_6 solution (8 wt.%) and Nafion 1100EW (5 wt.%) were purchased from Sigma-Aldrich. Ar gas (99.999%) was purchased from Air Liquid and H_2 gas (99.999%) was produced by Messer Schweiz AG.

Synthesis of NiCo_2O nanowires with oxygen vacancies (Ar-NCO): NiCo_2O_4 nanowires coated on the carbon papers (NCO) were synthesized by the method as reported in our previous works [S1-S2]. After that, the NCO sample was put into a glass tube reactor and modified by radio frequency (27.12 MHz) Ar plasma treatment. The applied power was 200 W, the working pressure was maintained at 20 Pa and the treatment duration was 7.5 min.

Synthesis of Pt decorated NiCo_2O nanowires with oxygen vacancies (Pt/Ar-NCO): Pt atoms were anchored on the Ar-NCO sample using an impregnation-plasma reduction method. Briefly, 0.1 mL H_2PtCl_6 solution was first slowly added to the mixed solution of 9 mL water and 1 mL ethanol. Afterwards, one Ar-NCO substrate was immersed in this solution for 30 min. After drying overnight, the sample was reduced by H_2/Ar plasma for 10 s. The working power and pressure of the plasma were controlled at 50 W and 20 Pa, respectively. For comparison, Pt atoms were also anchored on the NCO sample without Ar plasma pre-treatment as Pt/NCO.

Characterization: The crystal structure of the samples was obtained from X-ray diffraction (XRD, Stoe Stadi P diffractometer system) with $\text{Mo K}\alpha$ radiation ($\lambda = 0.7093 \text{ \AA}$). The morphologies, structure and element contribution of the samples were characterized by scanning electron microscopy (SEM, Zeiss EVO 10 with LaB6 filament, 20kV acceleration voltage for imaging) with energy-dispersive X-ray spectroscopy (EDS, OXFORD Xplore 15, 10 kV acceleration voltage for increased surface sensitivity) and transmission electron microscope (TEM, Tecnai F30 G2 STwin). The surface composition and element valence of the samples were investigated by X-ray photoelectron spectroscopy (XPS, PREVAC Sp. z o. o.) with Al-anode (300W). All binding energies were corrected with C 1s at 284.8 eV. The chemical composition of the samples were further studied by Raman spectroscopy (532 nm, alpha 300 RA).

Electrochemical measurements: The OER and ORR measurements were performed by an electrochemical workstation (Wave Driver 200, Pine Research) with a standard three-electrode system in 1 M KOH electrolyte, where an Ag/AgCl electrode (3 M KCl), a Pt wire, and the electrode with the prepared

catalysts were used as the reference electrode, the counter electrode, and the working electrode, respectively. All reported potentials (vs. Ag/AgCl) in this work were referenced to the reversible hydrogen electrode potentials (vs. RHE). All cyclic voltammetry (CV) and linear sweep voltammetry (LSV) curves were modified by iR compensation.

For OER measurements, the samples were cut to 1 cm × 1 cm and directly used as the working electrode and the RuO₂ catalyst (1 mg cm⁻²) coated on carbon paper was used as the benchmark. Before testing, the catalyst was first activated by the CV cycling at a scan rate of 100 mV s⁻¹ for several cycles until the current became stable. CV scans were performed at a scan rate of 10 mV s⁻¹ from 1.2 to 1.8 V vs. RHE. LSV curves were collected at a scan rate of 5 mV s⁻¹ from 1.2 to 1.8 V vs. RHE. The electrochemical double-layer capacitance (C_{dl}) was obtained through the CV curves from 1.03 to 1.13 V vs. RHE under different scan rates (2 to 12 mV s⁻¹). The OER stability of the catalysts was evaluated by the chronopotentiometric test at 10 mA cm⁻².

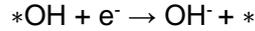
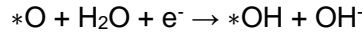
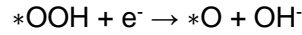
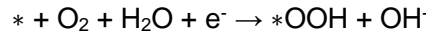
Before ORR measurements, the catalyst inks were prepared first. In brief, 5 mg of the catalyst powder was scraped off from the carbon paper and mixed with 1000 μL of isopropanol and 40 μL of Nafion solution. After sonicated for at least 30 min, 12 μL of the catalyst ink was cast onto the polished glassy carbon electrode (GCE, Ø 6 mm) and dried for 15 min at 65 °C. The loading amount of the catalyst was approximately 0.2 mg cm⁻². For ORR measurements, the rotation rate was controlled at 1600 rpm first, then the electrode was also activated by CV tests at a scan rate of 100 mV s⁻¹ for several cycles until current became stable. Electrochemical impedance spectroscopy (EIS) data were collected at 0 V vs. Ag/AgCl from 100 kHz to 1 Hz. CV scans were performed in N₂-saturated and O₂-saturated electrolytes at a scan rate of 100 mV s⁻¹ from 1.2 to 0.2 V vs. RHE. LSV curves were recorded from 1.2 to 0.2 V vs. RHE at a scan rate of 5 mV s⁻¹. The LSV curves were also recorded at a scan rate of 5 mV s⁻¹ and different rotation rates from 400 to 2500 rpm from 1.2 to 0.2 V vs. RHE to evaluate the electron transfer numbers (n) during the ORR process by the Koutecky-Levich (K-L) equation [S1].

Battery test: An aqueous rechargeable zinc-air battery was assembled by a polished Zn anode electrode, a mixed electrolyte of 6 M KOH and 0.2 M Zn(Ac)₂ and the air cathode with the as-prepared catalyst. The cycling tests were performed by recurrent galvanostatic pulses at a current density of 5 mA cm⁻² with 20 min per cycle (charge for 10 min and discharge for 10 min) and other tests were recorded on the electrochemical workstation. For comparison, a commercial Pt/C + RuO₂ (1mg cm⁻², 1:1) catalyst

coated on CP was employed as the reference.

DFT calculation: The density functional theory (DFT) calculation was performed based on Vienna Ab-initio Simulation Package (VASP) with the generalized gradient approximation (GGA) of Perdew-Burke-Ernzerhof (PBE) functional for exchange correlation functional and the projector augmented wave (PAW) method [S3-S4]. The cut-off energy of Plane-Wave basis was set at 500 eV and the K-points grid sampling of Monkhorst-Pack scheme was $3 \times 3 \times 1$. All geometrie structures were optimized until the residual force was smaller than $0.02 \text{ eV } \text{\AA}^{-1}$, and the energy convergence is $10^{-6} \text{ eV } \text{\AA}^{-1}$. All geometries were supercells with 15 \AA of the vacuum layers to prohibited interactions among neighboring layers. The dispersion corrections using DFT-D2 method by Grimme et al. were used to describe van der Waals (vdW) interactions in all the calculations [S5].

In alkaline electrolyte, the ORR process presents the following four steps:



namely, O_2 is adsorbed at the active sites (labelled by $*$) and hydrogenates to $*\text{OOH}$, $*\text{OOH}$ decomposes to $*\text{O}$ and OH^- , $*\text{O}$ hydrogenates to $*\text{OH}$, and finally $*\text{OH}$ is reduced to OH^- [S6].

The Gibbs free energy change (ΔG) is given by the formula: $\Delta G = \Delta E + \Delta ZPE - T\Delta S$ with ΔE , being the formation energy change of intermediates obtained from DFT calculations, ΔZPE being the zero-point vibration energy change, and ΔS being the entropy change. In this work, the free energy values of these intermediates ($*\text{OOH}$, $*\text{O}$, $*\text{OH}$) were calculated by the following formula:

$$\Delta G_{*\text{OOH}} = G_{*\text{OOH}} - G_* - (G_{\text{O}_2} + \frac{1}{2} G_{\text{H}_2})$$

$$\Delta G_{*\text{O}} = G_{*\text{O}} - G_* - (G_{\text{O}_2} + G_{\text{H}_2} - G_{\text{H}_2\text{O}})$$

$$\Delta G_{*\text{OH}} = G_{*\text{OH}} - G_* - (G_{\text{O}_2} + \frac{3}{2} G_{\text{H}_2} - G_{\text{H}_2\text{O}})$$

With G_* being the Gibbs free energy of the catalyst surface. The $G_{*\text{OOH}}$, $G_{*\text{O}}$ and $G_{*\text{OH}}$ are the Gibbs free energies of adsorption of OOH, O, and OOH species, respectively. The G_{H_2} and $G_{\text{H}_2\text{O}}$ are the calculated Gibbs free energies of H_2 and H_2O in gas phase, respectively. The G_{O_2} is calculated by $G_{\text{O}_2} = 2G_{\text{H}_2\text{O}} - 2G_{\text{H}_2} + 4.92$ and the free energy of a proton and electron pair ($\text{H}^+ + \text{e}^-$) is equivalent to that of a half of gaseous H_2 . In conclusion, the Gibbs free energy change for the four steps of ORR process can be

calculated by the following formula:

$$\Delta G_1 = \Delta G_{*OOH} - eU$$

$$\Delta G_2 = \Delta G_{*O} - \Delta G_{*OOH} - eU$$

$$\Delta G_3 = \Delta G_{*OH} - \Delta G_{*O} - eU$$

$$\Delta G_4 = 4.92 - \Delta G_{*OH} - eU$$

where U is the potential measured against normal hydrogen electrode (NHE) at standard conditions.

Supplementary Figures

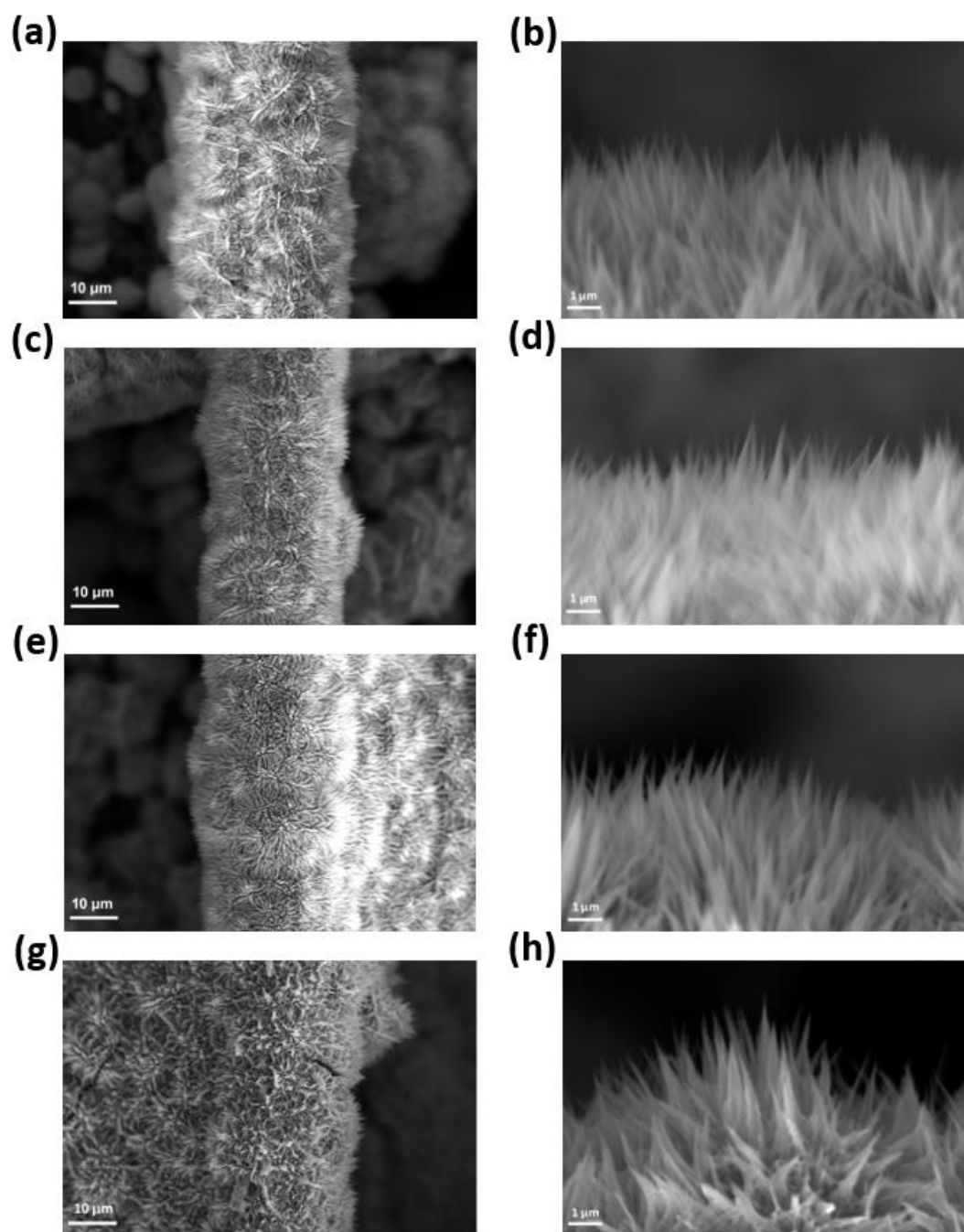


Figure S1. SEM images of (a, b) the NCO sample; (c, d) the Ar-NCO sample; (e, f) the Pt/NCO sample and (g, h) the Pt/Ar-NCO sample.

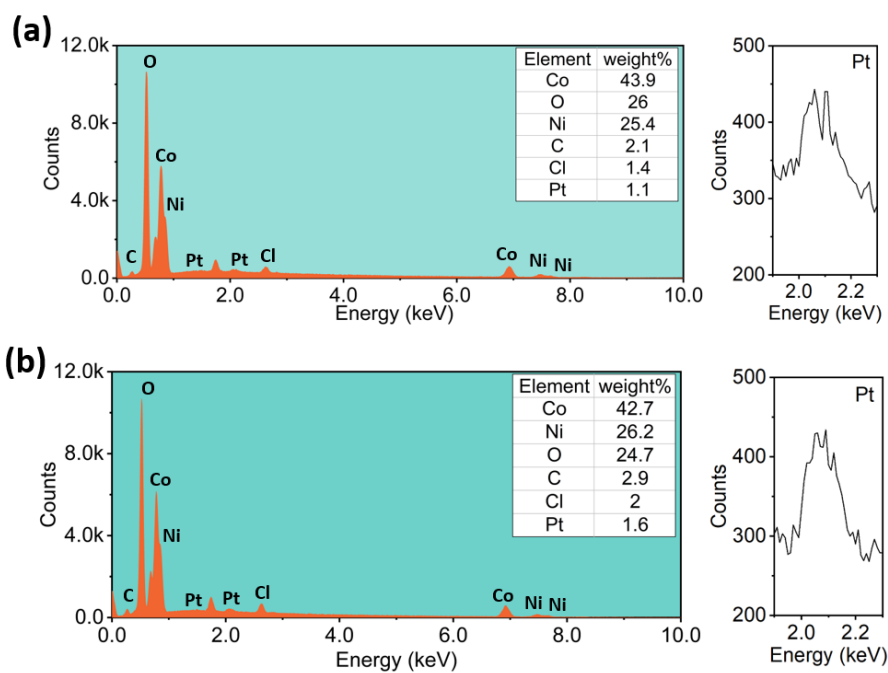


Figure S2. SEM-EDS results of (a) the Pt/NCO sample and (b) the Pt/Ar-NCO sample.

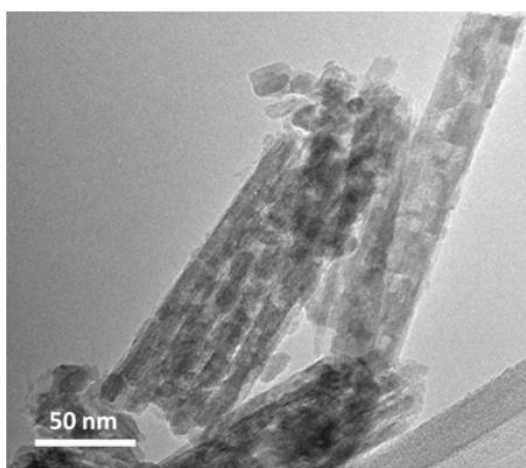


Figure S3. TEM image of the NCO sample.

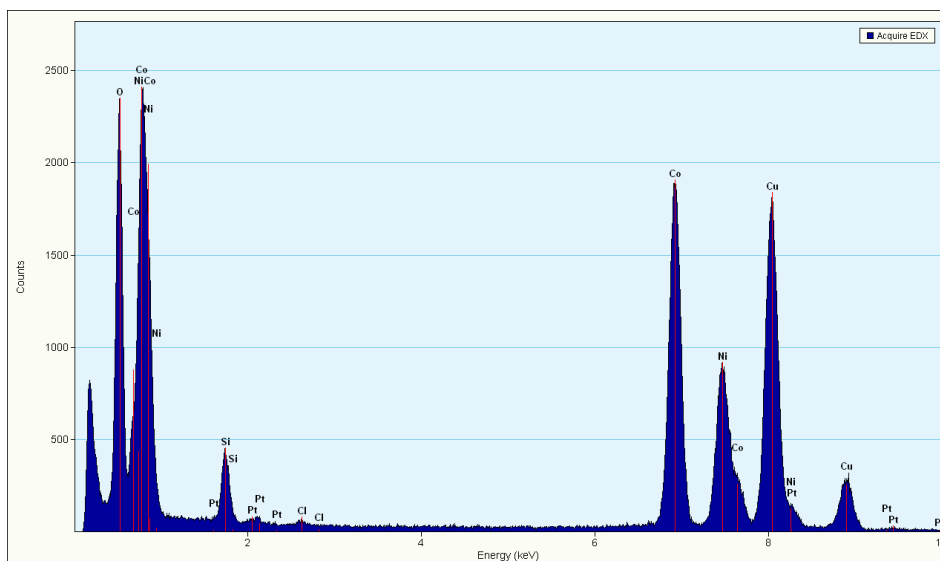


Figure S4. TEM-EDS result of the Pt/Ar-NCO sample.

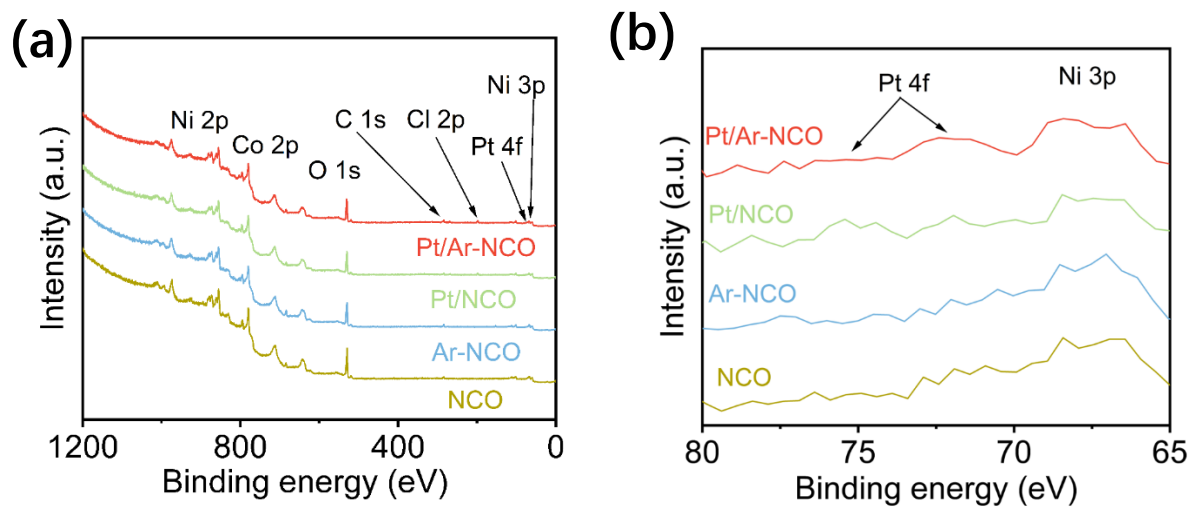
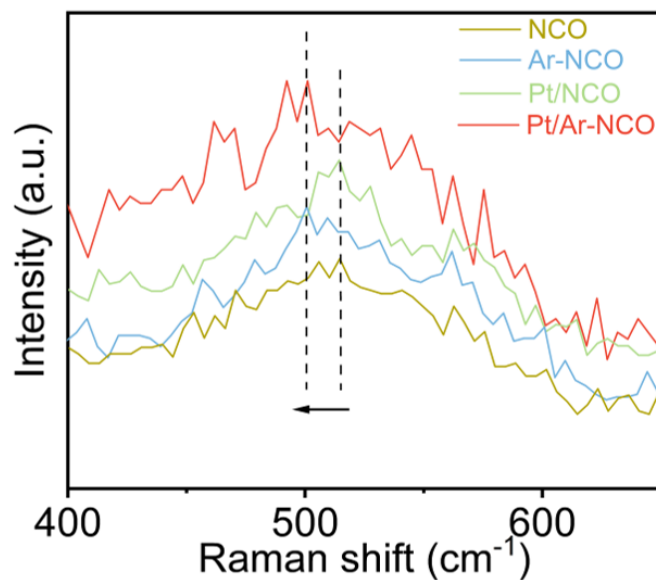
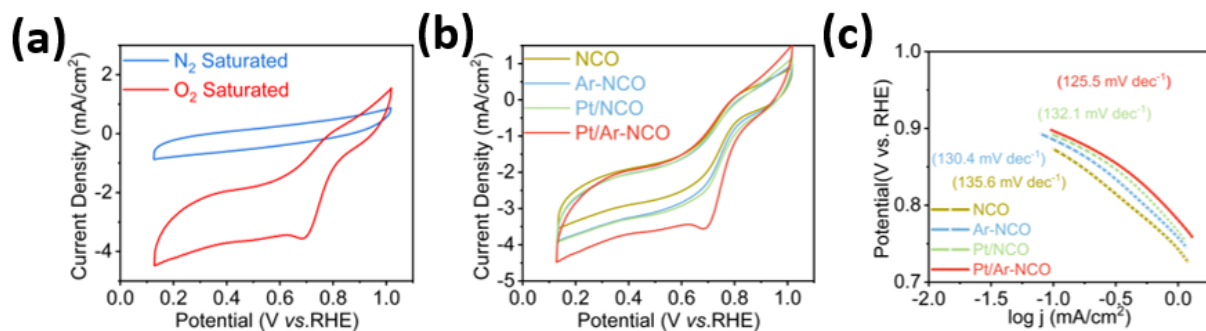


Figure S5. full range XPS spectra (a) with the zoom-in image (b) of the samples.

Figure S6. Raman spectra of the samples from 400 to 600 cm^{-1} .Figure S7. CV curves of the Pt/Ar-NCO catalyst in N_2 - and O_2 - saturated 1 M KOH for ORR, (b) CV curves of the catalysts in O_2 -saturated 1 M KOH for ORR, (c) Tafel plots of the catalysts for ORR.

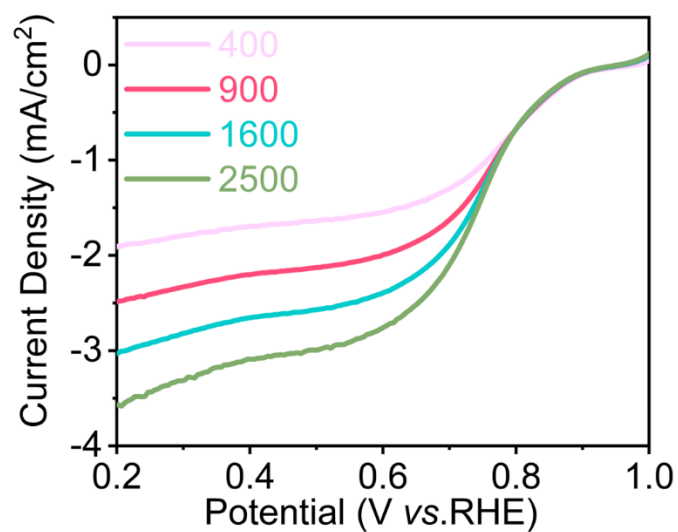


Figure S8. ORR LSV curves of the Pt/Ar-NCO catalyst under different rotation rates.

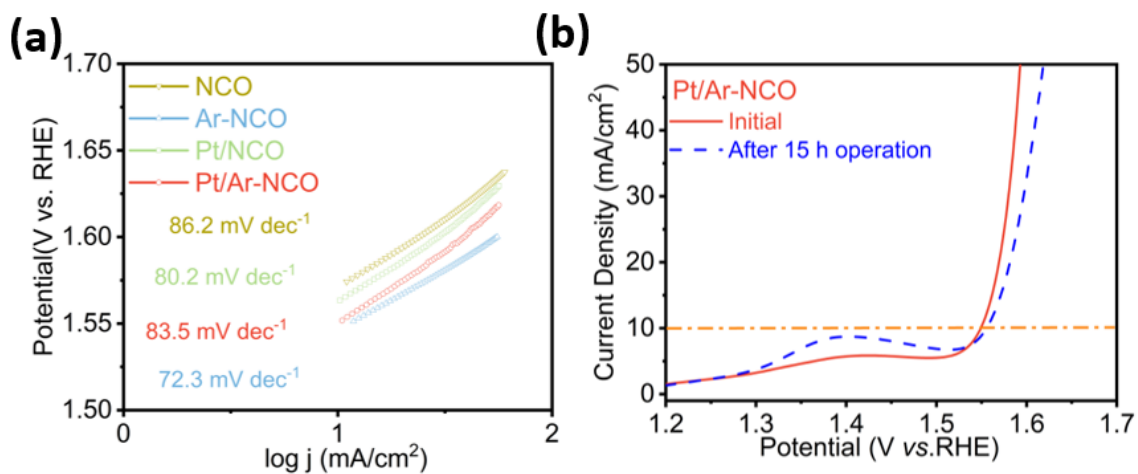


Figure S9. (a) Tafel plots of the catalysts for OER, (b) LSV curves of the Pt/Ar-NCO catalyst before and after the long-term operation.

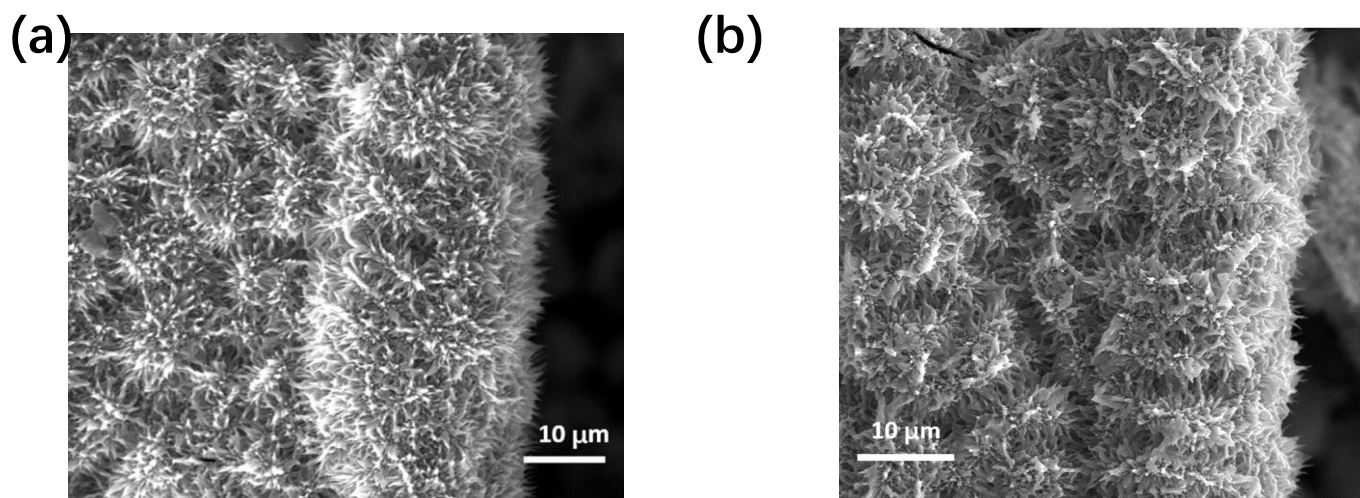


Figure S10. The SEM image of the Pt/Ar-NCO catalyst (a) before and (b) after 15 h of operation.

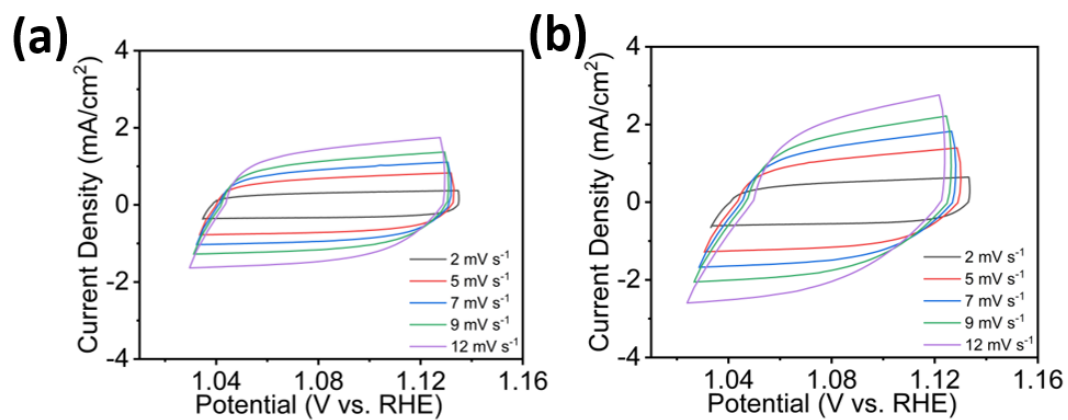


Figure S11. The CV curves of (a) the NCO catalyst and (b) the Pt/Ar-NCO catalyst at different scan rates.

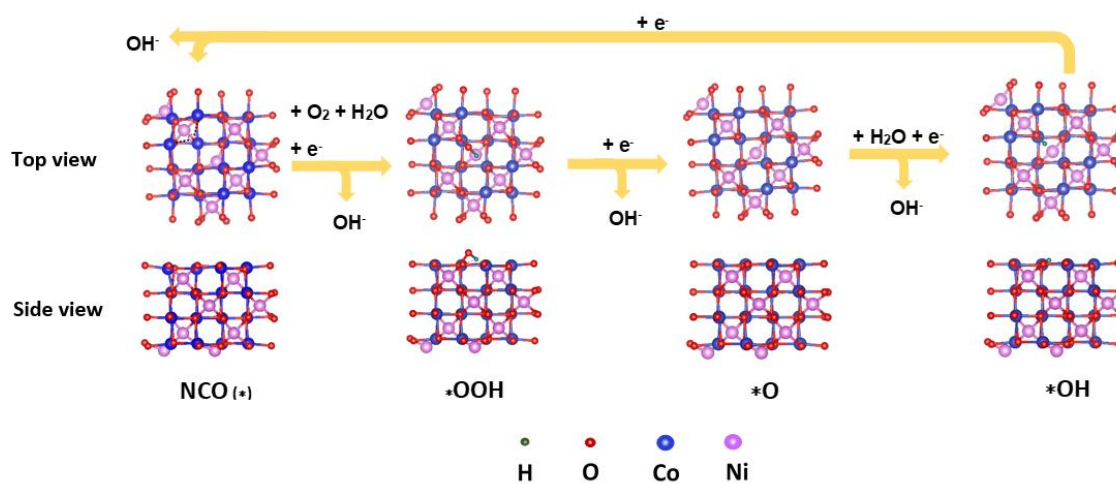


Figure S12. Schematic illustration of the proposed electrochemical ORR pathway by the NCO catalyst.

Supplementary Tables

Table S1. The element states of the sample surfaces.

Sample Name	Co ²⁺ /Co ³⁺	Ni ²⁺ /Ni ³⁺	O2/O1
NCO	0.58	1.00	0.79
Ar-NCO	0.67	1.11	1.03
Pt/NCO	0.65	1.03	0.90
Pt/Ar-NCO	0.75	1.20	1.31

Reference:

- [S1] H. Li, S. Askari, J. H. Wang, N. Wolff, M. Behrens, L. Kienle, J. Benedikt, Nitrogen-doped NiCo₂O₄ nanowires on carbon paper as a self-supported air cathode for rechargeable Zn-air batteries, *Int. J. Hydrogen. Energ.*, 2023, 48, 26107-26118.
- [S2] H. Li, J. H. Wang, T. Tjardts, I. Barg, H. Y. Qiu, M. Müller, J. Krahmer, S. Askari, S. Veziroglu, C. Aktas, L. Kienle, J. Benedikt, Plasma-engineering of oxygen vacancies on NiCo₂O₄ nanowires with enhanced bifunctional electrocatalytic performance for rechargeable zinc-air battery, *Small*, 2024, 2310660.
- [S3] C. Chen, H. Su, L. N. Lu, Y. S. Hong, Y. Z. Chen, K. Xiao, T. Ouyang, Y. L. Qin, Z. Q. Liu, Interfacing spinel NiCo₂O₄ and NiCo alloy derived N-doped carbon nanotubes for enhanced oxygen electrocatalysis, *Chem. Eng. J.*, 2021, 408, 127814.
- [S4] J. B. Luo, X. Z. Wang, Y. F. Gu, S. T. Wang, Y. P. Li, T. Y. Wang, Y. Liu, Y. Zhou, J. Zhang, Hierarchical sheet-like W-doped NiCo₂O₄ spinel synthesized by high-valence oxyanion exchange strategy for highly efficient electrocatalytic oxygen evolution reaction, *Chem. Eng. J.*, 2023, 472, 144839.
- [S5] S. Grimme, Accurate description of van der Waals complexes by density functional theory including empirical corrections, *J. Comput. Chem.*, 2004, 24, 1463-1473.
- [S6] S. Z. Liu, L. Cheng, K. Li, Y. Wang, Y. W. Yang, Z. J. Wu, The reaction pathways of the oxygen reduction reaction on IrN₄ doped divacancy graphene: A theoretical study, *J. Mol. Graph. Model.*, 2018, 80, 293-298.

Acknowledgement

I would like to thank everyone who has accompanied me during my research. Without them, I cannot finish it.

I would like to sincerely thank Prof. Dr. Jan Benedikt for the opportunity to conduct this research in his group. Thank you for his constant support, trust and guidance on my research. He is very friendly and confident and I really enjoyed working with him.

A big thank you to Prof. Dr. Lorenz Kienle as the second reviewer for my thesis. I also appreciate his support in my published papers.

I would like to thank Dr. Sadegh Askari for his guidance in the early stages of my research. He taught me how to use all setups in my lab.

I would like to thank Dr. Luka Hansen for his support in the final examination of my thesis.

Of course, without the help of my dear colleagues in the group, this research would not be finished. I would like to thank Mr. Michael Poser, Mr. Volker Rohwer and Mr. Frank Brach for making the research go well. I would like to thank Kerstin Sgonina, Maren Dworschak, Tristan Winzer, Alexander Quack, Christian Schulze, Natascha Blosczyk, Yang Liu, Armin Mengel, Jana Mergemeier, Andreas Petersen, Alexander Schmitz, Sören Wohlfahrt, Görkem Bilgin, Isabel König for their support and friendship. I had a lot of fun working with them.

I would like to thank Dr. Martin Müller for his support in my research. It was really happy working with you.

I would like to thank Prof. Dr. Malte Behrens, Prof. Dr. Rainer Adelung, Prof. Dr. Cenk Aktas, Dr. Jihao Wang, Dr. Haoyi Qiu, and Mr. Tim Tjardts for their support on material characterizations.

I would like to thank the China Scholarship Council for the funding support.

Finally, I would like to thank my parents for their unconditional support and love. I really appreciate my wife who gave up everything to accompany me in a foreign country. I also appreciate my daughter who has brought me a lot of happiness.

Publication list

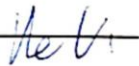
This thesis is based on following publications, which have been published in different journals.

1. H. Li, S. Askari, J. H. Wang, N. Wolff, M. Behrens, L. Kienle, J. Benedikt, Nitrogen-doped NiCo₂O₄ nanowires on carbon paper as a self-supported air cathode for rechargeable Zn-air batteries, *Int. J. Hydrogen. Energ.*, 2023, 48, 26107-26118.
<https://doi.org/10.1016/j.ijhydene.2023.03.146>
2. H. Li, J. H. Wang, T. Tjardts, I. Barg, H. Y. Qiu, M. Müller, J. Krahmer, S. Askari, S. Veziroglu, C. Aktas, L. Kienle, J. Benedikt, Plasma-engineering of oxygen vacancies on NiCo₂O₄ nanowires with enhanced bifunctional electrocatalytic performance for rechargeable zinc-air battery, *Small*, 2024, 20, 2310660.
<https://doi.org/10.1002/sml.202310660>
3. C. Schulze, H. Li, L. Mohn, M. Müller, J. Benedikt, Chamber with inverted electrode geometry for measuring and control of ion flux-energy distribution functions, *Plasma*, 2022, 5, 295-305.
<https://doi.org/10.3390/plasma5030023>

Declaration

I declare that this thesis has been finished solely by myself, apart from the advice of my supervisor Prof. Dr. Jan Benedikt. This dissertation has not been submitted either partially or wholly as part of a doctoral degree to another examining body. Parts of this thesis have already been published in scientific journals or have been submitted for publication. This thesis was prepared with regard to the Rules of Good Scientific Practice of the German Research Foundation. I further declare that none of my academic degrees have ever been withdrawn.

Kiel, den



18. 06. 2024